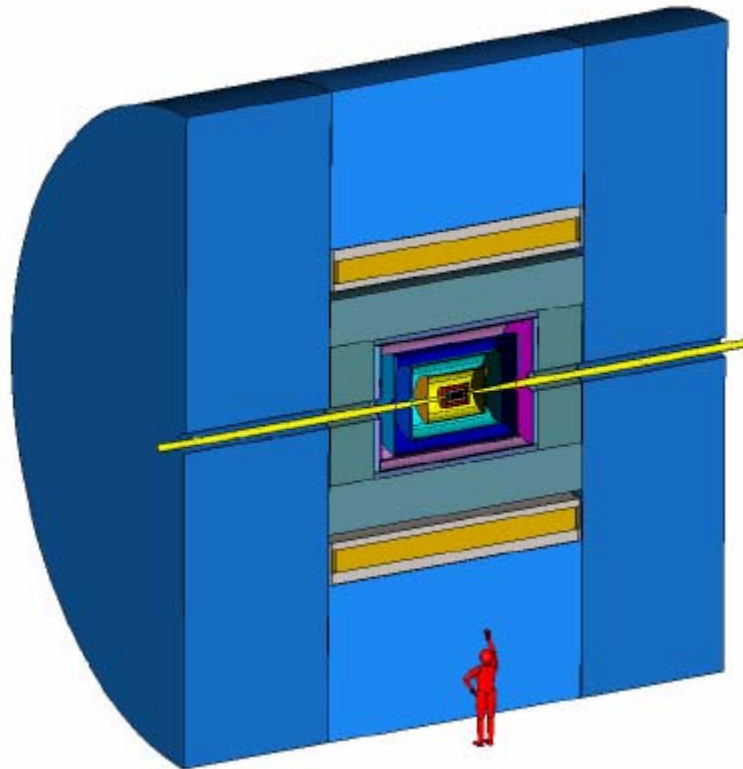


SiD Detector Outline Document

Version of 19 May 2006 1:11:36 PM CST



Contents

SiD Detector Outline Document.....	1
Contents	2
Figures.....	4
I. Introduction	10
I.A The ILC Physics Menu	10
I.B The ILC Environment	11
I.C SiD Rationale.....	12
I.D SiD Starting Point, Integrated Performance, and the Optimization Process	13
I.E Design Study Origins, Organization, and Plans: SiD Snapshot on Road to CDR14	
I.F Authors	17
II. Detector Design Requirements.....	20
II.A Subsystem Performance Required by the Physics	20
II.B Physics, Environment, and Costs Drive the SiD Detector Design	25
II.B.1 ILC Environmental Concerns.....	25
II.B.2 Expected Backgrounds at the ILC	28
II.C. Costing Overview.....	34
III. The SiD Detector	36
III.A Global Issues	36
III.A.1 IR Hall: Detector footprint, assembly and access strategy	36
III.A.2 Machine/detector interface issues	39
III.B Beamline.....	44
III.B.1 The 2 mrad Beamline Layout.....	44
III.B.2 The 20 mrad Beamline Layout.....	45
III.B.3 The 14 mrad Alternate Beamline Layout.....	47
III.C Tracking System.....	50
III.C.2 Vertex Detector Design.....	50
III.C.3 Tracker Design	67
III.C.4 Tracking Simulation and Reconstruction.....	71
III.C.5 Simulated tracking Performance	81
III.D Calorimeter concept.....	85
III.D.1 The Electromagnetic Calorimeter (ECAL).....	86
III.D.2 The hadronic calorimeter	92
III.D.3 Performance evaluation.....	106
III.D.4 Calorimeter R&D program	119
III.E Forward Detector.....	122
III.E.1 Detector Hermeticity with the BeamCal/LumCal	122
III.E.2 Monitoring the Instantaneous Luminosity with BeamCal and GamCal	124
III.E.3 LumCal Physics Requirements.....	125
III.E.4 Occupancy Issues in the Forward Direction.....	126
III.E.5 Radiation Damage Issues in the Forward Direction.....	128
III.E.6 Space, Support and Integration Issues.....	129
III.E.7 Readout Issues	131
III.E.8 R&D Plan	133

III.F Magnet Systems.....	134
III.F.1 Detector Main Solenoid.....	134
III.F.2 Adding the Detector Integrated Dipole.....	141
III.F.3 Conclusions.....	143
III.F References.....	144
III.G Muon System	144
III.G.1 Muon System Overview.....	144
III.G.2 General Design Goals	144
III.G.3 Physics requirement	145
III.G.4 Detector Choices.....	145
III.G.5 Backgrounds.....	146
III.G.6 Design	147
III.I SiD Electronics.....	150
III.J DAQ.....	152
IV. Physics Performance and Benchmarking	153
IV.A Simulation of SiD.	153
Beampipe:	156
Vertex Detector:.....	156
Tracker:.....	157
Calorimeters:.....	158
Solenoid:	159
Muon System:	159
Masks and Far Forward Detectors	160
IV.B Benchmark Reactions	160
Benchmark Processes for Studying SiD	161
Fast Monte Carlo Physics Object Simulation	162
IV.C Performance of SiD.....	164
IV.C.1 Tracker Physics Performance.....	164
IV.C.2 Calorimeter and Energy Flow Physics Performance	169
V. SiD R&D Needs.....	174
V.A. R&D Issues	174
V.B Schedule for answering Issues	182
V.C Beam Tests needed.....	182
V.D Estimating R&D costs.....	183
VI Costs	183
VII. Conclusions and future plans	188

Figures

Figure 1 Illustration of a quadrant of SiD.	13
Figure 2. Organization chart for the Silicon Detector Design Study, circa Snowmass 2005.....	15
Figure 3 Jet Jet mass assuming a jet energy resolution of $60\%/\sqrt{E}$, on the left and $30\%/\sqrt{E}$, on the right.....	20
Figure 4: Error on the Higgs mass for Z decaying in hadrons as a function of the jet energy resolution.....	21
Figure 5 Fraction of photon energy per event closer to a charged track than some distance.	22
Figure 6 Higgs branching fraction as a function of the Higgs mass.....	23
Figure 7 Higgs recoil mass for various parametrizations of the momentum resolution for the $e^+e^- \rightarrow ZH \rightarrow \ell \ell X$ process.	24
Figure 8 Physics backgrounds from gamma-gamma produced e^+e^- pairs, muon pairs, and hadronic events integrated over 150 bunch crossings (left) and a single bunch crossing (right).....	27
Figure 9 IR region with 20 mrad crossing angle used in the detector background calculations	29
Figure 10 VXD Hits / mm^2 / train for Barrel Layer 1 for the various ILC beam parameter sets.....	30
Figure 11 The number of charged particles / BX which reach a maximum radius between R and R + 2 cm, as a function of radius R, for nominal 500 GeV beam parameters. The e^+e^- pairs are shown in red; hadrons and muon pairs in green.	32
Figure 12 The density of electron and positron tracks / cm^2 / BX in Layer #1 of the forward tracker, as a function of the radius of the hit.	33
Figure 13 Photon density in the Barrel Tracker Layer #1 for different beam conditions.....	34
Figure 14 SiD footprint in closed, on-beamline position. Note that only half of the longitudinal extent is shown.	37
Figure 15 SiD footprint in open, on-beamline position. Note that only half of the longitudinal extent is shown.	38
Figure 16 SiD footprint in assembly position. Note that only half of the longitudinal extent is shown.....	39
Figure 17 SiD inner radial region and machine/detector interface for 20mrad crossing angle. Note that only half of the longitudinal extent is shown.	40
Figure 18 Inclusive particle energy distributions assuming 100 fb^{-1} at $E_{\text{cm}}=500 \text{ GeV}$ (red) and 1 fb^{-1} at $E_{\text{cm}}=M_Z$ (black).	43
Figure 19 Layout of the 2 mrad beamline near the IP for an L^* of 3.5m.	44
Figure 20 Plan view of the 20 mrad beamline near the IP for an L^* of 3.5m.	45
Figure 21 Longitudinal design of the IP side of QD0/QDEX magnet package with the cold mass and effective L^* indicated by the dashed line marked A. The cold to warm transition to the independent beampipes that traverse BEAMCAL are to the left. ..	46
Figure 22 Cross section of the beampipes and magnet cryostats at $L^*=3.5\text{m}$	46

Figure 23	12mm beam pipe at the interaction point with VXD and maximum envelope of the e+e- pair backgrounds in a 5 Tesla field.	47
Figure 24	Cross section of the 14mrad cryostat at L*=3.5 m. The separation between incoming and outgoing beams at that point is 49mm.	48
Figure 25	Geant3 layout of the 14 mrad extraction line. Detailed designs of the indicated quadrupoles have been created and coded into the simulation.	49
Figure 26	R-Z view of the central pixel region.....	51
Figure 27	Configuration with detector open for access to the vertex detector region.....	52
Figure 28	R-Z view of the vertex detector and its support structures.....	53
Figure 29	R-Phi view of the vertex detector barrel.....	53
Figure 30	Cooling air flow paths	56
Figure 31	Average temperatures of barrel sensors	57
Figure 32	End-to-end temperature differences of barrel sensors.....	57
Figure 33	VXD hit pattern and material summary as a function of polar angle.....	62
Figure 34:	Elevation view of the outer tracker	68
Figure 35:	Cross sectional view of the outer tracker. The inset shows the overlap in z and ϕ of the silicon modules.....	69
Figure 36	Total material budget of the tracker as function of polar angle as modeled in the Monte Carlo.	70
Figure 36	CCD spatial resolution as function of electronics noise. Pixel size is 20 μm . 74	
Figure 37	Efficiency of cluster separation as a function of the distance between tracks. Pixel size 20 μm	74
Figure 38	Reconstruction efficiency as a function of track impact parameters. Reconstruction cuts are set at 3.0 cm for the XY impact parameter and 5.0 cm for Z. Solid lines correspond to high Pt (> 1 GeV), dashed to low Pt (< 0.5 GeV) tracks.	76
Figure 39	Reconstruction efficiency as a function of tracks Pt and dip angle.....	76
Figure 40	Pt distribution and distribution of the number of assigned to track hits for fake tracks. Solid curves are for fake tracks in the presence of background hits, long dashed - for fake tracks in the pure physics events (without background hits), and short dashed - for good physics tracks. Histograms are normalized to the maximum.	77
Figure 41	Calorimeter backscatter track reconstructed with the calorimeter assisted track finder. Identifying such tracks makes it possible to avoid double-counting their energy in particle flow algorithms.	79
Figure 42	Results from the calorimeter-assisted tracking on a Z0-pole data sample. The figure on the left shows the reconstructed KS0 mass spectrum. The figure on the right shows the reconstruction of a KS0 in a hadronic Z-pole decay. The KS0 decays to $\pi^+\pi^-$ and the decay vertex is located at the 9 o'clock position between the first and second outer tracker layer. The lines indicate the reconstructed track stubs.	80
Figure 43:	Tracking efficiency versus angle relative to the jet core, for tracks originating from within 1 cm of the interaction point.	82
Figure 44:	Curvature resolution as a function of curvature, comparing between rms residuals, square root of the appropriate error matrix element, and the LCDTRK.f expectation. The points at smallest curvature (largest transverse momentum) are from dimuon tracks; the remaining points are from a QQbar sample.	83

Figure 45: Momentum resolution for the standard SiD detector layout and three variants.	84
Figure 46: Momentum resolution of the SiD detector and three variants as function of the angle of the track.	85
Figure 47 Baseline barrel ECAL configuration.	87
Figure 48 Cartoon of a silicon detector wafer (left) segmented into 12 mm ² pixels. The green rectangle at center depicts the KPiX ASIC. Right: The bump bond pads and signal trace metalizations on the silicon wafer in the vicinity of the ASIC.	88
Figure 49 View into a readout gap in the vicinity of the KPiX readout chip. Representative bump bond connections are indicated by the small blue circles. Traces (dark blue lines) connect the KPiX serial readout stream, control signals, and power to the polyimid.	88
Figure 50 Functional diagram of one channel (of 1024) of the KPiX chip. The silicon detector pixel is indicated by the diode and capacitor at left.	89
Figure 51 Top: Distribution of total deposited energy in the baseline ECAL for 250 GeV electrons. Bottom: Energy depositions by longitudinal layer for 250 GeV electrons. Layers 21-30 have twice the thickness of layers 1-20.	91
Figure 52. Energy resolution for photons as a function of photon energy for two longitudinal configurations. The “20+10” configuration is the baseline design.	92
Figure 53 (a) A profile plot of energy deposit vs number of cells hit used for hit-to-energy conversion. (b) A scatter plot of energy deposit. A saturation at the higher energy deposit is apparent.	93
Figure 54 Side view of and cross section through the barrel structure of the hadron calorimeter.	94
Figure 55 View of a single wedge.	94
Figure 56 Schematic diagram of a typical Resistive Plate Chamber.	95
Figure 57 Shown is MIP detection efficiency as a function of operating voltage; hit multiplicity as a function of efficiency for varying operating voltages. Red points are streamer contributions.	96
Figure 58 Cell structure of the HCAL. The thickness of the gas gap is kept uniform with the help of fishing lines indicated as circles in the drawing.	97
Figure 59 Schematic of double GEM detector(left) and the GEM-DHCL concept (right)	98
Figure 60 10cmx10cm prototype(left) and pad layout on right.	99
Figure 61 New 30cmx30cm GEM foil on left and magnified section of new 3M foil on right.	100
Figure 62 Scintillator with on-board SiPM.	102
Figure 63 A prototype TCMT cassette under construction. Individual extruded scintillator strips runs left to right.	102
Figure 64 Response of TCMT ScSiPM to electron beam (left figure).	103
Figure 65 Schematic view of the Micromegas detector.	104
Figure 66 The T2K Micromegas chambers	105
Figure 67 Perfect PFA for SIDaug05, Z-pole events.	107
Figure 68 Ingredients of the PFA.	108
Figure 69 Event energy after applying PFA.	111
Figure 70 Event energy for barrel events.	112

Figure 71 Event energy for endcap events.....	112
Figure 72 Results of directed tree clustering in the EM calorimeter. Left: The angular separation between the primary cluster and the parent particle (top) and that between the fragments and their parent (bottom). Right: the reconstructed energy-to-parent energy ratio for the primary cluster (top) and that for the sum of all fragments (bottom).....	115
Figure 73 Results of directed tree clustering in the hadron calorimeter. Left: The angular separation between the primary cluster and the parent particle (top) and that between the fragments and their parent (bottom). Right: the reconstructed energy-to-parent energy ratio for the primary cluster (top) and that for the sum of all fragments (bottom).....	116
Figure 74 Confusion distributions for hadronic Z-pole events in the sidaug05 detector. For each event, the fraction of charged energy incorrectly identified as neutral (and vice versa) is measured in the ECAL. The same distributions are shown for the HCAL using the fraction of hits instead of energy.	118
Figure 75 Maximum missing P_T as a function of the LSP mass for smuon masses: 100, 200, and 300 GeV/c ² . The beam energy is 300 GeV ($\sqrt{s} = 600$ GeV).....	123
Figure 76 The mean number occupancy per pixel per train from Bhabha pairs versus polar angle.....	127
Figure 77 Maximum betatron amplitude (cm) of e^+/e^- vs. e^+/e^- energy at $L_{IP} = 2$ m and 0.5m from a simple analytical calculation.	128
Figure 78 The bottom diagram shows an elevation view with the IP at the left, the near LumCal in the middle, and the BeamCal/Far LumCal at the right. The middle diagram shows the plan view with the BeamCal/Far LumCal region circled. The top diagrams show the end and plan views of the circled region in more detail.	130
Figure 79 Plan and end views of the BeamCal/Far LumCal showing the detector segmentation, and the beam pipes	131
Figure 80 Possible readout architecture for the BeamCal.	132
Figure 81 Over view of existing and planned solenoids.....	135
Figure 82 The CMS conductor design.....	136
Figure 83 The SiD coil winding design	137
Figure 84 Detail of Von Mises stresses in the high purity aluminum, SiD cold and energized (outer 3 layers omitted from figure).....	138
Figure 85 Vertical cross section of the SiD steel model used in ANSYS. R is up in the figure, and Z is horizontal to the right. The central barrel steel plates form an octagon aout the cylindrical coil (shaded), and the octagonal end plates contain a circula hole at $R = 0$ to permit the beam to enter the detector.....	139
Figure 86 SiD central field contours in $ B $, fields in the iron shown by intensity scale. Outer layers of barrel steel omitted from the figure.. The cryostat (not shown in the figure) has a clear bore radius of 2.5 m and extends to $ Z = 2.8$ m.....	140
Figure 87 Detector Integrated Dipole saddles	142
Figure 88 The DID field on the colliding beam axis. The small deviations at $ Z \sim 2.8$ m align with the upsteam edges of the muon steel in the endcaps of SiD.....	142
Figure 89 Radial forces on a DID saddle.....	143
Figure 91 Muon system	147

Figure 92 Layout of a barrel muon scintillator plane. The length of the module is 5.7m and the variable height of the module shown is 2.9m. The long strips are 4.1 m and the width of the scintillator strips is 4.1 cm.	148
Figure 93 Layout of quadrant strips for the forward muon system.	149
Figure 93	155
Figure 94 Distributions of ΔE_{jet} for 250 GeV light quarks jets for different values of the Fast Monte Carlo jet energy resolution parameter c	163
Figure 95 Higgs recoil mass spectra for several values of parameters characterizing the tracker momentum resolution.	165
Figure 96 Muon energy spectrum for muons from the decay of 224 GeV smuons into a 212 GeV neutralino and a muon at $\sqrt{s} = 500$ GeV.....	166
Figure 5 Energy spectrum for electrons from the decay of 143 GeV selectrons into a 95 GeV neutralino and an electron at $\sqrt{s} = 1000$ GeV.....	167
Figure 98 Accuracy of the determination of the selectron mass as a function of the beam energy spread. ILC has an energy spread about 0.1%. Accuracies are shown for the SiD tracker and for a perfect tracker.....	167
Figure 99 Error in E_{cm} as a function of the parameters describing the tracker momentum resolution coming from several possible measurements.	169
Figure 100 Reconstructed mass of Higgs candidate jet-pairs using particle flow information only (no beam energy-momentum constraint is used).	170
Figure 101 Reconstructed mass of Higgs candidate jet-pairs with beam energy-momentum constrained fits of jet 4-vectors included. Both the Higgs signal (red) and Standard Model background (white) are shown.	171
Figure 102 Measurement of $BR(H \rightarrow WW^*)$ from $e^+e^- \rightarrow ZH \rightarrow ZWW^* \rightarrow qqql\nu$	172
Figure 103 The jet energy resolution is important in reconstructing final state W, Z, and H bosons in the signal process $e^+e^- \rightarrow ZHH$ and in the backgrounds $e^+e^- \rightarrow ZZ, ZH, ZZH, WW, tt$	173
Figure 104 Muon Identification and Purity vs. Interaction lengths for inclusive b-pair production at 500GeV. Preliminary studies have been carried out for barrel muons only where the minimum muon momentum is required to be greater than 3 GeV/c.	179
Figure 105 Crude estimate of cost of CMS style solenoid parameterized by stored energy. The curve is $AE^{0.662}$, where E is the stored energy.	184
Figure 106 SiD total cost vs R_Trkr, holding BR^2 fixed. See caveats in the text.	185
Figure 107 SiD costs by subsystem. Note that labor and contingency are included in each technical system.	186
Figure 108 SiD Costs by category.	187

Tables	
Table 1 Key parameters of SiD starting point. (all dimension are given in cm.)	13
Table 2 Background sources for the nominal ILC 500 GeV beam parameters.	28
Table 3 Sensor geometry (units = mm unless otherwise noted)	53
Table 4 Barrel flow and rise in air temperature versus Reynold's number	56
Table 5 Percentages of a radiation length contributed by barrel materials (normal incidence)	59
Table 6 Percentage of a radiation length contributed by disk materials (normal incidence)	60
Table 7 Outer tracker geometry	68
Table 8 BeamCal and LumCal parameters.	125
Table 9 Comparing SiD and CMS	140
Table 10 Data rates for subsystems.	152
Table 11 Estimated R&D costs by subsystem.	183

I. Introduction

I.A The ILC Physics Menu

SiD has been designed to address questions of fundamental importance to progress in particle physics:

- What is the mechanism responsible for electroweak symmetry breaking and the generation of mass?
- How do the forces unify?
- Does the structure of space-time at small distances show evidence of extra dimensions?
- What are the connections between the fundamental particles and forces and cosmology?

These are addressed through precision measurements by SiD at the International Linear Collider (ILC) of the following:

- Higgs boson properties;
- Gauge boson scattering;
- Effects resulting from the existence of extra dimensions;
- Supersymmetric particles; and
- Top quark properties.

The Higgs boson studies will measure in detail the properties of the Higgs boson in order to determine its consistency with Standard Model expectations, and the nature of any deviations. These measurements will include the mass, width, spin, branching ratios and couplings, and the Higgs self-coupling. The precision anticipated is a function of the Higgs mass and is sufficient to discriminate between competing theories for electroweak symmetry breaking. With the decay independent detection of Higgstrahlung events by Z tagging, sensitivity to a wide range of models is possible. Such measurements would establish the role of the Higgs boson in electroweak symmetry breaking, and the generation of mass. Should Nature choose a Higgs-less scenario, it could be addressed by studying the coupling of gauge bosons.

Should additional Higgs bosons beyond the one of the Standard Model exist, SiD will be prepared to detect these up to very large masses. For example, in the MSSM, the additional four Higgs bosons can be detected if they are within the kinematic reach of the ILC .

If they are produced at the ILC, supersymmetric particles will be studied by SiD, establishing an important link in the couplings of the forces at low and high energies, and experimentally testing the unification of forces.

SiD has a reach up to ~ 3 TeV in Higgs-less strong coupling scenarios. Such models would include the Little-Higgs model, strongly interacting W and Z bosons, and extra dimensions models. A universe with extra dimensions of a scale within reach of the ILC

can be probed, with sensitivity to the separate parameters of scale and number of dimensions. By observing masses and widths of excited graviton states, the length scale and the curvature in an additional fifth dimension of space-time can be determined.

SiD plans to study the top quark at the ILC, including the precise measurement of the top quark mass, and its Yukawa coupling.

A number of connections to issues of interest in cosmology would be realized through many of the measurements described above. These focus on two fundamental issues:

- The mechanism behind the present day baryon asymmetry
- The nature of the cold dark matter

1.B The ILC Environment

The ILC Environment is discussed in detail in Section II.D. Here we summarize the key features of the environment, in which SiD has been designed to operate optimally. A critical feature of the SiD design is its sensitivity only to particles generated in a selected, single bunch crossing.

The ILC time structure results in collisions of bunches at the interaction point every 308 nsec. Bunch trains consisting of 2820 bunches in each beam pass through the IP five times per second. Consequently, the bunch trains are about one millisecond long, separated by 199 milliseconds. The design luminosity is $2 \times 10^{34} \text{ cm}^{-2} \text{ sec}^{-1}$. Backgrounds generated by stray beam particles upstream, and collisions of the bunches themselves (beamstrahlung and beam-beam interactions), consist of large numbers of low energy (\sim MeV) photons, and electron-positron pairs. Furthermore, the hadronic collision rate itself, including the two-photon events, is about 200 events per bunch train. Other than the two-photon events, high energy interactions comprise only one event in about every ten bunch trains. Therefore, the pile up of the two-photon events could significantly confuse detection of the principal signal of interest unless the detector can cleanly select single bunch crossings, which SiD is designed to do. For example, only a few Higgstrahlung events per hour, or less, might be produced, motivating clean separation of the overriding two-photon events, and the lower energy backgrounds.

The electron-positron pairs, largely produced in beam-beam interactions, while soft, are a particular problem for the inner-most layers of the detector. SiD's high solenoidal field is an effective protection from the bulk of these pairs, and allows the smallest possible beam pipe radius, optimizing vertexing resolution.

A further complication comes from lessons learned at the first linear collider, the SLC. There, bunch-to-bunch variations in the beam parameters were large, and hard to predict, model, and control. Individual bunches with anomalous backgrounds were problematic to operation of the SLD detector. Significant precautions are being taken at ILC to deal with this, but experience suggests the need for robust detectors. SiD's reliance on silicon sensors for vertexing, tracking, and electromagnetic calorimetry promises the needed robustness.

The environmental issues, and the strategy used by SiD to address them, are discussed in more detail in Section II.D. Each of the subsystems is addressed. The sensitivity to single bunch crossings, made possible by silicon detectors, is the key to immunity.

1.C SiD Rationale

SiD is a detector concept based on silicon tracking and a silicon-tungsten sampling calorimeter, complemented by a powerful pixel vertex detector, and outer hadronic calorimeter and muon system. Optimized forward detectors are deployed. In order to meet the ILC physics goals, we have designed the general purpose detector taking full advantage of the silicon technology. The silicon detector is fast, robust against machine-induced background, fine in segmentation and, by now, a mature concept. The detector performance goals set by ILC physics include:

- i) unprecedented jet energy resolution of $\sigma_E/E = 30\%/\sqrt{E}$, where E is the jet energy in GeV,
- ii) a superb momentum resolution $\sigma(1/p_T) = 5 \times 10^{-5}$, where p_T is the momentum perpendicular to the beam axis measured in GeV/c and
- iii) the impact parameter resolution of $\sigma_{r\phi} \approx \sigma_z \approx 5 \oplus 10/(p \sin^{3/2} \theta) \mu\text{m}$, where p is the momentum of the charged track in GeV/c and θ is the polar angle with respect to the beam axis.

The jet energy resolution, which is a factor of 2 better than SLC and LEP calorimeters, and even well beyond that of the ZEUS uranium-plastic scintillator calorimeter, is required in order to cleanly isolate multi-jet final states arising from processes such as $e^+e^- \rightarrow Z(\rightarrow q\bar{q})H(\rightarrow b\bar{b})$ and $e^+e^- \rightarrow t\bar{t} \rightarrow bW^+(qq') + \bar{b}W^-(\bar{q}\bar{q}')$. The momentum resolution required for the tracker is a factor of 10 better than LEP experiments or a factor of 3 better than CMS at LHC. The impact parameter resolution, which is a factor of 3 better than what SLD achieved, allows us to tag the flavor of a jet with high efficiency and cleanly discriminate charm, bottom, and the light quarks.

In addition, the detector must have the capability to isolate the bunch crossing, in which the recorded collision event has occurred. In the ILC nominal beam parameters set, there are five trains of 2,820 bunches, separated by 308 ns, every second. This bunch separation could be shorter (150 ns) in another set of beam parameters (so called low Q set). Thus the detector must be capable of identifying the right bunch crossings, separated by as short as 150 ns.

SiD is conceived as the-state-of-the-art detector that meets all the above requirements with built-in robustness against machine-induced backgrounds at the ILC. Starting with the all important calorimetry performance, particle flow calorimetry is needed, with the coil must be located outside the calorimeter. Fine granularity is required to achieve the particle flow calorimetry, leading to a natural choice of a finely grained silicon-tungsten electromagnetic calorimeter. Since this high granularity silicon-tungsten calorimeter is expensive, the detector architecture calls for a compact geometry. Tracking precision can

be achieved in the compact configuration with the large magnetic field and silicon tracking. An ancillary benefit of the large magnetic field is the possibility of a small beampipe with very close vertexing.

1.D SiD Starting Point, Integrated Performance, and the Optimization Process

SiD, illustrated in Figure 1, is compact, with a 5 Tesla solenoidal field, surrounding a high granularity calorimeter.

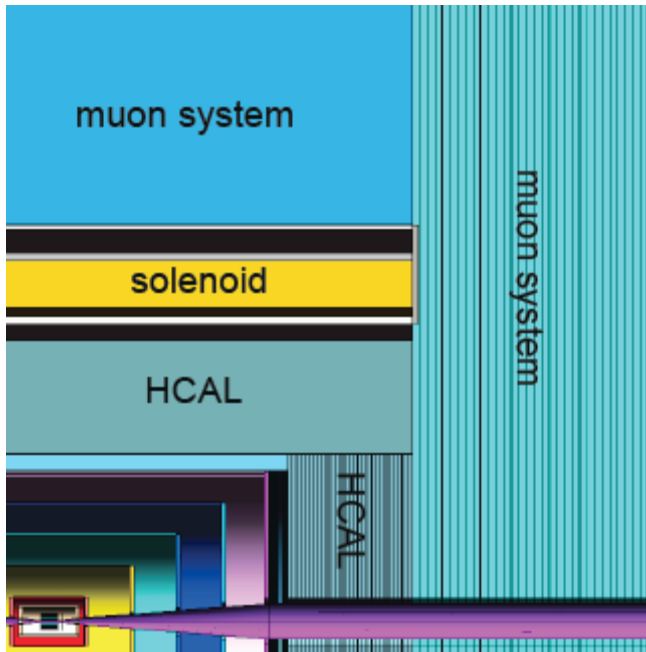


Figure 1 Illustration of a quadrant of SiD.

The key parameters of the SiD design starting point are listed in Table 1.

Table 1 Key parameters of SiD starting point. (all dimension are given in cm.)

SiD BARREL	Technology	Inner radius	Outer radius	Z max
Vertex detector	Pixel	1.4	6.1	6.25
Tracker	Silicon strips	20.0	126.5	± 167.9
EM calorimeter	Silicon-W	127.0	140.0	±180.0
Hadron calorimeter	RPCs	141.0	250.0	± 277.2
Solenoid	5 Tesla	250.0	330.0	± 277.0
Muon chambers	RPCs	333.0	645.0	± 277.0
SiD FORWARD	Technology	Inner Z	Outer Z	Outer radius
Vertex detector	Pixel	71.9	172.0	71.0
Tracker	Silicon strips	26.7	165.4	126.5
EM calorimeter	Silicon-W	168.0	182.0	127.0

Hadron calorimeter	RPCs	182.0	277.0	140.7
Muon chambers	RPCs	277.5	589.5	645.0
LumCal	Silicon-W	170.0	183.0	19.0
GamCal				
BeamCal	Silicon-W	321.0	334.0	18.0

SiD is centered on high quality particle flow calorimetry. The electromagnetic calorimeter (EMCal) is made of plates of tungsten with 1 mm gaps for silicon detectors with pixels ~ 3.5 mm across. This arrangement largely preserves the Moliere radius (9 mm) of tungsten and permits separation of close energetic electromagnetic showers. The EMCal is backed by a hadronic calorimeter (HCal) located within the coil. While the final configuration has not yet been selected, layers of tungsten with 1 cm^2 pixels on Resistive Plate Chambers (RPCs) are adopted as a baseline design.

The momentum measurement is done by a very high resolution silicon strip tracker in a 5 T solenoidal field, thus achieving excellent resolution in a relatively modest radius of 1.25 m. The vertex tracker has both cylindrical and end plate pixellated sensors to provide tracking and vertexing coverage to small angles with a relatively short sensor array. It brings particles through the sensors closer to normal incidence than for cylinders alone. The high field helps contain the pair backgrounds produced by beam-beam interaction.

The flux is returned by a laminated steel structure that also includes sensors for muon identification, probably the same technology used in the HCal.

In addition to exceptional momentum resolution for charged particles and jet resolution using the momentum measurement for charged particles and the calorimeters for neutrals, the SiD uses only technologies which are expected to be quite tolerant of background mishaps from the linear collider. The silicon of the vertex detector, the tracker, and the calorimeter should all take significant radiation bursts without “tripping” or other damage.

The SiD design study is engaged in optimizing all of the values of parameters for all sub-systems from the starting values of **Error! Reference source not found.** In the process of optimizing the detector design for performance, the SiD study group has explicitly considered cost as a critical parameter, and has developed tools to estimate the cost as the detector parameters vary. The Study believes that cost is an important constraint in order to reach a credible design even at the early stage of the ILC project, and must be considered along with performance optimization.

1.E Design Study Origins, Organization, and Plans: SiD Snapshot on Road to CDR

This document presents the current status of the SiD Design Study’s effort to optimize the parameters of the general concept. It presents detailed designs for SiD’s various sub-systems, the full Geant4 description of the starting point, new studies of the required detector performance, the status of new tools being developed to evaluate performance,

an assessment of what detector R&D is needed to prove the viability of the SiD concept, as well as a basis for estimating the cost.

The original concept for a Silicon Detector for the ILC came from M. Breidenbach and J. Brau, and was presented in 2004, at the Extended Joint ECFA-DESY Workshop in Amsterdam. (ref - THE SILICON DETECTOR (SID) AND LINEAR COLLIDER DETECTOR R&D IN ASIA AND NORTH AMERICA.

By J.E. Brau (Oregon U.), M. Breidenbach (SLAC), Y. Fujii (KEK, Tsukuba),. SLAC-PUB-11413, DESY-PROC-2004-01H, DESY-04-123GH, Mar 2004. 11pp.

Prepared for 4th ECFA / DESY Workshop on Physics and Detectors for a 90-GeV to 800-GeV Linear e+ e- Collider, Amsterdam, The Netherlands, 1-4 Apr 2003.)

Subsequently, the SiD Design Study was initiated with the encouragement of the World Wide Study of Physics and Detectors for a Future Linear Collider Organizing Committee. The Study was introduced at the ALCPG Victoria meeting in the summer of 2004. Subsequent regional meetings in the fall of 2004, at the ECFA Workshop in Durham and the ACFA Workshop in Taipei, saw kick-off meetings for the other major detector concepts and the introduction of SiD to European and Asian audiences.

The SiD organization, shown in Figure 2, was put in place during late 2004 and early 2005, and was largely in place for the SiD Workshop which preceded LCWS05 at Stanford. Working groups were created, leaders recruited, and plans debated on how to proceed toward the first full SiD Design Study meeting, which was held in conjunction with the ALCPG Snowmass Meeting in 2005. That gathering marked the first opportunity for the Design Study participants to meet and interact for a protracted period, and it was the first meeting where the design had been captured completely in GEANT4, and available for detailed study.

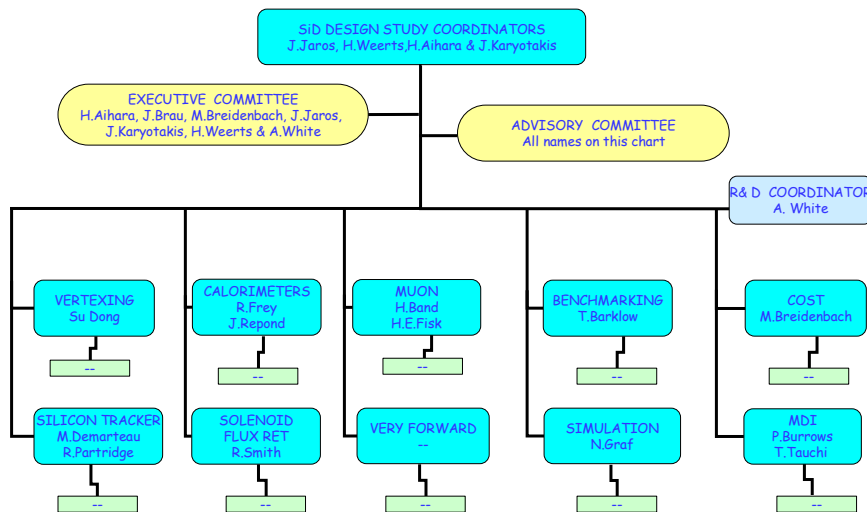


Figure 2. Organization chart for the Silicon Detector Design Study, circa Snowmass 2005.

The goal of the Design Study has been, since its inception, to design a detector optimized for studies of 0.5-1.0 TeV e+e- collisions, which is rationally constrained by costs, and which utilizes Si/W electromagnetic calorimetry and all silicon tracking. Complementary goals have been to identify and encourage the R&D needed to realize the SiD detector, and to document SiD's mechanical designs, sub-systems and physics performance.

The steps toward design optimization have begun by first fleshing out the starting point given above. This is being done by developing conceptual mechanical designs that realistically account for the material budget of sensors, supports, and readout, and that are buildable and serviceable. These designs are being captured in the Geant4 description of SiD in sufficient detail that SiD's physics performance can be reliably simulated.

Full Monte Carlo tracking pattern recognition code, calorimeter particle flow algorithms, detailed device simulations, and realistic background simulations are all in development in the effort to characterize SiD performance realistically. The goal is to develop a full Monte Carlo simulation of the detector's response to physics, backgrounds, and noise, evaluate subsystem performance and perform physics analyses in this environment.

Detector technologies for each of the SiD subsystems are under development and critical review, with the aim to assess the optimal technology for each system, and to plan the R&D needed to establish proofs of principle for the various systems.

Evaluating the sub-system performance requirements, and the as-designed performance obtained, and benchmarking the integrated detector performance on key physics measurements, are the final ingredients to the optimization process. Studies are underway to revisit the requirements LC physics imposes on the subsystem performance, and sample analyses are being readied for evaluating the integrated detector performance.

The organization of this document is as follows. Section II describes the physics requirements, environmental constraints, and cost constraints that dictate the design of SiD. Section III reviews the SiD detector, subsystem by subsystem. SiD's simulation tools, current status in Geant4, and physics performance are given in Section IV. R&D needs are discussed in Section V. Section VI gives SiD's costing methodology. Conclusions and Future Plans are given in Section VII.

I.F Authors

(As of: 4/20/2006 ; Number of Authors: 130)

T. Abe	University of Tokyo
Bob Abrams	Indiana U.
C. Adloff	LAPP Annecy
Hiroaki Aihara	University of Tokyo
Justin Albert	Cal Tech
David Bailey	University of Manchester
Charles Baltay	Yale Univ
Henry Band	Wisconsin
Tim Barklow	SLAC
Jerry Blazey	NIU
Jim Brau	University of Oregon
Martin Breidenbach	Stanford Linear Accelerator Center
Philip Burrows	Queen Mary, University of London
F. Cadoux	LAPP Annecy
Christian Carimalo	LPNHE-Universite Pierre et Marie Curie/CNRS-IN2P3
Ron Cassell	SLAC
Dhiman Chakraborty	NIU
Matthew Charles	SLAC
Byung Gu Cheon	Chonnam National University
Young-Il Choi	Sungkyunkwan University
Bill Cooper	FNAL
Colin Daly	University of Washington
Chris Damerell	Rutherford Appleton Lab
Wilfrid Dasilva	LPNHE-Universite Pierre et Marie Curie/CNRS-IN2P3
Guillaume Daubard	LPNHE-Universite Pierre et Marie Curie/CNRS-IN2P3
Jacques David	LPNHE-Universite Pierre et Marie Curie/CNRS-IN2P3
G. De Geronimo	BNL
P. Delebecque	LAPP Annecy
Marcel Demarteau	Fermilab
Christophe Evrard	LPNHE-Universite Pierre et Marie Curie/CNRS-IN2P3
Gene Fisk	Fermilab
D. Fougeron	LAPP Annecy
Raymond Frey	University of Oregon
Dieter Freytag	Stanford Linear Accelerator Center
Jean Francois Genat	LPNHE-Universite Pierre et Marie Curie/CNRS-IN2P3
Joel Goldstein	RAL
Norman Graf	SLAC
Jeffrey Gronberg	LLNL
Gunther Haller	Stanford Linear Accelerator Center
Ryan Herbst	Stanford Linear Accelerator Center

R. Hermel	LAPP Annecy
Sonja Hillert	University of Oxford
M. Iwasaki	University of Tokyo
John Jaros	SLAC
Tony Johnson	SLAC
Joo Sang Kang	Korea University
T. Kapusta	
Frederic Kapusta	LPNHE-Universite Pierre et Marie Curie/CNRS-IN2P3
Yannis Karyotakis	LAPP Annecy
Hongjoo Kim	Kyungpook National University
Guinyun Kim	Kyungpook National University
Kurt Krempetz	FNAL
Steve Kuhlmann	Argonne National Lab, USA
Young Joon Kwon	Yonsei University
F. Lanni	BNL
Herve Lebbolo	LPNHE-Universite Pierre et Marie Curie/CNRS-IN2P3
Jik Lee	Seoul National University
Z. Li	BNL
Guilherme Lima	Northern Illinois University
Ronald Lipton	fermilab
D. Lissauer	BNL
Xia Liu	Argonne
Changguo Lu	Princeton University
Henery Lubatti	University of Washington
Vera Luth	SLAC
Pierre Lutz	Saclay
Steve Magill	ANL
Usha Mallik	university of Iowa
Thomas Markiewicz	SLAC
Takashi Maruyama	SLAC
J. Mead	BNL
Niels Meyer	
Caroline Milstene	Fermilab
Winfried Mitaroff	Austrian Academy of Sci. / HEPHY, Vienna
Kenneth Moffeit	SLAC
William Morse	BNL
Uriel Nauenberg	University of Colorado
Tim Nelson	SLAC
Dmitry Onoprienko	Kansas State University
Vladimir Rykov	RIKEN
Mark Oreglia	University of Chicago
Hwanbae Park	Kyungpook National University
B. Parker	BNL
Richard Partridge	Brown University
Thanh Hung Pham	LPNHE-Universite Pierre et Marie Curie/CNRS-IN2P3
Veljko Radeka	BNL

Jose Repond	Argonne National Laboratoy
S. Rescial	BNL
Keith Riles	University of Michigan
Francois Rossel	LPNHE, Universites de Paris
Francois Rossel	LPNHE-Universite Pierre et Marie Curie/CNRS-IN2P3
Valeri Saveliev	University of Atomic Energy,Obnisk,
Aurore Savoy-Navarro	LPNHE-Universites Pierre et Marie Curie/CNRS-IN2P3
Bruce Schumm	UC Santa Cruz
Rachid Sefri	LPNHE-Universite Pierre et Marie Curie/CNRS-IN2P3
Y. Semertzidis	BNL
Nikolai Sinev	Stanford Linear Accelerator Center
Rick Smith	FNAL
A J Stewart Smith	Princeton University
Dongchul Son	Kyungpook National University
David Strom	University of Oregon
Jan Strube	University of Oregon
Dong Su	SLAC
Toshiaki Tauchi	
T. Tauchi	KEK
Geoffrey Taylor	University of Melbourne
Geoffrey Taylor	University of Melbourne
Eric Torrence	University of Oregon
Tracy Usher	SLAC
Rick Van Kooten	Indiana University
Daniel Vincent	LPNHE-Universite Pierre et Marie Curie/CNRS-IN2P3
Eckhard Von Toerne	Kansas State University
Vaclav Vrba	Institute of Physics, AS CR, Prague
Steve Wagner	
Harry Weerts	Michigan State Univ./Fermilab
William Wester	Fermilab
Andy White	U. Texas at Arlington
Eunil Won	Korea University
Mike Woods	SLAC
Steve Worm	RAL
Douglas Wright	LLNL
Stefania Xella	Zurich University
Lei Xia	Argonne National Laboratory
Haijun Yang	University of Michigan
Michael Young	UCSC
Jae Yu	UTA
Tianchi Zhao	University of Washington
Vishnu Zutshi	Northern Illinois University
W. daSilva	

II. Detector Design Requirements

II.A Subsystem Performance Required by the Physics

The key issues for designing the SiD detector are the ability to perform high precision measurements and the capability to detect and discover new phenomena. Exploring the electroweak symmetry breaking mechanism requires a precise measurement of the Higgs branching ratio to different species, and therefore an excellent b/c tagging and τ reconstruction. Discovering supersymmetric particles requires an excellent missing energy determination and therefore a very hermetic detector. Precision measurements are often dominated by systematic errors and redundancy is required to control them. Robustness to the beam conditions affects seriously the detector performance, and is one of our main requirements. Finally the accelerator design and operation impacts the detector requirements. Using few key physics cases below, we derive the sub detector requirements for the SiD detector.

It has been realized quite early during these studies that the calorimeter requirements, both electromagnetic and hadronic, dominate the design of the whole detector. For many ILC specific physics measurements, ex: the tri-linear Higgs coupling, where the beam energy constrain is not possible, ex: $e^+e^- \rightarrow \nu\nu W^+W^-$, $\nu\nu ZZ$ or $e^+e^- \rightarrow \chi^+\chi^-\chi^0_1 \rightarrow \chi^0_1\chi^0_1 W^+W^-$, it is mandatory to separate W and Z hadronic jets by measuring precisely their energy. For a typical jet energy resolution, $60\%/\sqrt{E}$, achieved by LEP experiments, WW and ZZ events are not distinguishable, see Figure 3. A much better resolution is required, which can be achieved by the particle flow algorithm (PAF), as described in the calorimeter section.

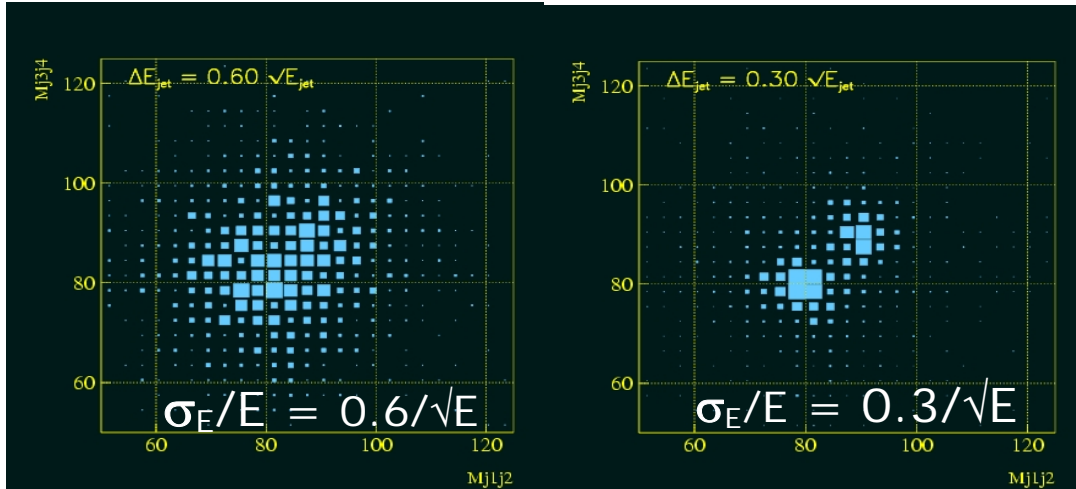


Figure 3 Jet Jet mass assuming a jet energy resolution of $60\%/\sqrt{E}$, on the left and $30\%/\sqrt{E}$, on the right.

The Higgs mass is measured precisely using Higgsstrahlung events ($e^+e^- \rightarrow ZH$) where the Z decays into leptons. For a Z decaying to hadrons the Higgs mass error depends on the jet energy resolution as shown on Figure 4.

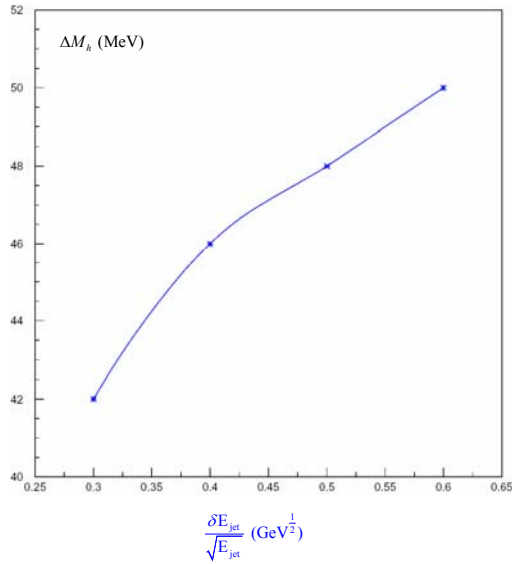


Figure 4: Error on the Higgs mass for Z decaying in hadrons as a function of the jet energy resolution

The PFA algorithm to be efficient uses tracking and calorimeter information to distinguish inside a jet, individual particle contributions. Therefore the challenge for the calorimeters is extremely high granularity, high density, reasonable energy resolution and affordable internal radius. The figure of merit is empirically described by the ratio BR^2/σ where B is the magnetic field, R the internal radius, and $\sigma=4 r_{\text{pixel}} \oplus r_{\text{Moliere}}$. For the electromagnetic calorimeter we require the smallest Moliere radius, a cell size of the order of 12mm^2 and an energy resolution of $\sim 14\%/\sqrt{E} \oplus 1\%$. The photon isolation with respect to charged tracks for $e^+e^- \rightarrow ZH$ events is shown on Figure 5. The best approach for this sub detector is 30 layers of Silicon-Tungsten sampling calorimeter, with the smallest gap between tungsten plates.

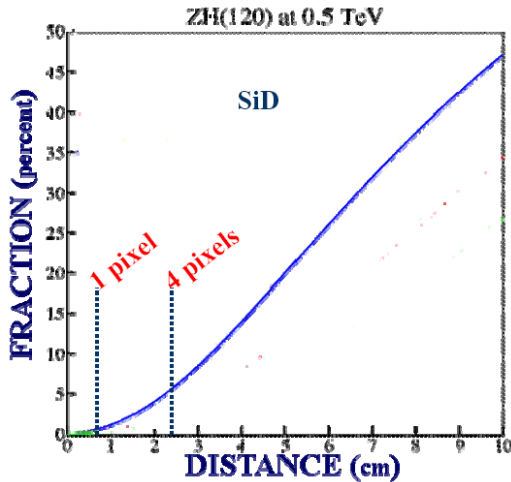


Figure 5 Fraction of photon energy per event closer to a charged track than some distance.

The role of the hadronic calorimeter is to isolate and measure the energy of neutral hadrons. Simulation models for this sub detector are not tested enough today to completely rely on them. More data are needed. An energy resolution of $50\text{-}60\%/\sqrt{E}$ and a cell size of 100mm^2 are sufficient.

For Higgs masses below 160GeV , it is possible to measure the Higgs couplings to b/c quarks, τ leptons, and gluons. Although the dominant decay is a bb pair as shown on Figure 6 it is still possible to measure the couplings to cc , provided we have enough separation between bb and cc events. The Higgs branching ratio is a strong function of its mass mainly due to the kinematic phase space factor of Higgs decay into a W -pair. The Higgs boson is expected to couple to fermions with a strength proportional to the fermion mass. In the MSSM the partial decay width of the b - b bar and c - c bar decay modes of the lightest Higgs boson scale with the ratio of $\sin^2\alpha$ and $\cos^2\beta$, where α is the mixing angle and β is the ratio of the vacuum expectation values of the Higgs doublet. To be able to discriminate between production of a SM Higgs or extensions of the SM, branching ratios need to be measured to unprecedented precision. This will require superb performance from the vertex detector.

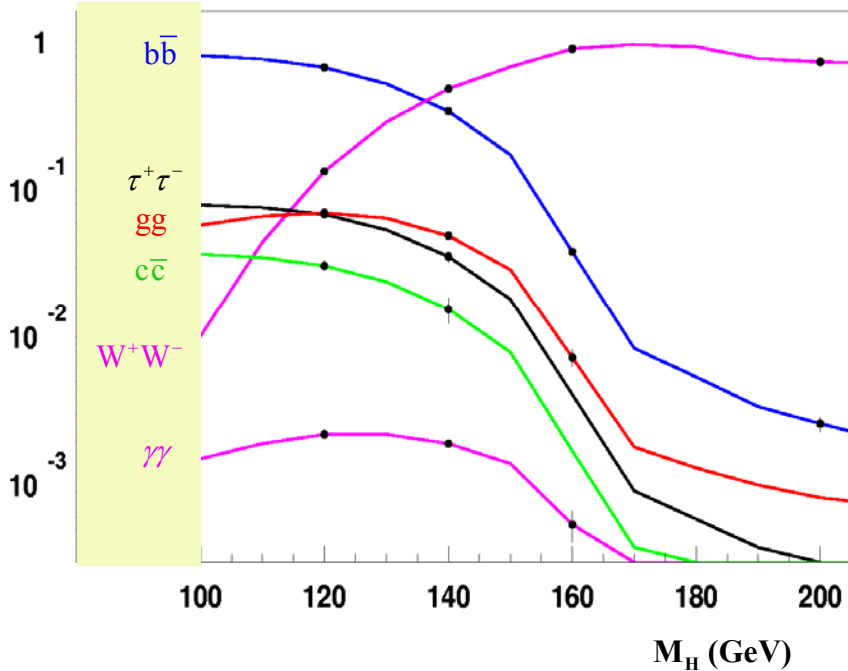


Figure 6 Higgs branching fraction as a function of the Higgs mass

A high b tagging efficiency with high purity is required to study decays where a Higgs is involved, ex: $e^+e^- \rightarrow ZHH$ with a $4b$ final state to be identified or $e^+e^- \rightarrow ttH$. τ lepton tagging is also useful for reducing backgrounds. b tagging efficiency depends on a vertex detector located quite close to the beam pipe, with an excellent space point and impact parameter resolution, $<4\mu$ and $\sim 5\mu \oplus 10\mu/(p\sin^{3/2}\theta)$ respectively. Tracking capability for the vertex detector, stand alone, is also mandatory. Transparency, for improved momentum resolution and limited photon conversion rates, is also an issue as we aim for $\sim 0.1\%$ X_0 per layer.

To illustrate some of the requirements the physics places on the design of the tracker, two aspects of the production of a Higgs boson in association with a Z-boson will be considered: the measurement of its mass and the measurement of the partial decay branching ratios. Using the leptonic decays of the Z-boson, the mass of the Higgs boson can be reconstructed using the recoil-mass technique. This method is independent of the decay channel of the Higgs and the resolution of the reconstructed Higgs mass improves with improved momentum resolution in the tracker. Figure 7 shows the improvement in resolution of the Higgs mass determination with improved momentum resolution.

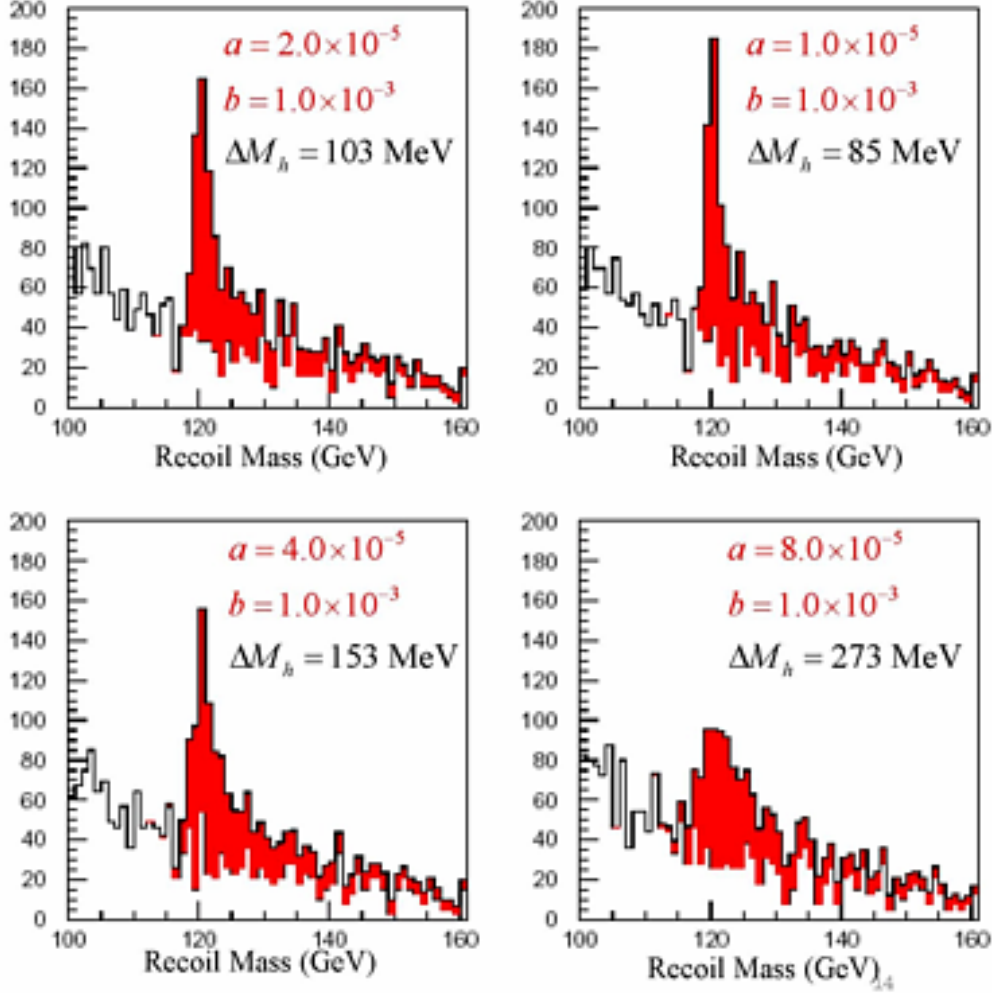


Figure 7 Higgs recoil mass for various parametrizations of the momentum resolution for the $e+e- \rightarrow ZH \rightarrow \ell \ell X$ process.

The momentum resolution has been parametrized as $\sigma(p_T) / p_T^2 = a + b / p_T \sin\theta$. Momentum resolution $\sigma(p_T) / p_T^2 < 5 \times 10^{-5}$ is needed for an accurate mass measurement; further improvements continue to pay benefits. A precise measurement of the Higgs mass with an accuracy of less than 100 MeV is necessary in order to obtain optimal results from the measurement of the branching ratio, especially for Higgs masses around 120-150 GeV.

Whatever momentum resolution is achieved for particles produced with polar angles $\sim 90^\circ$, the performance generally degrades at small polar angles due to the increased distance of the first hit from the IP, the increased thickness of material traversed by the oblique tracks and the shorter lever arm for measuring the momentum (most important). Maintaining good momentum resolution and efficient tracking over as much solid angle as possible is clearly desirable, since there is a significant probability that at least one of the jets is found in the forward or backward regions and, secondly, because much of the physics relies on having spin-polarised electrons and/or positrons where the significance of events becomes weighted in favor of the forward-backward direction.

Very precise angular resolution is needed for charged particle tracks down to the lowest angles. This requirement is set by the desire to measure the differential luminosity spectrum to high precision. Doing so is needed, for example, to measure the top quark mass to a precision of 100~MeV from a threshold scan. Since the available center of mass energy is not a delta-function but has a spread due to the intrinsic energy resolution of the machine, beamstrahlung and initial state radiation, the luminosity spectrum will have to be determined from Bhabha scattering. Being able to extract the top mass with the precision required, demands an angular measurement at the level of 10^{-5} .

Muon identification must be provided outside the coil. Still some critical questions, space resolution, or the role of the muon system as a tail catcher, are under study.

SUSY searches require a very hermetic detector, especially in the forward region, which has to be carefully instrumented to provide also precise luminosity measurements, monitor the beamsstrahlung or shield the tracking volume. Dark matter density measurements favor a SUSY parameter space including a very challenging region where

the s - τ and $s\chi^0_1$ are almost degenerated, resulting to events $e^+e^- \rightarrow \tilde{\tau}^+ \tilde{\tau}^- \rightarrow \tau^+ \tau^- \chi^0_1 \chi^0_1$ where the τ leptons are of very low energy. Observation of these events has to fight against a huge production of $\gamma\gamma$ events $e^+e^- \rightarrow e^+e^- \tau^+\tau^-$ which can be reduced by an efficient veto system covering an angular region down to 0.2-0.6 degrees.

II.B Physics, Environment, and Costs Drive the SiD Detector Design

The design of the SiD detector seeks to optimize physics performance, rationally constrain costs, and provide robust operations in the ILC environment. The ILC physics menu pushes detector performance well beyond the current state of the art; the ILC community has explored how these requirements translate to subsystem performance specs, and it continues to refine and substantiate its estimates of what is needed. Any realistic detector design must consider costs. SiD recognized the importance of assessing detector component costs at the beginning of its design exercise, and has developed tools to explore how costs will change as the fundamentals parameters of the detector change. Design optimization requires striking the right balance between costs and performance. The final constraint is imposed by the ILC environment: the accelerator's bunch structure and the presence of physics and machine backgrounds. These constraints impose requirements on radiation hardness, detector segmentation and thickness, detector livetime, and allowable readout times.

II.B.1 ILC Environmental Concerns

The ILC's bunch structure, which consists of trains of 2820 bunches which are spaced 308 ns apart, repeated 5 times per second, and the physics and machine backgrounds resulting from bunch-bunch collisions, impose many constraints on ILC detector technologies and on the readout electronics.

While these constraints are mild compared to those imposed on LHC detectors, the high flux of photons concomitant with the collisions, from virtual sources and beamstrahlung, results in the copious production of e^+e^- pairs as well as the frequent production of muon pairs and hadronic interactions. The e^+e^- pairs account for most of the background in the inner detectors, directly as charged tracks with low transverse momentum. They also cause a general flux of \sim MeV photons which result when they shower in the beam calorimeters on the front face of the final quadrupoles. These photons, and the higher transverse momentum muons and charged and neutral hadrons which also result from photon-photon interactions, spray the entire detector with charged particles and photons.

SiD is largely immune to these backgrounds because the detector as a whole is only sensitive to backgrounds associated with a single bunch crossing. The silicon microstrip and pixel detectors used in the vertexing, tracking, and electromagnetic calorimetry can be made sensitive to ionization which is deposited within just 1 μ s of the interaction time, and the resultant hits can be uniquely associated with a single bunch crossing. A channel-by-channel buffer, which is 4 deep in current designs, will store hits over the course of the entire bunch train, and record each responsible bunch crossing. (The KPiX readout chip is described in detail in Section III.D.1.a below.) Consequently, SiD is sensitive only to the physics and backgrounds of a single bunch crossing, in contrast to detectors with longer inherent livetimes, which can be sensitive to \sim 150 bunch crossings or more. Figure 8 contrasts the gamma-gamma backgrounds when the detector livetime is short or long. Pattern recognition benefits tremendously from this cleanest possible environment, and physics ambiguities are minimized. Channel-by-channel deadtime inefficiencies are minimal, and the event buffering insures that essentially no physics data is lost because of noise hits.

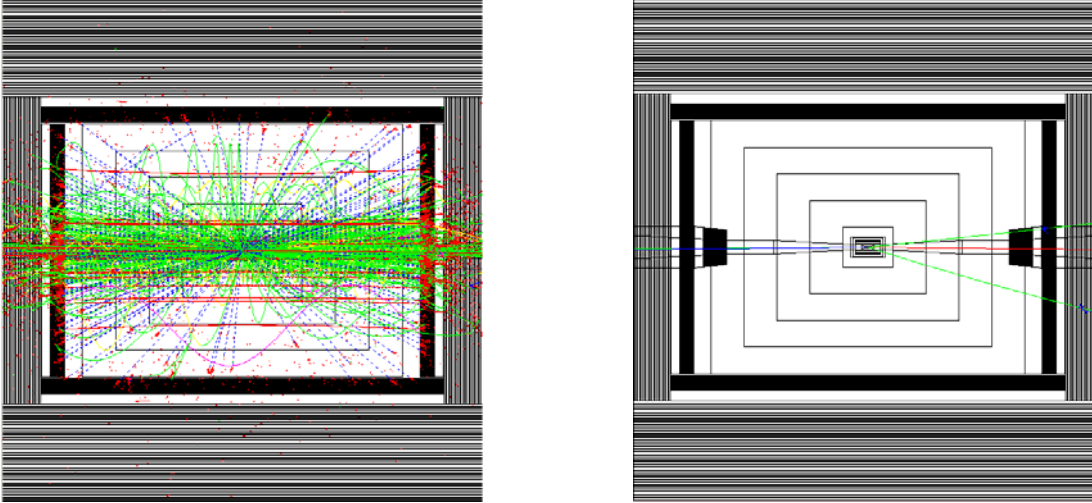


Figure 8 Physics backgrounds from gamma-gamma produced e^+e^- pairs, muon pairs, and hadronic events integrated over 150 bunch crossings (left) and a single bunch crossing (right).

Background hits do remain in SiD, of course, which could complicate pattern recognition in the vertex detector, tracker, and calorimeter. In fact, as we show in detail below, pattern recognition in SiD is uncompromised by these backgrounds, even allowing for considerable margin, because the material budget is kept to a minimum, and because the detector is only sensitive to a single bunch crossing's worth of background. This is not to say that these background levels are inconsequential. In fact, they will dictate how rapidly the vertex detector must be readout, impact the design of the forward tracking sensors, and determine the depth of buffering required for those sensors at small radii, where rates are high.

Experience at the first linear collider, the SLC, taught that bunch-to-bunch parameter variations are to be expected, that populations in the tails of the beam phase space were hard to predict and control, and that, in general, backgrounds beside those intimately related to the production of luminosity, like the gamma-gamma induced backgrounds discussed above, are to be expected and will likely be unpredictable, at least in the beginning. At the SLC, synchrotron radiation backgrounds were far beyond naïve expectation, leading to low energy photons backscattering into the detector, and occasionally off-energy electrons showered in the interaction region. The net radiation dose from these backgrounds was not a problem, but the high instantaneous dose was often enough to trip-off gas chambers at the SLC. Silicon sensors in the SLC experiments registered very large occupancies in these background events, but kept on running, with no ill effect. SiD, relying on silicon sensors, is especially robust against such backgrounds at the ILC.

In the following, we discuss the ILC backgrounds and their evaluation in more detail and quantify occupancies for each of the SiD detector subsystems, for the range of machine parameters under consideration.

II.B.2 Expected Backgrounds at the ILC

Detector backgrounds are expected to come from the following sources:

IP Backgrounds	Machine Backgrounds
Disrupted primary beam	Direct beam loss
Beamstrahlung photons	beam-gas scattering
e+e- pairs from beam-beam interactions	collimator edge scattering
Radiative Bhabhas	Synchrotron radiation
Hadrons/muons from $\gamma\gamma$ interactions	Muon production
	Neutron back-shine from Dump
	Extraction line loss

Each of these sources has been studied. Among these sources the most dominant source is e+e- pairs from beam-beam interactions. The pairs are produced at the IP, interact with the beam pipe, inner vertex detector layers, mask and beamline magnets, and produce a large number of secondary e+e-, photons and neutrons which in turn contribute background in the vertex detector and in the Si tracker and calorimeter at large radius.

Guinea-Pig is used to simulate the beam-beam interaction and to generate pairs, radiative Bhabhas, disrupted beams and beamstrahlung photons. The ILC beam parameters are used for the simulation. Table 2 summarizes the number of particles per bunch and average energy for the nominal ILC 500 GeV beam parameters. Gamma-gamma interactions are included without a transverse momentum cut, to be sensitive to the entire cross sections for these processes. The gamma gamma hadronic cross section is approximated in the scheme of Peskin and Barklow (ref).

Table 2 Background sources for the nominal ILC 500 GeV beam parameters.

Source	#particles/bunch	$\langle E \rangle$ (GeV)
Disrupted primary beam	2×10^{10}	244
Beamstrahlung photons	2.5×10^{10}	4.4
e+e- pairs from beam-beam interactions	75K	2.5
Radiative Bhabhas	320K	195
$\gamma\gamma \rightarrow$ hadrons / muons	0.5 events / 1.3 events	-

Detector backgrounds are calculated in the SiD detector and IR layout shown in Figure 9. The detector parameters are described in <http://www.lcsim.org/detectors/#sidmay05>. The beamline magnets up to about 20 m from the IP are included, and the three crossing angle options, 20 mrad, 14 mrad and 2 mrad, are considered. The nearest quadrupole magnet of the final doublet ends at 3.51 m for all three options. The BeamCal has two holes (1 cm radius for incoming beam and 1.5 cm radius for outgoing beam) for the 20 mrad and 14 mrad options, while there is only one 1.5 cm radius hole for the 2 mrad option. The detector solenoid field is 5 Tesla, and the

field map instead of a constant field is used for the calculations. GEANT 3 is used to calculate e^+e^- and photon background. Since GEANT 3 does not simulate photo-nuclear interactions, FLUKA is used to calculate neutron background.

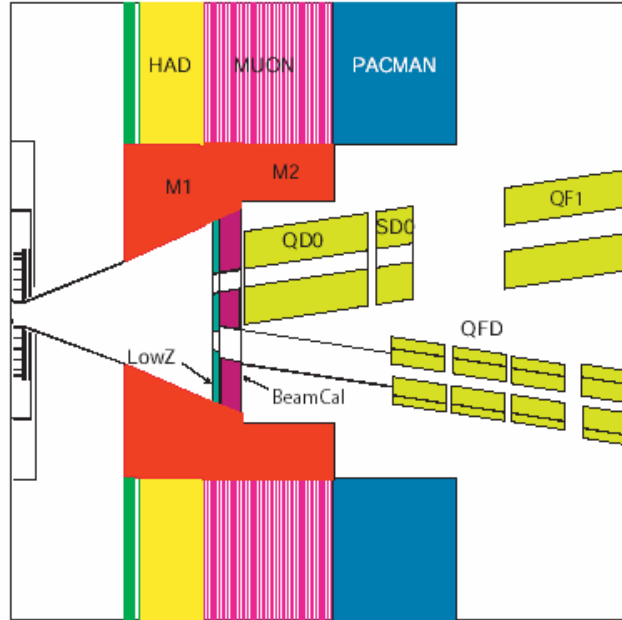


Figure 9 IR region with 20 mrad crossing angle used in the detector background calculations

II.B.3 Impact of Backgrounds on SiD Subsystem Design.

II.B.3.a Vertex Detector

The background hits in the vertex detector come predominantly from the e^+e^- pairs. The number of VXD hits / mm^2 / train in the first barrel layer of the vertex detector, is shown in Figure 10 for the various beam parameters considered for the ILC. The backgrounds fall off rapidly with the radius of the sensor layer, so this represents the worst case. For the nominal ILC beam parameters, nearly 80 hits / mm^2 are expected over the full train for 500 GeV operations; at 1 TeV, in the high luminosity option, this number rises to about 400 hits / mm^2 .

Pattern recognition studies (Ref. Sinev, LCWS05 and Snowmass05) have demonstrated fully efficient pattern recognition in a five layer pixel vertex detector with $20 \times 20 \mu\text{m}^2$ pixels, even with backgrounds accumulated over >150 beam crossings. Taking this level of background as a conservative pattern recognition tolerance limit imposes a constraint on the vertex detector readout. The readout must limit the vertex detector sensitive time to ≤ 150 BX (beam crossings), which corresponds to a maximum of about 6 hits / mm^2 . To handle higher energies, or more aggressive collision parameters, the readout must limit sensitive time to 30 BXs. This constraint has been long appreciated, and is motivating the development of several new technologies for pixelated

vertex detectors, including those being considered for SiD. (See Vertex Detector Section III.C.2.b.)

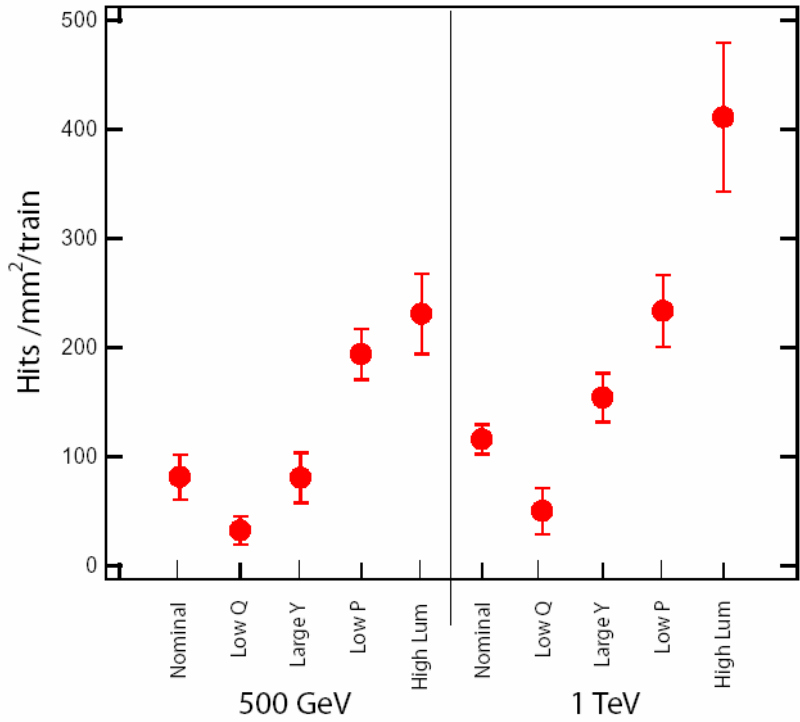


Figure 10 VXD Hits / mm² / train for Barrel Layer 1 for the various ILC beam parameter sets.

The hit densities from pairs in the forward vertex disks at their innermost radii match the densities in the barrel section of the detector, and the densities fall off with increasing radius. So the limits determined above for the barrel detector should apply also to the forward disks.

In general, the radiation damage to detectors at the ILC is very modest compared to detectors at the LHC. For the vertex detector, the radiation dose arising from the pairs on layer 1 is about 10 kRADs/ year. Neutrons are especially damaging to silicon sensors. They are produced both in the beam dump, which is more than 400m distant, and in the beamcal, where roughly 100MRADs / year is deposited by the e⁺e⁻ pairs, and which is only a few meters distant from the vertex detector. Neutrons produced in the EM showers at the beamcal produce the dominant flux at the VXD, integrating to about 5 x 10⁸ n's / cm² / year. So it is essential that the vertex detector sensors not significantly degrade with a few 10's of kRADs of EM radiation, or neutron fluences near 10⁹ / cm² / year. They must also endure exposure to sporadic doses of radiation, coming from errant beam particles showering in the IR.

Finally, the possibility has been raised that the high frequency RF pulse which accompanies passage of each beam could leak beyond the beampipe to produce electromagnetic interference (EMI) in the vertex detector readout, and limit data

transmission to the times between trains. This would impose severe constraints on local data storage and the vertex detector readout. Hopefully tests now in the planning stages will determine if this problem is real or imagined.

II.B.3.b Forward Tracker

Figure 11 shows the number of charged particles / BX which reach a maximum radius between R and $R + 2$ cm, as a function of radius R . It clearly shows that the charged backgrounds are appreciable only at the very small radii affecting the vertex detector and inner most sections of the forward tracking system. The SiD forward tracking is naturally divided into disks extending beyond 20 cm in radius, which are mostly immune from these high rates, and disks extending from small radii out to about 20 cm. The innermost radii of the forward tracking system for layers 1, 2, 3, and 4 are respectively, 4 cm, 5 cm, 6 cm, and 7 cm.

Figure 12 shows the density of hits in the forward tracker layer #1 from e^+e^- pairs, which dominate. At a radius of 4 cm, the hit density is about 0.045 hits / cm^2 / BX. For a radial microstrip channel of length 10 cm and width 50 microns, extending from a radius of 4 cm to 14 cm, this would correspond to an occupancy of about 7×10^{-4} / BX, or about 1.9 hits/train in each channel, for nominal beam conditions. The occupancy is safely below the maximum allowable occupancy for pattern recognition (which we assume to be an about 0.01 / BX), but is large enough to require additional buffering (beyond the presently conceived 4 deep buffer) to maintain high efficiency, especially in the case of the higher energy and higher luminosity beam parameter sets. Microstrip detectors do have sufficiently low occupancies to operate in even the extreme forward tracking direction, although pixel detectors may make pattern recognition easier.

At larger radii in the forward tracker, two backgrounds are significant, charged tracks from gamma-gamma produced muon pairs and hadrons, and interactions of the ~ 1 MeV photons which were produced by pairs in the beamcal. Figure 13 shows the density of these photons hitting layer 1 of the forward tracker, which is roughly uniform over the entire layer 1 disk. Under nominal beam conditions at 500 GeV, between 0.5 and 1 photons hit / cm^2 / BX. Detailed Geant 3 simulations of the interactions of these photons in silicon, including the subsequent interactions of the Compton electrons produced, have shown that the total number of hits resulting in the microstrip detector is approximately 2% of the number of incident photons. Consequently, the photon flux accounts for 0.02 hits / cm^2 / BX in each detector layer, which corresponds to an occupancy of about 10^{-3} / BX in a radially oriented microstrip channel. The sum of the charged and neutral backgrounds in the forward tracking disks, would produce a maximum density of 0.065 hits / cm^2 / BX, equivalent to an occupancy of 3.3×10^{-3} / BX, still below the limit considered tolerable for pattern recognition, but without enough margin to handle the highest backgrounds expected with high luminosity running. The average number of hits per channel per train would be about 9, at least at the innermost radii. This would result in unacceptable efficiency losses unless the buffering depth were increased well beyond 4.

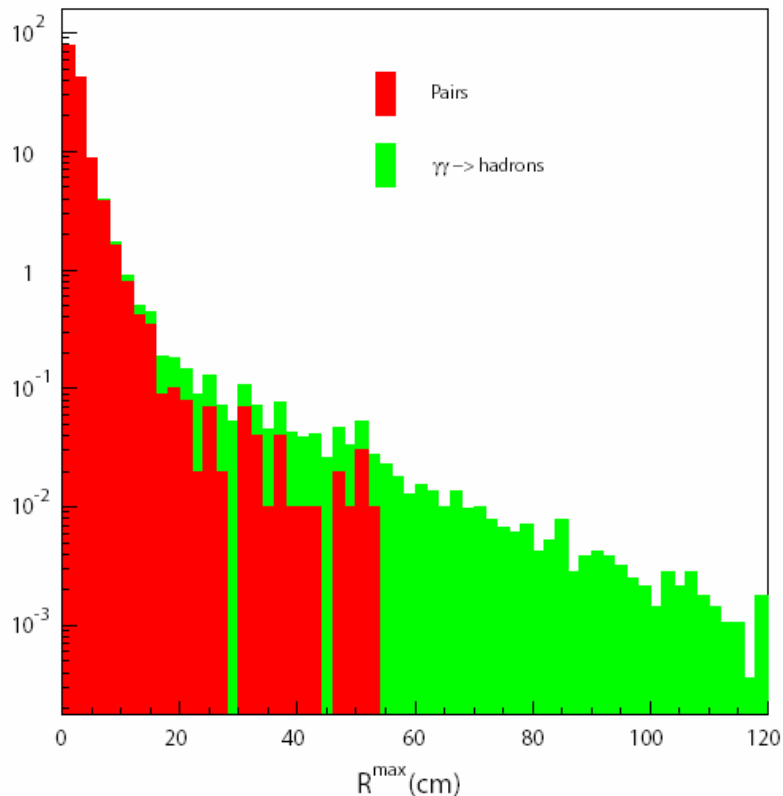


Figure 11 The number of charged particles / BX which reach a maximum radius between R and $R + 2$ cm, as a function of radius R , for nominal 500 GeV beam parameters. The e^+e^- pairs are shown in red; hadrons and muon pairs in green.

II.B.3.c Barrel Tracker

In comparison with the forward tracker, the SiD barrel tracker background rates are benign. Even in the innermost layer, at radius 20 cm, the total rate of charged tracks from e^+e^- pairs, muon pairs, and hadrons, has dropped off to about 1.5 / BX over all of layer 1. The photon interactions dominate the background, but as Figure 13 shows, under nominal beam conditions, the photon density is less than 0.1 / cm^2 / BX in barrel layer 1, corresponding to 0.002 hits / cm^2 / BX (assuming microstrip channels 10 cm long and 50 microns wide), or an occupancy of 1×10^{-4} / BX. Background hits will pose no pattern recognition problem in the barrel tracker. In fact, studies of pattern recognition in the barrel tracker have shown that it is fully efficient for backgrounds that are even 200 times nominal (Ref. Sinev, Wagner). Since the average number of hits over an entire train per microstrip channel is just 0.3, a buffer depth of 4 is adequate. With other beam conditions, the photon rates could increase as much as 20 times. Pattern recognition efficiency would be unaffected, but additional buffering would be required to store the average of 6 hits / channel.

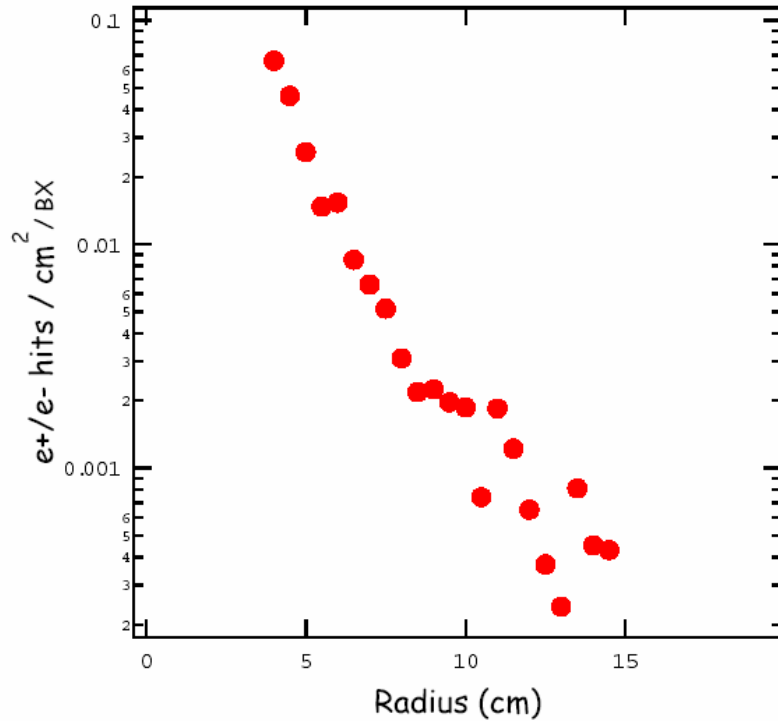


Figure 12 The density of electron and positron tracks / cm² / BX in Layer #1 of the forward tracker, as a function of the radius of the hit.

II.B.3.d Electromagnetic Calorimeter

Backgrounds in the electromagnetic calorimeter arise from the \sim MeV photons originating in the beamcal, and photons and occasional charged particles arising from gamma-gamma interactions. Muons produced upstream of the IP in collimators also contribute, but at an insignificant level. The electromagnetic calorimeter is highly segmented, with 30 layers of silicon pixel detectors, each with transverse pixel size about 4 mm, interspersed with tungsten absorber. Simulations have shown that the occupancy rate resulting from the sum of the backgrounds cited is at most 1×10^{-4} / BX. Noise is thus expected to be inconsequential in calorimetric pattern recognition, and the electronic buffer size is more than adequate to insure full efficiency.

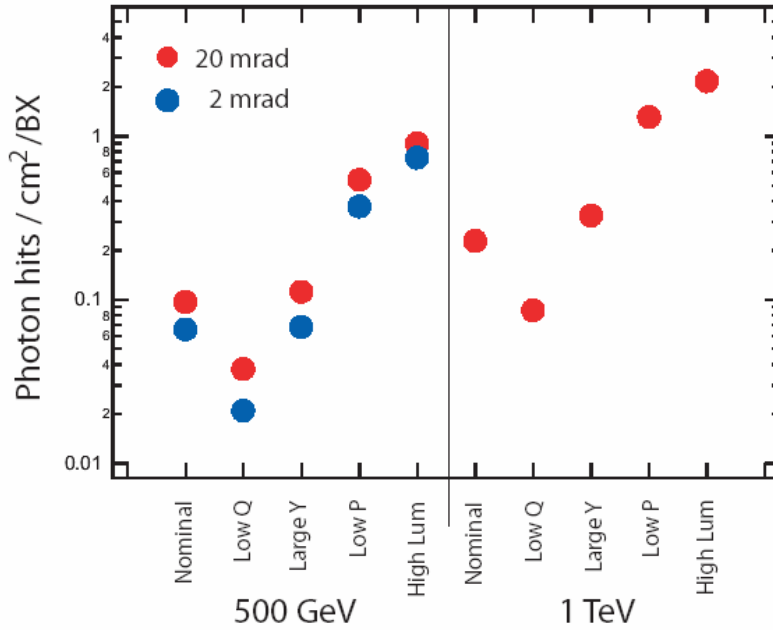


Figure 13 Photon density in the Barrel Tracker Layer #1 for different beam conditions.

II.B.3.e Beamcal and Lumcal.

These calorimeters are both situated very near the beam line, in the vicinity where most of the energy of the e^+e^- pairs is intercepted. Consequently, high radiation doses must be tolerated for normal operation. Occupancies approach 100%/ BX in many of the beamcal channels, and are high in the Lumcal as well. The ILC environment thus imposes severe requirements on radiation hardness and readout speed. These are addressed below in section III.E.

II.C. Costing Overview.

Detector performance and detector cost will depend on the chosen subdetector technologies and the overall detector parameters, particularly the magnitude of the B field, the outer radius of the tracking chamber (which determines the inner radius of the electromagnetic calorimeter), and the length of the tracking chamber (which determines the length of the calorimeter). Particle Flow calorimetry is expected to improve as the distance between the showering particles is increased; this occurs when the radius and length of the calorimeter or the magnitude of the B field are increased. Costs will increase as the stored magnetic field energy, proportional to B^2V , increases, and as the volume of silicon and tungsten required to construct the Ecal increases. Determining an optimum detector configuration will require an understanding of how the physics performance varies with the detector parameters, and how the costs do.

A preliminary cost model for SiD has been developed consisting of two components, a static set of costs for detector components that depend only weakly on the major SiD

parameters, and a parametric cost model for those costs that strongly depend on the parameters. The parametric model allows the calculation of cost derivatives. The driving term appears to be the cost of the superconducting solenoid, but this is preliminary. Some of the other costs are also significant, particularly those of the Ecal and Hcal. The cost model is discussed below in more detail in Section VI.

The SiD starting point has been chosen as a compromise between making the calorimeter and the magnet relatively compact, to save money, and maintaining good particle flow response, to save performance, by boosting the B field, and increasing the segmentation and minimizing the Moliere radius in the Ecal. Detailed simulation studies, and eventual checks of the expected calorimeter performance in beam tests, will be needed to test these assumptions.

III. The SiD Detector

III.A Global Issues

III.A.1 IR Hall: Detector footprint, assembly and access strategy

III.A.1.a Detector footprint

A schematic of the detector footprint in the on-beamline location is shown in Figure 14.

We have assumed:

barrel radius = 6.450m

barrel half-length = 2.775m

endcap yoke thickness = 3.120m

In closed-up mode this yields a total footprint area of 12.900m (x) by 11.790m (z). We assume an additional radial ‘reserved space’ of 1.55m on the outside of the barrel section for services and ‘dressing’, yielding a total reserved radius of 8m, i.e. total extent in x of 16m. In addition, the endcap must be supported by feet, appropriately sized to satisfy site-dependent earthquake support standards. In Figure 14 the feet are shown sized as c. 3.2m in length (25% of door height), projecting beyond the outer wall of the endcap. It is possible that this is a conservative assumption and that shorter feet (possibly half the length) would be acceptable when full engineering considerations are taken into account.

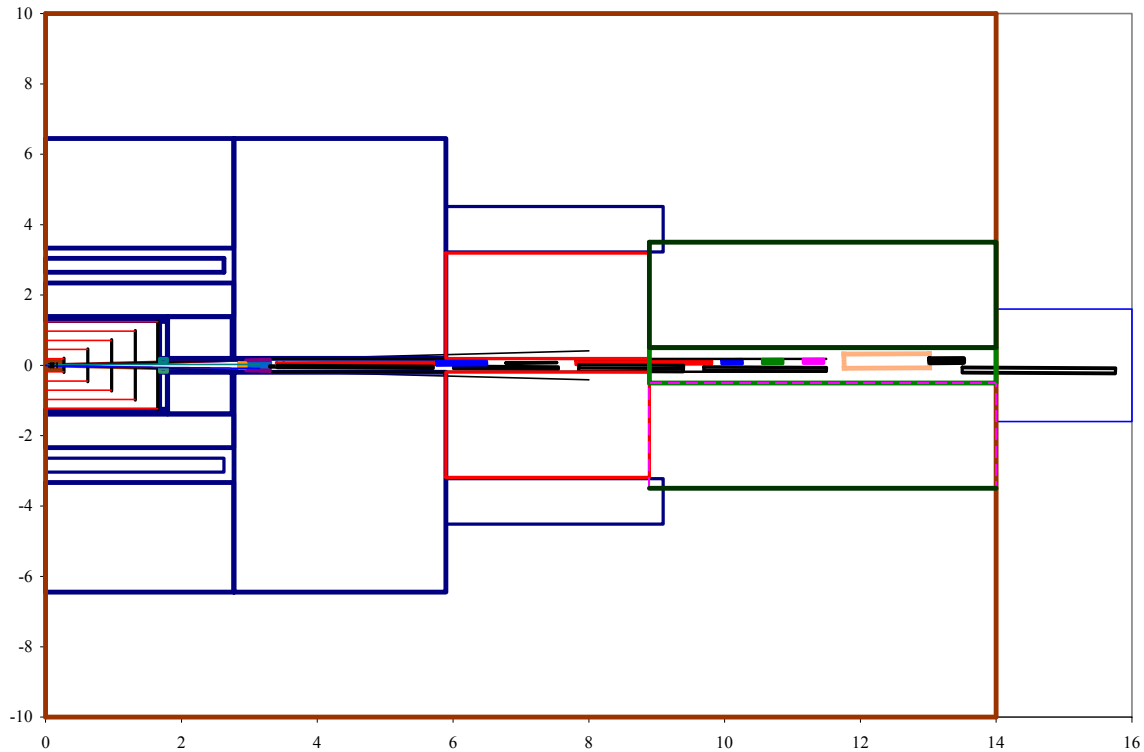


Figure 14 SiD footprint in closed, on-beamline position. Note that only half of the longitudinal extent is shown.

Following the SLC/SLD model, concrete/steel beamline shielding rings (‘Pacman’) are shown in Figure 14 to provide radiation shielding between the end of the final-focus tunnel and the outer wall of the endcap detector. We assume that the detector itself is ‘self-shielding’ so that Pacman allows personnel access to the hall during beam operations. Two Pacman elements are envisaged:

- a 3m-long moveable section in two half-rings which join in the vertical plane; the two halves would be retracted laterally (x-axis) to allow access to the beamline, and for the purposes of endcap door opening. The annular thickness is roughly 3m, comprising 2m concrete, 1m steel.

- a 5.105m-long fixed section between the moveable section and the end of the pit wall. In this model the endcap support feet would project beneath the Pacman sections.

III.A.1.b Detector access

In order to open the endcap door the moveable Pacman halves would both be retracted laterally. This would allow up to 3m for access between the open door and barrel section. An additional 2m of radial space is assumed for access between the pit wall and the dressed outer radius of the barrel sections. The open, on-beamline configuration is shown in Figure 15.

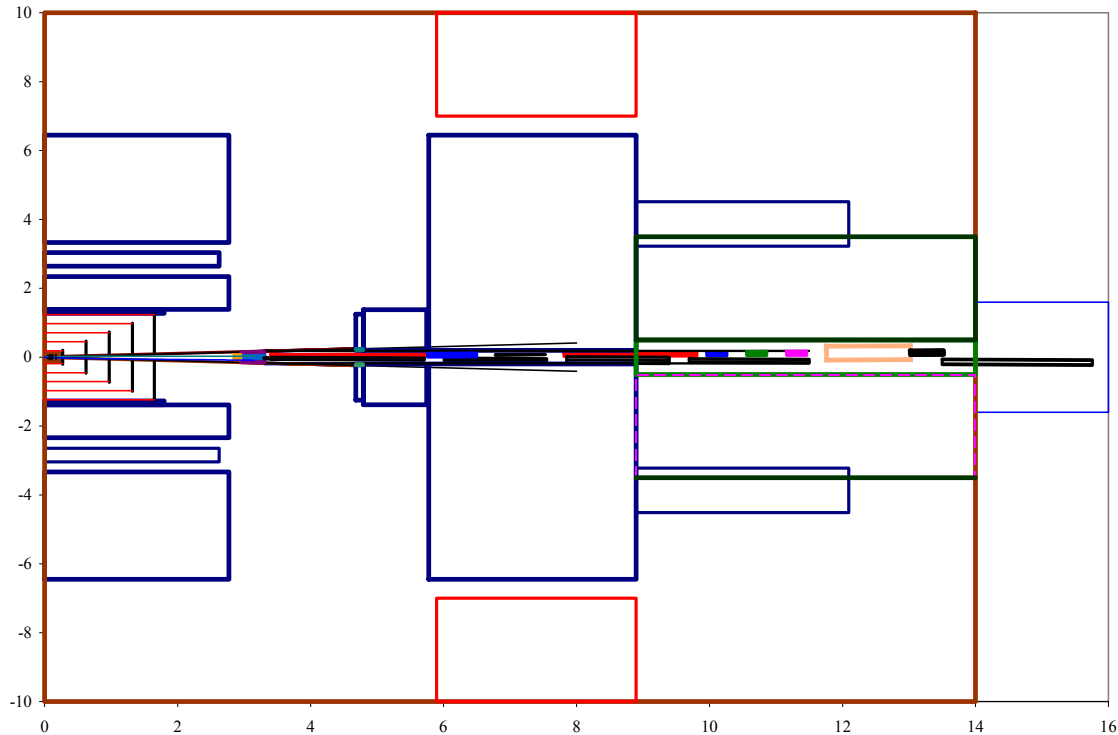


Figure 15 SiD footprint in open, on-beamline position. Note that only half of the longitudinal extent is shown.

The total pit area required for the on-beamline configuration is therefore 20m (x) by 28m (z).

III.A.1.c Detector assembly

For assembly we have assumed the hall must extend in x to accommodate:
 a 3m-thick shielding wall. This would allow work on assembly to proceed during beam commissioning periods.

a 5m space between the shielding wall and a rotated barrel yoke section. This assumes 2m of access space, a 2m assembly fixture, and a further 1m of free space.

A 4m space between the rotated barrel yoke section and the rotated barrel HCAL. This assumes ± 1 m of free space and a 2m assembly fixture.

A 5m space between the rotated barrel HCAL and the pit wall. This assumes 2m of access space, a 2m assembly fixture, and a further 1m of free space.

The assembly configuration is shown in Figure 16. Assuming a rectangular IR hall the total area would be 48m (x) by 28m (z). However the assembly area does not necessarily need to be the full 28m in z extent.

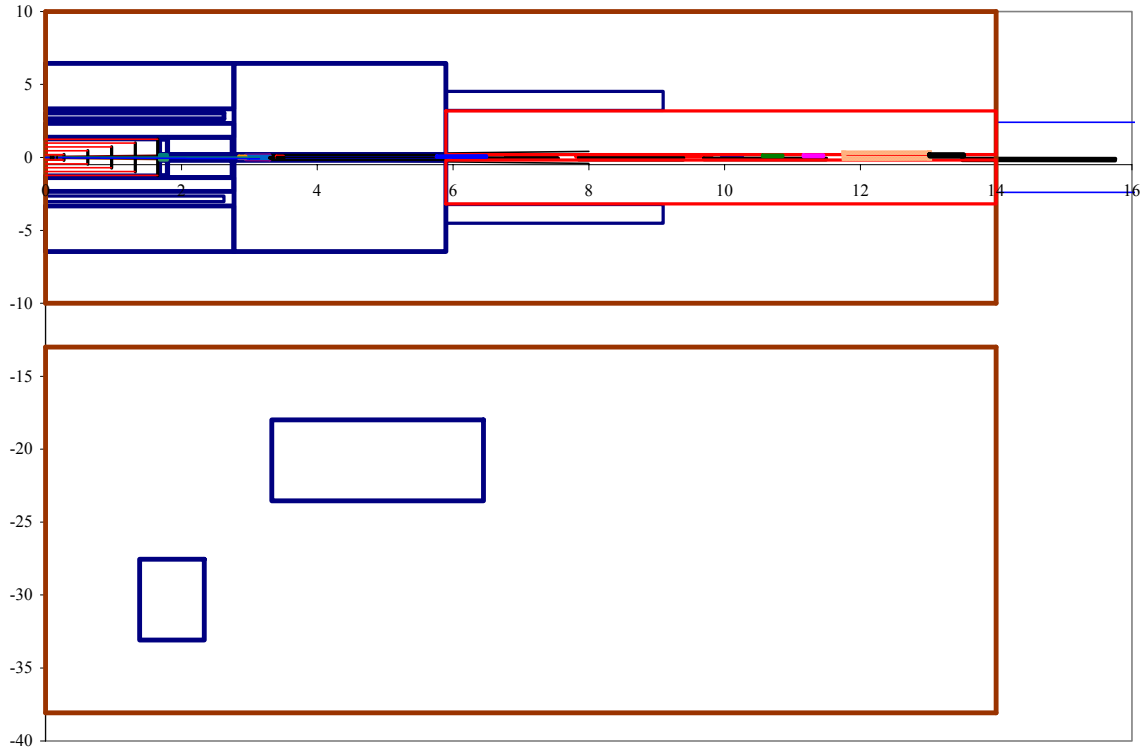


Figure 16 SiD footprint in assembly position. Note that only half of the longitudinal extent is shown.

For the hall height we assume:

The beamline sits at the detector radius +1m from the pit floor.

A clear space equal to the detector diameter (12.9m) is needed above the detector for lifting of detector segments.

6m is required for the crane bridge and hook lifting features.

This yields a hall height of c. 33m.

Note that no detailed consideration has yet been given to the placement of the pit access shaft(s) and the detailed strategy for lifting and moving large components into and around the pit in the space above the detector.

III.A.2 Machine/detector interface issues

The inner radial region of the SiD MDI is shown in Figure 17 for a 20mrad crossing angle scheme. The forward elements downstream of the vertex detector comprise the low-Z mask (graphite), the instrumented mask (Si/W) and the luminosity monitor. The details of this forward region remain to be optimised, and would need to be re-engineered for an alternative intermediate crossing angle between 0 and 20mrad. We comment briefly below on a number of salient MDI issues.

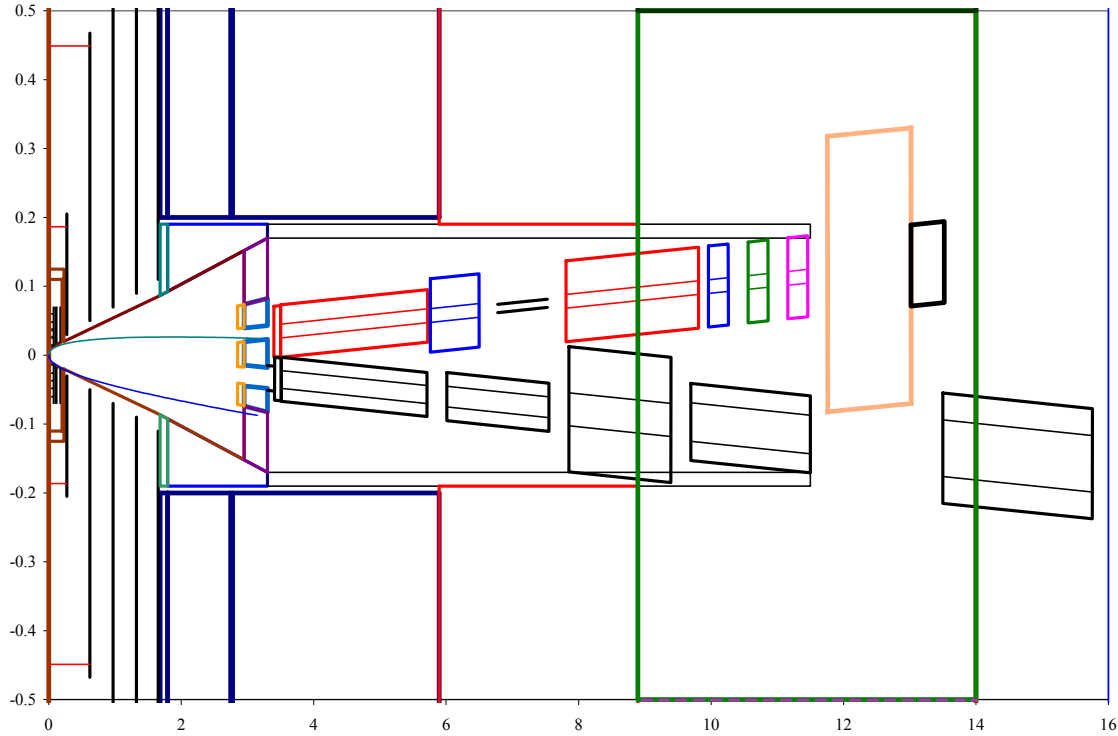


Figure 17 SiD inner radial region and machine/detector interface for 20mrad crossing angle. Note that only half of the longitudinal extent is shown.

III.A.2.a Focal length of final focus system (L^*)

We have no strong preference for particular L^* values within the proposed range $3.5\text{m} < L^* < 4.5\text{m}$. On general grounds we would favour the L^* that is most likely to produce the most luminosity with the least background, while not interfering with the detector acceptance.

III.A.2.b Crossing angle

On general grounds we favour the smallest crossing angle that does not compromise downstream energy and polarisation measurement, does not increase backgrounds, does not significantly increase the risk of backgrounds, and does not reduce the reliability of the machine. We need to work out optimized SiD geometries for the luminosity calorimetry for both the 2 and 20 mrad cases (and any intermediate possibilities) and investigate the impact on low-angle electron tagging for benchmark physics channels.

III.A.2.c Beampipe radius and vertex detector design

Our current design comprises a shortened vertex detector barrel plus four layer endcap, but this approach needs some engineering to know just how thin the endcap can be, and additional study of how it performs given a realistic material budget. On general grounds we would prefer a smaller radius for the inner layer of the barrel vertex detector, but radii in the range between 10 and 20mm appear to be acceptable.

III.A.2.d Local solenoid compensation and anti-solenoids

We have considered, but not studied in any detail, the impact of inhomogeneous fields within the detector fiducial volume due to the local solenoid compensation and anti-solenoids. Our gut feeling is that this will not be an issue provided the field is known reasonably well. However both the VXD and central tracker will have Lorentz effects for the ionization electron paths in the silicon at some level. This will need study.

The mechanical issues of forces and supports for the anti-solenoids will require a detailed study, but we do not think these will be insurmountable.

III.A.2.e Bunch spacing

We have considered whether a bunch spacing of 150ns, vs. the current default of c. 300ns, would impact the SiD design. Since the SiD detector technology that we have considered so far is all intrinsically fast on the scale of 150 ns, this is essentially an issue for the electronics. The SiD electronics concept (so far) for non-very-forward systems involves measurement of the amplitude and time of signals as they occur, buffered up to four measurements per train. When the issue of 150 ns first came up, we changed the clock (and ADC) architecture to 13 bits, so we think that, unless the background per train were to go up by a large factor, we would not be concerned about the difference between 300 and 150ns bunch spacing.

The very-forward detectors would measure every pulse. Again, given the primitive state of thinking, we do not believe we mind whether there are 3000 or 6000 buffers. Note that this design may have some relevance for the machine instrumentation.

The vertex detector is most likely going to evolve from some CMOS like structure that does not involve shifting charge as in a CCD. Since the number of hit pixels per train would not change significantly, and 150 ns is slow compared to the logic times involved in these structures, it should not matter. Note that this conclusion is based on the rather minimal R&D that has been accomplished to date.

III.A.2.f Polarimetry and spectrometry

We think it is desirable to have both upstream and downstream polarimetry. Similar conclusions can be drawn for energy measurements. The downstream energy

spectrometer and polarimeter can be closer to the IP with less extrapolation error from their measurements to the relevant beam quantities at the IP. Given the high precision desired for both energy and polarization measurements, it is also very desirable to have redundant measurements of these quantities by independent techniques with different systematics. In addition, the extraction line more easily accommodates a back-scattered Compton gamma measurement to complement the back-scattered Compton electron measurement. Beam-beam collision effects can be directly measured with extraction line diagnostics by comparing measurements with and without collisions. Having both upstream and downstream polarimeters helps the spin alignment procedure and ability to estimate errors. We are still exploring the design issues for both upstream and downstream systems. In the case of a 2 mrad crossing angle more work is needed to demonstrate the feasibility of both the downstream polarimeter and spectrometer.

III.A.2.g Z0 pole calibration

We have not yet given this issue real study, but expect that a very large number of tracks will be required to align the tracking detectors and perhaps to cross calibrate the calorimeters. If Z calibration runs are utilized then the data should be collected at full field. Experience from SLD shows that of order 500k Zs was just about sufficient to align a system of 96 CCDs including non-planar shape corrections for the sensors in the vertex detector. We think that the trackers need to be designed with an alignment friendly awareness - nice overlap regions and lever-arms and preferably a high degree of symmetry. We have not thought much about aligning the endcap yet. That could require more data.

If the central tracker alignment were based on the SLD VXD alignment strategy, the statistics required may well be higher given the larger volume and many more overlapping regions to deal with.

We would expect to have to (re-)align after each major detector access. In principle this ought to be no more than a few times per year.

With regard to whether or not dedicated Z calibration runs are required, we note that there are actually more charged hadrons, electrons, muons, photons and neutral hadrons produced at $E_{cm}=500$ GeV than at $E_{cm}=M_Z$ assuming an integrated luminosity ratio of 100:1 for the two energies. This is true for all particle energies and angles, and is due to high cross-section processes such as $e^+e^- \rightarrow e\nu W$, eeZ , γZ and $\gamma e \rightarrow \nu W$, eZ . Figure 18 shows the inclusive particle energy distributions for charged hadrons, electrons, photons, and neutral hadrons for the two center-of-mass energies assuming a 100:1 luminosity ratio. For particle energies greater than about 25 GeV, the number of charged and neutral particles at $E_{cm}=500$ GeV is much greater than at $E_{cm}=M_Z$.

Missing at $E_{cm}=500$ GeV is the large number of 45 GeV monochromatic back-to-back quark jets and leptons. This will make some calibration tasks more complicated if only $E_{cm}=500$ GeV data is used. However, many charged track pairs at $E_{cm}=500$ GeV will be

back-to-back in r - ϕ , and the knowledge of the Z and W masses along with precise cross-section calculations can probably be used to obtain excellent energy scale calibrations using $E_{\text{cm}}=500$ GeV only. We conclude that further studies are called for in order to determine if Z calibration runs are necessary.

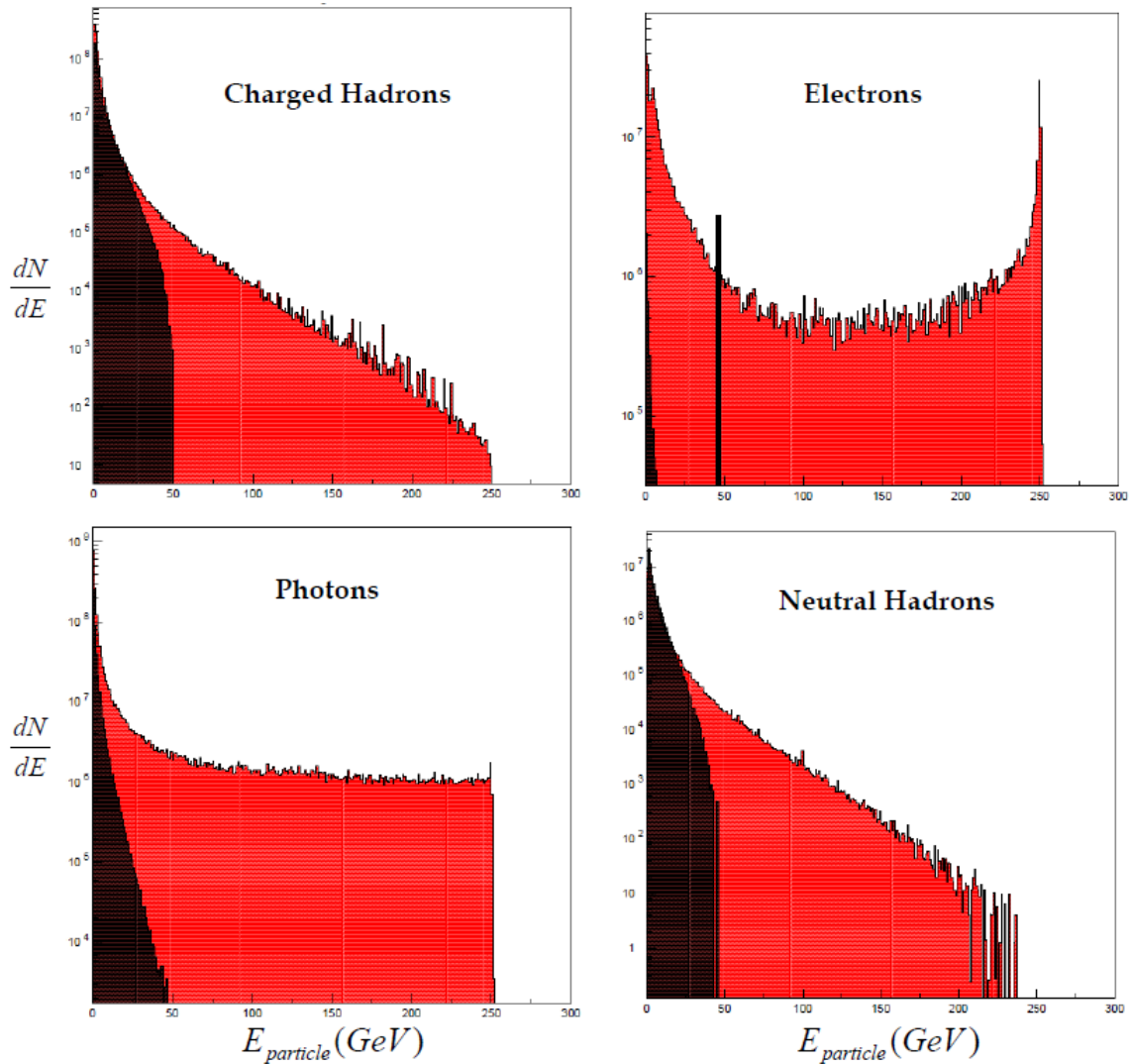


Figure 18 Inclusive particle energy distributions assuming 100 fb^{-1} at $E_{\text{cm}}=500$ GeV (red) and 1 fb^{-1} at $E_{\text{cm}}=M_Z$ (black).

III.B Beamline

Beamlines based on 3 crossing angle schemes have been developed for the ILC: 2 mrad, 14 mrad and 20 mrad.

III.B.1 The 2 mrad Beamline Layout

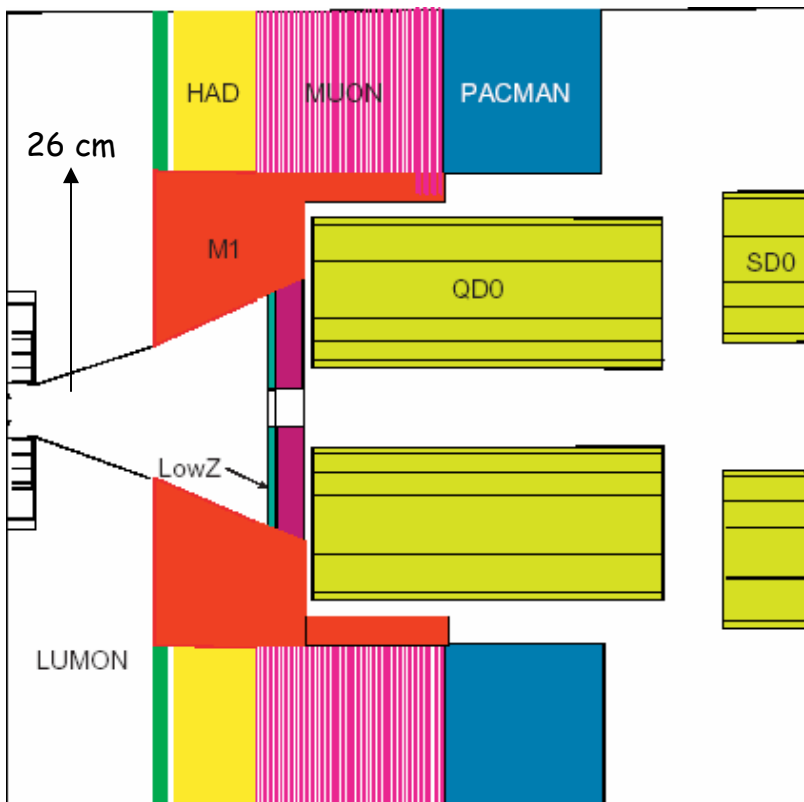


Figure 19 Layout of the 2 mrad beamline near the IP for an L^* of 3.5m.

The 2 mrad beamline requires a large aperture quadrupole QD0 as the closest element of the beamline to the IP. In Figure 19, which has been used for the GEANT3 based Monte Carlo background simulations, an inner aperture of 90mm and a length of 4m has been assumed. The outer radius of the cryostat has been set at 21cm based on scaling laws for NbTi SC magnets. The detector could then begin at a radius of 26cm, assuming 1cm clearance on each side of a 3cm thick support tube.

Other optics designs are under consideration that have shorter length and/or smaller aperture based on Nb₃Sn SC cable. The eventual mechanical design of these magnets is expected to reduce the outer radius of the cryostat. As no design exists to date, we have

assumed that 10cm in z will be required for the cold to warm longitudinal end of the cryostat which in turn determines the back end of the beam calorimeter.

III.B.2 The 20 mrad Beamline Layout

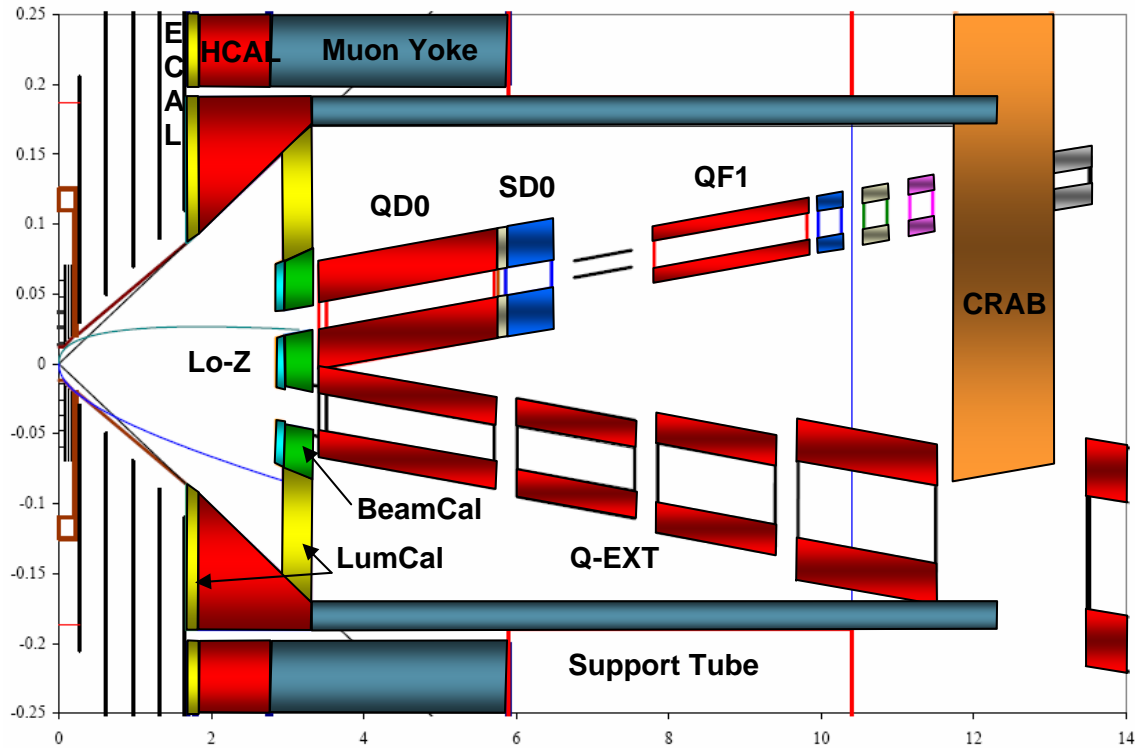


Figure 20 Plan view of the 20 mrad beamline near the IP for an L^* of 3.5m.

The layout of the 20mrad beamline is based on the compact SC direct wind technology developed at BNL and in use, for example, at HERA. At this IP there will be independent beamlines for the incoming beam and for the outgoing disrupted beam and beamstrahlung photons. The magnets, in independent cryostats, are compact enough to reside comfortably with a 19cm outer radius tube, allowing the detector to begin at 20cm. Figure 20 shows the plan view of the region around 3.5m, with a 10cm long warm to cold transition. The backend of BEAMCAL is at 3.4m. Notionally, the beam pipe passes through BEAMCAL and immediately expands to the radius of the tungsten mask at the corresponding z location of its front face. Inside the beam pipe covering the area that his severely impacted by the low energy e+e- pairs, is 10cm of a low Z material, such as Be or C. The beam pipe then follows the mask down at its acceptance angle to interface with the vertex detector (Figure 23).

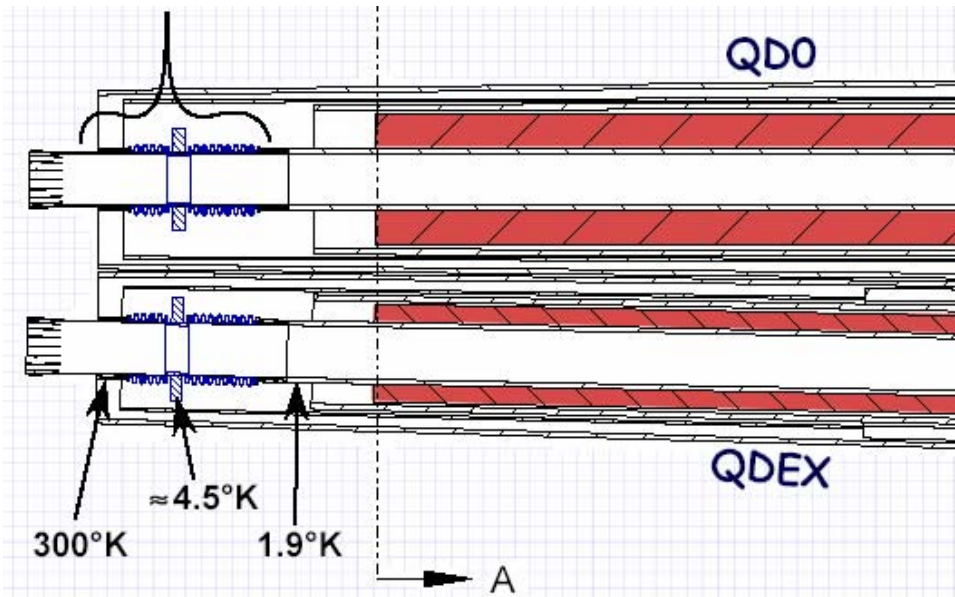


Figure 21 Longitudinal design of the IP side of QD0/QDEX magnet package with the cold mass and effective L^* indicated by the dashed line marked A. The cold to warm transition to the independent beampipes that traverse BEAMCAL are to the left.

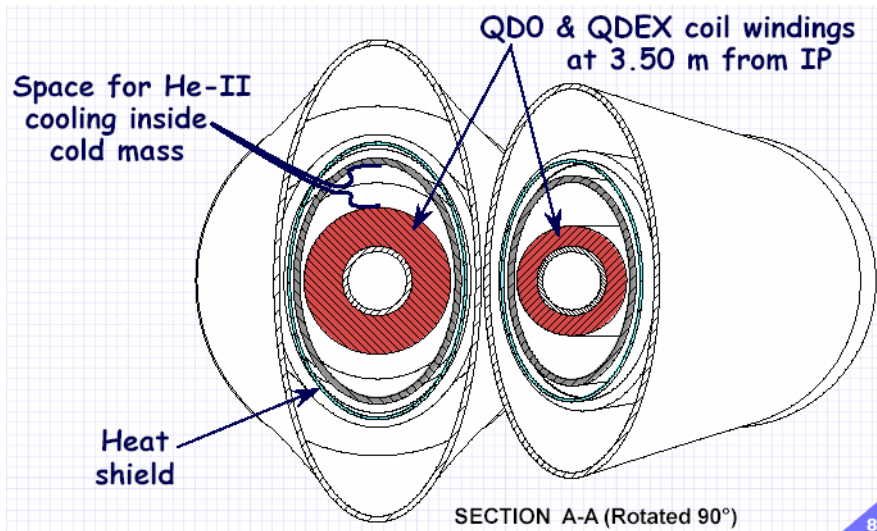


Figure 22 Cross section of the beampipes and magnet cryostats at $L^*=3.5\text{m}$

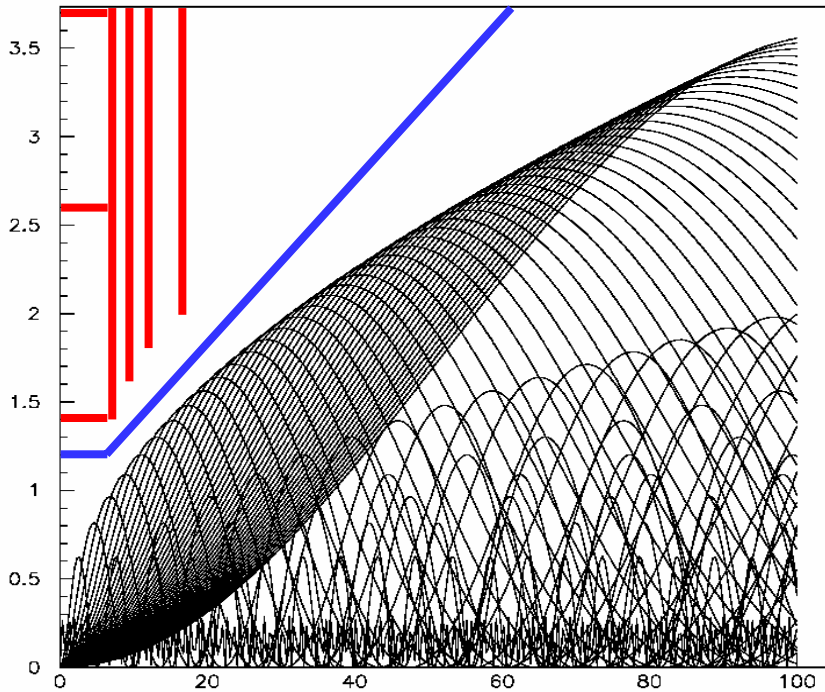


Figure 23 12mm beam pipe at the interaction point with VXD and maximum envelope of the e^+e^- pair backgrounds in a 5 Tesla field.

III.B.3 The 14 mrad Alternate Beamline Layout

While not in the ILC Baseline configuration, work has begun on the engineering of a compact SC magnet pair that could support a 14 mrad crossing angle. The motivation is to be able to provide the minimum crossing angle that would still support a dedicated extraction line and thus minimize the deleterious effects produced by the transverse component of the detector's solenoid field. Furthermore, it is assumed that improvements to the magnet layout will be incorporated into the 20 mrad baseline in the next iteration of its design.

To accomplish this, the extraction line quad begins at 6m from the IP and the QD) of the incoming beam has an additional winding layer at large radius that runs a low current in the opposite direction to the main windings, designed to null the field along the path of the extracted beam (Figure 22). The tapered extraction line beam pipe and the shielded QD0 reside in a common cryostat of very modest radius. Figure 25 shows the GEANT3 model of the beam lines for the 14 mrad scheme. Everything fits within the same 19cm radius support tube. Thus, except for the fact that the centers of the input and exit apertures in the BEAMCAL are 30% closer together, the rest of the design is identical to that of the 20 mrad baseline.

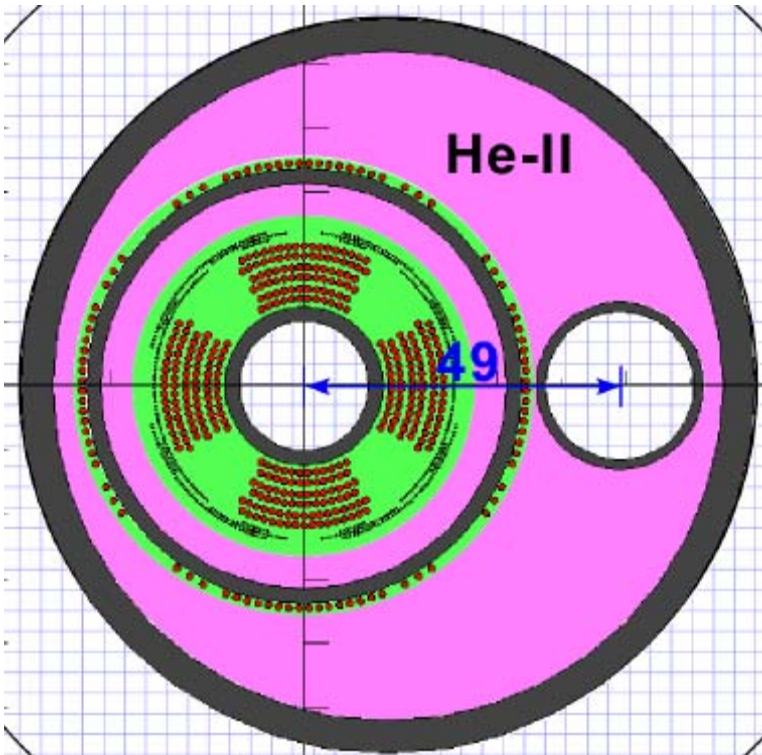


Figure 24 Cross section of the 14mrad cryostat at $L^*=3.5$ m. The separation between incoming and outgoing beams at that point is 49mm.

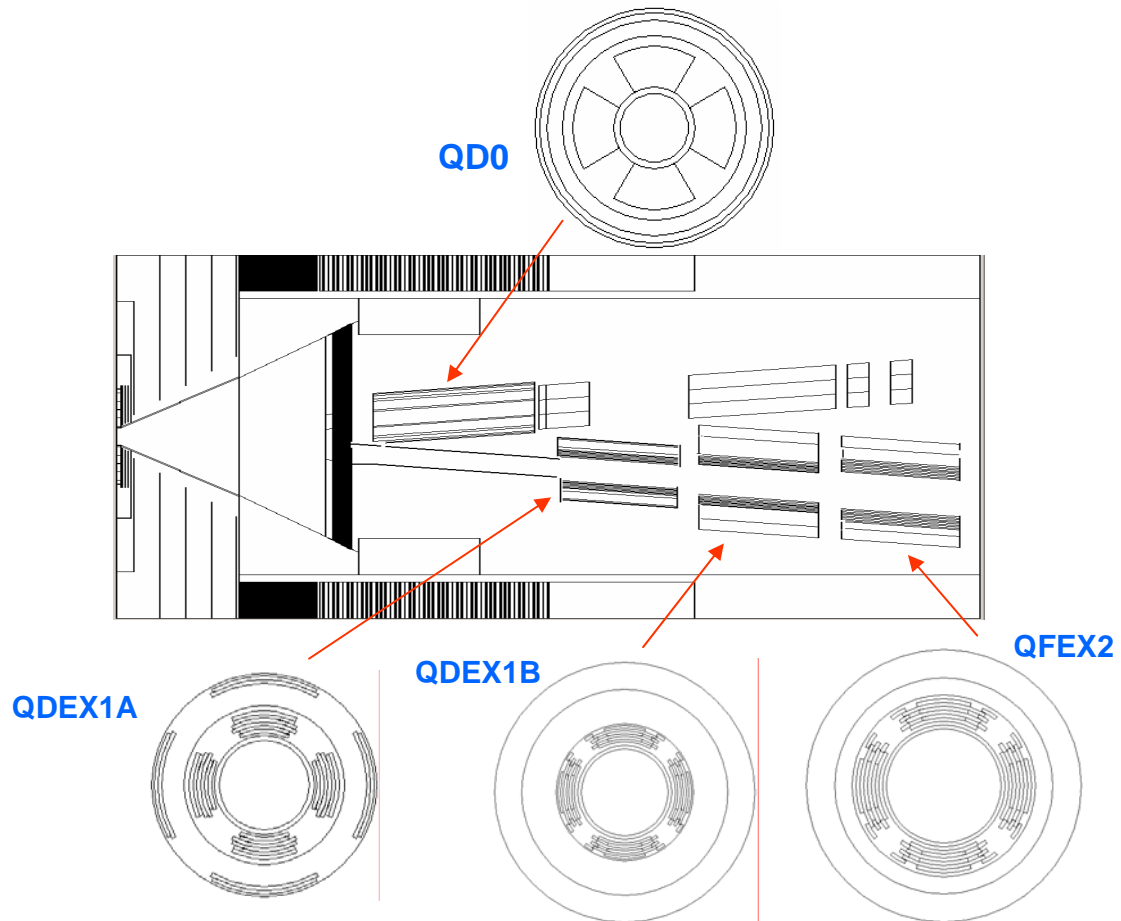


Figure 25 Geant3 layout of the 14 mrad extraction line. Detailed designs of the indicated quadrupoles have been created and coded into the simulation.

III.C Tracking System

III.C.1 Vertex and Tracking System: Introduction

Within the SiD detector concept the tracking system is to be regarded as an integrated tracking system. Individual detector components can be identified in the vertexing and tracking system, but the overall design is driven by the combined performance of the pixel detector at small radius, the outer strip detector at large radius and the electromagnetic calorimeter for the identification of minimum ionizing track stubs.

The physics at the ILC requires good track reconstruction and particle identification for a wide array of topologies. The main element for the pattern recognition is the highly pixellated vertex detector. The first step in track finding relies on identifying tracks in the vertex detector, where pattern recognition is simplified by the fact that precise three-dimensional information is available for each hit. Tracks found in the vertex detector are then propagated into the outer tracker, picking up additional hits and measuring the track curvature. However, an important class of events, notably highly boosted b-quarks, will decay at radii that do not allow for pattern recognition in the vertex detector because there are either too few hits, or simply because the decay occurs outside the vertex detector. The tracks from these decays are reconstructed by a stand-alone tracking algorithm using the outer tracker. In a third class of events, tracks produced by the decay products of long-lived particles that decay outside the second or third layer of the outer tracker cannot possibly be reconstructed with neither the standard vertex detector-based pattern recognition nor the stand-alone outer-tracker track finder. Obvious examples are long-lived particles such as K_S^0 and Lambdas. However, the detector should also be capable of detecting new physics signatures that would include long-lived exotic particles like those predicted by some gauge-mediated supersymmetry breaking scenarios. There are also issues of reconstructing kinked tracks produced by particles that lose a substantial portion of their energy in the tracker, as well as reconstructing backscatters from the calorimeter. The tracks from these event topologies are captured with a calorimeter-assisted tracking algorithm. This algorithm uses the electromagnetic calorimeter to provide seeds for pattern recognition in the tracker. The very fine segmentation of the EM calorimeter allows for detection of traces left by minimum ionizing particles and uses them to determine the track entry point, direction, and sometimes curvature with a precision sufficient for extrapolating the track back into the tracker.

This set of complementary algorithms provides for very robust pattern recognition and track finding and it is the performance of this integrated tracking system that determines the overall physics reach of the detector. This section described the mechanical layout of the vertex detector and the outer tracker. The current status of the performance of the various tracking algorithms is described.

III.C.2 Vertex Detector Design

III.C.2.a Mechanical Design

Introduction

The vertex detector consists of a central barrel with five silicon pixel layers and forward and backward disk regions, each with four silicon pixel disks and three silicon disks at larger $|Z|$. Barrel layers and disks are arranged to provide good hermeticity for $|\cos \theta| < 0.99$ and to guarantee good pattern recognition capability for charged tracking and excellent impact parameter resolution over the whole solid angle. The central region is shown in Figure 26.

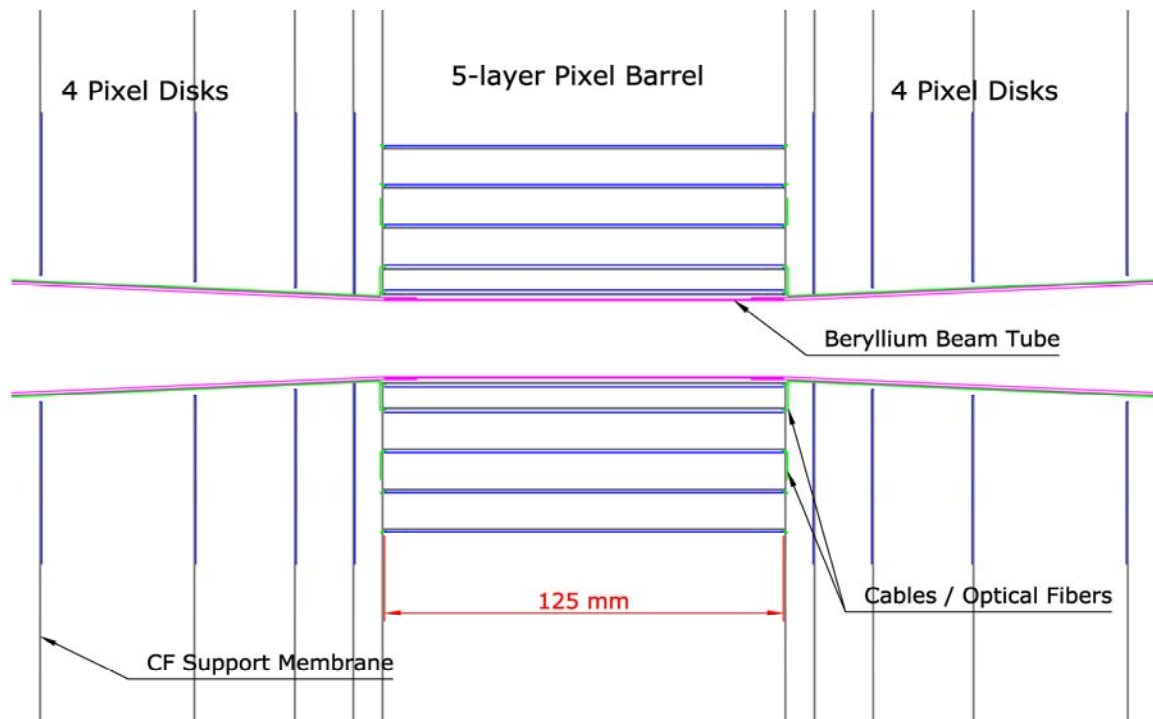


Figure 26 R-Z view of the central pixel region

At this point in time, no choice can be made yet for the sensor technology. The candidates for sensor technology are discussed at the end of this section. The design presented here only makes one assumption with regard to the operating temperature of the sensors, independent of technology. The novel support structure that has been designed assumes fabrication and assembly at room temperature and a sensor operating temperature $> -10^{\circ}\text{C}$. Carbon fiber - resin laminates have been selected to provide good stability of sensor positions while limiting the number of radiation lengths and accommodating thermal contractions. Sensors are to be cooled by flow of dry gas.

Some practical considerations have been incorporated into the design. To allow assembly about the beam pipe and later servicing, the vertex detector is split about the vertical plane into left and right sub-assemblies. Once mated, the two sub-assemblies are supported from the beam pipe and stiffen the portion of the beam pipe passing through them.

During silicon servicing, the vertex detector and beam pipe remain fixed while the outer silicon tracker rolls longitudinally (see Figure 27).

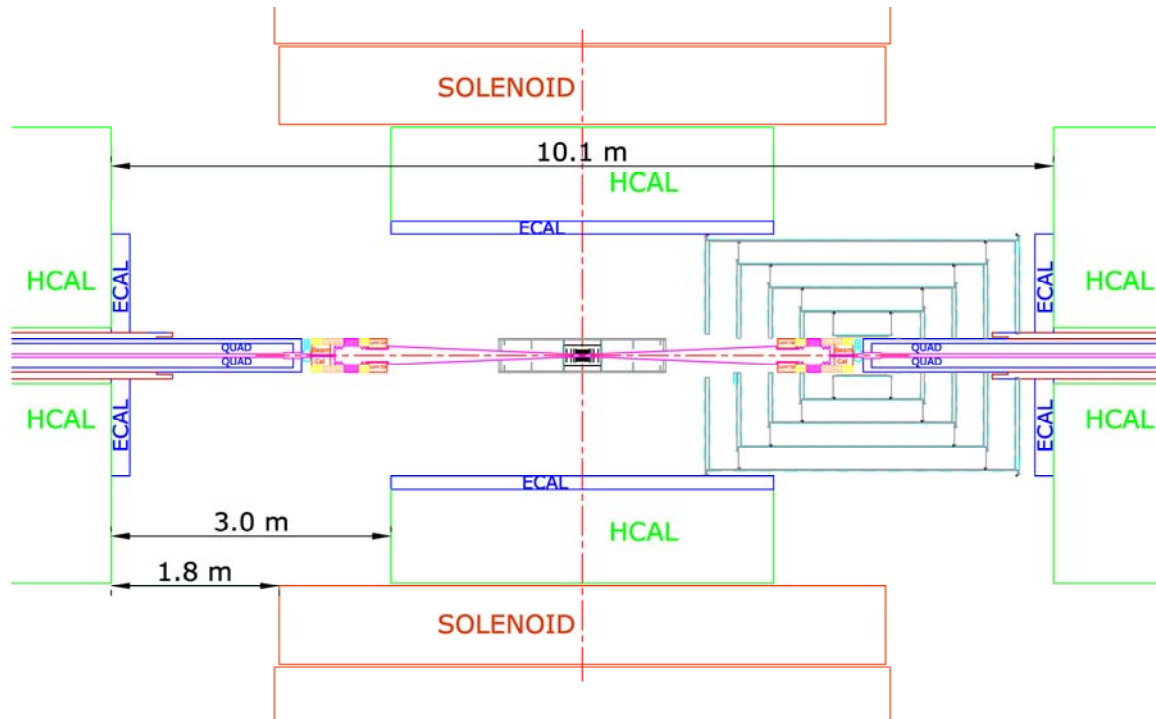


Figure 27 Configuration with detector open for access to the vertex detector region

To allow that motion, to allow the outer silicon tracker elements to be at the lowest possible radius, and to leave space for any additional thermal insulation which might be needed, the outer radius of the vertex detector, including its support structures, has been limited to 18.5 cm. To maximize physics potential, the inner radius of vertex detector elements has been chosen to be as small as practical consistent with beam-related backgrounds and the beam pipe profile. In the barrel region, the minimum radius to a sensor surface is 1.4 cm, governed by the beam backgrounds, as discussed earlier.

Geometry

The overall vertex detector and inner tracker layout is shown in Figure 28. This figure is an R-Z view with R measured normal to the surface of a feature. The innermost barrel layer, which has been located as close to the beam tube as practical, is difficult to see in this figure. A beam's eye view of the vertex detector barrel is given in Figure 29. Note that the barrel sensors in each layer are positioned at one of two possible radii, A and B, and are 125mm long. The five layers are arranged at radii ranging from 14 to 60 mm (A), or 15.2 to 60.7 mm (B). The vertex detector also has four disk layer sensors which are attached to carbon fiber support disks at z positions ranging from about

72 to 172 mm. The innermost disk covers radii from 14 mm out to 71 mm; the outermost, from 20 mm to 71 mm. Forward tracker layers continue beyond the vertex detector, extending in Z from about 207 to 834 mm. Their inner radii range from 29 to about 117 mm, and their outer radius is about 166 mm.

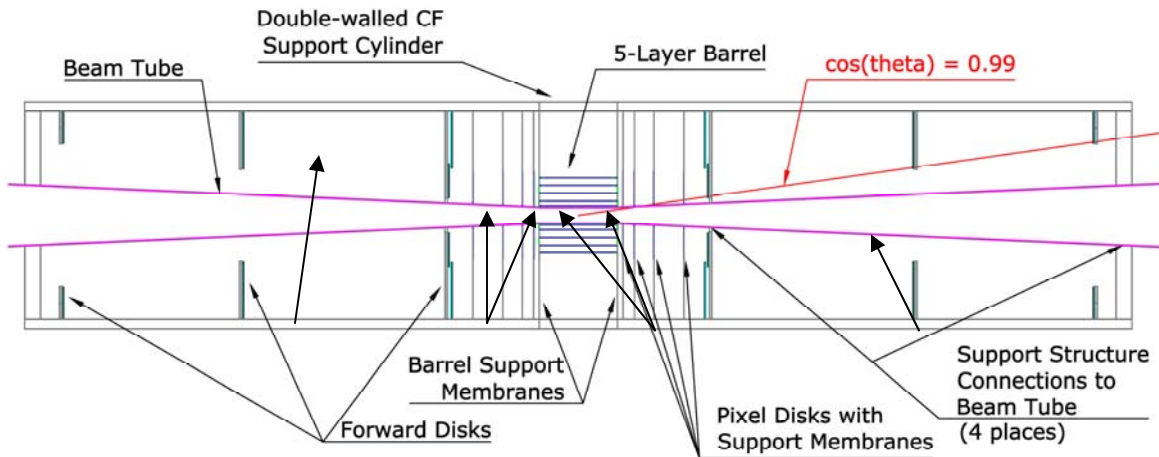


Figure 28 R-Z view of the vertex detector and its support structures

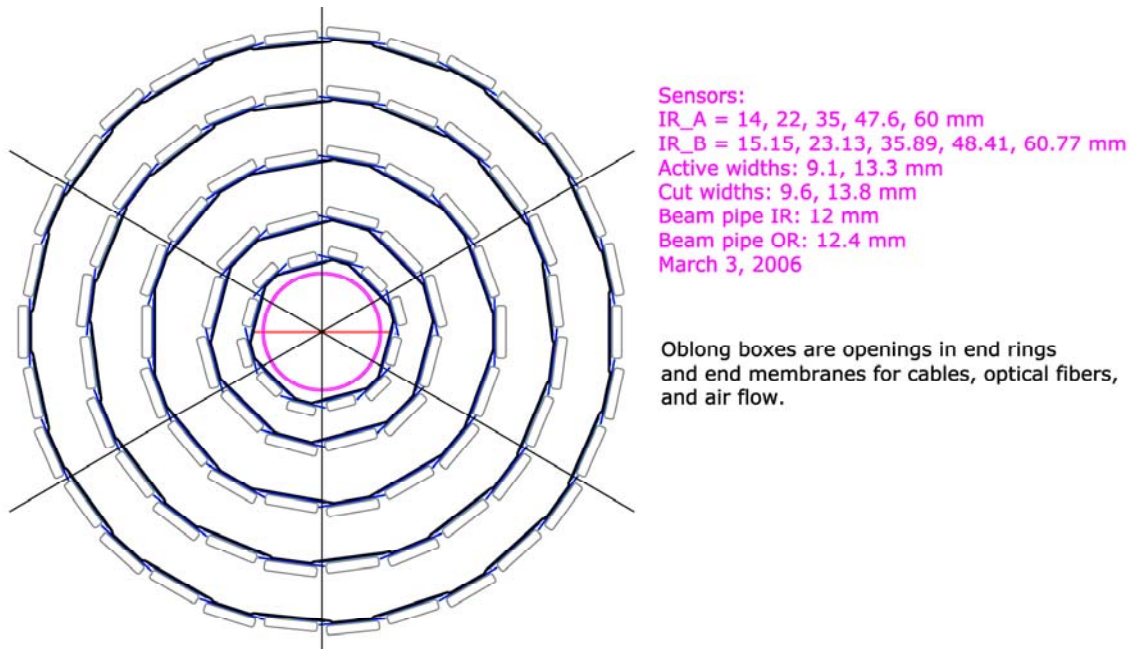


Figure 29 R-Phi view of the vertex detector barrel

Table 3 Sensor geometry (units = mm unless otherwise noted)

Barrel	R_perp inner sensor surface	Cut length	Cut width
Layer 1a	14	125	9.6
Layer 1b	15.154	125	9.6
Layer 2a	22	125	13.8
Layer 2b	23.132	125	13.8
Layer 3a	35	125	13.8
Layer 3b	35.890	125	13.8
Layer 4a	47.6	125	13.8
Layer 4b	48.409	125	13.8
Layer 5a	60	125	13.8
Layer 5b	60.770	125	13.8

Pixel disks	R_perp inner edge	R_perp outer edge	Z_center
Disk 1a	14	71	71.918
Disk 1b	14	71	72.638
Disk 2a	16	71	91.683
Disk 2b	16	71	92.403
Disk 3a	18	71	123.072
Disk 3b	18	71	123.792
Disk 4a	20	71	171.283
Disk 4b	20	71	172.003

Forward disks (if pixels)	R_perp inner edge	R_perp outer edge	Z_center
Disk 5a	28.531	165.953	206.650
Disk 5b	28.531	165.953	208.625
Disk 6a	75.831	165.953	541.102
Disk 6b	75.831	165.953	543.077
Disk 7a	117.309	165.953	832.186
Disk 7b	117.309	165.953	834.161

Beam Pipe

The beam pipe through the central portion of the vertex detector is all-beryllium. Within the barrel region of the vertex detector, the beryllium beam pipe has been taken to be a straight cylinder with inner radius of 1.2 cm and a wall thickness of 0.04 cm. At $Z = \pm 6.25$ cm, a transition is made to a conical beam pipe with a wall thickness of 0.0875 cm. The half angle of the cone is $\sim 2.773^\circ$. Transitions from beryllium to stainless steel are made beyond the tracking volume, at approximately $Z = \pm 37.5$ cm. The initial stainless steel wall thickness is 0.0875 cm; it increases to 0.15 cm at approximately $Z = \pm 120$ cm.

The inner profile of the beam pipe is dictated by the need to avoid the envelope of beam related backgrounds. That envelope and the beam pipe envelope are shown in the Physics Environment section.

A titanium liner of thickness ~ 0.0025 cm is expected to be needed within the central beryllium portions of the beam pipe. The liner provides shielding against gammas and x-rays. Washers to shield against back-scattering may also be necessary, but their locations and geometry remain to be determined. The titanium liner in the cone section of the beam pipe is expected to be a factor of ~ 3 thicker than central region due to the larger angle with respect to the incident photons originated near beam exit hole.

To prevent bending of the small-radius portion of the beam pipe and ensure good stability of vertex detector position, the outer vertex detector support cylinder is coupled to the beam pipe at four longitudinal locations: ± 21.4 and ± 88.2 cm. The support cylinder is separated into left and right halves, as are all vertex detector structures. Inner and outer support cylinder walls are 0.26 mm thick. They are made from four plies of high modulus carbon fiber – resin pre-preg. Wall separation is 15 mm. Use of the support cylinder to distribute cooling air is described in the section which follows.

Cooling

Technologies appropriate for vertex detector readout will be discussed in more detail later in this section. Here it suffices to say that any technology will at least be required to readout the entire detector in ≤ 100 beam crossings, just so that pattern recognition is not overwhelmed by background, and ideally they will associate hits with single beam crossings. Electronics to do this will likely be incorporated into the vertex detector sensors, and will generate heat locally which must be removed. Hence strategies to cool the detector must be incorporated in the design.

Cooling in the SiD vertex detector is based upon forced convection with dry air. Air flow paths are indicated in the upper portion of Figure 30. For our initial investigation (based upon a spreadsheet calculation), the flow for barrel cooling was assumed to be from one barrel end to the other. The average power dissipated in a sensor was taken to be $131 \mu\text{W}/\text{mm}^2$. That corresponds to a total power of 20 watts for the 5-layer barrel considered. These numbers presume power cycling, i.e., that most power is dissipated during the roughly 1 ms during which the beam train is present, and that power is turned off in the 199 ms between trains. We assumed that power is distributed uniformly over the sensor active surface and that both sensor surfaces participate in heat removal. Supply air temperature was taken to be -15°C . For a given sensor, power transferred inward through the carbon fiber cylinder was taken to be proportional to the surface contact between the sensor and carbon fiber. Thermal impedance through silicon, epoxy, and carbon fiber laminate has been included, but turns out to not to be particularly significant. The remaining power was assumed to be transferred outward into the layer to layer gap. For flow and heat transfer calculations, the gap between barrel layers was taken to be 1 mm less than the nominal layer spacing. Laminar flow was assumed.

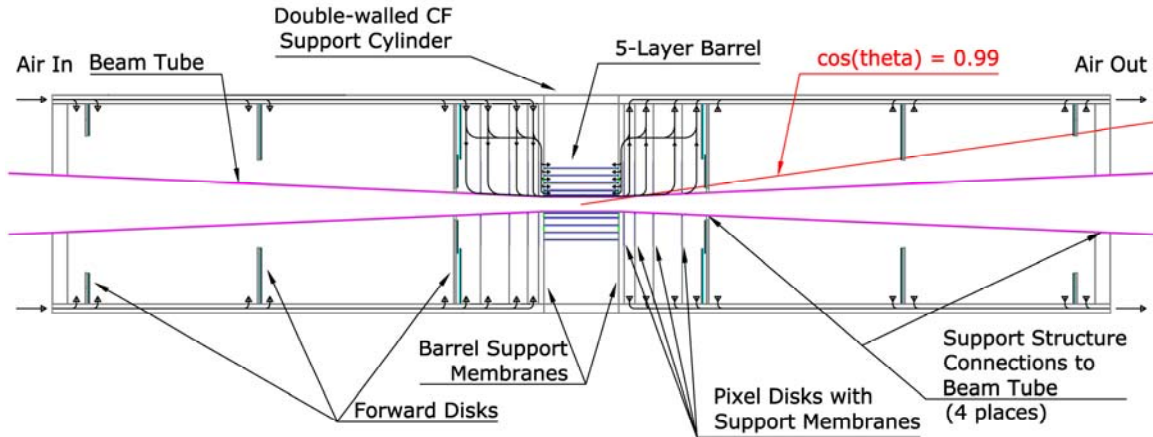


Figure 30 Cooling air flow paths

The cooling power was evaluated as a function of Reynold's number, which was required to be the same for all barrel gaps. To provide laminar flow and limit the likelihood of vibration, a maximum Reynolds' number of 1800 was considered. Cooling with turbulent flow and acceptable stability of sensor positions may also be possible, but remains to be investigated. Results are summarized in Table 4, Figure 31, and Figure 32.

Table 4 Barrel flow and rise in air temperature versus Reynold's number

Reynold's number	Total barrel flow (g/s)	Ave. ΔT air ($^{\circ}\text{C}$)	Max sensor T ($^{\circ}\text{C}$)
800	9.0	2.21	-2.44
1200	13.5	1.47	-4.61
1800	20.2	0.98	-6.36

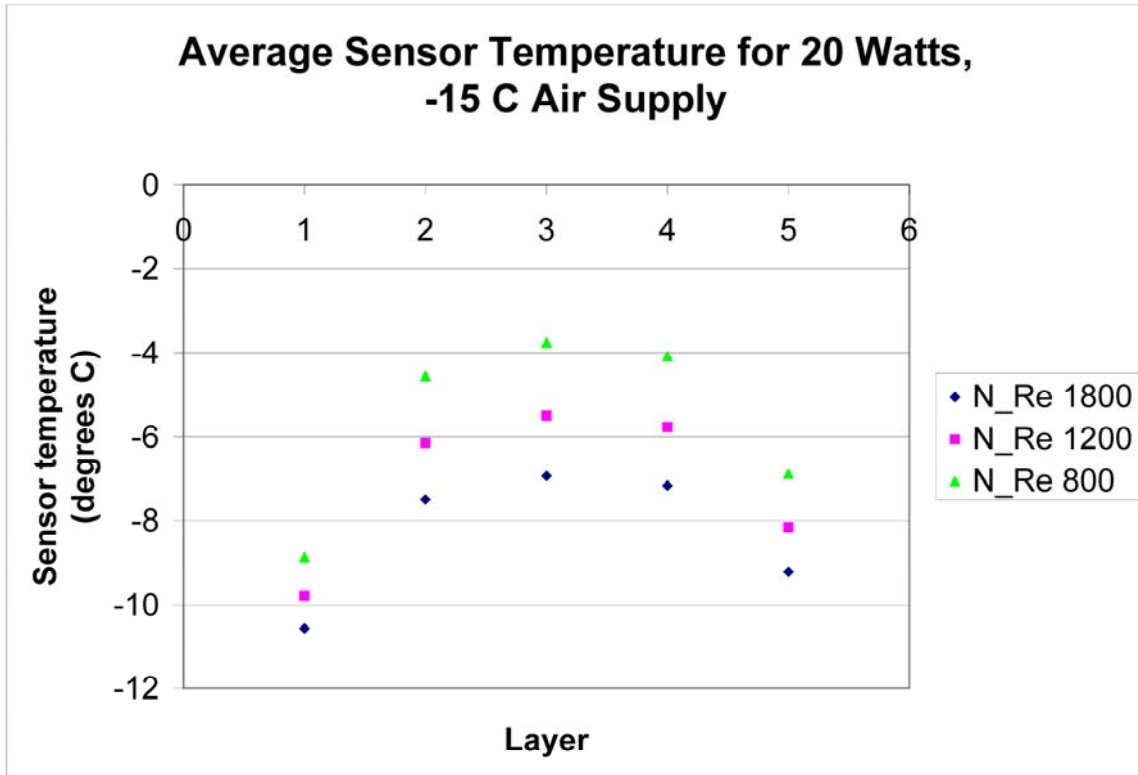


Figure 31 Average temperatures of barrel sensors

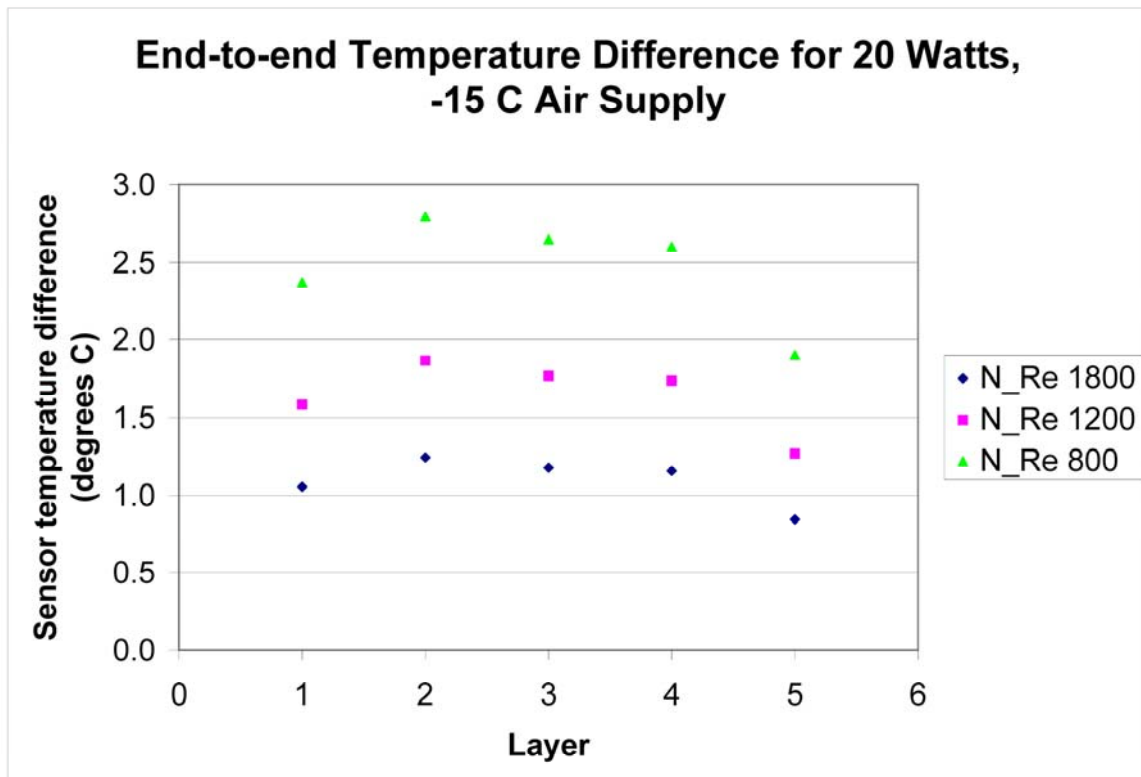


Figure 32 End-to-end temperature differences of barrel sensors

The sensors of the outermost layer, where it is easier to provide cross-section for air flow, and sensors in the innermost layer, where we have assumed that the beam pipe includes thermal intercepts and will introduce no heat, are noticeably cooler than sensors of the three middle layers, rather independent of the flow. In the outermost layer, the cross-section provided for air flow could be reduced to raise the temperature of that layer. In the gap between the innermost layer and the beam tube, flow is likely to be lower and temperature higher, once supply and return distribution patterns of air flow have been taken into account.

Higher flow rate clearly improves the uniformity of sensor temperatures end to end and reduces the difference between the temperature of a sensor and the cooling air. All flow rates which have been considered lead to temperature variations which should be acceptable for dimensional stability, which is crucial for high precision vertexing. The time-dependent effects of power cycling remain to be investigated. Those depend on the thermal mass presented by the barrels and the details of the way in which power is cycled.

External heat input to the barrel has been assumed to be negligible. Satisfying that assumption will require reasonable care in designing cables, in providing heat intercepts should they be needed, and in providing an external thermal enclosure. The outer support cylinder of the vertex detector offers a natural thermal enclosure.

Details of end openings in barrel membranes remain to be included. Those openings provide a natural mechanism for adjusting relative flow between barrel layers. A membrane between the outermost barrel layer and the vertex chamber support cylinder would ensure that flow does not excessively bypass the barrel-to-barrel gaps.

Similar calculations have been made to understand disk cooling. Those calculations are based upon barrel results with a Reynold's number of 1800 (barrel flow = 20 g/s). Disk power dissipation is dependent upon the sensor technology chosen, and that choice remains to be made. At each end of the barrel region, the first four disks have been assumed to employ pixel sensors. For heat removal calculations, they have been assumed to dissipate the same power per unit area as the pixel sensors of the barrels. The result is a total power of 16.9 Watts for all eight disks and an air flow of 16.4 g/s.

Two different assumptions have been made for the next three disks outboard at each end. First, sensors have been treated as silicon micro-strips with a power dissipation of 17.6 μ Watts per channel. The result was a total power of 6.9 Watts for all six disks and an air flow of 6.7 g/s. Second, sensors were treated as silicon pixels with $\frac{1}{4}$ the power dissipation per unit area as that of barrel pixels; that assumes pixels which are twice as large. The result was a total power of 13.25 Watts for all six disks and an air flow of 12.8 g/s. Subsequent flow calculations assumed the flow of this second option, 12.8 g/s.

The total required flow is the sum of that for the barrel, inner disks and outer disks, that is, 48.65 g/s. To take into account warming of air and to allow a small margin, flow calculations assumed an air temperature of -20° C and a flow rate of 50 g/s.

We propose to deliver air via the vertex detector outer support cylinder. To allow that, the two walls of the cylinder would be separated by radially-oriented ribs running the full cylinder length. Calculations assumed ribs at 60 azimuths. Openings, each approximately 12.2 mm x 15 mm, at 18 Z-locations in the inner cylinder wall distribute flow to the various disk locations and to the barrel. At each azimuth, the cell through which flow passes was approximated by a rectangle of height 15 mm and width 18.246 mm. The wall thickness was assumed to be 0.26 mm for both cylinders and for all ribs. The result was a Reynold's number of 3105 in the portion of the cell which sees full flow, which indicates flow will be turbulent. Since a portion of the flow exits the cell at each opening, the Reynold's number drops to 1725 at approximately $Z = 51.9$ cm (a short distance inboard of the two outermost disks). While entrance effects may remain, flow should gradually become laminar after that point.

Supply and return connections to the outside world remain to be fully evaluated. With eight connections per end, each represented by a 20 mm x 40 mm rectangular passage, the Reynold's number is 12900 and flow is turbulent.

Material related to Readout and Services

The detailed readout scheme is still to be defined, which in turn depends on the sensor technology. The power delivery is expected to be a major source of material contribution. The instantaneous power of many of the sensor technologies could be 50W or more per sensor. One naïve scheme is to deliver power through short copper wires with e.g. 300 μ m diameter to each sensor and use bulkhead panel on the beam pipe at $Z \sim 10-12$ cm for DC-DC conversion from higher voltage supplies externally. There are concerns with regarding the mechanical force on these wires with high current in the magnetic field in this naïve scheme. A low mass local DC-DC conversion near the sensors with higher incoming voltage would be more favorable in many respect if can be realized. An extension of the radiation hard optical transmission technology used for LHC detectors could be foreseen as the means of control and data transmission. The material from the thin fibers are expected to be significantly less than the material involved in power delivery. However, the major issue for both power delivery and signal transmission is the connection to the thin sensors. The miniaturization of the connectors and the transceivers will be key R&D projects to ensure the material minimization. For simulation purposes the readout section at each end of a sensor is assumed to be a 2mm tall and 5mm long block spanning the full width of the sensors with same radiation length as G10.

Geometry and Material Summary

The number of radiation lengths represented by vertex detector structures, averaged over phi in most cases, is given in Table 5 and Table 6.

Table 5 Percentages of a radiation length contributed by barrel materials (normal incidence)

Element	Description	% of a radiation length
---------	-------------	-------------------------

Beam pipe	0.025 mm titanium	0.070
	0.4 mm beryllium	0.113
Sub-total		0.253
Each of 5 pixel layers		
Carbon fiber	0.26 mm carbon fiber – epoxy with 3/4 of area cut away	0.027
Epoxy	0.05 mm	0.014
Silicon	0.1 mm	0.107
Readout and cables	0.05 mm silicon equivalent	0.054
Overlap of sensors		???
Sub-total per layer		0.202
Sub-total for 5 layers		1.010
Outer support cylinder	Double-walled carbon fiber support cylinder with 60 ribs, thickness of material = 0.26 mm	0.304
Air		0.065
Total sensors		0.670
Total inactive		0.892
Total		1.572

Table 6 Percentage of a radiation length contributed by disk materials (normal incidence)

Element	Description	% of a radiation length
Beam pipe	0.025 mm titanium	Need to take into account range of incidence angles
	0.4 mm beryllium	Need to take into account range of incidence angles
Barrel end support membrane	0.26 mm carbon fiber – epoxy with 3/4 of area cut away	0.108
Each of 4 pixel disks		
Carbon fiber	0.26 mm carbon fiber – epoxy with 3/4 of area cut away	0.027
Epoxy	0.05 mm	0.014
Silicon	0.1 mm	0.107
Sub-total per disk		0.148
Sub-total for 4 disks		0.492
Readout and services		
Barrel readout/service connection	See subsection above	Concentrated at end of barrel sensors, locally ~1%
Barrel service just outside barrel face	Power wires and fibers concentrating toward beam pipe	0.05-0.5 depending on radius

Endcap readout/services	See subsection above	Concentrated at inner and out rims of the disks, locally ~1%
Forward disks		
Carbon fiber	Four membranes of 0.26 mm carbon fiber –epoxy with 3/4 of area cut away	.108
Epoxy	0.1 mm	.028
Silicon	0.2 mm	0.214
Readout and cables	0.1 mm silicon equivalent	0.108
Sub-total per disk		0.458
Sub-total for 3 disks		1.374
Outer support cylinder	Double-walled carbon fiber support cylinder with 60 ribs, thickness of material = 0.26 mm	Need to take into account range of incidence angles
Air		0.313
Total sensors		1.070
Total inactive		>1.425
Total		>2.495

The VXD hit pattern and material sum as a function of polar angle is shown in Figure 33. The irregular features of the readout and service contributions are due to the blocks at the end of the sensors. Most of the readout material are beyond the first few layers of the VXD hits so that their influence on the impact parameter resolution are limited. The fact that the effective readout and service material integrates to comparable amount as sensors or mechanical support, calls for close attention in the realization of low mass design for power delivery and signal transmission. If the readout and service material can indeed meet what is in the current model, the material balance would be more favorable for considerable portion of the endcap region compared to the $1/\sin\theta$ growth for a long barrel geometry. With this material balance, the benefit of the endcap geometry in spatial resolution with better track entrance angle and less radial alignment effect, is translating to more meaningful advantage.

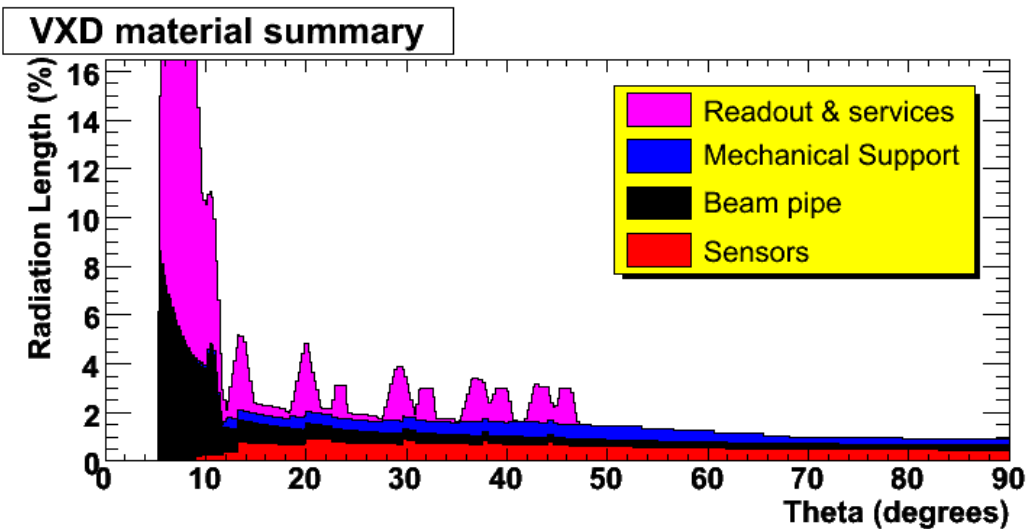
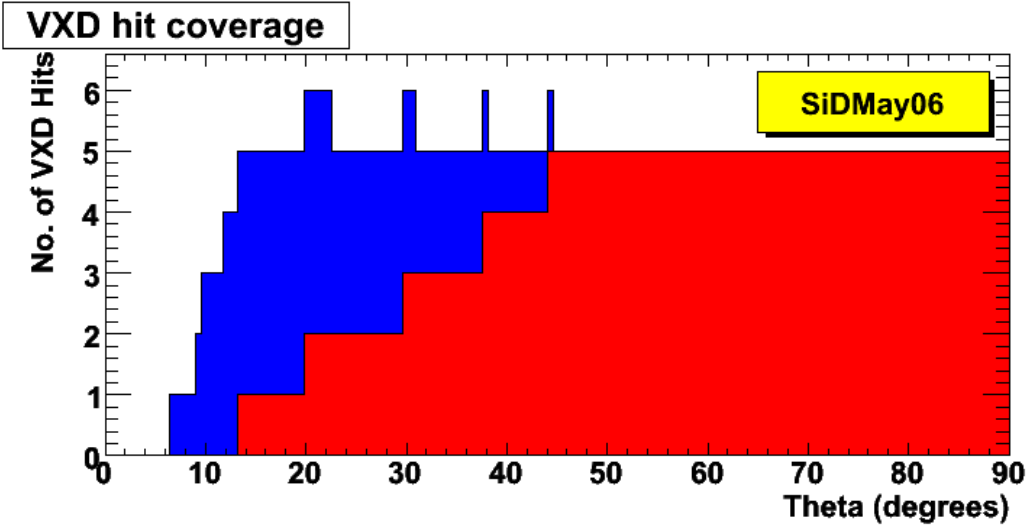


Figure 33 VXD hit pattern and material summary as a function of polar angle.

III.C.2.b Sensor Technology

Basic requirements

A precise and highly pixellated vertex detector is essential for the full exploitation of the physics potential of the linear collider. The ILC is a machine built for precision measurements, and as such it requires sensors that are at the limits of current technology in terms of high segmentation and low mass. The long bunch trains of the ILC beams also demand innovative readout schemes to handle the effective hit density for tracking. This combination of demands represents as-yet uncharted territory for charged particle detection, and one that pushes the current efforts to new areas in sensor development. The goals for the sensors for use in the SiD vertex detector include:

1. Space-point measurements with a resolution of 5 μm or better in both directions in the measuring plane, for tracks with entrance angles of 15° - 90° to the detector plane.
2. Two-track resolution of 40 μm or better.
3. Present approximately 0.1% X_0 of material in their active volume to normally incident particles, including all necessary electronics and support structures.
4. Power consumption of at most a few tens of watts for the whole barrel and similar amount for the end-cap disks, including all components inside active volume. This allows the use of a gas cooling system for minimal material penalty.
5. Ability to operate in a magnetic field with strength up to 5 Tesla without significant degradation of hit resolution.
6. Ensure an effective hit density for tracking to be <5 hits/ mm^2 at the inner layer (radius 1.4 cm) and <1 hit/ mm^2 for the outer layers (radii >2.2 cm), through a readout scheme which can separate hits from different times during the bunch train. This implies the need of time resolution equivalent to ~ 50 frames of readout at 20 μs per frame or better during the train, given current background estimates.
7. Electronic readout noise should be sufficiently low as to allow threshold settings ensuring $>99\%$ hit efficiency for perpendicular entrance tracks, with a hit rate from noise not exceeding other hits in raw data and contributing $<30\%$ of the hit density after offline processing for tracking.
8. Insensitivity of the readout to RF radiation generated by the ILC beams and to noise produced by other components of the ILC detector.
9. Ability to withstand a radiation dose of at least 20 krad per annum resulting from pair production background and survive an annual dose of 10^9 cm^{-2} 1 MeV equivalent neutrons originating from the beam and beamstrahlung dumps.

The first four requirements above are driven primarily by the physics considerations and the need to make high-precision measurements of low-momentum tracks within dense jets, and to achieve excellent flavour identification. The latter requirements arise from the environment in which the sensors must operate and from the usability of the data for tracking. Currently, there are no sensors which meet all these criteria, and thus the sensors that will be deployed for the ILC vertex detector are unlike any other being used today.

The discussion to follow first considers the general implications of the basic requirements listed above, and then moves on to a few specific sensor options being considered.

Low-mass and precision considerations

The requirements which are driven primarily by the physics include the precision of the vertex detector and also its mass. Pixels of roughly $20 \times 20 \mu\text{m}^2$ or smaller will be required to obtain the necessary resolution, especially in the inner layers of the pixel detector. This resolution is driven

by the need to resolve the densely packed hits resulting from jets and to allow highly precise extrapolation of tracks in order to make high performance reconstruction of decays of heavy flavour.

There are many different strategies in pixel design to maintain the necessary precision. In general the requirement on hit resolution at large entrance angles strongly favors sensors with an active depth of $20\mu\text{m}$ or less, while signal to noise considerations encourage an active thickness of $>10\mu\text{m}$. Charge collection with partially depleted sensitive layers combined with analog readout can benefit from the cluster diffusion to make improved resolution through cluster centroid calculation, so that a pixel size of $20\mu\text{m}$ can deliver $<4\mu\text{m}$ spatial resolution. However, the readout will require more complex clustering or higher bandwidth to preserve pixels with small pulse heights around the primary pixel. Another strategy is to have smaller pixels (e.g. $10\times 10\mu\text{m}^2$) and digital readout. This simplifies the digital processing downstream. However, reducing the pixel size below $20\mu\text{m}$ will be technically challenging, and issues such as power consumption, the effects of delta rays, alignment and the increased read-out complexity would need to be carefully considered.

To minimize multiple scattering, an extremely low-mass detector is required, and in conjunction the inner layer should be placed as close as possible to the interaction point. This requirement presents several serious design constraints as the target thickness of $\sim 0.1\% X_0$ is for the sum of both sensitive region and peripheral support structures. The overall target thickness per layer is equivalent to 0.1 mm silicon, so a thinned sensitive region will be required. The desire to keep the mass uniformly distributed implies that the non-sensitive region at the ends or sides of the sensor should be minimized. Similarly, large-area silicon sensors, from either stitching or full-wafer exposures, are important to minimize gaps and dead areas.

The effort to keep the overall mass low also results in gaseous cooling and hence the requirement for low power consumption. For SiD, it is expected that the temperature of the silicon sensors will be between -20 C and 10 C . Such modest cooling will make mechanical considerations much less complicated, and will aid in the realization of desirable geometries. Preliminary indications are that a flow rate of a few tens of litres per minute are possible, which limits the power consumption to a few tens of watts each for barrel and endcap.

The final consideration for a truly low-mass vertex detector is that the forward region will also need to be free of extraneous material, and this limits the choices of silicon support schemes. The SiD vertex detector features short “barrel” structures followed by “disks”. Detector modules must therefore be free of large dead areas or concentrations of mass at the end of the barrels. The plans for the SiD mechanical layout (details in a later section) feature a carbon fibre shell structure which is well suited for maintaining the flatness of thinned vertex detector sensors over their length, which in turn means that less complicated mechanical attachments are needed at the barrel ends.

Readout scheme and the operational environment

The operational environment at the ILC also places restrictions on the type of vertex detector to be built within SiD. The beam structure for example has significant implications for the design and readout of the vertex detector sensors. The choice of superconducting cavities as the accelerator technology leads to very long bunch trains. Ideally, the ability to readout every bunch or time tag each bunch will provide the ultimate clean tracking environment. However, the high granularity of the proposed pixel sensors can generally tolerate pileup from a significant number of bunch crossings. The present background estimates indicate that the innermost barrel layer hit density could be as high as 250 hits/mm^2 per train, taking into account the variations of machine configurations. The tracking performance simulation with full stand-alone reconstruction has

been tested to ~ 1 hit/mm² before noticeable degradation was seen for the barrel. Preliminary indications are that endcap tracking may be somewhat more sensitive to background pileup. Several different approaches to sensor read-out are being investigated to keep the effective hit density low: a) Read-out a few times *during* the long bunch trains; b) to *store* the hit information and reading out in the quiet time after the bunch train has passed. In the section to follow, sensors will be discussed that make use of each of these options.

For sensor design, other environmental issues that must be kept in mind include the high magnetic field (5T) and the radiation environment. The magnetic field can potentially create large Lorentz drift and spread of generated charge. The sensors currently under consideration are all collecting electrons instead of holes, which makes them somewhat sensitive to the B field, but on the other hand they are generally expected to have a thin sensitive region (10-20 μm) which helps to limit this effect. The radiation environment is generally mild, with yearly expectations of a few tens of kilorad from beam related backgrounds and on the order of 10^9 cm^{-2} 1 MeV equivalent neutrons, primarily from the beam dumps. Stray RF radiation directly from the beam can also influence the sensors as can noise from other SiD detectors, so care must be taken to make the sensors insensitive and the beam delivery region well-shielded.

Sensor Technologies

The field of sensor development for the ILC vertex detector is an extremely active one. The difficulty and novelty of the sensors, as outlined above, drives the investigation of many different sensor designs world-wide. Many approaches are being explored, but currently no sensor technology has satisfied all of the criteria listed above. For the SiD detector we will therefore discuss a few representative technologies which might be used in the final vertex detector.

Readout During the Bunch Train:

For vertex detection in a linear e^+e^- collider environment, the SLD Experiment has demonstrated one possible approach. The successful implementation of Charged-Coupled Devices (CCDs) for a low-mass pixel detector have yielded the highest performance vertex detector yet constructed and that closest to the specifications needed for the ILC. This device contained 307 million pixels, each at $20 \times 20 \mu\text{m}^2$, and on modules constituting 0.4% X_0 . The readout speeds achieved at SLD were orders of magnitude lower than those required for SiD however, and the material budget, while the best of any vertex detector to date, is still significantly above the target.

Pixels based on CCD technology in SiD would still be preferably buried-channel CCDs, with charge collected from the thin epitaxial silicon layer. Typically only part of this epitaxial layer is depleted, and electrons created in this layer diffuse and are eventually collected in potential wells—the buried channel. The electrons generated during the passage of a charged track can be spread over several pixels by diffusion, and can serve to improve the resolution (to better than $1/\sqrt{12}$ of the pixel size) by cluster centroid finding. As the thin epitaxial silicon layer yields a small amount of charge (10-20 μm yields on the order of a thousand e^-), noise must be kept to a minimum. This is possible to achieve as the output node capacitance is low.

After collecting the charge in the pixel, it can then be transferred out (for each column) to an analogue-to-digital converter at the outer edge of the sensor (ADC). This is accomplished by shifting the charge row-by-row out to the output nodes, where they are read out in parallel for each column. In the ILC the radiation expected is relatively moderate, but CCD design must take into account radiation-induced charge traps as the generated signal may travel several centimetres to the output node. Also the operating temperature must be kept as low as possible to allow efficient charge transfer. Read-out will then be accomplished once per approximately 50 μs , with a clock frequency of 50 MHz required to keep occupancy low in the inner-most layer. Features

of the readout include correlated double sampling (at the ADC), threshold application, cluster-finding, and sparcification.

The Monolithic Active Pixel (MAP) sensors are becoming commonplace in commercial electronics and are developing at a rapid pace. Utilising the same approach for charge generation as a CCD, charge is usually generated in a thin epitaxial layer which is only partially depleted, and is collected (after some diffusion) on a photodiode. As with CCDs, the pixels can be made very small, and the resolution should benefit from cluster centroid finding.

The MAPs sensors also need to be read-out effectively every 50 μs or so for the inner layers, for the same reasons of occupancy. The read-out approach is rather different, however. Rather than shifting the charge out to the ends of the sensor for read-out, MAPs devices read the charge (via an in-pixel source-follower) on a row-by-row basis, and send a voltage level signal (for each column) to be read by the ADC. Once the read-out is finished with the columns it goes back to the beginning again in a “rolling shutter” fashion. By connecting each pixel to a readout line along the column, the capacitance can be relatively large (pF) and may limit the speed of the readout. Also the integration of readout logic in the pixels and on the periphery of the sensor can add a few millimetres of “dead” material on the sensor edge. By contrast to CCDs, MAPS benefit from CMOS processing and should have comparatively better performance with radiation.

The DEpleted Field Effect Transistor (DEPFET) detector is another major branch of sensor R&D, with similar readout strategy and speed as other device in this category. It combines the sensor and readout amplifier into the pixel FET structure such that the signal charge is collected on the internal gates of the transistors. Readout is performed by cyclically enabling transistor rows by a combination of steering and readout ASICs mounted at the ends and along the edges of the sensors. DEPFETs have the potential to be one of the technologies with the lowest power consumption. The prospect of a thin sensitive layer but with good signal to noise, in conjunction with smaller pixels, would be particularly important to compete with the other devices in spatial resolution.

Readout Between the Bunch Trains:

As discussed above, the expected beam structure at the ILC features long bunch trains followed by even longer gaps. The beam structure, coupled with non-negligible occupancy, has created a situation where data storage in-pixel is an attractive approach.

The In-situ Storage Image Sensor (ISIS) under development features an array of CCD storage registers within each pixel. The charge generated by particles passing through the sensor is collected on a photogate as with a normal CCD, but then it is transferred to a CCD storage register located in-pixel. Rather than being read out, it is stored in this register until the bunch train has passed, and only then is read-out started. By including 20 such storage cells within each pixel (every ~ 150 beam crossings), read-out of the sensor is effectively accomplished every 50 μs . Read-out then proceeds in much the same fashion as the MAPS devices described above.

By waiting for the gaps after the bunch trains have passed, the timescale for read-out is greatly relaxed (e.g. 1 MHz). Slower read-out allows relatively longer shaping times and hence relatively lower noise. Also, as the number of charge transfers is reduced by a large factor compared to the Column-Parallel CCD, the effect of the radiation-induced charge transfer inefficiency and hence the sensitivity to radiation backgrounds is sharply reduced. ISIS has the advantage also of storing the raw charge associated with the event, and performs the minimal amount of manipulation of the charge during the bunch train. Furthermore, the ISIS should be able to operate at much higher temperatures than traditional CCDs. Finally it should be noted that as the ISIS requires elements of both CCD and CMOS processing, its development is potentially more difficult.

Similarly, the Flexible Active Pixel (FAP) integrates storage cells in a traditional MAPs pixel, to be read out in the relatively long period after the bunch train. As in a standard MAPs pixel, the photogate is connected to a reset transistor and also an amplifier. Charge is acquired (e.g. for 150 crossings) and then the write amplifier is activated, passing a voltage level to one of several memory cells within the pixel. The process is repeated until the cells are full. Readout is accomplished in much the same way as a normal MAPs sensor, but with a select transistor to pass the voltage in the storage cells out individually.

The FAPs approach combines many of the strengths of MAPs sensors with a much relaxed read-out speed and added flexibility. As with MAPs sensors, all pixels in a column are connected to the same output line. The resulting capacitance is less of a problem, however, as there is much more time in which to read out the pixels. For the FAPs, the storage elements are MOS transistors used as a capacitor, and they are accessed through transistors used as switches. Challenges for the development of a FAPs sensor for SiD would include the optimization of the number of storage cells, their type, the leakage from these cells, together with the timing of the eventual beam structure. A variety of FAPs-like configurations are currently under study (with a variety of different names).

A relatively new approach of monolithic CMOS sensor currently under development is to use on pixel memory to store bunch crossing time tags instead of hit analog pulse heights. The pixel storage is envisaged to be able to record time tagged hits at single bunch crossing level to completely resolve the hit density concerns. This feature distinguishes this approach from all other existing sensor developments. The pixel design also incorporates resets after each bunch crossing and allows storage of up to 4 hits of the same pixel (digital information only) for different times during each train. To preserve the spatial resolution, a smaller pixel size of 10-15 μm will be used. The sensitive silicon thickness is also targeted at the desired 10-15 μm range with full depletion. The initial R&D is expected to start with the existing technology for a 50 μm sized pixel, while the real target of 10 μm sized pixels is banking on the continued development in industry to make 45nm technology available by 2009. Another major challenge is to keep the power consumption under control as the number of pixels, and their complexity, is higher than for most other approaches.

Final Observations

The sensors listed are by no means the entirety of sensors under consideration for the SiD vertex detector, merely a manageable and self-consistent subset. Substantial advances have been made in developing fine-pixel sensors, sensors making use of fully-depleted high-resistivity silicon, and sensors incorporating the latest technology such as wafer-bonding and SOI techniques to list but a few. As no sensor type for the SiD vertex detector has solved all the challenges posed simultaneously, we will keep an open mind and monitor several fronts of R&D.

III.C.3 Tracker Design

III.C.3.a Tracker Layout

The outer silicon tracker consists of five nested barrels in the central region and five disks in each of the end regions. The barrel supports are continuous cylinders formed from a sandwich of pre-impregnated carbonfiber composite around a Rohacell core. The disks

are also double-walled carbonfiber structures around a Rohacell core. Each disk is supported off a barrel. Spoked annular rings support the ends of each barrel cylinder from the inner surface of the next barrel out. It is envisioned that the electronics and power cables that supply entire segments of the detector are mounted on these spoked rings. The dimensions of the barrels and disks are given in Table 7. Figure 34 shows an elevation view of the outer tracker.

Table 7 Outer tracker geometry

	Barrel		End Cap	
	R (cm)	Z (cm)	Z (cm)	R (cm)
Layer / Disk 1	20.0	26.7	28.7	4.0 – 24.5
Layer / Disk 2	46.3	61.7	63.7	7.9 – 50.8
Layer / Disk 3	72.5	96.7	98.7	11.8 – 77.0
Layer / Disk 4	98.8	131.7	133.7	15.6 – 103.3
Layer / Disk 5	125.0	166.7	168.7	19.5 – 129.5

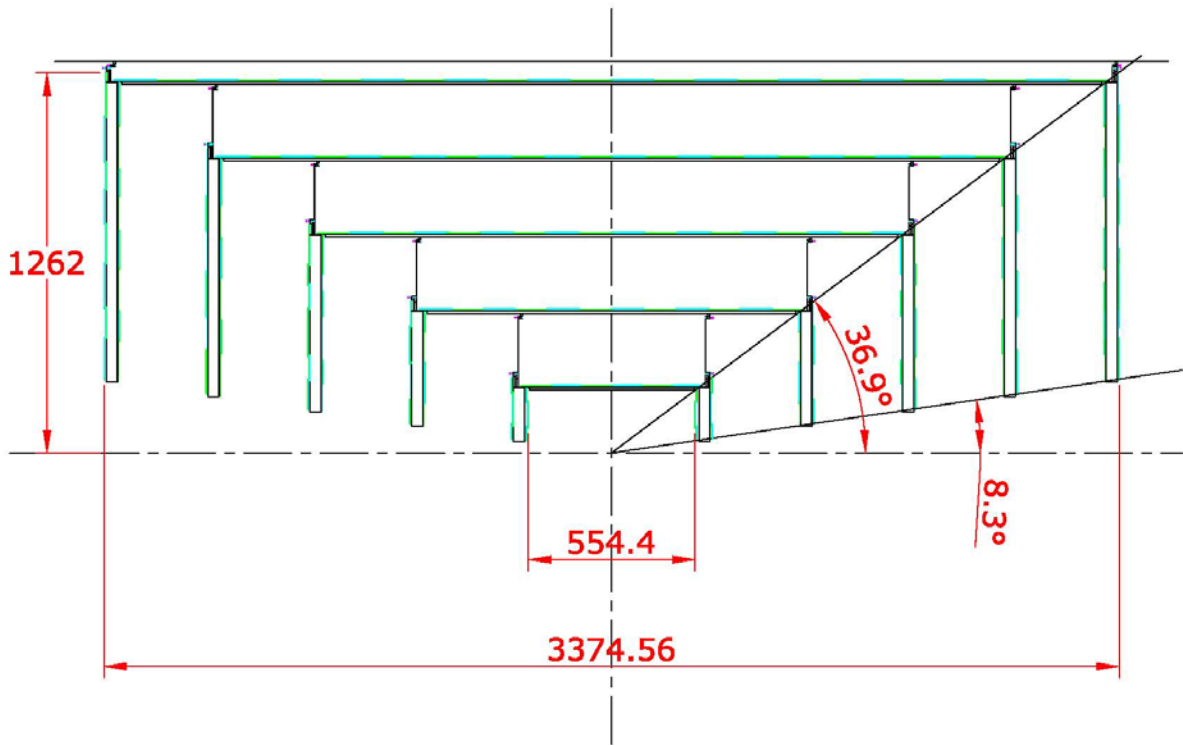


Figure 34: Elevation view of the outer tracker

Because of the very low occupancies in the outer barrel, the nominal design for the outer tracker employs only axial readout in the barrel region. In the baseline design, the barrels are covered with silicon modules. Modules are comprised of a carbon fiber composite frame with rohacell/epoxy cross bracing and have one single-sided silicon sensor bonded to the outer surface. Sensors are obtained from one single 6" wafer and are approximately

10cm by 10cm. This size sets the longitudinal readout segmentation of the barrel detectors. The sensors are 300 μm thick with a strip pitch of 50 μm with intermediate strips. Full coverage is obtained by ensuring small overlap both longitudinally and azimuthally. Azimuthal overlap is obtained by slightly tilting the sensors. The angle by which the sensor is tilted compensates for the Lorentz angle of the collected charge in the 5T field of the solenoid. Longitudinal overlap is obtained by placing alternate sensors at slightly different radii. Figure 35 shows an $R\phi$ -view of the barrel region of the outer tracker. Modules are attached to the cylinder using a PEEK mounting clip. The readout chips and cables are mounted directly to the outer surface of the silicon sensors. The cables supply power and control to the readout chip from electronics located at the ends of the barrel.

For pattern recognition, the disks will provide 3d-space points. The current design has both sides of the disks covered with silicon modules. The modules on one side provide the R-readout and the modules on the other side provide the ϕ -readout. Also in the forward region sensors will be 300 μm thick with intermediate strips. Since the sensors will be wedge shaped, the pitch will vary with radius.

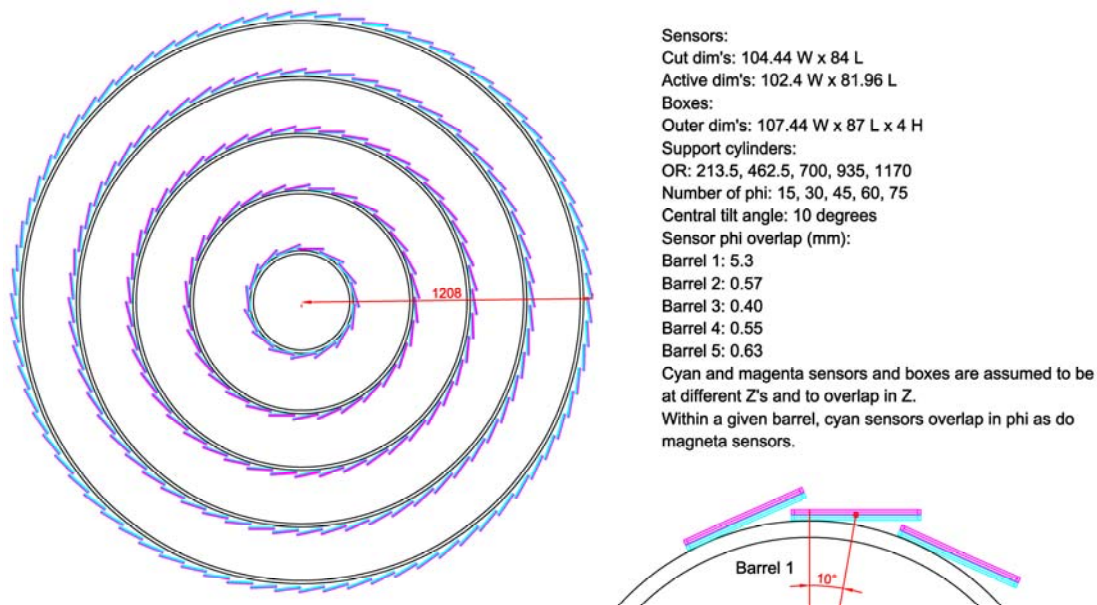


Figure 35: Cross sectional view of the outer tracker. The inset shows the overlap in z and ϕ of the silicon modules.

The outer tracker is designed such that it allows for servicing of the vertex detector. During servicing, the vertex detector and beam pipe remain fixed while the outer silicon tracker rolls longitudinally, as shown in Figure 15. To allow that motion, no element from the outer tracker can be at a radius smaller than the radius of the vertex detector

outer support cylinder. To allow for good acceptance and pattern recognition, the small angle region is covered by three small silicon disks at each end with radius below 20cm, which has been described in the section on the mechanical layout of the vertex detector.

Figure 36 shows the cumulative amount of material as function of polar angle as modeled in the Monte Carlo. The lowest curve shows the contribution from the beampipe and the readout for the vertex detector. The material corresponding to the various readout elements has conservatively been assumed to be uniformly distributed in the tracker volume. The following two curves indicate the additional material due to the active vertex detector elements and the supports, respectively. The outer curve gives the amount of material of the tracker as a whole, that is, the sum of the vertex detector and the outer tracker and anticipated dead material in the tracking volume. Overall a material budget of about 0.8% X_0 per layer is achieved for the outer tracker.

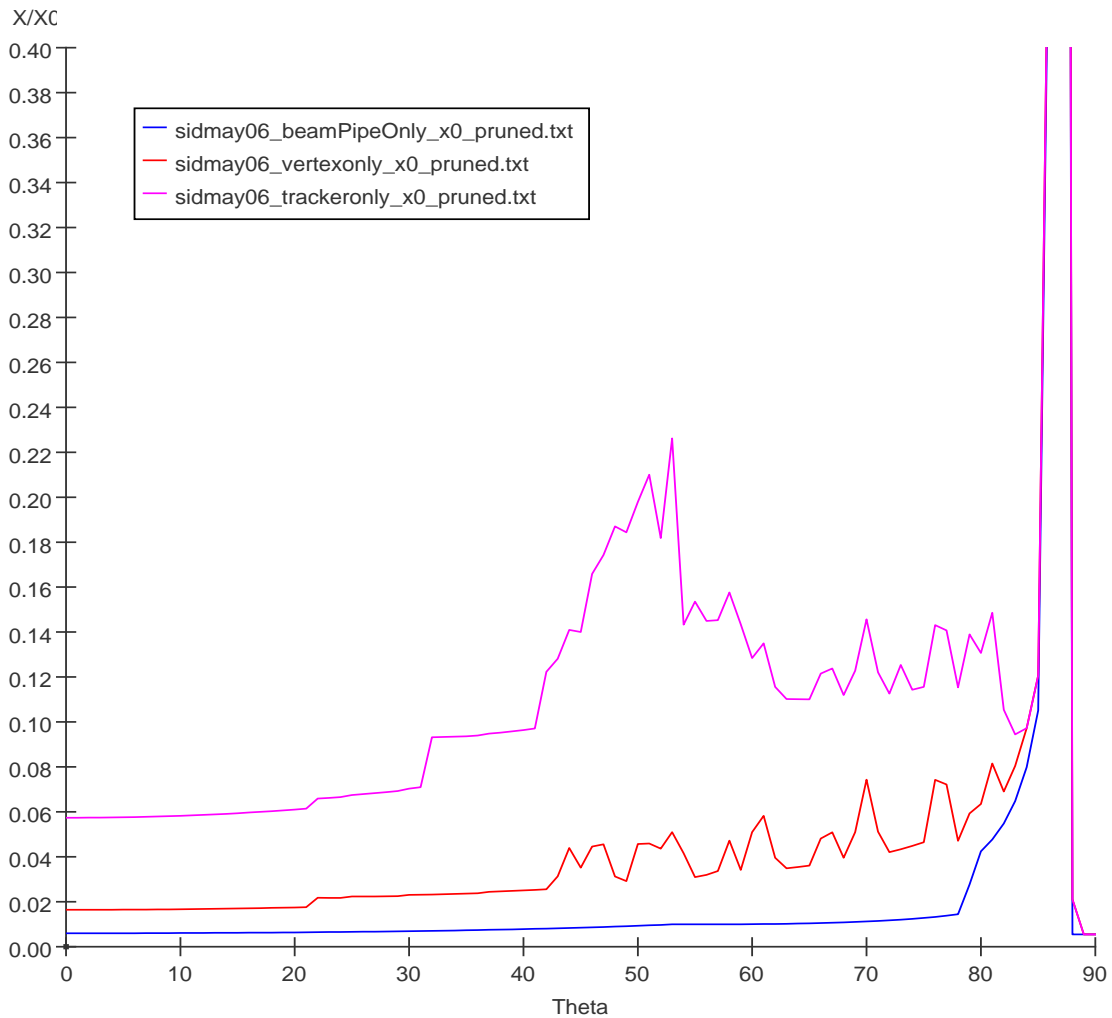


Figure 36 Total material budget of the tracker as function of polar angle as modeled in the Monte Carlo.

III.C.3.b Tracker Alignment

The unprecedented track momentum resolution contemplated for linear collider detectors demands minimizing systematic uncertainties in sub-detector relative alignments. At the same time, there is a strong impetus to minimize the amount of material in the tracking system, which is likely to compromise its stability. These two requirements put a premium on accurate alignment of the various elements of the tracker. The short time scales on which alignment could change (e.g., from beam-driven temperature fluctuations) may preclude reliance on traditional alignment schemes based on detected tracks, where it is assumed the alignment drifts slowly, if at all, during the time required to accumulate sufficient statistics. A system that can monitor alignment drifts “in real time” would be highly desirable in any precise tracker and probably essential to an aggressive, low-material silicon tracker. The tradeoff one would make in the future between low material budget and rigidity will depend critically upon what a feasible alignment system permits.

The capability of a novel and precise alignment scheme based on Frequency Scanned Interferometry (FSI), first developed by the Oxford group for the Atlas Detector has been investigated [1]. The FSI system incorporates multiple interferometers fed by optical fibers from the same laser source, where the laser frequency is scanned and fringes counted, to obtain a set of absolute lengths.

With a test apparatus (reference), the state of the art in precision DC distance measurements over distance scales of a meter under laboratory-controlled conditions has been reached and even extended. Precisions better than 100 nm have been attained using a single tunable laser when environmental conditions are carefully controlled. Precisions under uncontrolled conditions (e.g., air currents, temperature fluctuations) were, however, an order of magnitude worse with the single-laser measurements. Hence a dual-laser FSI system was commissioned, that employs optical choppers to alternate the beams introduced to the interferometer by the optical fibers. By using lasers that scan over the same wavelength range but in opposite directions during the same short time interval, we are able to eliminate major systematic uncertainties, a technique pioneered by the Oxford ATLAS group.

A number of significant technical complications had to be overcome in implementing the dual-laser system. As a result, precisions of 200 nm under highly unfavorable conditions were achieved, using the dual-laser scanning technique [2]. This system thus has the potential to align of the detector modules in the SiD tracker to the required accuracy. It should be noted that this method, developed for central and forward tracker alignment, may also prove useful for the vertex detector., Similarly, this method may prove useful for alignment monitoring of accelerator components far upstream of the detector.

III.C.4 Tracking Simulation and Reconstruction

III.C.4.a VXD Hit Digitization

Effects Simulated in the CCDSim Package

Although no baseline sensor technology has been established for the vertex detector, the vertex detector sensor simulation is currently based on a CCD simulation from SLD. The package, called `hep.lcd.mc.CCDSim` and originally developed in 2004, has been migrated to the new `org.lcsim` framework and is called `org.lcsim.mc.CCDSim`.

The main process to be simulated in a CCD is the diffusion of the charge from a charged particle track. In a CCD the larger part of the active layer is not depleted. That is, there is no electrical field in that part and the charge collection occurs because of a slow diffusion of the charge into the CCD channel. In this case transverse diffusion has the same scale as the un-depleted layer thickness. To simulate the diffusion, we assumed a Gaussian distribution of the probability of an electron generated at some point deep in the active layer to reach collection point at a certain distance from the projection of generation point. The width of this distribution is proportional to the depth of the generation point. In fact, there are two Gaussians here - one from electrons directly diffused toward the CCD channel, and another - from electrons, reflected at the epitaxial layer - substrate boundary, where there is a potential barrier.

An important role in the performance of a tracking detector is played by the generation of the δ -electrons (large energy transfer by the ionizing particle to a single electron). We simulated this effect by assuming that the energy loss in the tail of the Landau distribution is due to such δ -electrons. The width of Landau distribution is simulated according to empirical formula, which is in good agreement with experiment to thicknesses as small as about 10 μm of silicon.

Our simulation package also includes special functions for simulating low-energy electrons (for example, Compton electrons generated by photon) hits.

Apart from the physics effects in the silicon detector, its performance is affected by noise level of the readout electronics and the parameters of a signal digitization. All these effects have been simulated. This package does have its limitations, however, and was not designed for detailed study of sensor effects. For example, it does not take into account specific effects in the energy loss in very thin layers ($\sim 1 \mu\text{m}$), and it does not include Lorentz angle of electrons moving in the depleted part of the sensitive layer. Such effect may be added later, if the need for more detailed simulation arises.

Description of the Simulation Algorithm

The package consists of several Java classes. The wrapper class `FullCCDSimulation` is the processor, which takes care of everything needed for including such simulation in the event reconstruction. Users only need to include this class in the reconstruction driver. In the old implementation (in the `hep.lcd` framework) the result of `FullCCDSimulation` was the replacement of Monte Carlo hits (generated by GEANT) with new ones whose parameters were extracted in the process of simulating CCD signals and the processing of these signals. In the new implementation the original hits are kept, and the result is the creation of a duplicate set of hits, which can be used by the track reconstruction code instead of the original hits.

As soon as the first event is read out from the input data stream, the package FullCCDSimulation determines the geometry of the detector used, and creates CCD objects according to such geometry. In addition to these parameters the CCD objects include additional parameters defined by classes internal to this package, such as CCDSpec and CCDElectronicsSpec. These classes define such specific parameters as the CCD active layer thickness, the depletion depth, pixel size, electronics noise level, ADC conversion scale, ADC range and so on.

After the CCD objects for a given detector geometry have been created, they are kept as tools for all subsequent event processing. Also, before starting the event processing, lookup tables are generated for the simulation of electron diffusion. We are not simulating the movement of each electron in this package, but rather are using pre-calculated density functions for distribution of electrons generated at a given depth inside the active layer.

The next step in the simulation includes processing of every hit in the CCD detector. For every such hit, first the CCD and the pixel in the CCD is found where the hit is located. The CCD active layer is then divided in thin sublayers and the energy deposition in every sublayer is simulated. If energy deposition in any sublayer is in the tail of Landau distribution, the generation of a δ -electron is assumed. The charge is propagated to the CCD surface according to diffusion density functions, and charge signals in the central pixel, as well as in neighboring ones are found. After that, electronics noise is added, and the ADC digitization algorithm is applied.

The resulting ADC outputs for all pixels in the CCD are fed to the cluster finding routine, which finds clusters of pixels and the coordinates of their centers. Different algorithms may be used for coordinate finding. The simple center of gravity is most often not the most accurate. Users can choose from a set of predefined algorithms.

After the coordinates of the pixel clusters are found, new objects, called ReconstructedCCDHits, are created and recorded into the event data. These objects are implemented in a similar fashion as the original SimulatedTrackerHit objects, so they may be used for tracking reconstruction. Figure 37 and Figure 38 show some results obtained with full CCD simulation.

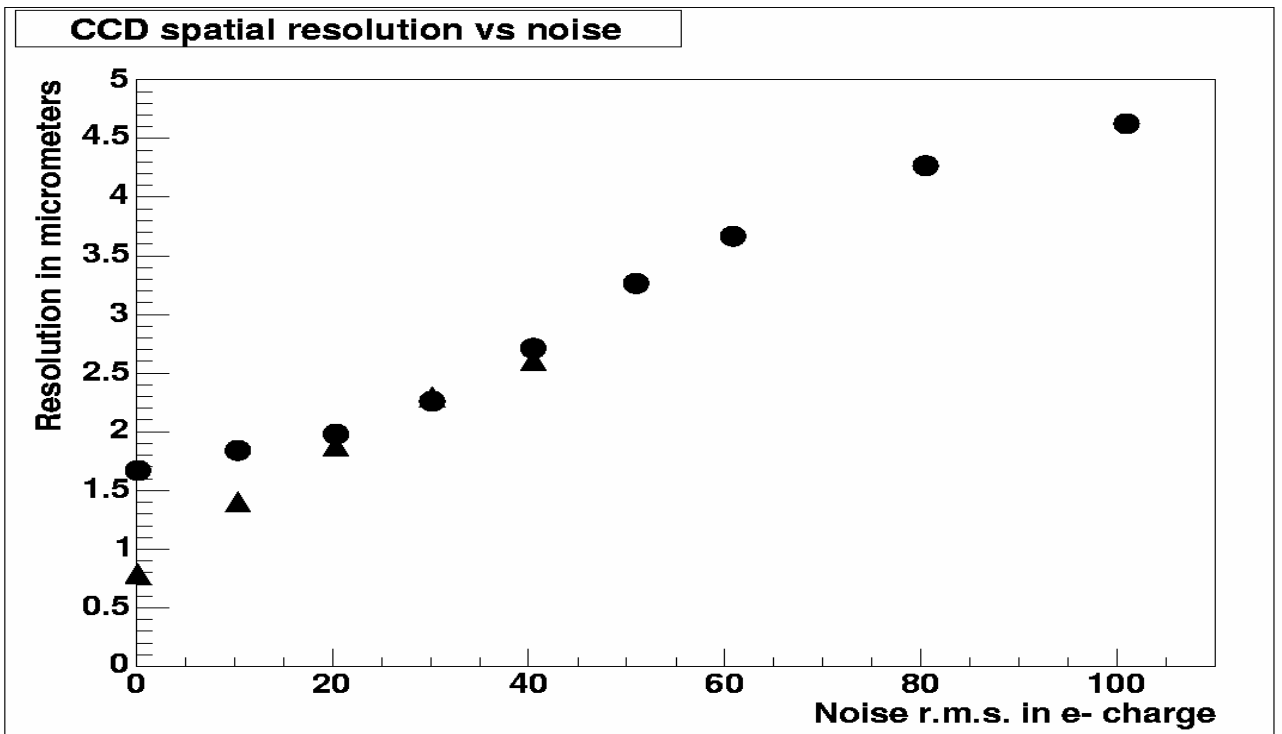


Figure 37 CCD spatial resolution as function of electronics noise. Pixel size is 20 μm

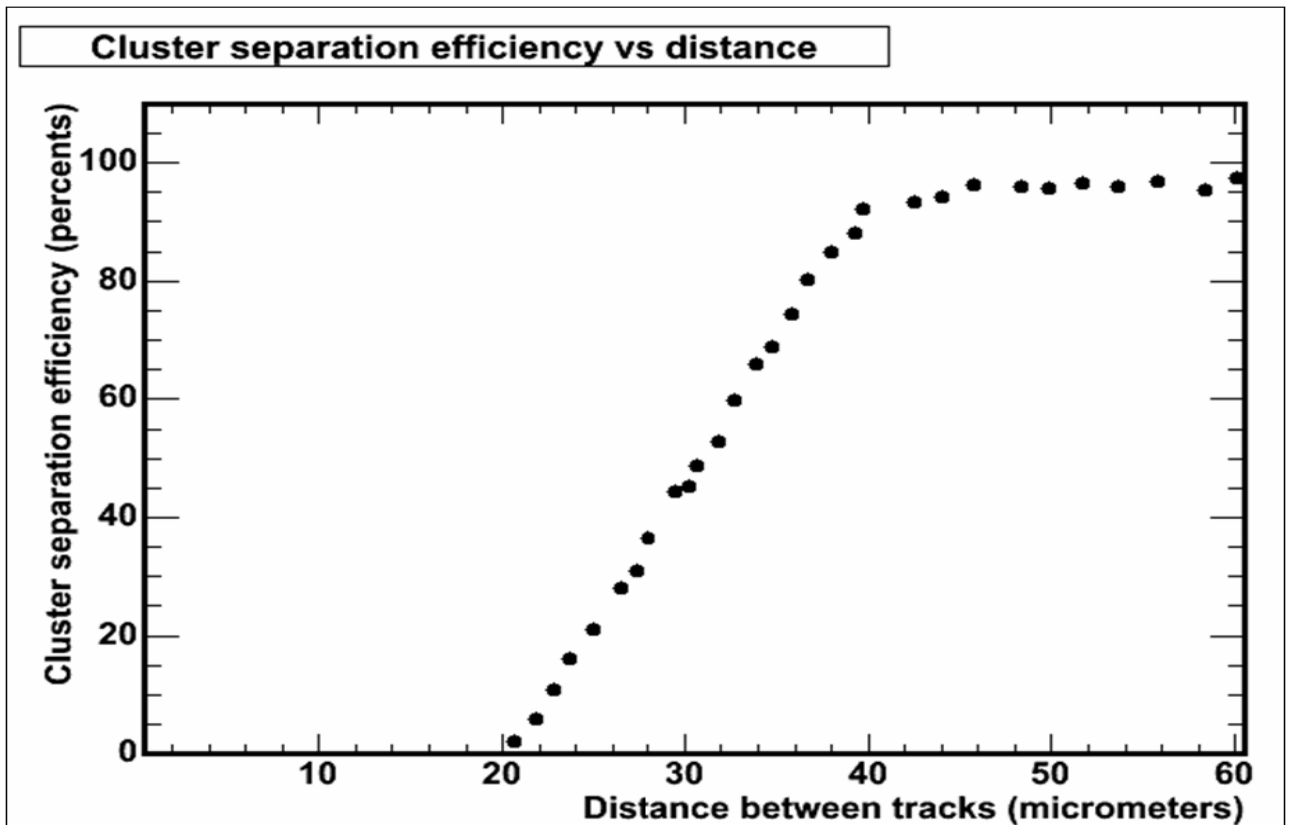


Figure 38 Efficiency of cluster separation as a function of the distance between tracks. Pixel size 20 μm .

III.C.4.b Vertex Detector Based Tracking Reconstruction

Overview of Existing Tracking Packages

In the SiD concept detector the main tracker consists of five layers of microstrip detectors with coarse longitudinal segmentation. While the stand-alone pattern recognition in such a detector is difficult, especially in the case of a high density of background hits, the pattern recognition capability of the vertex detector, with its high precision and high pixellation, is nearly perfect. Therefore, the standard track finding algorithm for the SiD detector is an 'inside-out' track finding algorithm. That is, pattern recognition begins in the vertex detector, and proceeds by extrapolating tracks into the main tracker. This section will describe the algorithm which does so and its performance. In the sections following, two additional algorithms will be described. The stand-alone tracking algorithm is based on pattern recognition using only the hits in the outer tracker. The calorimeter assisted track finder uses the tracking capability of the electromagnetic calorimeter to associate hits in the outer tracker with calorimeter "track stubs". Both additional methods allow for reconstruction of tracks which originate outside the vertex detector.

Description of Vertex Detector Based Tracking Algorithm

The pattern recognition begins by selecting 3 hits in 3 different layers of the tracking detector [1]. If a helix can be traced through these hits, an attempt is made to associate additional hits with it. If the total number of associated hits exceeds a set threshold, the helix is considered a track candidate. For most studies a threshold of 5 hits is used. Before accepting the candidate tracks, additional criteria are applied. First, we eliminate tracks which share common hits, allowing no more than one hit in common between two different tracks. When two track candidates have share more than 1 hit, we retain the candidate which has the greater number of hits or which has a better chi-square. Another cut removes tracks associated with multiple turns of the same helix in the tracking detector. Additional criteria are imposed to reduce the number of fake tracks. By requiring a least four of the assigned hits to be in the vertex detector, the extrapolation into the main tracker is improved and false associations with noise hits are reduced. This requirement also lowers the number of track combinations that must be considered in the vertex detector, and speeds up track finding. (I'm trying to simplify this discussion. It is too detailed. I'm not sure if it is still accurate, however.)

Because of the large number of background hits in the vertex detector, the number of hit combinations from 3 layers can be huge if we combine any hit in one layer with any combination of hits in two other layers. To reduce processing time we can impose two other requirements: 1) the track must originate close to the interaction point; 2) the transverse momentum must exceed some minimum, typically ~ 200 MeV/c.

Reconstruction Efficiency

The reconstruction efficiency for single tracks as a function of their impact parameter in the xy and rz planes is shown in Figure 39. If we are not concerned about reconstruction speed, and want to see all the tracks from B decays -- which may even occur centimeters

away from the interaction point -- we can set the parameters of the algorithm to allow for the reconstruction of tracks which originate far from the interaction point. Obviously, we can't reconstruct tracks that originated outside the vertex detector. The vertex detector layout is determined by the requirement that tracks from the interaction point traverse at least 5 layers of the vertex detector. If tracks originate far from the interaction point, either in Z or in R, then for some values of the track dip angle not all layers will be traversed. This leads to a reduced average efficiency of the track reconstruction which can be seen from Figure 39. For this test single track hits were generated and then the reconstruction algorithm was applied. Hit smearing and layer inefficiency was applied before reconstruction. (Any background?) There was, however, no simulation of multiple scattering in this simple test. You can see from the plots that even tracks that originate outside the first layer of the vertex detector are reconstructed with good efficiency, albeit with an 8% decrease in efficiency for tracks from the interaction point.

The track reconstruction efficiency as a function of transverse momentum and the cosine of the polar angle is shown in Figure 40, based on Monte Carlo TTbar events. We believe that part of the efficiency drop at large $|\cos\Theta|$ can be attributed to a bug in the geometry used, where there were small gaps in the coverage in the vertex detector endcaps. (Backgrounds included? Aren't there K's and lambdas—why is efficiency so high?)

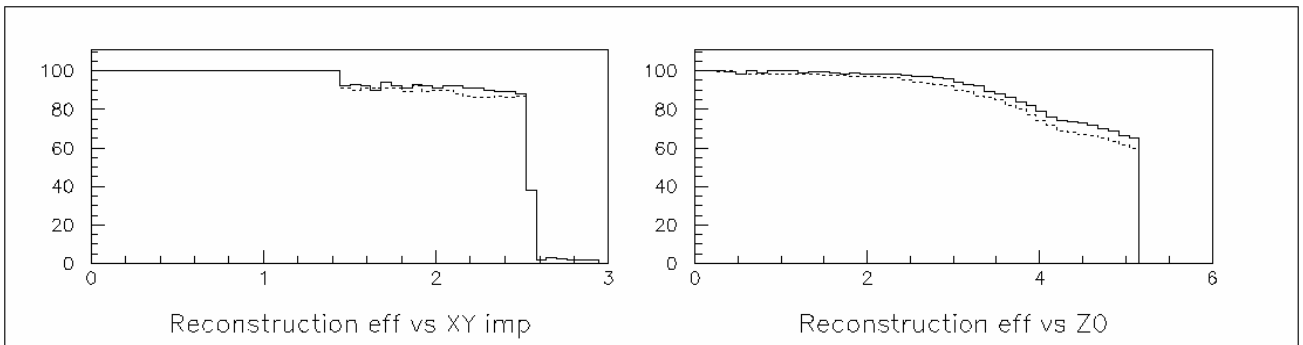


Figure 39 Reconstruction efficiency as a function of track impact parameters. Reconstruction cuts are set at 3.0 cm for the XY impact parameter and 5.0 cm for Z. Solid lines correspond to high Pt (> 1 GeV), dashed to low Pt (< 0.5 GeV) tracks.

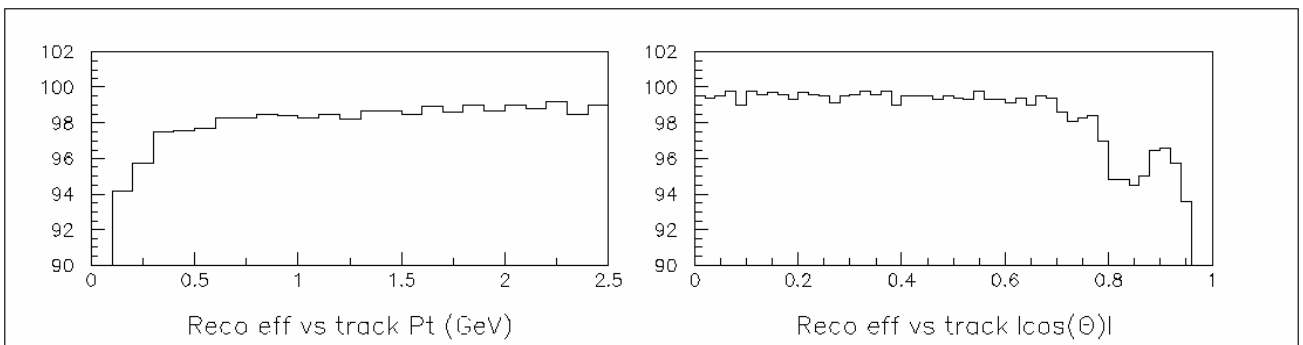


Figure 40 Reconstruction efficiency as a function of tracks Pt and dip angle.

Fake Tracks and Effect of Backgrounds

Sometimes it is observed that more than one track has the same Monte Carlo particle designated as its parent. This may happen when two tracks are close to each other and hits assigned to such tracks may be confused. In that case the track "purity", defined as the fraction of hits generated by a single Monte Carlo particle among all hits assigned to the track, is low. If some track "steals" the majority of assigned hits from another track, we call such track a "fake" track. In pure physics (TTbar) events the fraction of such fake tracks is about 0.8%.

If we superimpose backgrounds, the number of fake tracks goes up. Let us assume a timing resolution of our tracking detectors such that 10 beam crossings are piled up together. (this is reasonable, perhaps, for the vertex detector backgrounds; it is not reasonable for the tracker where only one BX will be recorded. It would be interesting to see the answer when one BX of background is included.) In that case, hits from background particles can increase the number of fake tracks to up to 15% of all reconstructed tracks. Since this is not acceptable we need either to use detectors with better timing resolution, or find cuts to suppress the reconstruction of fake tracks. Looking at the parameters of fake tracks displayed in Figure 41, it is obvious that increasing the minimum Pt cut to 0.2 GeV and requiring not 6 but 7 hits for accepting a track will almost completely eliminate fakes (of course at a price of slightly reduced efficiency for reconstruction of good tracks).

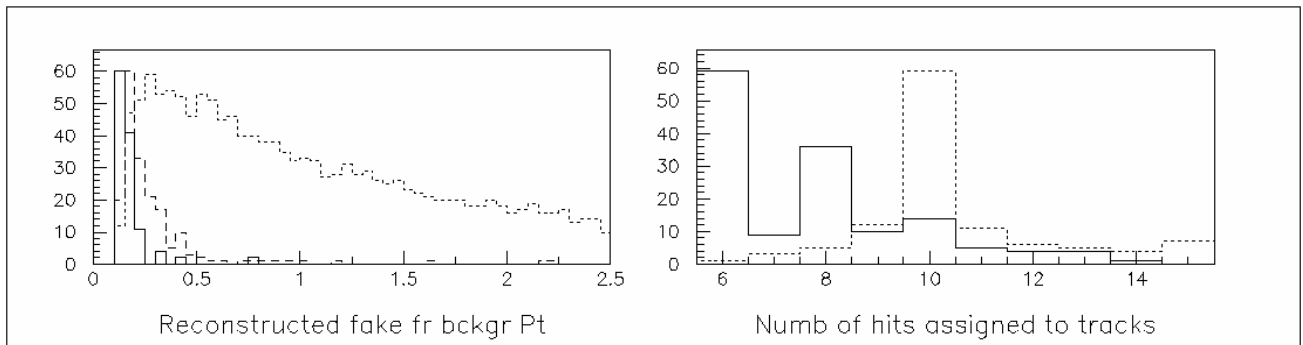


Figure 41 Pt distribution and distribution of the number of assigned to track hits for fake tracks. Solid curves are for fake tracks in the presence of background hits, long dashed - for fake tracks in the pure physics events (without background hits), and short dashed - for good physics tracks. Histograms are normalized to the maximum.

- [1] The basic algorithm we are using here was developed a long time ago by Henry Videau for use in the PEP TPC track reconstruction and was later adapted for BaBar by Henry Lynch and Orin Dahl.

III.C.4.c Silicon Tracker Standalone Tracking Reconstruction

The pattern recognition from the hermetic five-layer pixel vertex detector is very powerful, as shown in the previous sections. For this reason, it is assumed that the default tracking pattern recognition in SiD will rely upon the vertex tracker to bootstrap the process. As shown, studies show that the algorithm that seeds tracks with all three-hit

combinations in the vertex detector achieves greater than 98% efficiency with very low fake rate for barrel tracks with transverse momentum greater than about 500 MeV. While the efficiency for forward tracks is similar, the fake rate is somewhat higher than in the barrel due to higher occupancy and ghosting effects in the forward silicon disks. This performance in the forward region, while acceptable, can likely be significantly bettered as more advanced algorithms are developed and the design of the forward tracker disks is refined.

One obvious shortcoming of the “inside-out” approach is that a significant number of tracks originate beyond the inner layers of the vertex detector. These include tracks from K-shorts and long-lived heavy mesons that are at the foundation of many important physics measurements. Although the outer tracker for the SiD detector has only single-sided axial layers, we have studied the stand-alone pattern recognition capability of the outer tracker. The relatively low track multiplicity per crossing at large radius, together with the very high B-field, results in very low occupancies in the short-module design of the outer tracker. In essence, the readout segments are short enough that the tracker strips behave as long pixels for the purpose of pattern recognition. A simple pattern recognition algorithm that uses circle fits to all valid three-hit combinations has been studied in the barrel tracker. The algorithm was tested using single high p_T muons. For these events a tracking efficiency of 99.2% was achieved for muons with a hit on all five layers. For $T\bar{T}$ events, using only hits close to the trajectory of the initial seed track, a track finding efficiency of 94% is obtained. In 83% of the cases, all hits were found on the reconstructed tracks. Further refinement of this technique is expected to yield similar results in the forward tracker as well as finding many tracks that originate beyond the vertex detector. Given the primitive nature of these three tracking tools and the excellent performance provided by each alone and all together, there is every reason to expect not only excellent momentum and impact parameter resolution, but also very high tracking efficiency and purity from the SiD tracking system.

III.C.4.d Calorimeter-Assisted Tracking

The development of the calorimeter-assisted tracking algorithm is motivated by the need to reconstruct long-lived particles in the SiD detector. To minimize multiple scattering and energy loss in the tracker, while providing accurate vertex finding and high-precision momentum measurement for charged particles, the SiD baseline design utilizes a compact five-layer silicon pixel vertex detector and a five-layer outer silicon tracker. The standard track finding algorithm relies on identifying tracks in the vertex detector, where pattern recognition is simplified by the fact that precise three-dimensional information is available for each hit. Tracks found in the vertex detector are then propagated into the outer tracker, picking up additional hits and measuring the track curvature. As shown, this algorithm achieves high efficiency in reconstructing most types of tracks. However, its heavy reliance on seeds provided by the vertex detector raises a number of questions that need to be addressed. This has motivated the development of the calorimeter-assisted tracking algorithm.

Tracks produced by decay products of long-lived particles that decay outside the third layer of the vertex detector cannot possibly be reconstructed with the standard vertex detector-based pattern recognition since they do not leave enough hits in the pixels to produce a track seed. Obvious examples of long-lived particles that produce such secondary vertices are K_S^0 and Lambdas. However, the detector should also be capable of detecting new physics signatures that would include long-lived exotic particle like those predicted by some gauge-mediated supersymmetry breaking scenarios. There are also issues of reconstructing kinked tracks produced by particles that loose a substantial portion of their energy in the tracker, as well as reconstructing backscatters from the calorimeter. Finally, the availability of an alternative track finding algorithm that would not rely on seeds from the vertex detector would significantly increase the overall robustness and cross check the capability of the SiD tracker.

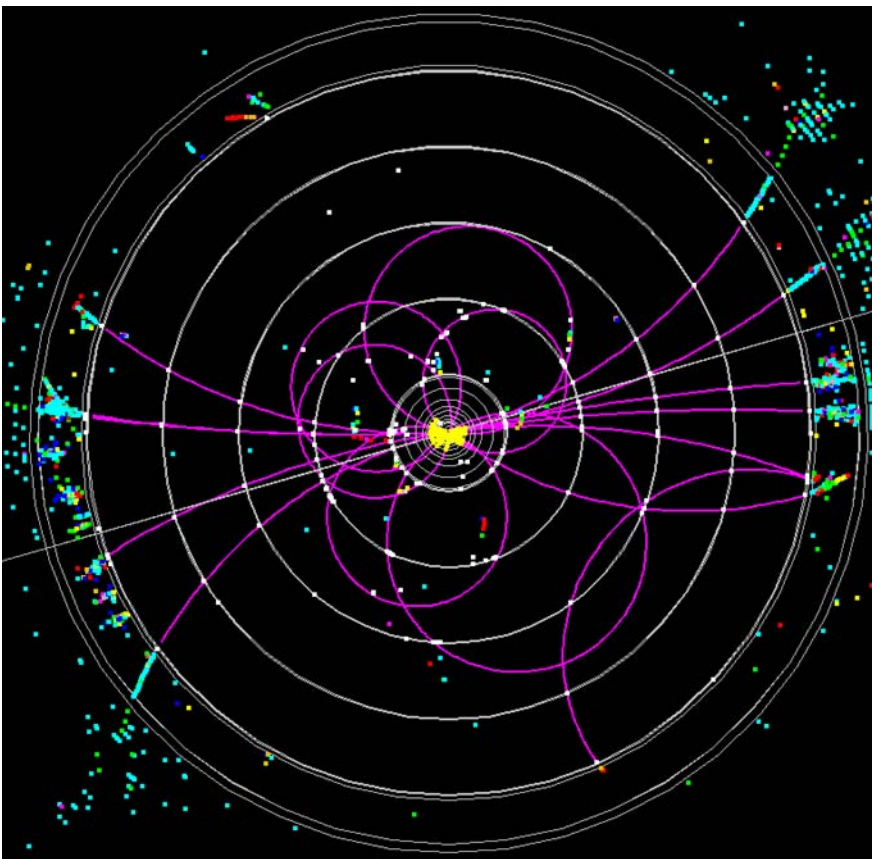


Figure 42 Calorimeter backscatter track reconstructed with the calorimeter assisted track finder. Identifying such tracks makes it possible to avoid double-counting their energy in particle flow algorithms.

In order to address these issues, a track finding algorithm has been developed that uses the electromagnetic calorimeter to provide seeds for pattern recognition in the tracker. The very fine segmentation of the EM calorimeter allows for detection of traces left by minimum ionizing particles – so-called MIP stubs - and uses them to determine the track entry point, direction, and sometimes curvature with a precision sufficient for extrapolating the track back into the tracker.

A proof-of-principle implementation package for this algorithm was developed within the hep.lcd Java-based framework. The track finding goes through the following main steps:

- 1) The standard vertex detector assisted track finder is run. Outer silicon tracker hits that are associated with successfully reconstructed tracks are removed.
- 2) MIP stubs in the electromagnetic calorimeter are identified. Several alternative algorithms can be used at this step, such as a generic nearest-neighbor clustering or a dedicated MIP-stub finder developed for the SiD geometry.
- 3) For each MIP stub, the track helix parameters are determined. The track is extrapolated back into the tracker, picking up hits in each layer. Every time a hit is added to the track, the track is re-fitted to get a more precise estimate of its parameters. If multiple hit candidates are found in a given layer, the track finding process is branched and several independent track candidates are created.
- 4) Quality cuts are applied to track candidates; duplicate tracks that share too many hits are discarded.
- 5) Track intersections are determined; if track intersections are found, the original particles that produced the secondary vertices are reconstructed.

The package was tested by reconstructing hadronic events simulated in the SiD detector with the Geant4-based LCDG4 package. Since proper digitization software for silicon strips was not available, point-like hits produced by the simulator were smeared with the expected position resolution, and the actual tracker segmentation was modeled by creating two-dimensional hits representing silicon strips. These two-dimensional hits were used in both track finding and fitting. In a sample of simulated Z -pole event, this proof-of-principle implementation package was able to reconstruct about 61% of all charged pions with transverse momentum above 1 GeV, produced by K_S^0 decays. For comparison, the standard vertex detector assisted pattern recognition found less than 2% of such pions. Ways to improve the performance of the algorithm have been identified, but implementation has been deferred until the package has been ported to the new org.lcsim framework.

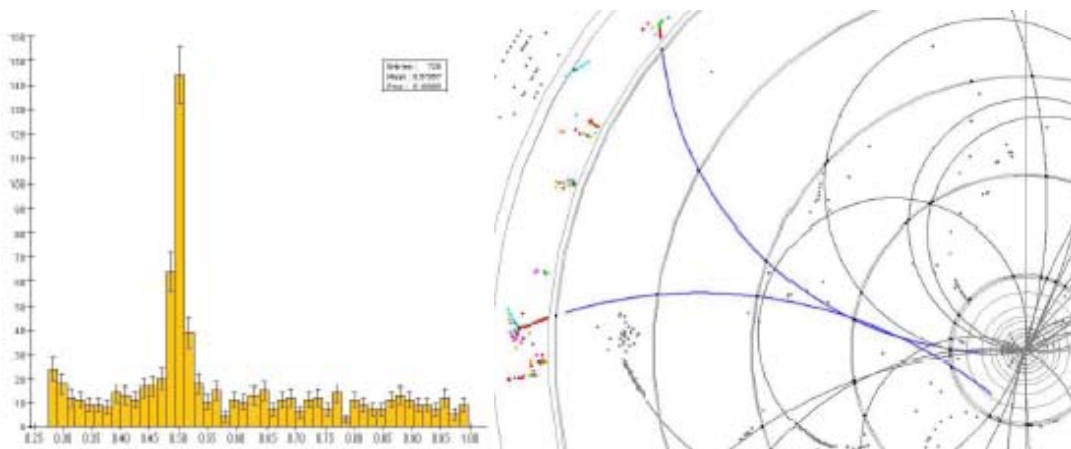


Figure 43 Results from the calorimeter-assisted tracking on a Z^0 -pole data sample. The figure on the left shows the reconstructed K_S^0 mass spectrum. The figure on the right shows the reconstruction of a K_S^0 in a hadronic Z -pole decay. The K_S^0 decays to $\pi^+\pi^-$ and the decay vertex is located at the 9 o'clock position between the first and second outer tracker layer. The lines indicate the reconstructed track stubs.

III.C.5 Simulated tracking Performance

The standard track finding algorithm for the SiD detector is an ‘inside-out’ track finding algorithm. Pattern recognition begins in the vertex detector, and proceeds by extrapolating tracks into the main tracker. In this section the performance of an algorithm that augments vertex detector patterns with hits from the central tracker, will be described along with its associated track-parameter fitter. The algorithm is called VXDBasedReco. Efficiencies have been estimated, and track-parameter errors are compared to expectations from the Billior-based LCDTRK.f track-parameter error tool [1]. The goal of these studies is to evaluate the overall performance of the SiD tracking system with the most realistic simulation available. While available simulation tools did include the effects of material on charged tracks, and did incorporate a full pulse-development model for the baseline CCD vertex detector, a pulse-development model was not yet available for the silicon central tracker. Instead, hits were assigned to layers with 100% efficiency, with no noise hits generated, and were smeared according to established detector smearing parameters (typically 7 μm for the silicon central tracker). The data samples studied, QQbar and di-muon events at $\sqrt{s}=500$ GeV, included no machine backgrounds.

The study focused on the efficiency and reconstruction accuracy of tracks that lie well within the fiducial volume of the central tracking system. For the QQbar sample, events were required to have $\cos(\theta)_{\text{thrust}} \leq 0.5$, with a thrust magnitude of 0.94 or greater. For both di-muon and QQbar events, individual tracks were also required to have $\cos(\theta) \leq 0.5$ and $p_T \geq \text{GeV}/c$. No requirement was made on the quality of the track-parameter fit.

For this sample of tracks from QQbar events, the tracking efficiency of the algorithm was found to be 94.3%. However, most of the inefficiency was due to tracks from charged particles that originated outside the vertex detector. Since VXDBasedReco requires an initial stub from the vertex detector, one would expect the efficiency to be zero for such tracks. Thus, for all subsequent studies, tracks were required to originate within 1 cm of the origin.

For such tracks, the overall tracking efficiency was found to be approximately 99.0 % when pulses were simulated with the CCD pulse-development model, and 99.5% when Gaussian smeared hits were used in the vertex detector. Figure 1 shows, in the case that the pulse development simulation is used for the vertex detector, the efficiency as a function of the angle α between the track and the thrust direction. Since the direction of the jet core should be well approximated by the direction of the thrust axis for events for which the thrust value is greater than 0.94, it appears that the tracking efficiency for stiff tracks is not significantly degraded in the core of jets. On the other hand, fully isolated tracks from di-muon events exhibit a reconstruction efficiency of 99.7%.

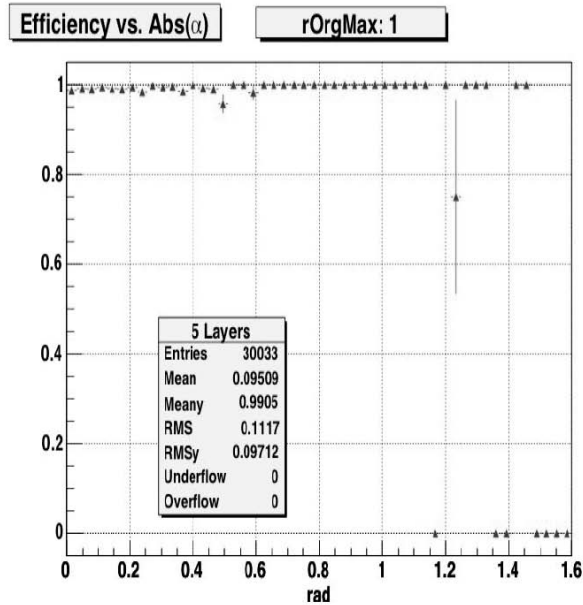


Figure 44: Tracking efficiency versus angle relative to the jet core, for tracks originating from within 1 cm of the interaction point.

Track parameter performance was studied by comparing three different resolution results: the closed-form result from the track-parameter error tool LCDTRK.f, the square-root of the appropriate error matrix element, and the reconstructed residual, that is, the rms difference between the true and reconstructed track parameter value. These studies were primarily focused on the p_T resolution for which the related track parameter is the curvature ω , given by $\omega = 1/R = 0.003 B \times 1/p_T$, with the radius of curvature R in cm, the magnetic field B in Tesla and the track transverse momentum p_T in GeV/c. For these studies, Gaussian smearing of hits was used for the vertex detector (as opposed to the realistic pulse development simulation), since this was the assumption made for the LCDTRK.f calculation. In addition, the comparison was made only for tracks with hits on all five tracking layers from the vertex detector and all five layers from the central tracker.

Figure 2 shows the results of this comparison as a function of curvature for the QQbar and high-momentum di-muon samples. Although in good agreement at low curvature (high momentum), the residuals diverge from the LCDTRK expectation, reaching a disagreement of close to a factor of two at high curvature (low momentum). The LCDTRK and error matrix expectations are in somewhat better agreement, although again the results diverge at high curvature. This suggests that there is a problem with the incorporation of material in the track parameter fitting algorithm.

The di-muon sample point suggests that the agreement between the three values is rather good at high momentum, for which material plays little role. For this high-momentum sample, the rms curvature residual, matrix element, and LCDTRK.f calculation are $3.40 \cdot 10^{-7}$, $3.12 \cdot 10^{-7}$ and $3.26 \cdot 10^{-7} \text{ cm}^{-1}$, respectively. Finally, using the realistic pulse-development simulation rather than Gaussian smearing for the vertex detector hits, the di-muon rms curvature residual is found to be $3.29 \cdot 10^{-7} \text{ cm}^{-1}$, somewhat better than the value achieved with the assumption of Gaussian smearing with a $5 \text{ }\mu\text{m}$ width.

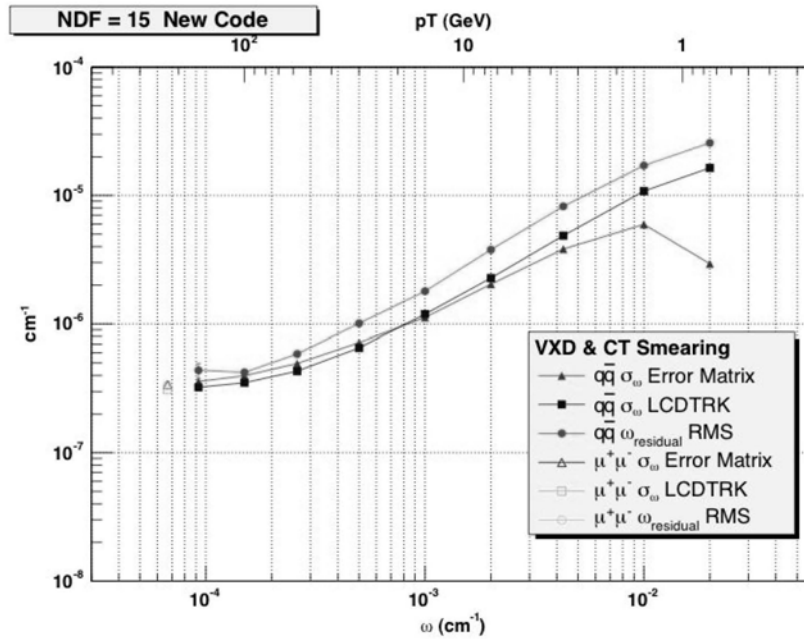


Figure 45: Curvature resolution as a function of curvature, comparing between rms residuals, square root of the appropriate error matrix element, and the LCDTRK.f expectation. The points at smallest curvature (largest transverse momentum) are from dimuon tracks; the remaining points are from a QQbar sample.

The track-parameter error tool has also been used to study the performance of the tracker for variants of the SiD detector design. Three alternate detector configurations were studied: the same overall layout of the detector but lowering the magnetic field from 5T to 4T ('Low Field'), extending the length of the barrel region from 150 cm to 180 cm ('Long'), and decreasing the outer radius of the outer tracker from 125 cm to 100 cm ('Petit'). Tracks were required to originate from the beamline, and a $2 \text{ }\mu\text{m}$ $r\phi$ beam constraint was imposed. Figure 3 shows the momentum resolution $\sigma(p_T)/p_T^2$ as function

of p_T for tracks at normal incidence. The performance is compared to the TESLA performance with an $r\phi$ spatial resolution of $100 \mu\text{m}$. Figure 4 shows the momentum resolution as function of $\cos(\theta)$.

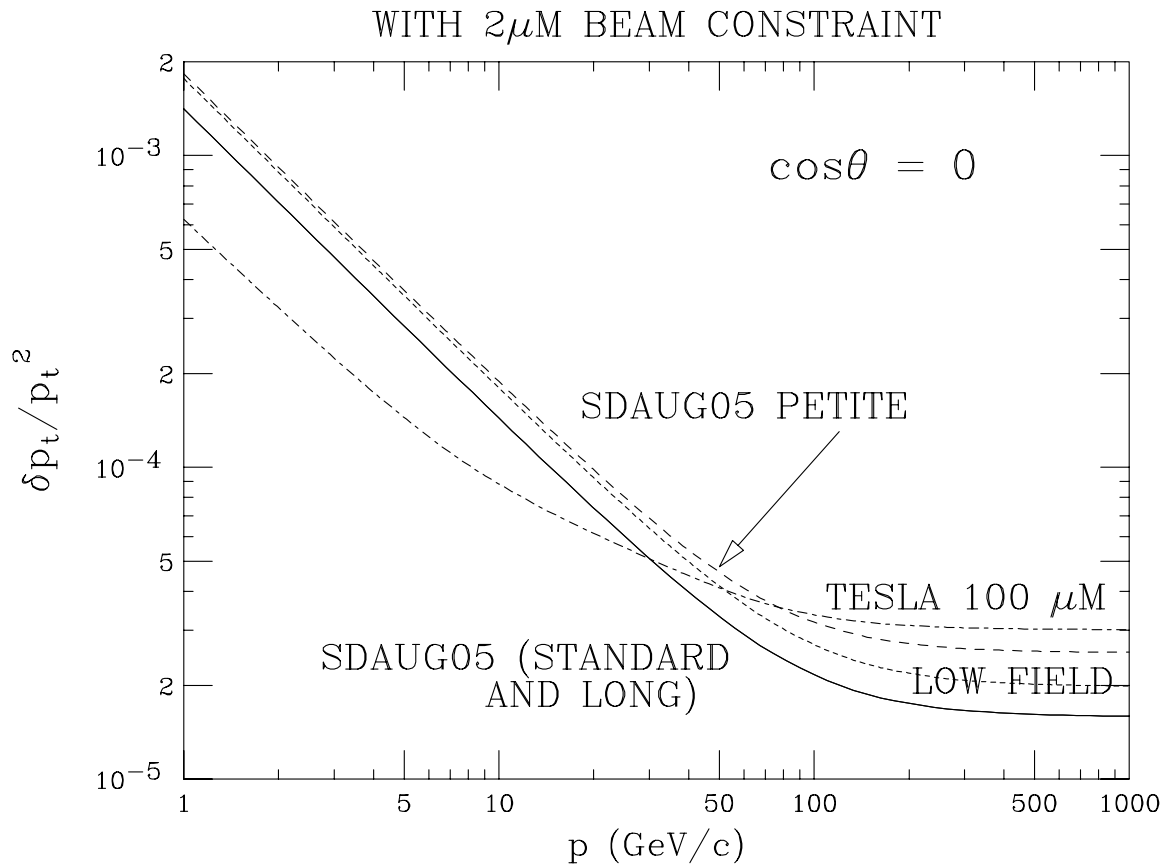


Figure 46: Momentum resolution for the standard SiD detector layout and three variants.

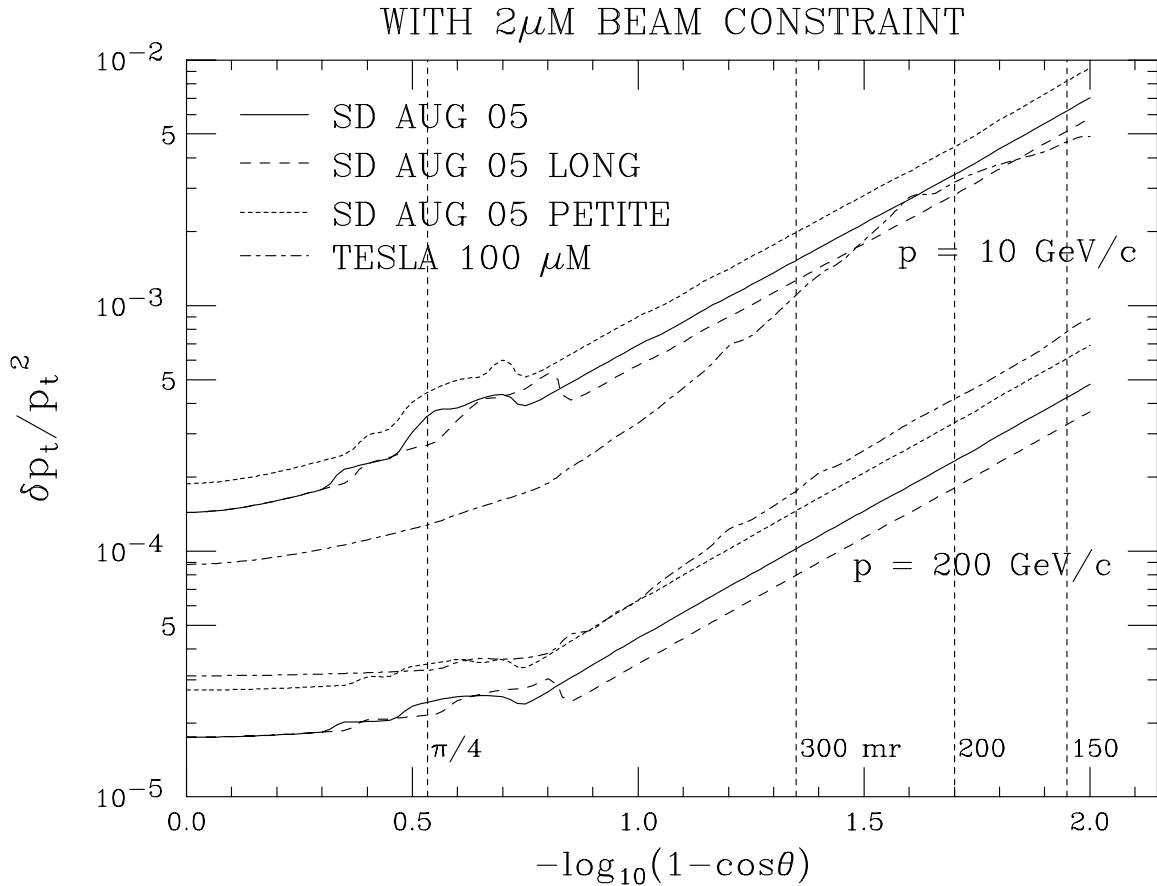


Figure 47: Momentum resolution of the SiD detector and three variants as function of the angle of the track.

[1] B. A. Schumm, <http://www.slac.stanford.edu/~schumm/lcdtrk20011204.tar.gz>

III.D Calorimeter concept

To measure hadronic jets of particles produced in high-energy collisions of electrons and positrons, with sufficient precision it is widely accepted that a new approach is necessary. The most promising method, named Particle Flow Algorithm (PFA), utilizes both the tracking information for charged particles and the calorimeter for the measurement of the energy of neutral particles. PFAs applied to existing detectors, such as CDF and ZEUS, have resulted in significant improvements of the jet energy resolution compared to methods based entirely on the calorimetric measurement. However, these detectors were not designed with the application of PFAs in mind. The SiD concept on the other hand accepts that a PFA is necessary and is designing the detector to optimize the PFA

performance with the goal of obtaining jet energy resolutions of the order of $30\%/\sqrt{E}$ or better.

The major challenge imposed on the calorimeter by the application of PFAs is the association of energy deposits with either charged or neutral particles impinging on the calorimeter. This results in several requirements on the calorimeter design:

to minimize the lateral shower size of electromagnetic clusters the Molière radius of the ECAL needs to be minimized

Both ECAL and HCAL have to have imaging capabilities which allow assignment of energy cluster deposits to charged or neutral particles, which implies that the readout of both calorimeters needs to be finely segmented transversely and longitudinally.

HCAL needs to be inside the solenoid to be able to do particle cluster association.

In addition, the design of the calorimeter needs to be as uniform as possible, minimizing the use of different technologies, extendable to small angles to ensure hermeticity, and to provide enough depth for the longitudinal containment of hadronic showers. The design needs to consider the cost as an additional boundary condition.

Following is a short description of the baseline designs for the ECAL and the HCAL, as defined by the study group in August 2005. For more details see the sections which follow.

III.D.1 The Electromagnetic Calorimeter (ECAL)

The ECAL consists of alternating layers of tungsten radiator and large-area silicon diode detectors. This combination provides for a dense, highly segmented calorimeter, as required for the application of Particle Flow to hadronic jets, but which is also desirable for the reconstruction of tau leptons, electrons, and photons, and provides tracking of charged hadrons and muons.

Silicon detectors are readily segmented. To provide pattern recognition of EM showers and particle separation, we wish to provide segmentation which is a fraction of the Molière radius, which is 9 mm for pure tungsten. For our baseline design, the silicon detectors are segmented into pixels of area 12 mm^2 . All pixels are read out and digitized via an ASIC which is mounted on the detector.

The longitudinal structure of the baseline ECAL consists of 30 alternating layers of tungsten and silicon. The first 20 layers of tungsten each have thickness equivalent to 2.5 mm (or $5/7$ radiation lengths) of pure tungsten (about 2.7 mm for a 92.5% alloy). The last 10 layers have double this thickness, making a total depth of about 29 radiation lengths at normal incidence. The readout gaps must be kept small to maintain the small EM shower widths. We believe that 1 mm readout gaps between the tungsten plates are feasible as shown in Figure 3.

The inner radius (length) of the barrel is 127 (359) cm. The endcaps are located inside the barrel and start at a distance of 168 cm from the interaction point. The longitudinal structure and segmentations for barrel and endcap are the same in the baseline design.

III.D.1.a Mechanical and detector configurations

Figure 48 below shows the overall baseline ECAL mechanical concept. The readout layers are tiled with 15 cm silicon detector wafers. Each wafer consists of about 1000 readout pixels, each of areas 12 mm^2 . Figure 49 depicts one of these 15 cm detector wafers. At the center of each wafer is one readout ASIC, called KP*i*X, which provides full readout for all 1000 pixels. The digitized charge and bunch-crossing information is multiplexed and carried on a single line on the polyimide cables (see and Figure 50) to an edge of an ECAL module, as indicated by the green shaded regions in .

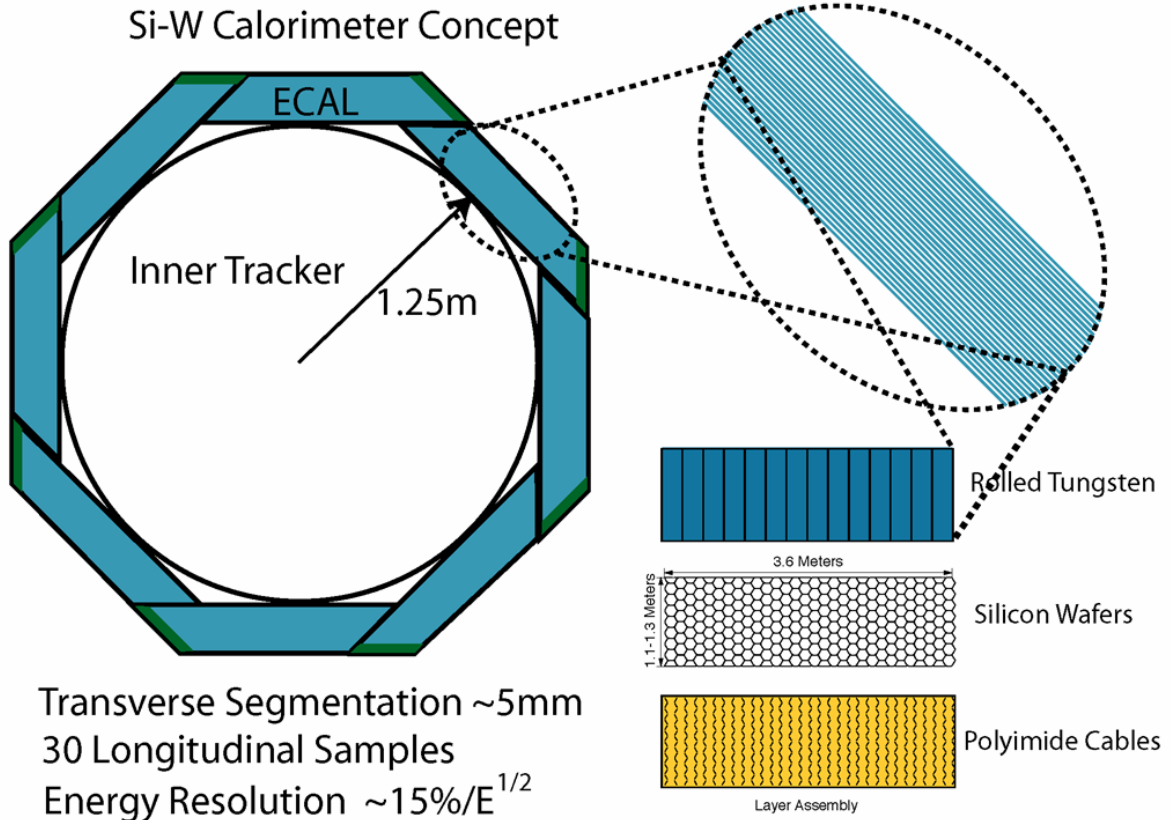


Figure 48 Baseline barrel ECAL configuration.

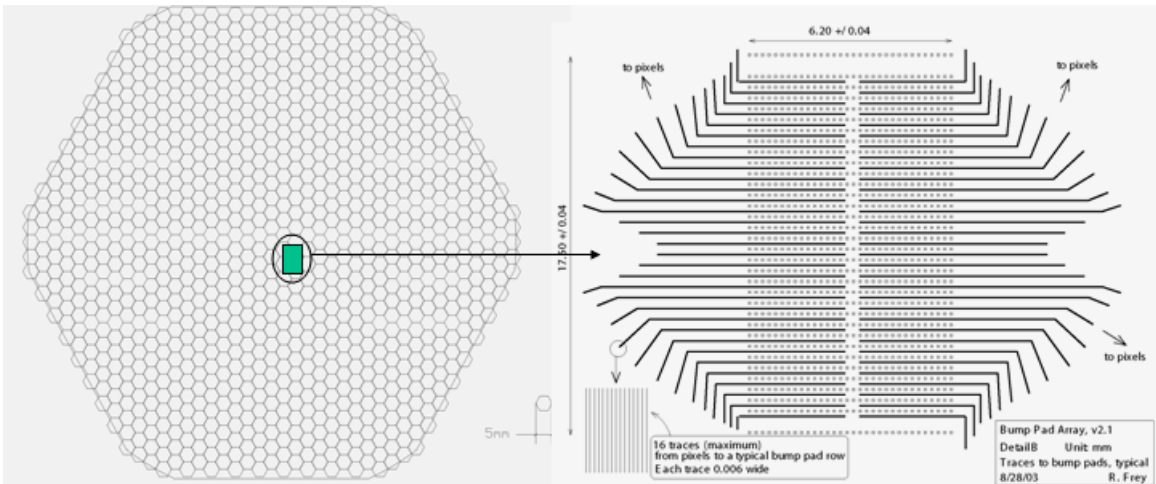


Figure 49 Cartoon of a silicon detector wafer (left) segmented into 12 mm² pixels. The green rectangle at center depicts the KPix ASIC. Right: The bump bond pads and signal trace metallizations on the silicon wafer in the vicinity of the ASIC.

The KPix chip is bump-bonded to the silicon wafers using the metallizations shown in Figure 3. This is a 32 x 32 array of bump bond pads, each of which is connected to a pixel by a trace on the detector wafer, and which connect to the 1032 channels of the KPix chip. Figure 50 gives a side view into a readout gap, showing (from bottom to top) mechanical standoffs, the silicon detector wafer (320 μm thick for the baseline), the KPix chip and the polyimide cables. The cables carry the one data line per wafer, along with power and control signals for the KPix chip, and bias voltage for the silicon detectors.

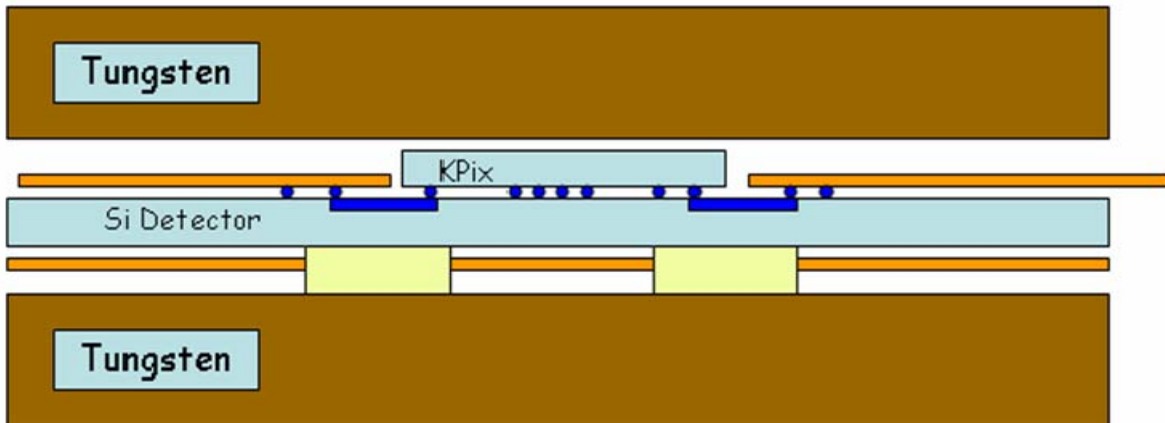


Figure 50 View into a readout gap in the vicinity of the KPix readout chip. Representative bump bond connections are indicated by the small blue circles. Traces (dark blue lines) connect the KPix serial readout stream, control signals, and power to the polyimide

Thermal management is a crucial feature of this design. The most power hungry elements of the KPix chip, particularly the analog front end, are switched off for most of the interval between bunch trains, giving a duty factor of 0.5%. Our requirement is to hold the average power dissipation per wafer to less than 40 mW. This will allow the heat to be extracted purely passively, providing a much simpler design, less subject to

destructive failure modes. The design of the KPiX chip in fact gives average power less than 20 mW. Without power cycling, this would not be possible. While we do not foresee the need for cosmic ray data, the power cycling eliminates this possibility.

III.D.1.b Electronic readout

Figure 51 is a diagram of a single channel of the 1024-channel KPiX chip, indicating its functional features. The energy density due to electromagnetic showers can be very large in this calorimeter – a 500 GeV electron can deposit up to 2500 MIP equivalents in a single pixel near shower max. Thus, the readout must be able to handle a large dynamic range. The KPiX chip uses a novel method by which the feedback path on the front end amplifier can be switched between two capacitors, switching in the large (≈ 10 pF) capacitor only when it is required. This allows the amplified charge for smaller input signals to be well above the noise. There is an event threshold, which can hold off bunch crossing resets in order to allow a fairly long integration time of $\sim 1 \mu\text{s}$. The calculated noise level is about 1000 e's, to be compared with a MIP signal charge of 25 times this. Charge digitization uses two overlapping 12-bit scales. The chip also allows up to four hits per bunch train to be stored for each pixel.

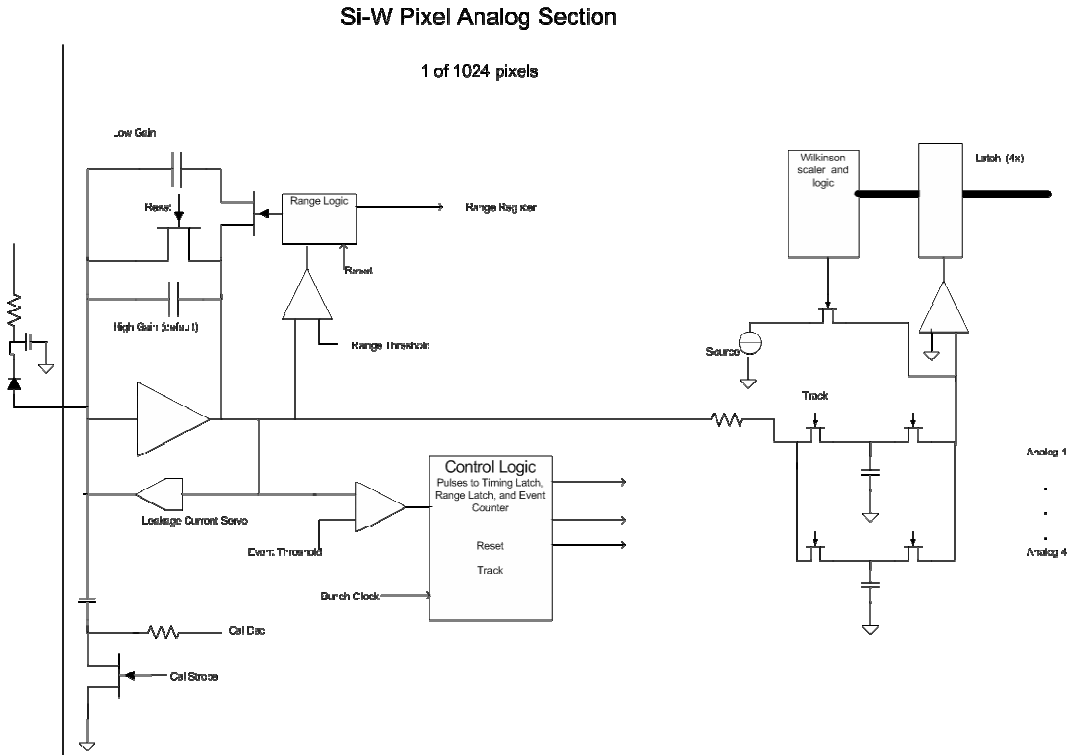


Figure 51 Functional diagram of one channel (of 1024) of the KPiX chip. The silicon detector pixel is indicated by the diode and capacitor at left.

III.D.1.c Performance goals

With a PFA, electromagnetic energy resolution is not expected to limit jet resolution. However, particle separation – photon-photon and charged hadron-photon – is crucial. These same features will also be put to good use for reconstruction of specific tau decay modes to enable final-state polarization measurement, for example.

Based on past experience with silicon-tungsten luminosity calorimeters at LEP and SLD, two electromagnetic showers can be usefully resolved when separated transversely by about half of the effective Molière radius. Here, “effective” includes the shower spreading in the readout gaps. In our case, this implies that two showers can be resolved when their separation is about 6 mm or more. The current algorithms have not yet attained this level of performance.

Charged track – shower separation should be possible when the tracks are on average separated from the shower core by about 10 mm or more. Due to bending in the field, it may be possible to do better than this, by taking advantage of diverging or crossing charged trajectories and showers.

Finally, about half of charged hadrons begin to shower in the ECAL. While it is in principle not difficult to separate these showers from the electromagnetic showers based on longitudinal and transverse profiles, good separation efficiency in a busy jet environment needs to be demonstrated.

For the baseline design, the first 20 layers have thickness $5/7$ radiation lengths (2.5 mm of pure tungsten), and the back 10 layers are two times this thickness. Figure 52 shows that this gives reasonably good shower containment at high energy, while Figure 53 shows that the energy resolution at low energy does not suffer relative to a design with 30 layers all having $5/7$ radiation length thickness. The simulations were made with EGS4. This can be duplicated in Geant4 only if one takes special care with the cutoff parameters. The resolution of the baseline design is well fit by the function $0.17/\sqrt{E}$.

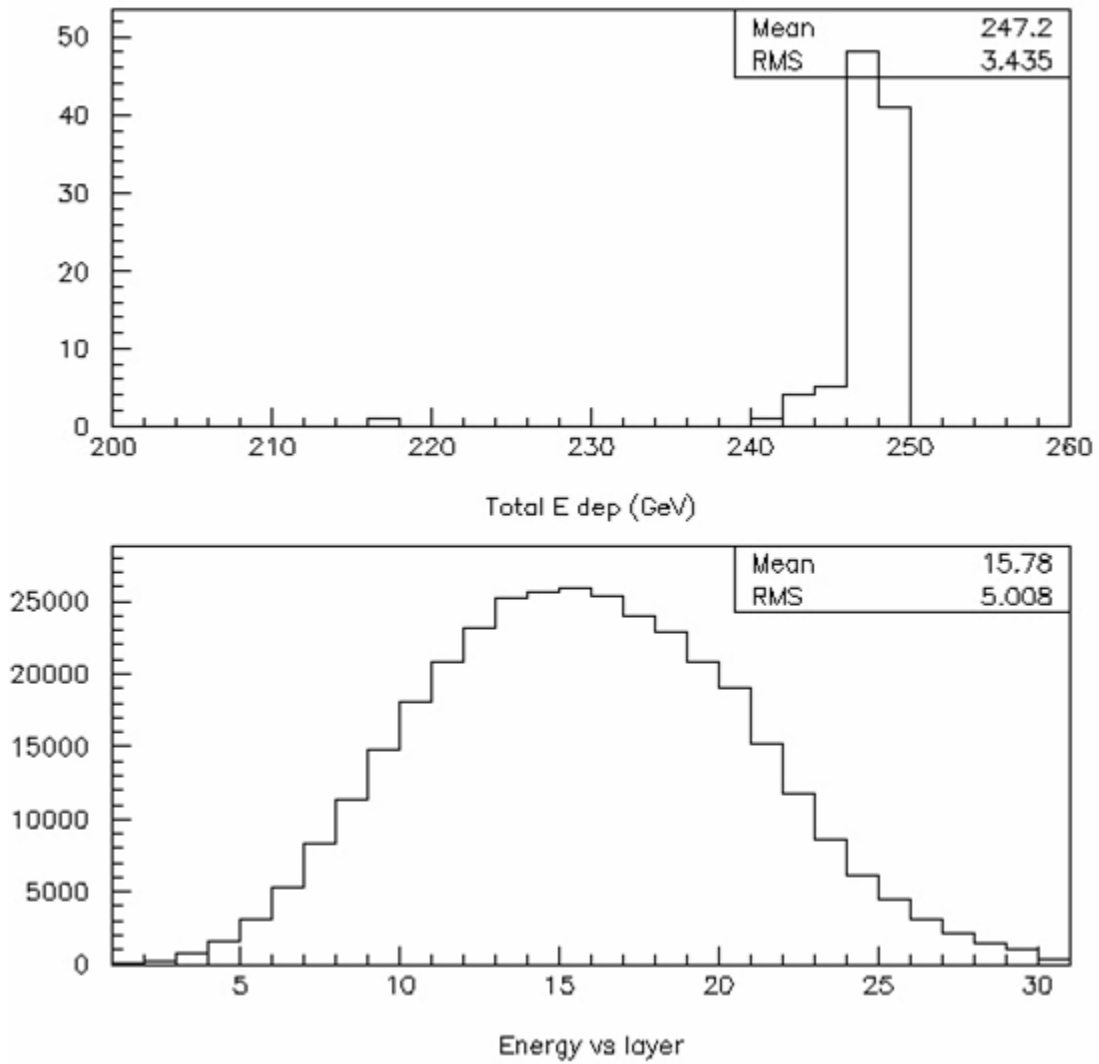


Figure 52 Top: Distribution of total deposited energy in the baseline ECAL for 250 GeV electrons. Bottom: Energy depositions by longitudinal layer for 250 GeV electrons. Layers 21-30 have twice the thickness of layers 1-20.

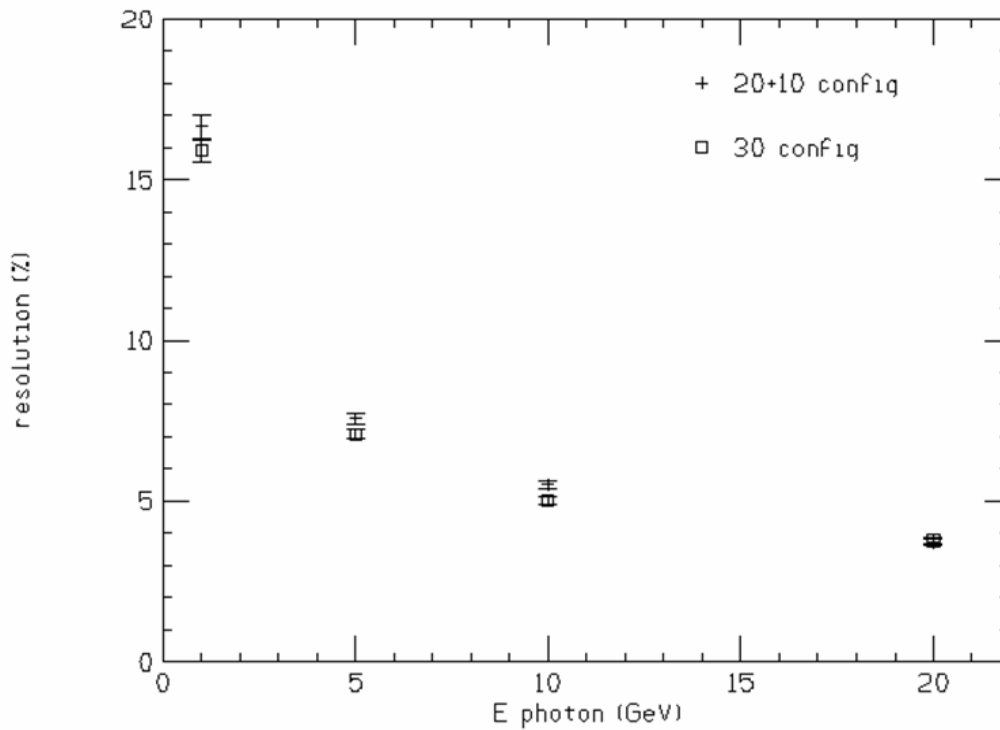


Figure 53. Energy resolution for photons as a function of photon energy for two longitudinal configurations. The “20+10” configuration is the baseline design.

III.D.2 The hadronic calorimeter

The HCAL is a sandwich of absorber plates with gaps instrumented with active detector elements. The current baseline uses steel for the absorber and resistive plate chambers as the detector. Alternate detector possibilities, consisting of Gas Electron Multipliers (GEMs) or scintillator are described as well below. One of the criteria for the HCAL is to minimize the gap, because an increase in the gap size has a large impact on the overall detector cost. The current gap size is 12mm.

To satisfy the stringent imaging requirements of the PFA algorithm, the transverse segmentation is required to be small of order a few cm^2 and every layer is read out separately. This in principle allows an analog or digital treatment of the signals. **Figure 54** shows the response of a digital GEM calorimeter and indeed a linear response is observed up to high energies, with some deviation above 50 GeV.

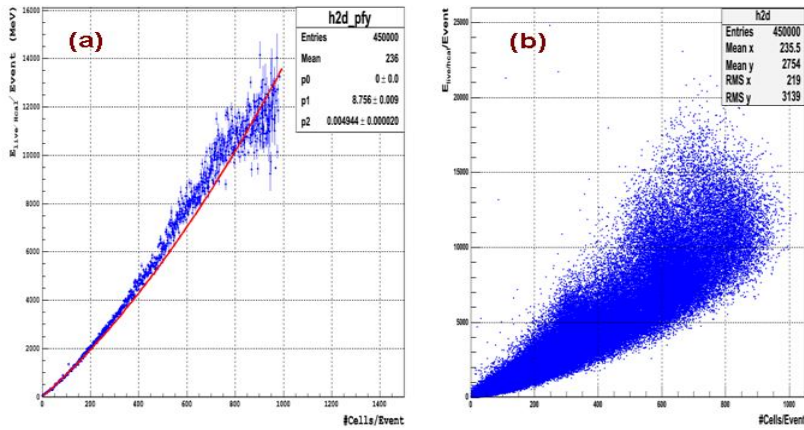


Figure 54 (a) A profile plot of energy deposit vs number of cells hit used for hit-to-energy conversion. (b) A scatter plot of energy deposit. A saturation at the higher energy deposit is apparent.

The absorber consists of steel plates with a thickness of 20 mm or approximately $1.1 X_0$. The cell structure, which is again identical for the barrel and the endcaps, is repeated 34 times, leading to an overall depth of the HCAL corresponding to four interaction lengths λ_I . Tungsten has been and will also be considered as an absorber, but is currently not the baseline.

The inner radius of the HCAL is 138cm and the outer radius (length) of the barrel is 233.7 (554.0) cm. The endcaps start at a distance of 179.65 cm from the interaction point.

II.D.2.a Absorber and mechanical structure

The SiD baseline design uses steel as absorber material in the HCAL. Steel with a radiation length $X_0 = 1.8$ cm and an interaction $\lambda_I = 16.8$ cm offers the smallest X_0 / λ_I of all commonly used absorber materials. A small ratio permits a one radiation sampling, while keeping the number of active layers manageable for a hadron calorimeter with a depth equivalent to four interaction lengths at 90° to the beam pipe.

The first attempts at a mechanical structure foresee a barrel and two endcaps, which are inserted into the barrel structure. The barrel is subdivided along the beam direction into three sections, as shown in Figure 55 and there are 12 modules to make a complete ring in phi.

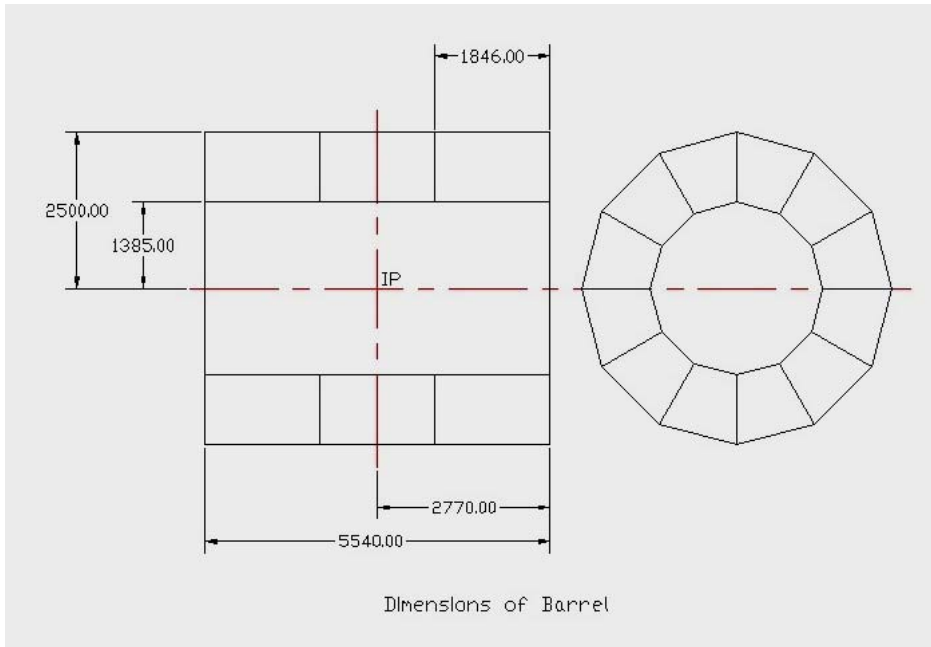


Figure 55 Side view of and cross section through the barrel structure of the hadron calorimeter.

The steel plates are held in place by a set of picture frames located at each end, see Figure 56.

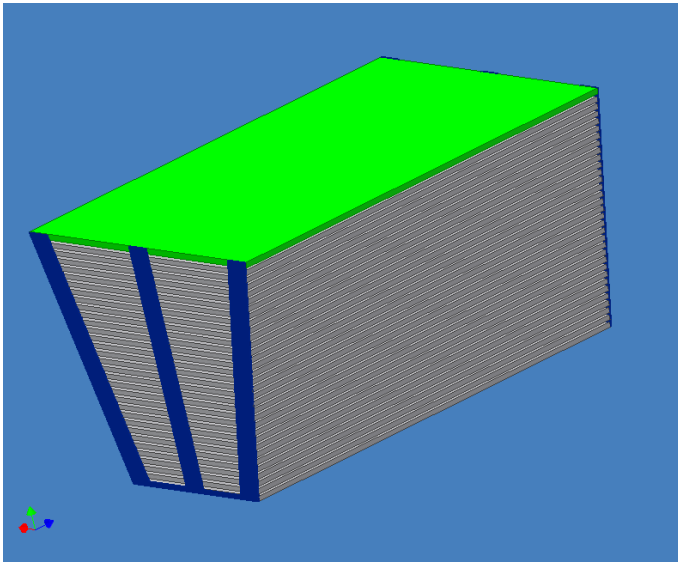


Figure 56 View of a single wedge.

Readout cables, high voltage cables and the gas lines are routed to the outer radius of the barrel structure through the openings in the picture frames. In azimuth the barrel structure is subdivided into twelve modules. Each module weighs approximately 10 tons and will be held in place through supports in the cryostat of the solenoid. Deflections have been calculated and do not exceed 0.5 mm at any point of the structure.

III.D.2.b Resistive Plate Chambers

Resistive Plate Chambers (RPCs) with small readout pads are one of the candidates for a hadron calorimeter designed to optimize the application of PFAs. They allow a segmentation of the readout pads of down to 1 cm^2 , which is required for PFA performance, and they can be built to fit small active gaps (of order 10 mm) to keep the outer radius of the calorimeter as small as possible. Glass RPCs have been found to be stable in operation for long periods of time, especially when run in avalanche mode, and the rate capabilities are adequate for the ILC and for test beam studies of hadronic showers. RPCs are inexpensive to build since most parts are available commercially. Signals in avalanche mode are large enough, in the range of 100 fC to 10 pC, to simplify the design of the front-end electronics. The readout electronics can in principle be simplified to a one-bit per pad resolution, if required.

Figure 57 shows a schematic diagram of a single-gap RPC. The chamber consists of two glass plates with high electrical resistance. Readily available window glass with a thickness of 0.8 to 1.1 mm provides the required electrical and mechanical properties. High voltage is applied to a resistance coating on the outside of the glass plates. The resistance of the coating must be low enough to re-charge the glass locally after a signal hit, and high enough to allow the electric field of the electron avalanche in the gas to reach the external signal pick-up pads. The glass plates enclose a gas volume in which ionization and electron multiplication takes place. Particles traversing the gas gap ionize the gas, creating an avalanche of electrons drifting towards the glass plate at positive high voltage. The signal is picked up inductively with pads located on the outside of the glass.

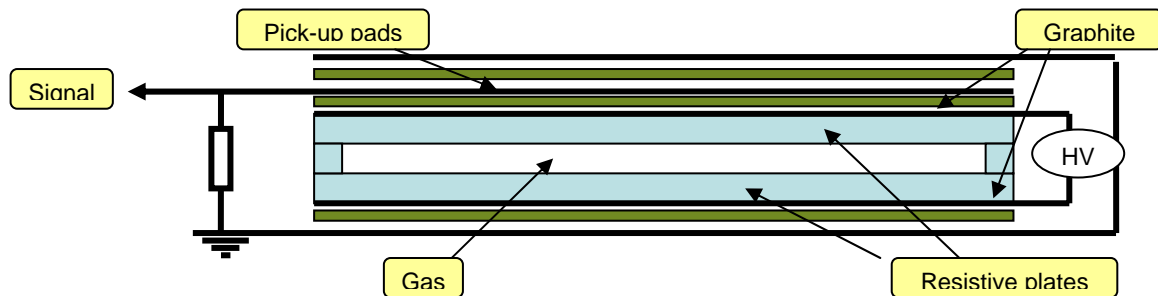


Figure 57 Schematic diagram of a typical Resistive Plate Chamber.

The RPCs are operated with a gas mixture of Freon (R134A), Isobutane (about 5%) and SF_6 . The mixture is not flammable and environmentally safe. The high voltage is set for operation in avalanche mode, giving signal charges in range of 100 fC to several pC.

III.D.2.c Measurements with RPCs

RPCs have been extensively tested by many groups and for this report we concentrate on test done at IHEP Protvino and at Argonne National Laboratory.

To illustrate the performance of RPCs, Figure 58 shows the single MIP detection efficiency as a function of the operating voltage.

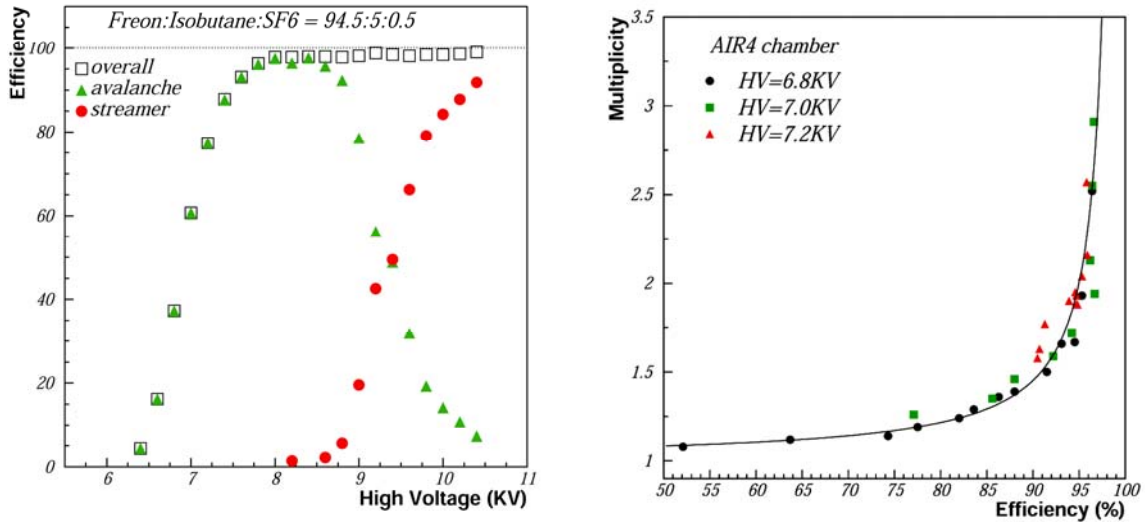


Figure 58 Shown is MIP detection efficiency as a function of operating voltage; hit multiplicity as a function of efficiency for varying operating voltages. Red points are streamer contributions.

At voltages above 7.4 kV the chambers are close to 100 % efficient. Streamers start to appear at voltages of 8.4 kV or more (red points in Figure 58). Thus, the chambers provide a large plateau, where the efficiency is high, but the streamer fraction is negligible. The figure also shows the pad (each with a $1 \times 1 \text{ cm}^2$ area) multiplicity as a function of MIP detection efficiency. The measurements were performed with three different high voltage settings. In this study, for a given high voltage, the discriminator threshold was adjusted to vary the detection efficiency and to measure the corresponding hit multiplicity. For efficiencies in the range of 90 to 95%, an average of 1.4 to 1.7 pads are hit. Ideally this number is close to unity. Provided the average pad multiplicity can be monitored during data taking (see the section on calibration), no degradation of the single particle resolution is expected as a result of these multiple hits. (What about jets/PFA?)

III.D.2.d Cell structure and overall depth

Figure 59 shows the cell structure of alternating steel plates and RPCs. The thickness of the absorber plates is 20 mm or about $1 X_0$. The active gap measures 8 mm and contains an RPC and a 1.6 mm air gap for tolerances. The RPC glass plates measure 1.1 mm each,

the gas gap 1.2 mm and the readout board, containing the pick-up pads as well as the front-end ASIC, 3 mm. The thickness of the gas gap is kept uniform with the help of fishing lines running the entire length of the module and placed approximately 5 cm apart. The cell structure is repeated 34 times for an overall thickness of the HCAL of 952 mm. The depth of the HCAL corresponds to $4 \lambda_I$ at normal incidence.

III.D.2.e Pad structure and readout

The readout pad area is chosen to be $1 \times 1 \text{ cm}^2$ on average, with the assumption that this results in one hit/pad in a jet. To accommodate the varying width of layers given by the wedge shape of HCAL modules, the lateral dimension will be adjusted to minimize the area of inefficiency between modules. Each pad is read out individually, which results in roughly $50 \cdot 10^6$ channels. The front end could be done with a multi bit readout (making the pulse height available for further analysis) or with a single-bit readout. The assumption is that this is a digital calorimeter i.e. in the end the information retained will be a simple “on” or “off” per pad indicating the passage of a single particle. This assumption and the exact final approach, including electronics needs to be verified in an extensive worldwide calorimeter testbeam program. However it should be noted that simulations of this digital mode readout have been carried out and indicate excellent results.

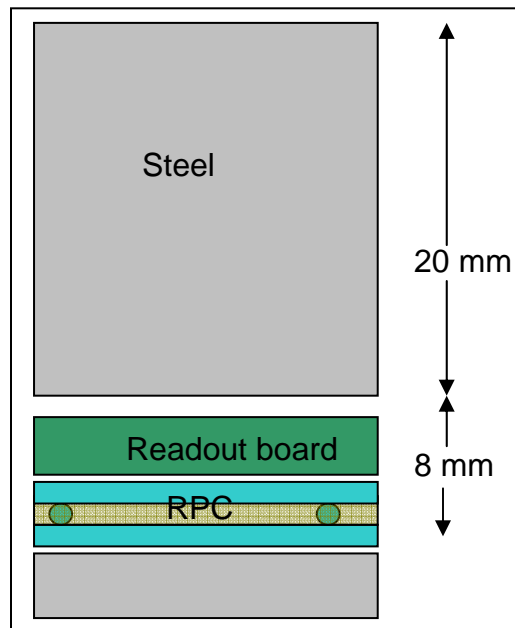


Figure 59 Cell structure of the HCAL. The thickness of the gas gap is kept uniform with the help of fishing lines indicated as circles in the drawing.

III.D.2.f Calibration of the efficiency and hit multiplicity

In a calorimeter with single-bit readout, the energy E_{inc} of an incident particle is reconstructed according to

$$E_{\text{inc}} = c_{\text{sampling}} N_{\text{pad}} / (\epsilon_{\text{MIP}} \cdot \mu_{\text{MIP}}),$$

where c_{sampling} corresponds to the sampling term of a multi-bit calorimeter and converts the number of firing pads N_{pad} into an energy. The terms in the denominator are related to the performance of the chambers and denote the detection efficiency ϵ_{MIP} and the hit multiplicity μ_{MIP} for single particles in a given layer of the calorimeter. Their values depend on the operation point of the chambers, as defined by the gas mixture, the high voltage setting and the readout threshold. In the ILC environment any non-interacting particle traversing a given layer can be used to measure their values. Since both ϵ_{MIP} and μ_{MIP} are expected to assume a constant value for all pads of a given chamber, high precision measurements of their values will be possible despite the low event rate of the ILC.

III.D.2.g Alternative approaches: Gas Electron Multipliers

Gas Electron Multiplier(GEM) technology is one of the alternative approaches to gas calorimetry considered here. GEM-based calorimetry offers many advantages in terms of low operating voltage, simple gas mixtures, low hit multiplicity at high efficiency, easy readout segmentation, and robust operation. show schematics of this approach.

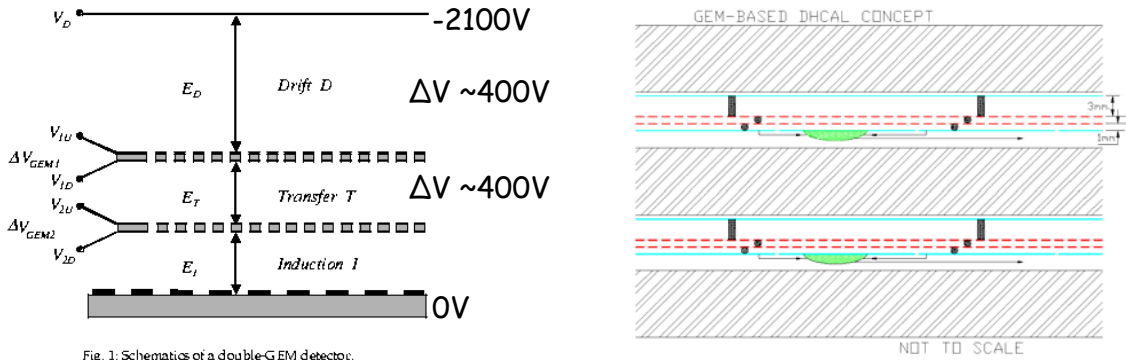


Fig. 1: Schematics of a double-GEM detector.

Figure 60 Schematic of double GEM detector(left) and the GEM-DHCL concept (right)

The ionization signal from charged tracks passing through the drift section of the active layer is amplified using two-stage GEM foils. The amplified charge is collected at the anode, or readout pad, layer, which is at ground potential. This layer is subdivided into the small ($\sim 1\text{cm} \times 1\text{cm}$) pads needed to implement the digital approach. The potential differences required to guide the ionization are produced by a resistor network with successive connections to the cathode, both sides of each GEM foil, and the anode layer. The pad signals are amplified, discriminated, and a digital output produced. The GEM design allows a high degree of flexibility with, for instance, possibilities for microstrips for precision tracking layer(s), variable pad sizes, and optional, initial ganging of pads for

finer granularity future readout if required by cost considerations. Figure 60 shows how the GEM approach is incorporated into a digital calorimeter scheme.

In order to be able to design a hadron calorimeter system based on GEM technology, it is necessary to establish the basic characteristics (signal sizes, efficiency, hit multiplicity, magnitude and frequency of crosstalk, rate capability) of GEM chambers with small anode pads, to develop the capability to make large area GEM foils, and to be able to reliably simulate the behavior our prototypes. We have constructed and learned how to reliably operate small GEM chambers. We have made a number of essential measurements with our small chambers, have obtained and characterized our first large-area GEM foils, and have produced simulation results.

A view of a GEM chamber prototype and the 3 x 3 array of 1cm² anode pads is shown in Figure 61. Signal amplification is achieved using QPA02 chips from Fermilab (originally developed for readout of a silicon-based detector). We originally used an Ar/CO₂ 70:30 gas mixture and obtained gain values close to those measured by the GDD group at CERN. However, we have recently changed to an 80:20 mixture, which yields signals about three times larger for the same potential across the foils and has not caused any deterioration in chamber performance or stability.

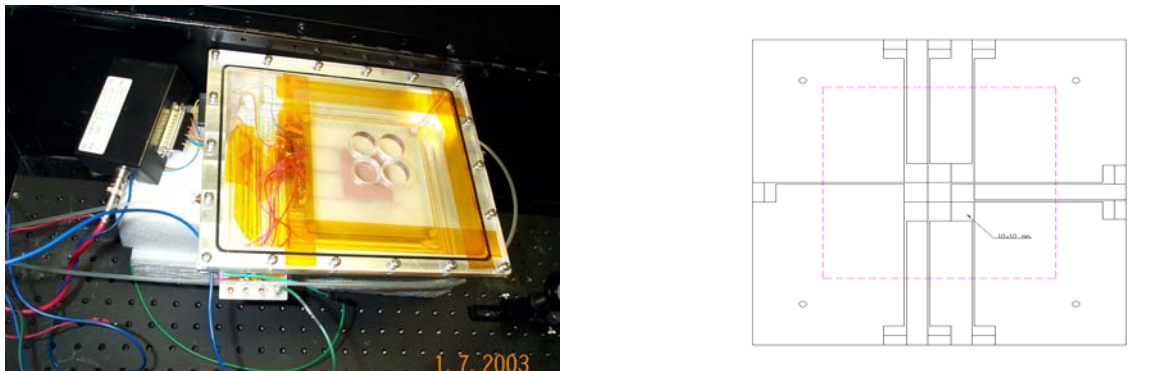


Figure 61 10cmx10cm prototype(left) and pad layout on right.

To measure the efficiency of our prototype we used cosmic rays at essentially normal incidence. The physical separation of the anode pads is 250 μ m. However, this gap should not lead to a loss of efficiency as the field lines, and hence the electrons, all end on one of the copper pads. With a 40mV threshold (compared with a typical average signal size of 200mV after amplification) we obtain an efficiency of 94.6%. This is in good agreement with the expectations from our simulations.

To measure the hit multiplicity on our 3 x 3 pad array, we used a Sr-90 source, collimated so that the decay electrons hit the central pad region only. A cosmic ray veto also covered the complete area of the pad array. The thresholds on all nine channels were set to the 40mV value that gave the 94.6% efficiency described above. The hit multiplicity is the ratio of the number of hits in all nine pads to the number of hits on the central pad. We obtained a value of 1.27, giving the GEM technology an advantage over, for example, RPC's for which a hit multiplicity in the range 1.6 – 1.7 has been measured.

We have worked with 3M Corporation to specify, produce, and test 30cm x 30cm foils. This was a precursor to producing the 1m x 30cm foils needed for a GEM-DHCAL test beam module. The 30cm x 30cm size was mainly dictated by the available etch window of the 3M reel-to-reel flex circuit production process. A view of one of the first foils and a high magnification view of a section of foil is shown in Figure 62.

We have made initial measurements of the currents drawn when various potential differences were applied across each high voltage sector on each foil. We defined a foil to be acceptable if it passed visual inspection, and if all HV sectors drew a current less than 10nA.

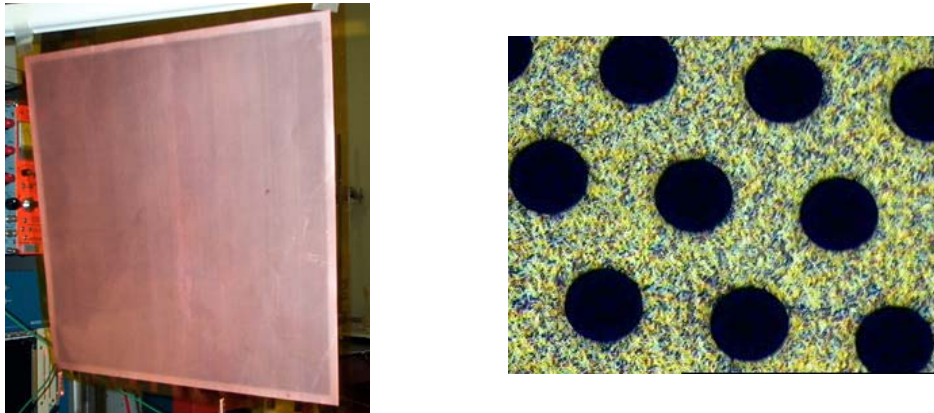


Figure 62 New 30cmx30cm GEM foil on left and magnified section of new 3M foil on right.

We are now assembling five 30cm x 30cm double-GEM chambers for exposure in test beams in Korea and at Fermilab in 2006.

III.D.2.h Alternative approaches: Scintillator

The use of plastic scintillator as the active medium in the SiD hadron calorimeter is under investigation as well. The scintillator option has been proven to work for jet energy measurements (although not yet tried for particle-flow), has a large sampling fraction and can be operated in analog mode with or without PFA (which will be a very important consideration if digital PFAs fail to meet resolution expectations), and have few operational constraints since liquids, gases, and high voltage are not required. The primary challenges for successful implementation of scintillator based ILC calorimetry are related to the fine segmentation needed for PFAs, cost, and large-scale assembly. After detailed studies performed over the past four years, we are confident that these can be overcome.

The breakthrough lies in the relatively recent emergence of a new class of solid-state photodetectors commonly known as SiPMs. A SiPM is an array of ~ 1000 tiny APDs packed into an area of 1 mm^2 and operated in the limited Geiger mode. Although each APD is only capable of a binary output, the analog sum of all APD outputs remains proportional to the number of photons so long as that number is small ($< \sim 30$) such that the probability of the same APD receiving multiple photons during a single time gate is negligible. SiPMs are small enough to be mounted on the scintillator tiles without any significant compromise in uniformity of coverage. This feature eliminates the need for guiding light out of the detector volume, which would be expensive, technically challenging, and might compromise detector hermeticity. The SiPMs we are currently using measure $\sim 3 \text{ mm} \times 3 \text{ mm} \times 1 \text{ mm}$ including housing. They are fast, rugged, radiation hard, immune to magnetic fields, and, most importantly, potentially cheap. We have carried out extensive characterization of these devices and conclude they are well suited to our purpose.

By current estimates, the HCAL cost will be driven primarily by electronics. For segmentations presently under consideration (preliminary simulations suggest that $\sim 3 \text{ cm} \times 3 \text{ cm}$ should be adequate for PFAs with scintillators), the scintillator option is quite economical, thanks to the cost-effective production of the scintillating material by in-house extrusion or injection molding and the expected price of \$3-5 per SiPM photodetectors. Overall, $\sim \$1.5/\text{sq cm}$ of lateral area for sensitive layers is possible (materials only).

The basic scintillator/silicon-photomultiplier (ScSiPM) layer structure would be schematically similar to Figure 59 with absorber plates on the order of 20 mm thick and active gaps 10-15 mm thick. Within each active layer individual $3 \text{ cm} \times 3 \text{ cm}$, 5 mm thick scintillator cells would be attached to a read out board. The scintillator cells would have an embedded WLS fiber to transmit light to its photomultiplier. The SiPMs would either be attached to the scintillator as shown in Figure 63 or attached directly to the readout board. In either case, the scintillator would be mounted directly to the board. In addition to supporting the ScSiPM cell, the readout board would carry signal, bias, and monitoring traces. The ScSiPM cell structure will be repeated 30-40 times for an overall HCAL thickness of 100 cm and a thickness at normal incidence of $4 \lambda_I$. The precise layer and pad dimensions are under study with PFA simulations in progress. In addition, work is now underway to design and construct prototype integrated ScSiPM-readout board structures. The first integrated prototype will have approximately 100 cells and carry traces to passive collectors for off-board readout.

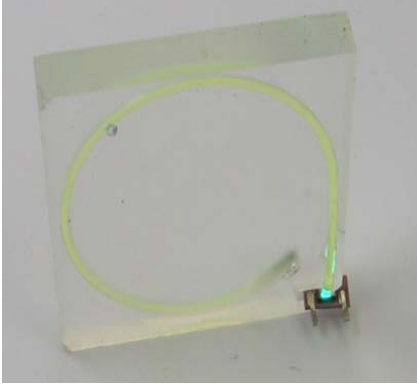


Figure 63 Scintillator with on-board SiPM

Construction and operating experience with the ScSiPM technology has been accumulated with the assembly and operation of prototype strip-based ScSiPM tail catcher-muon tracker (TCTM.) cassettes, shown during assembly in Figure 64. The full TCTM, now under construction, will include 16 cassettes with alternating layers of iron. Each cassette has ten extruded scintillator strips 103cm x 10cm and 5mm thick. Each strip has two embedded WLS fibers for transmission of light to SiPMs mounted at the end of the strips. The over all cassette thickness including scintillator, wrapping, and aluminum housing is 10mm, which fits comfortably into the nominal HCAL active gap dimensions.

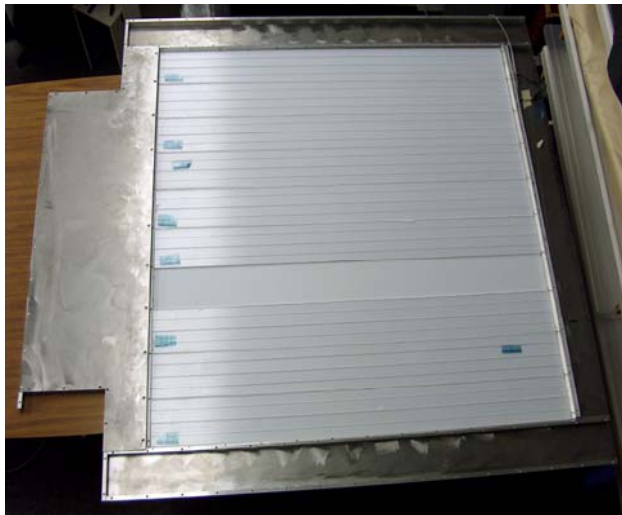


Figure 64 A prototype TCTM cassette under construction. Individual extruded scintillator strips runs left to right.

Figure 65 shows the response of the first prototype cassette to an electron beam at DESY using CALICE ECAL electronics. The histogram on the left represents the response of the cassette's 20 SiPMs and shows excellent discrimination between pedestal and MIP signals. Recently the same cassette was exposed to pion, proton, and muon beams at Fermilab. The electron and hadron data will be analyzed to understand the uniformity and stability of the ScSiPM technology. The CALICE collaboration has made similar studies of a finely segmented prototype ScSiPM DHC cassette at DESY and will study a

full EM, HAD, TCMT configuration with electron and hadron beams this summer at CERN.

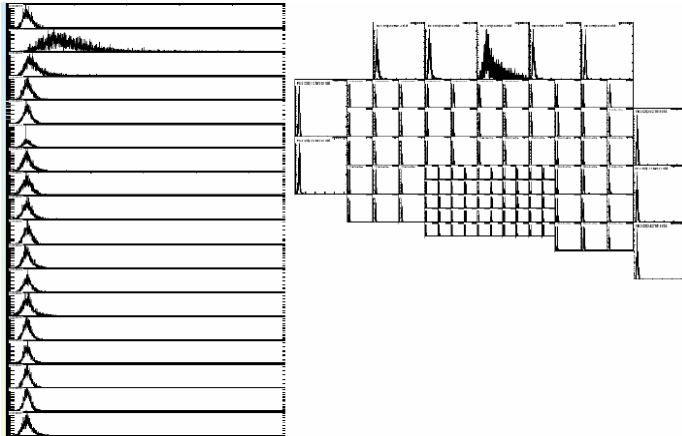


Figure 65 Response of TCMT ScSiPM to electron beam (left figure).

Conceptually the readout of the ScSiPM based DHC will be similar to the schematic shown in Fig. 5. The integrated read-out boards will also house custom ASICs with analog or two-bit digitizers, depending on cost. The ASIC will provide and control the $\sim 50\text{V}$ SiPM bias and any monitoring information required. Data concentrators will be housed at the end of each wedge and on the back-beams.

The technique for absolute calibration has yet to be determined but may involve a combination of cosmic rays, sources, and LEDs. This is an active area of R&D. If an analog readout is selected, the gain can be determined from the photo-electron spectrum of each SiPM by calculating the difference between the pedestal and the first peak. If a single or two bit readout is chosen, test-beam calibrations must be transferred to the actual detector with subsequent relative calibration. In any case, since the SiPM response has temperature dependence, temperature and relative response will require monitoring.

Extensive algorithmic studies have been performed with GEANT4-based simulation of full-detector concepts as well as prototype modules for beam tests. The performance of different tile geometries and readout schemes for the scintillator option has been evaluated for single particle energy resolution, two-particle separation, and jet energy resolution (which, with PFAs, is a function of the previous two). The nominal design ($3\text{ cm} \times 3\text{ cm} \times 0.5\text{ cm}$ tiles) has been compared with nominal RPC and GEM geometries. We have found that because of fundamental differences in shower development in scintillator as gas, the number of cell hits per GeV is a function of the hadron energy in scintillator. Thus, a 1-bit digital readout is not optimal, but a 2-bit “semi-digital” readout affording three thresholds instead of one, allows for complete use of the relationship between hits and energy deposited. Indeed, a 2-bit readout seems to suffice for the cell energy measurement, although it would not hurt to have a larger dynamic range if the cost differential is insignificant.

The improvement in the single particle energy resolution based on hit-counting is fairly rapid as one goes from coarser to finer segmentation down to about 15 cm^2 . After that, it becomes much slower. For the simple single particles/events studies so far, gains are very modest below the nominal 9 cm^2 design value. Differences in shower development in scintillator with respect to gas call for different clustering algorithms. With separately

optimized algorithms, we find single particle energy resolution, and two-particle separation capabilities of the ScSiPM option to be at par with or better than its gas counterparts across the relevant ranges (in energy and separation). Performance-wise, it is clearly a viable and sound solution.

III.D.2.i Alternative approaches: Micromegas

A compact approach : the Micromegas detector

Micromegas chambers can also be used for the HCAL. A Micromegas chamber is a gaseous detector, based on micropattern detector technology and widely used by many experiments: COMPASS, CAST, NA48, n-TOF, ILC TPC project, T2K TPC project. The COMPASS experiment is utilizing the largest size 40x40 cm² Micromegas for their up-stream small-angle tracking system. It has provided a stable high-rate operation, for three years, providing good performance.

A schematic view of the detector is shown in **Figure 66** : a commercially available fine mesh separates the drift gap (about 3 mm) from the amplification gap (about 100 μm). This simple structure allows full efficiency for MIPs and, thanks to the thin pillars, provides a good uniformity over the whole surface. Assuming a thin PCB structure for the anode pixel read-out, this compact structure provides an economic volume with a total depth of about 3.1 mm, including the drift space.

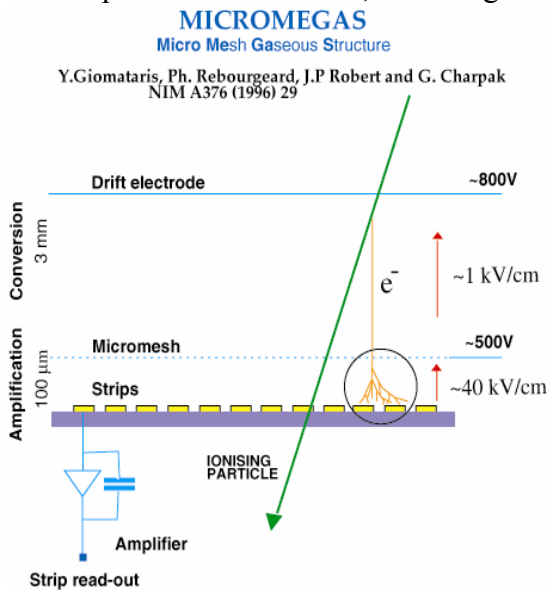


Figure 66 Schematic view of the Micromegas detector

A new promising technology technology ‘Micromegas Bulk’ allowing industrialization, has been recently developed in collaboration with the CERN PCB workshop for the

amplification gap. The basic idea is to build the whole detector in one process: the anode plane with the copper strips or pads, a photo resistive film having the right thickness and the cloth mesh, are laminated together at high temperature, forming a single object. By a photolithographic method then the photo resistive material is etched producing the pillars. The drift gap is then built separately and assembled afterwards.

The new industrial process allows easy implementation and provides uniform, light, low cost and robust detectors. There are no intrinsic limitations for building large surface detectors. Employing the bulk technology $30 \times 30 \text{ cm}^2$ detectors have been built for the TPC prototype of the T2K experiment. An example of the implementation of the detector in the T2K TPC, successfully tested last year, is shown in **Figure 67**. Two Micromegas detectors are assembled together on the same end-plate.

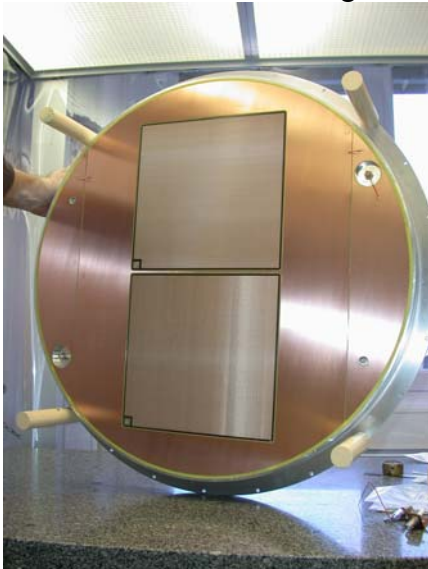


Figure 67 The T2K Micromegas chambers

Given the performance of this detector it can reliably be used for a hadronic sampling calorimeter.

Three large chambers $50 \times 50 \text{ cm}^2$ of 1 cm^2 pads, have been designed and will be available by the summer of 2006. Existing analog electronics, (~ 2000 channels) using the CERN Gassiplex chip will be used for the first tests. With this electronics the analog signal of each pad is recorded. Cosmic ray test as well as a test beam with hadrons at CERN is foreseen during 2006. Larger planes, $100 \times 50 \text{ cm}^2$ can be build for 2007.

III.D.2.j Alternative approaches: Tungsten absorber

The possibility of using Tungsten as absorber with a two radiation length ($X_0 = 7 \text{ mm}$) sampling frequency is being studied. For an overall depth of the HCAL corresponding to 4 interaction lengths at normal incidence 55 layers of Tungsten are needed. Including active gaps of 10 mm the outer radius of the HCAL is reduced to 232 cm compared to 250 cm with steel as absorber. The choice between Tungsten and Steel as absorber in the HCAL will be based on the comparison of their performance in simulation studies and on practical considerations, such as cost and mechanical feasibility.

III.D.3 Performance evaluation

III.D.3.a PFA development

The development of Particle Flow Algorithms has been pursued by a number of individuals and groups within SiD. This is a critical approach since no single algorithm or technique can be known *a priori* to be “correct”. Rather, allowing many attempts at implementing the various components of an overall PFA should eventually allow us to select the most efficient and complete final algorithm. In the following sections we present reports on PFA development from the groups at ANL, NIU, and U. Iowa. This is very much a work in progress, and it should be noted that relatively simple situations with well separated jets have been studied so far. The successful application of PFA’s to multi-jet physics processes with, for example, close-by high Pt jets will be challenging.

III.D.3.a.1 PFA development at Argonne

Introduction

Particle Flow Algorithms (PFA) achieve the best possible jet energy resolution by measuring the energy of each individual particle in a hadronic jet. In PFAs, the momenta of charged particles are measured with the tracking system, the energy of photons is measured with the EM calorimeter and the energy of neutral hadrons is measured with the combination of EM and hadron calorimeters. The momenta of charged particles (energy of photons) can be measured with high (reasonable) precision. On the other hand, the measurement of neutral hadrons is plagued by poor energy resolution. However, since neutral hadrons carry only 10% to 20% of the energy of a jet, an excellent jet energy resolution can still be achieved, provided the energy deposits of charged and neutral particles in the calorimeter can be identified as such. Under this assumption, a so-called *perfect PFA*, which uses the MC information to separate individual particles perfectly, achieves an energy resolution of ~ 2.3 GeV for di-jet events ($e^+e^- \rightarrow q\bar{q}$, $q = u, d, s$) generated at the Z-pole and using the SiDaug05 detector model. The result is shown in Figure 68. However, within PFAs the major contribution to the energy resolution originates from the wrong association of calorimeter deposits to charged and neutral particles. Therefore, when developing PFAs, the major task is to achieve the best identification of calorimeter energies originating from charged or neutral particles.

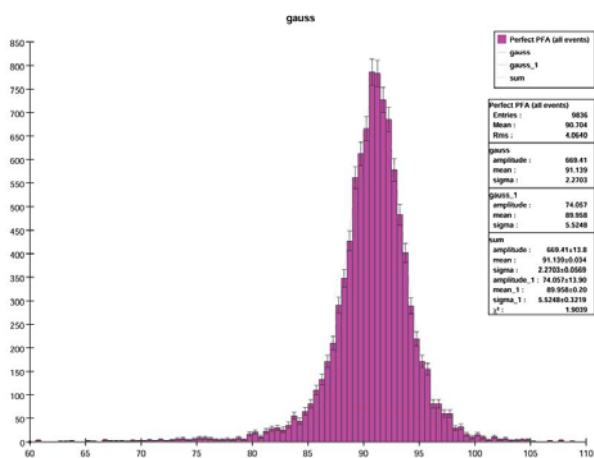


Figure 68 Perfect PFA for SIDaug05, Z-pole events

The PFA described in this section starts from calorimeter hits and uses a density driven clustering algorithm to group hits into clusters. Clusters originating from photon showers are identified first, by a photon finder (currently still missing, so MC information is used instead). Then MC charged tracks are extrapolated into the calorimeter and matched with the remaining clusters. Clusters matched to tracks are identified as originating from charged particles. In order to identify clusters originating from neutral hadrons, the unmatched clusters are further evaluated according to some geometrical variables. After these steps, the momenta of tracks, energies of photons and neutral hadrons are summed up to provide an estimate of the event energy. So far this algorithm has only been applied to di-jet events at the Z-pole. Therefore, no jet algorithm has been implemented at the moment.

Ingredients

The main ingredients of this PFA are described here. The relationship between the different parts is shown in

Figure 69. This description reflects the status of the algorithm at the time of the Boulder workshop. The program source code is available on the SLAC cvs repository.

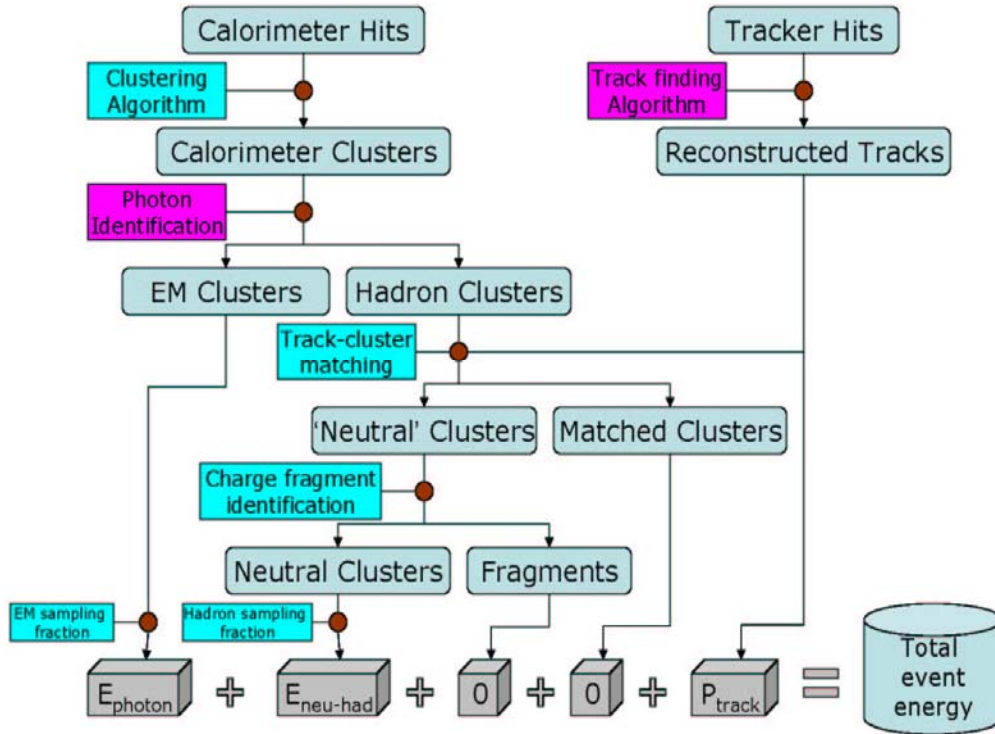


Figure 69 Ingredients of the PFA.

Sampling fraction calculation

This is a stand alone step independent of the Particle Flow Algorithms. The determination of the sampling fractions uses single particle MC samples of the SiDaug05 detector model. The MC samples include the simulation of single electrons, photons, pions, kaons, neutrons and anti-neutrons originating at the IP and impinging on the calorimeter at $\theta = 90^\circ$. The particle energies range from 2 GeV up to 50 GeV. The sampling fraction for a given particle and at a specific energy is calculated by fitting the slope of the 2D distribution of ECal raw energy vs. the HCal number of hits. Since the calorimeters show a linear response for EM showers, the sampling fractions obtained at different particle energies can be averaged and the energy of an EM shower is calculated as,

$$E_{EM}(\text{GeV}) = 82.5 \times E_{ECal,raw} + 0.11 \times N_{HCal,hit}$$

The calorimeter response for hadrons is not perfectly linear, leading to an energy dependent sampling fraction. Taking this into account, the energy of a hadron shower is calculated as,

$$E_{hadron}(\text{GeV}) = \frac{114. \times E_{ECal,raw} + 0.122 \times N_{HCal,hit}}{1 + 1.34 \times E_{ECal,raw} + 0.00122 \times N_{HCal,hit}}$$

The calorimeter response for different hadron species differs slightly. The sampling fraction shown here is calculated from the kaon sample which assumes a medium value among hadrons. It will be applied to all hadrons in later studies.

Dr. Ron Cassell pointed out an angular dependence of the calorimeter response.

(<http://nicadd.niu.edu/cdsagenda//askArchive.php?base=agenda&categ=a0589&id=a0589s1t0/transparencies>). In this PFA the angular dependence has been corrected according to the impact position of the particle onto the calorimeter.

MC particle list, track list and perfect PFA calculation

A list of MC particles is selected to represent all detectable particles in an event while minimizing double counting. In order to calculate the energy resolution with perfect particle separation (perfect PFA), all calorimeter hits are assigned to these MC particles according to their contributing particle. Using appropriate sampling fractions, the particle energy is then calculated from calorimeter hits assigned to each particle. From the MC particle list, those that passed more than 3 layers of the silicon tracker are further selected to form a list to represent measured tracks. In the perfect PFA, the event energy is calculated by summing up the momenta of all tracks and the energies of photons and neutral hadrons as measured by the calorimeter. The result is shown in Figure 68. This represents the theoretical limit for the measurement of the event energy using PFAs and a given detector model.

Clustering algorithm

All calorimeter hits are grouped into clusters to represent individual particle showers or fractions of a shower in the calorimeters. The clustering algorithm is based on a hit density calculation. Hit density of a particular hit ‘i’ is defined as the sum of contributions from each hit in a group of hits {j}:

$$D_i = \sum_{\{j \neq i\}} (e^{-\langle \vec{V}_1 \cdot \vec{R}_{ij} / |\vec{V}_1|^2 \rangle} \times e^{-\langle \vec{V}_2 \cdot \vec{R}_{ij} / |\vec{V}_2|^2 \rangle} \times e^{-\langle \vec{V}_3 \cdot \vec{R}_{ij} / |\vec{V}_3|^2 \rangle})$$

in which, V_1 , V_2 and V_3 are linearly independent vectors that start at cell i and stop at its nearest neighboring cells in the same layer (V_1 , V_2) and adjacent layers (V_3). R_{ij} is a vector that starts at cell i and stops at cell j. With this density definition the distance between cell i and j is normalized to the local cell density of cell i. To construct a cluster, the clustering algorithm first searches for a cluster seed which is defined as a hit that is not in any existing cluster and has the highest density when {j} runs over all hits in the calorimeters. Neighboring hits of the found seed are then attached to the seed to form a small cluster. A hit, which is not a direct neighbor to the seed cell, is also attached to this cluster if the cell density of that hit, when {j} runs over all hits already in the cluster, is over a threshold. The clustering for this seed is complete when no more hits can be attached to the cluster. The clustering algorithm then searches for the next seed, until all hits are uniquely assigned to a cluster.

Photon identification

After finding all clusters, a photon identification algorithm identifies clusters originating from EM showers. This part of the PFA is currently not implemented. Instead, MC information is used as a substitute. If the largest contributor of a cluster is a photon or an electron, this cluster is labeled as an EM cluster; otherwise, it is labeled as a hadron

cluster. This label is used to determine the appropriate sampling fraction when calculating the cluster energy. A real photon identification algorithm will be developed soon or will be adopted from other developers.

Track cluster matching

The trajectory of MC particles identified as charged tracks is extrapolated into the calorimeter assuming a helix. The energy lost along the path of the particle is not yet considered. The extrapolation is stopped either when the particle has traversed the entire calorimeters or when it starts to curl back. For each track, the distance between the extrapolated trajectory and each cluster is calculated. The distance is defined as the closest distance between any point on the trajectory and any hit in the cluster. If the distance is smaller than a given threshold, the track and the cluster are matched. All clusters that matched to a track are label as originating from charged particles.

Fragment identification

Those hadron clusters that don't match any tracks mainly come from neutral hadrons and detached fragments of charged hadrons. Some geometrical variables are used to evaluate these clusters in order to identify the two components. The variables are a) the distance between a cluster and its nearest neighboring track, b) the distance between a cluster and its nearest neighbor 'neutral hadron cluster' and c) the ratio of the two distances. There is no fool proof way to know which cluster originates from a neutral hadron. However, it has been shown that large clusters which don't match any tracks are very likely to be associated to neutral hadrons. So the 'neutral hadron cluster' in the above variable refers to any large enough cluster that doesn't match any track. After fragment identification, about 70% of the fragment clusters from charged particles are identified as such and the remaining clusters are labeled as neutral particles.

Performance

The performance of this PFA was studied with di-jet events $e^+e^- \rightarrow q\bar{q}$ ($q = u, d, s$) at the Z-pole using the SiDaug05 detector model.

Clustering algorithm

After clustering all calorimeter hits, 90% of the clusters have hits from exactly one MC particle. Half of the remaining 10% of the clusters have most of their hits from one MC particle and only one or two hits from other particles. The other half have merged showers from different MC particles. On average, there will be 1.2 clusters per Z-pole event that contain merged showers. Only when a cluster contain both charged and neutral particles, will it give trouble to PFA calculation which result in double counting energy (when the cluster is identified as a neutral particle) or losing energy (when the cluster is identified as a charged particle).

Track cluster matching

Most of the clusters that match a track are from charged particles. At this step, only 3% of the energy of matched clusters is from neutral hadrons. However, the remaining unmatched clusters have 55% of their energy coming from fragments of charged particles,

and only 45% from neutral particles. This shows that a fragment identification algorithm is necessary.

Fragment identification

The fragment identification algorithm removes 70% of the energy of charged fragments from clusters not matched to any track, while only 12% of the energy from neutral hadrons is misidentified as charged fragments. After this step, clusters labeled as neutral clusters have 70% of their energy coming from neutral hadrons.

Overall PFA for Z-pole events

By summing up the track momenta, the photon cluster energy and neutral hadron cluster energy, the event energy for the Z-pole sample is shown in Figure 70. There is no cut or event selection applied to this MC data sample. The distribution is fitted with two Gaussian distribution. The narrow Gaussian contains 59% of the events and has a width of 3.4 GeV, and the wider Gaussian contains 41% of the events and has a width of 10.2 GeV. Figure 71 and Figure 72 show the event energies when the data sample is divided into barrel events (60%) and endcap events (40%) according to the underlying quark direction. This PFA performs significantly better for barrel events. Compared with Figure 68, which shows the performance of a perfect PFA, this PFA is still dominated by misidentifications between charged and neutral particles. Further improvements are necessary.

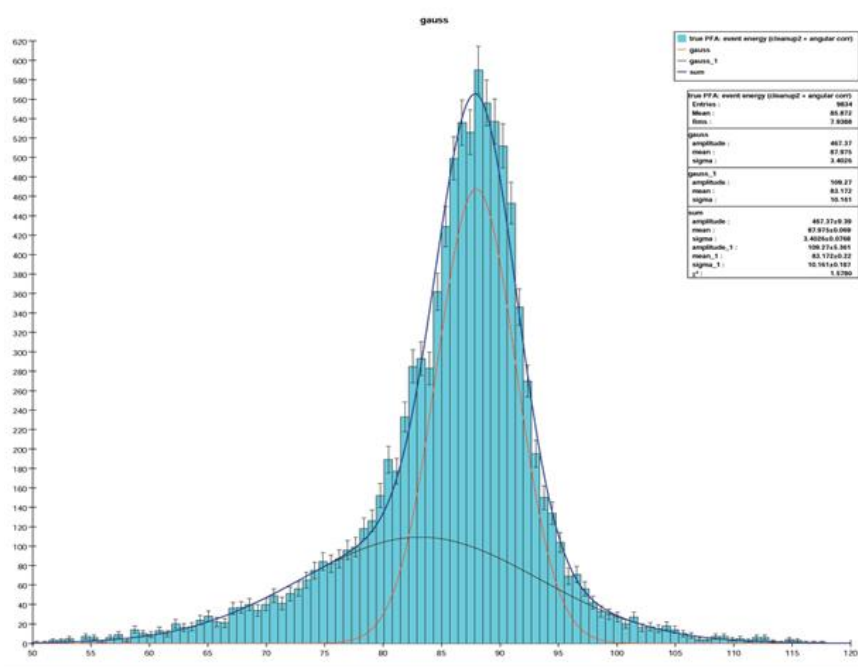


Figure 70 Event energy after applying PFA.

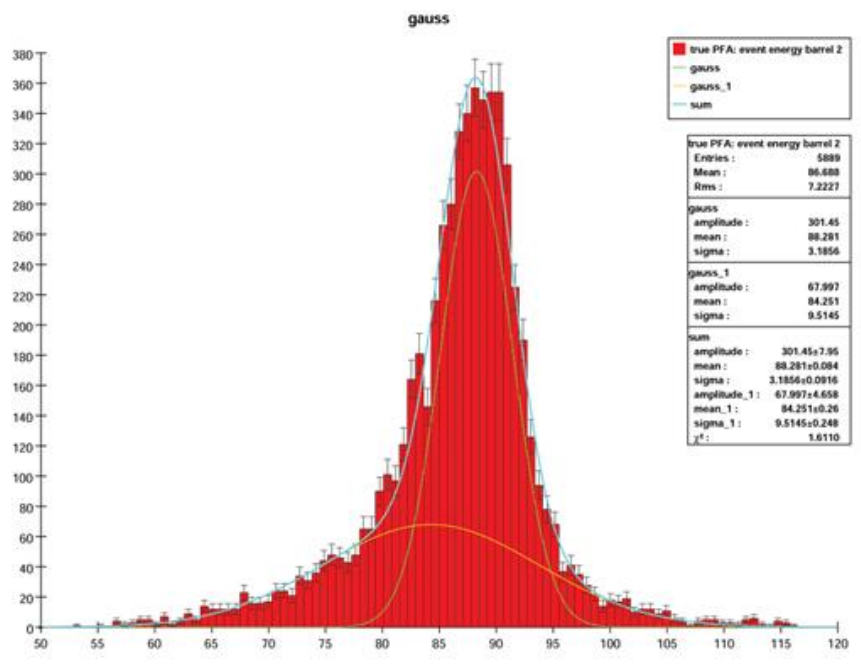


Figure 71 Event energy for barrel events.

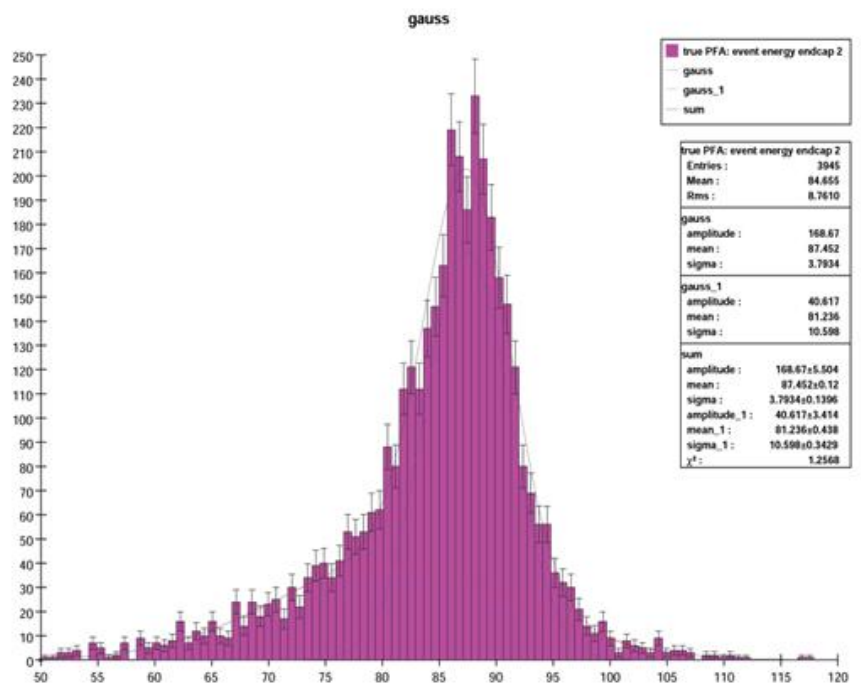


Figure 72 Event energy for endcap events.

Further work

Further developments of this PFA are foreseen in the following areas:

Common PFA template

The code will be re-written according to a common PFA template, which was proposed at the Boulder workshop. All its ingredients will be converted into modules with well defined interfaces, to facilitate the exchange and crosscheck of individual subprograms.

Missing components

All missing ingredients, like the photon identification and the jet algorithm will be implemented. Track finding will remain as is until some formally released code becomes available.

Jet energy resolution

The jet energy resolution will be studied more in greater detail and events with larger numbers of jets and at higher center-of-mass energies. In particular, the energy scale dependence of the PFA performance still needs to be established. New ideas, as they become available, will also be implemented to continuously improve the performance.

III.D.a.2 PFA Development at NIU

Introduction

The NIU group is developing a flexible “directed tree” clustering scheme as the central piece of a particle flow algorithm. The algorithm does not depend implicitly on any information outside the calorimeter (e.g. the tracker), but tracks can be used as seeds to begin the clustering process, if desired. The end product is a list of “clusters” of calorimeter hits. Each cluster is subsequently associated with at most one shower, depending on track propagation or proximity to other clusters. Typically, a shower will consist of multiple clusters, although most of its energy will be contained in one or two. The decisions made by the clustering algorithm are based on generic quantities like energy, local density of hits or energy and spatial properties like cluster shape, size, relative isolation. The parameters of the algorithm can be easily modified. For example, one can easily change the definitions for densities and distance metrics. As a result, the same algorithm, but with different parameters, can be used to reconstruct MIP stubs, EM or hadronic showers.

At a later stage, the PFA algorithm combines information from clusters and tracks (and, optionally, hits in the muon detector) to reconstruct hadronic jets.

Ingredients

The directed tree clustering algorithm consists of the following steps:
3-d neighborhoods are defined for hit clustering. Different definitions are used for EM and hadronic sections. The goal is to account for the maximum number of hits while keeping incorrect associations (a.k.a. “confusion”) to the minimum. This is not trivial, since situations vary widely with jet energy, composition, and overlap.

Generalized local density definition based on a pre-defined neighborhood around each hit. In an analog calorimeter, the energy density is available. For an intrinsically digital calorimeter, such as a gaseous HCal, hit density can be used to very good effect.

Cluster seeds, or “tree roots”, are taken to be those hits that have the highest generalized densities within their respective neighborhoods.

Hit association weights are determined between pairs of hits, using each hit's density and a generalized distance between them (for reference, $\text{weight} = (\text{jdens} - \text{idens}) / \text{distance}$).

The generalized distance can be a linear distance, an angular distance with respect to the IP (useful for radial showers) or some other distance definition which could, for instance, take into account (non-radial) shower shapes.

Non-seed hits get attached to that hit within its own neighborhood which contains the highest association weight. Ambiguities are possible at this point, specially for discrete, hit-counting based density definitions.

The critical step in optimizing the directed tree clustering algorithm is in finding the optimal association neighborhood. Small neighborhood definitions result in more clusters from a given particle shower, which will have to be properly identified by a subsequent pattern recognition algorithm. On the other hand, large neighborhood definitions promote confusion, which degrades the jet energy resolution. At the next stage, the reconstructed clusters are refined using pattern recognition algorithms, combining information from tracks and cluster shapes to merge some clusters as appropriate. Other steps in the PFA include photon identification, track propagation and matching, energy loss. Clusters are classified as arising from charged hadrons, photons or neutral hadrons. Charged clusters are replaced with very precise track momentum measurements. Neutral clusters are used for energy estimation.

Preliminary studies have shown a large number of fragments - typically small clusters separated from the cluster core - sometimes stray far from the primary cluster. A perfect association of such fragments to the right primary cluster is often impossible. On average, such hits do not carry much energy. We are trying to understand how these fragments should be treated to achieve the best possible resolution.

Our implementation of the algorithm is compatible with both projective and non-projective geometries.

Performance

We have used a PFA based on purely calorimeter-based directed-tree clustering for identification of EM and hadronic showers, replacing those associated with charged tracks (found using the Monte Carlo truth table, for the time being) with their respective momenta. The results for dijet mass resolution at the Z^0 pole is ~ 3.8 GeV, comparable to other algorithms. We expect this to improve as we tune the parameters of the algorithm, gain better understanding of sampling fractions, and of fragment association. It is not a good figure of merit for jet reconstruction. In fact, shower-to-jet association is trivial in such events with two jets in non-overlapping hemispheres. It is, however, a (optimistic) measure of the effects of fragment association and confusion in shower reconstruction. Degradation of energy resolution due to those effects will be more severe as the separation between showers decrease with increasing jet energy, and in busier events. At this point, a more direct measure of performance is the energy correctly reconstructed

in the primary shower, and the relative allocation to fragments. These are shown in the figures below, for $Z \rightarrow jj$ events at $\sqrt{s} = M_Z$. The top left panel of Figure 73 shows the angular separation (in θ_ϕ), in the EM calorimeter, between the primary cluster and the parent particle, while the bottom left panel shows that between the sum of fragments arising from the same parent, and the parent. The panels on the right show the ratio of primary cluster energy to parent energy (top) and fragment energy to parent energy (bottom). In Figure 74 same quantities are plotted for clusters in the hadron calorimeter. The nominal SiD geometry with scintillator HCal was used for these plots, but with a hit-density based clustering, that is readily applicable to RPC or GEM as well. Note that most of the fragments are close to the primary cluster, and will be associated to the correct shower. Therefore the angular separation for shower-to-parent are closer to 0 and the energy ratio closer to 1 than what is seen in the top plots.

Further work

Optimization of algorithm parameters for EM and hadronic showers, MIP stubs,
 Use of cluster direction to reduce incorrect association to shower (“confusion”),
 Precise tuning and use of sampling fractions, calibration using test-beam data,
 Full-chain PFA-based jet reconstruction for benchmark physics processes.
 Eventually, modeling of jet energy resolution for parametrized (fast) simulation of very large number of physics events to cover large volumes of parameter space in SUSY and other scenarios beyond the Standard Model.

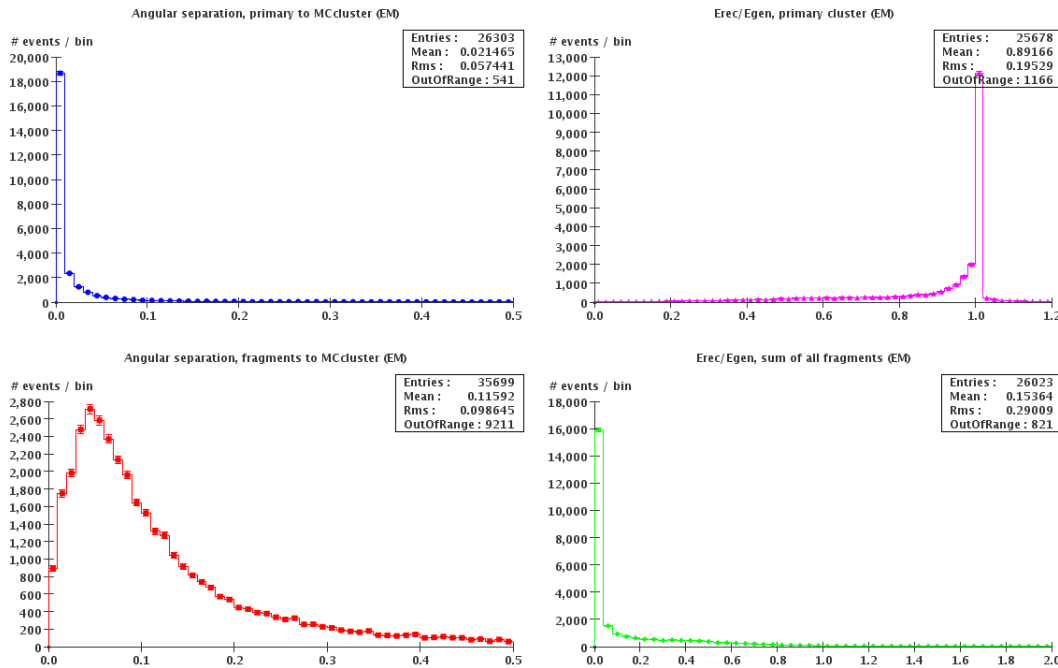


Figure 73 Results of directed tree clustering in the EM calorimeter. Left: The angular separation between the primary cluster and the parent particle (top) and that between the fragments and their parent (bottom). Right: the reconstructed energy-to-parent energy ratio for the primary cluster (top) and that for the sum of all fragments (bottom).

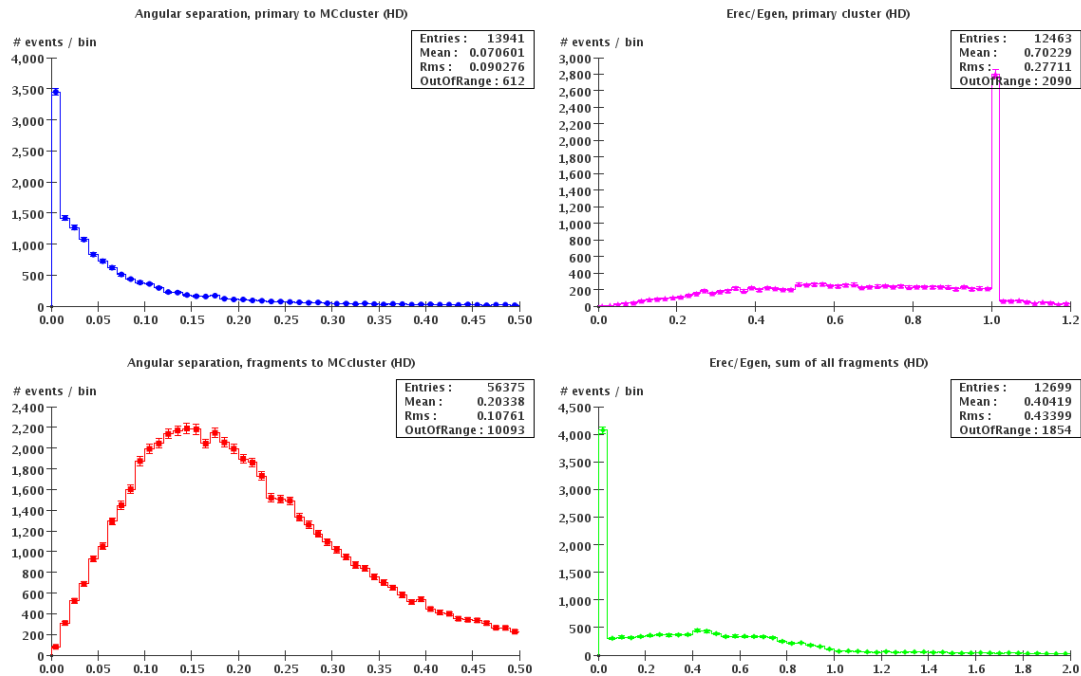


Figure 74 Results of directed tree clustering in the hadron calorimeter. Left: The angular separation between the primary cluster and the parent particle (top) and that between the fragments and their parent (bottom). Right: the reconstructed energy-to-parent energy ratio for the primary cluster (top) and that for the sum of all fragments (bottom).

III.D.3.a.3 PFA Development at U. Iowa

The goal of a Particle Flow Algorithm is to reconstruct physics events on the level of individual particles, identifying and separating charged and neutral energy deposits in the calorimeters so that the energy of each can be measured in the most precise way with minimal confusion. This is a complex process with many steps. The focus of the Iowa group has been on what we perceive to be the biggest challenge: reconstruction of clusters in the calorimeters.

Hadronic and electro-magnetic showers behave very differently, and with the fine granularity of the SiD detector these differences have a strong impact on the reconstruction. Electromagnetic showers are well-contained, consisting of a dense, almost needle-like longitudinal core plus a halo of nearby hits. Hadronic showers, by contrast, have clear internal structure and often produce secondary neutral particles which deposit energy far from the main cluster. To take these differences into account, we presented two separate clustering algorithms at Snowmass 2005 for electromagnetic and hadronic showers. Since then, work has focused on developing a full PFA around these clustering algorithms and understanding their shortcomings.

Ingredients

The PFA is under development and still changing. In particular, the results discussed below are taken from the last stable version of the PFA (presented at Boulder) and are now a little outdated with respect to the code. The following is a reasonable snapshot of the current status:

Prepare: Identify an internally consistent set of Monte Carlo (MC) particles. Run DigiSim and set up HitMaps from the output.

Find tracks: Currently, these are taken from the fast MC simulation.

Find MIPs and track segments: The `org.lcsim.recon.cluster.mipfinder` algorithm is used to find track segments in the calorimeters. Their hits are removed from the HitMaps.

Find EM showers; identify photons and electrons: The results presented at Boulder did not use a dedicated EM shower algorithm, instead treating photon and electron showers as generic clumps (see below). This step is now being added to the algorithm. In addition to cheating, there are multiple algorithms proposed for reconstructing EM showers (fixed cone, nearest neighbor, and the MST-based algorithm presented by Niels Meyer at Snowmass). The hits assigned to electromagnetic showers are then removed from the HitMaps.

Find clumps: Hadronic showers typically contain one or more dense clumps of hits following a hard interaction. These are reconstructed with a nearest neighbor clustering algorithm, `org.lcsim.recon.cluster.clumpfinder`. Hits are required (i) not to be assigned to a track segment or EM shower, and (ii) to have a local hit density of at least 7/75 in the surrounding 5 x 5 x 3 block of hits. Clumps are required to have at least 6 such hits in a contiguous block. Their hits are then removed from the HitMaps.

Find large-scale hadronic clusters with the MST: The track segments, clumps, and remaining hits in the HitMap are clustered with an MST algorithm (`org.lcsim.recon.cluster.mst`) to form large-scale hadronic clusters.

Use structural clustering algorithm with likelihood selector: The MST algorithm used in the previous step is efficient at finding entire contiguous clusters, but may have inadvertently merged together multiple showers if they passed close to one another or overlapped. In this step, the clumps and track segments within the clusters are identified and a likelihood-based selector is used on each pairing to decide whether they are genuinely linked. If the cluster can be broken down into disjoint sub-clusters, this is done.

Assign tracks: Tracks found previously in the tracking system are extrapolated as helices to the inner surface of the ECAL. If there is a nearby track segment cluster with a compatible direction, the two are paired. If not, the algorithm looks for any nearby cluster—if one is found, the track is paired with it; if not, the track is ignored.

Identify and merge fragments: Hadronic showers often produce secondary neutral particles which can travel significant distances before interacting with the detector material. The small, displaced clusters that result are referred to as fragments. These must be identified to distinguish them from primary neutral particles. Currently, this is done with a cut-based selector which checks (i) whether the cluster has an associated track; (ii) the number of hits in the cluster; and (iii) whether the principal axis of the cluster points towards the interaction point (if there are enough hits to calculate this). If a cluster is identified as a fragment, it is simply assigned to the nearest non-fragment cluster. An alternative strategy in which fragments are discarded has also been used.

Assign masses and energies: In principle, then entire shower has now been reconstructed and matched with its track (if any). A Reconstructed-Particle is formed from this information and assigned a mass and energy. Currently, the mass is taken from truth information.

Compensate for missing energy: In addition to the particles reconstructed through the procedure above, there are often further particles which were generated but deposited no

energy in the electromagnetic and hadronic calorimeters. These include neutrinos, particles at small angles to the beam, and neutral hadrons which passed through the calorimeters without decaying or interacting. The list of MC particles produced earlier is searched for these cases using truth information; when they are found, the event energy sum is corrected accordingly.

Determine confusion PDFs: One major source of jet energy resolution is the intrinsic resolution of the calorimeters; another is the confusion between charged and neutral energy deposits. The fraction of energy incorrectly assigned in the event is recorded. This is done separately for the ECAL and HCAL, and also for charged and neutral particles. (The special case of a charged particle whose track is not found is also considered). Integrated over many events, these distributions give the probability density functions for the amount of confusion.

Performance

When the PFA was run without cheating, the confusion distributions shown in Figure 75 were obtained. These illustrate that the bulk of the energy deposited in the calorimeters is identified correctly (charged as charged, and neutral as neutral)—but that there is a substantial tail for charged energy deposits in the HCAL which are misidentified as neutral energy. This is mainly due to secondary neutral particles from charged showers with an associated track which are incorrectly identified as primary neutral particles, or which are correctly identified as fragments but incorrectly assigned to a nearby neutral cluster¹.

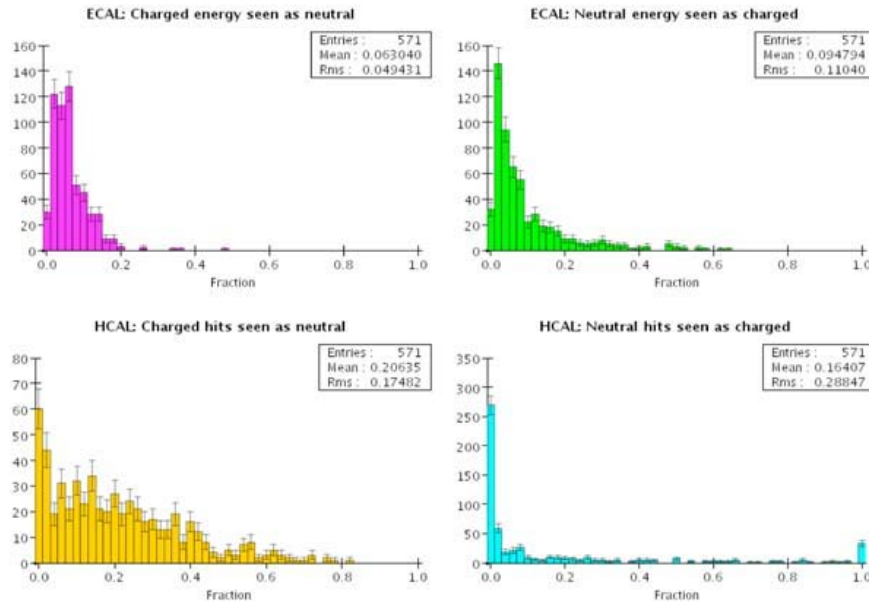


Figure 75 Confusion distributions for hadronic Z-pole events in the sidaug05 detector. For each event, the fraction of charged energy incorrectly identified as neutral (and vice versa) is measured in the ECAL. The same distributions are shown for the HCAL using the fraction of hits instead of energy.

¹ Pathologically, the nearby “neutral” cluster may itself be a misidentified charge fragment.

The most important experimental sources of jet energy resolution are expected to be the confusion between charged and neutral energy, and the intrinsic resolution of the detector elements. Taking the typical composition by energy of Z-pole events to be 70% charged particles (with negligible resolution), 22% photons (with $20\%/ \sqrt{E}$ resolution), and 8% neutral hadrons (with $68\%/ \sqrt{E}$ resolution), we can use the confusion functions to predict the jet energy resolution. This was found to be $49\%/ \sqrt{E}$ for the confusion distributions of Figure 1, which were produced without cheating. If cheating is used for the fragment identification and assignment steps but not for the rest of the algorithm (clustering, track-matching, etc.), this improves to $31\%/ \sqrt{E}$. For comparison, the energy resolution would be $21\%/ \sqrt{E}$ with perfect pattern recognition. Clearly, the handling of fragments is the main—though not the only—obstacle to achieving a jet energy resolution of $30\%/ \sqrt{E}$ with an algorithm of this form.

A note of caution: These results neglect other effects such as imperfect calibration and particles which are not reconstructed which will make the resolution worse in practice.

III.D.3.a.4 Further work

Presently, work is underway to convert the algorithm to the new PFA coding framework which was agreed upon at Boulder. This will standardize the design and make exchange of code among collaborators vastly easier. This should be completed soon.

The main challenge is the identification and assignment of fragments. A number of approaches are being considered here, including use of a likelihood-based selector in place of a cut-based selector for identification, and use of additional geometrical information beyond 3D proximity (e.g. the Argonne group has shown that the transverse distance to the nearest extrapolated track helix is a good discriminant). A different approach in which fragments are ignored entirely and the energy calibration of the main cluster is adjusted to compensate will also be studied for feasibility.

III.D.4 Calorimeter R&D program

III.D.4.a For the ECAL

The ECal R&D is advancing on several fronts. The highest priority near-term goal is to demonstrate the viability of the highly integrated design discussed in Section IIID1 above. This has included procurement of silicon detectors as described above, developing and fabricating the KPiX readout chip, and developing the electromechanical design consistent with small readout gaps, passive thermal management, and efficient data flow. We anticipate preparing a few layers for technical tests using cosmic rays and test beam in 2006, each layer consisting of one (15 cm wide) detector and one bump-bonded KPiX chip. At this stage, prototype KPiX chips, with limited channel count, may be used.

These technical tests are to be followed closely by the fabrication of a full-depth (30 layers) ECal module which can be evaluated in a test beam. Initially, the aim would be to

fully characterize the electromagnetic response and resolution. We anticipate that this response will be well modeled by existing EGS4 or GEANT4 codes.

As discussed in the next section, a key element of the SiD R&D program is that of testing the response of our finely segmented calorimetry to hadrons in order to have confidence in our ability to optimize the global design. Acquiring the ability to model this response can only be gained by a beam test. This is crucial for the HCal development, but since the ECal consists of about one interaction length of material, it is also essential to understand the response of the combined systems in a beam of hadrons. Hence, following the characterization of the electromagnetic response, the full-depth module will be combined with the HCal module(s) in a hadron beamline.

The overall mechanical design will continue in parallel. We anticipate incorporating some aspects of the developing mechanical design for the full-depth module fabrication. In particular, the module will include the means by which the mechanical definition of the readout gaps is determined, but with a minimal footprint and interference with the sensors.

While the cost of silicon detectors continues to decline, we anticipate that it will remain a crucial issue for this design. We have chosen a particularly simple, DC-coupled design in our prototype silicon detectors, with which our electronics design is fully compatible. A simple design means keeping the number of fabrication steps to a minimum. We will continue to pursue various fabrication and vendor options.

III.D.4.b For the HCal

The immediate goal is to build a prototype section of a HCal with very fine segmentation of the readout. The section will be instrumented in turn with scintillator (CALICE-AHCal effort), RPCs (CALICE-DHCal effort) and GEMs (CALICE-DHCal effort). The major reasons for constructing a prototype section of the HCal and subsequent tests in particle beams are summarized in the following:

Test of a calorimeter with RPCs and GEMs: even though RPCs and GEMs have been employed in a large number of HEP experiments, to date no calorimeter with finely segmented readout using RPCs or GEMs as active medium has been built and tested. These tests will validate the use of these devices in calorimetry.

Tests of the novel idea of single-bit readout: in simulation studies of single hadrons the resolution obtained with single-bit readout is comparable to the results obtained with multi-bit readout. Experimental verification of this and validation of the concept of a so-called Digital HCal is needed.

Study of design parameters: measurements with different configurations of the prototype section will provide a better understanding of the dependence of the response on the various design parameters, such as the choice of absorber, the size of the active gap, the segmentation of the readout, etc.

Measurement of hadronic showers: traditional calorimeters measure energy with a coarse segmentation, thus integrating over large volumes. Our HCal prototype section will

measure hadronic showers with unprecedented spatial resolution and provide very detailed information on hadronic showers.

Validation of Monte Carlo simulation of hadronic showers: the measurements obtained in particle beams will be essential to validate the Monte Carlo simulation of hadronic showers. To date differences of up to 60% are observed when comparing the results on shower shapes based on different MC models of the hadronic shower, see Figure 1. The design of a detector for the International Linear Collider is driven by the application of Particle Flow Algorithms for the measurement of hadronic jets. A realistic simulation of hadronic showers is a prerequisite for the development of a reliable design of such a detector.

Comparison of the different active media: comparison of the performance of the scintillator based and gaseous active media will provide the basis for a technology choice for the HCAL of the ILC detector.

In addition to the construction of and tests with the prototype section of the HCAL, further R&D is needed on the development of the three active media:

R&D on RPCs

The following areas will benefit from additional R&D:

Development of thinner chambers. The current design uses two glass plates enclosing the gas volume. The overall thickness of the chamber, excluding the readout board and the front-end electronics is about 4.5 mm. Chambers using a single glass plate together with the front-end readout board to enclose the gas volume reduce the thickness to about 3.2 mm. Further R&D on this type of chamber is needed to ensure its robustness and longevity.

Higher multiplexing at the front-end. The current ASIC is connected to 64 readout pads. Further R&D is needed to increase the number of channels connected to a single ASIC. Particular care needs to be devoted to the routing of the signal lines in the readout board and the cross-talk from digital lines onto the analog input.

Reduction of the thickness of the front-end ASIC. The thickness of the current ASIC is about 1.5 mm. Using different approaches, such as non-packaged ASICs, will reduce the thickness of the electronics located in the active gap and, therefore, the overall depths of the calorimeter.

Higher multiplexing at the data concentrator level. Currently 12 ASICs are read out by one data concentrator board. Using different technologies, such as token rings, the number of ASICs connected to a data concentrator board can be significantly increased, thus reducing the overall cost of the electronic readout system.

R&D on GEMs

In 2006 we will expose the five 30cm x 30cm chambers to beams in Korea and at Fermilab. We will repeat the measurements of efficiency, hit multiplicity, signal sharing, and gain operational experience with these chambers. We expect to have the first 1m x 30cm foils in Fall 2006. These will be tested and then used to build full-size GEM planes

for exposure in the test beam at Fermilab, as a precursor to building and testing a full 1m^3 stack of GEM-based hadron calorimetry in 2007-8.

R&D on Scintillator

We are currently addressing issues of mechanical and electronic engineering (in collaboration with Fermilab), large-scale production and assembly, and calibration. Each scintillator cell and on-board SiPM is a rugged self-supporting unit permitting maximum flexibility in the mechanical design. Detailed engineering remains to be done, but we don't expect a major conflict with any configuration, particularly in the barrel region. We are collaborating with engineers at Fermilab to integrate the unit cell with a readout board carrying signal, bias, and monitoring traces. After ScSiPM read out board integration has been prototyped and beam tested we will begin development of read out board ASICs for data concentration. . If we opt for the analog option, it may be possible to combine the readout chain with the electromagnetic calorimeter, which will result in considerable simplification.

For large scale production, the favored solution is to produce extrusion-based tiles or injection-molded tiles containing a few hundred to perhaps thousand cells. There's an interesting idea of doing away with the fiber by pressing the board-mounted SiPMs directly onto a scintillator tile. This would afford great simplification, but is contingent upon improvements in SiPM technology. Intense commercial R&D is underway to build economical blue-sensitive SiPMs with larger area ($5\text{mm} \times 5\text{mm}$ or larger) and lower noise per unit area. This may also allow us to construct smaller cells, should funds become available to take advantage of the modest benefit.

Calibration methods also require R&D. SiPMs can be auto-calibrated using the separation between the single photoelectron peaks. LED may be used for the scintillator and fiber assembly in beam tests. Use of radioactive source is also a possibility.

III.E Forward Detector

The forward region is defined as polar angles $\cos\theta > 0.99$ ($\theta < 140\text{mrad}$) forward of the SiD Endcap ECAL. The physics mission in this region is a precision measurement of the luminosity normalization using forward Bhabha pairs (LumCal), the beam-strahlung gammas and pairs (GamCal and BeamCal, respectively) to measure the instantaneous luminosity, and finally to extend the calorimeter hermeticity into the very forward region for physics searches. The detector challenges are good energy resolution, radiation hardness, interfacing with the final focus elements, high occupancy rate requiring special readout, and performing the physics measurements in the presence of the very high background in the forward direction. Two final focus beam crossing options are being discussed for the ILC: small angles, ie. less than 2mrad , and large angles: $14 - 20\text{mrad}$. The machine issues are more challenging for the small angle crossing, while the detector issues are a bit more challenging for the large angle crossing. For this section we integrated our very forward region with the 14mrad crossing angle 0.5TeV final focus conceptual design with the DiD at -0.02T .

III.E.1 Detector Hermeticity with the BeamCal/LumCal

In this section we discuss the BeamCal/LumCal hermeticity requirement. By hermeticity we mean an accurate measurement of the transverse momentum (P_T) balance in the event, which is achieved by: good energy resolution, avoiding cracks, dead areas, and by covering down to small polar angles. The measurement of $e^+e^- \rightarrow$ slepton pairs in the presence of the two photon background has been given as the performance detector design criteria for hermeticity. Figure 76 shows the maximum missing P_T for

$$e^+e^- \rightarrow \tilde{\mu}\tilde{\mu} \rightarrow \mu^+\chi^0\mu^-\chi^0$$

where the χ^0 is the LSP and escapes the detector. The maximum missing P_T plots for the selectron and stau decay products look very similar. From this plot, assuming a smuon mass of 200 GeV/c^2 , and an LSP mass of 150 GeV/c^2 , for example, then the maximum missing P_T is 130 GeV/c , and the measurement is relatively easy. However, as the LSP mass approaches the slepton mass, the missing P_T is less and the measurements become more difficult. The design philosophy now is to do as well as possible, while we eagerly await physics results² from the LHC.

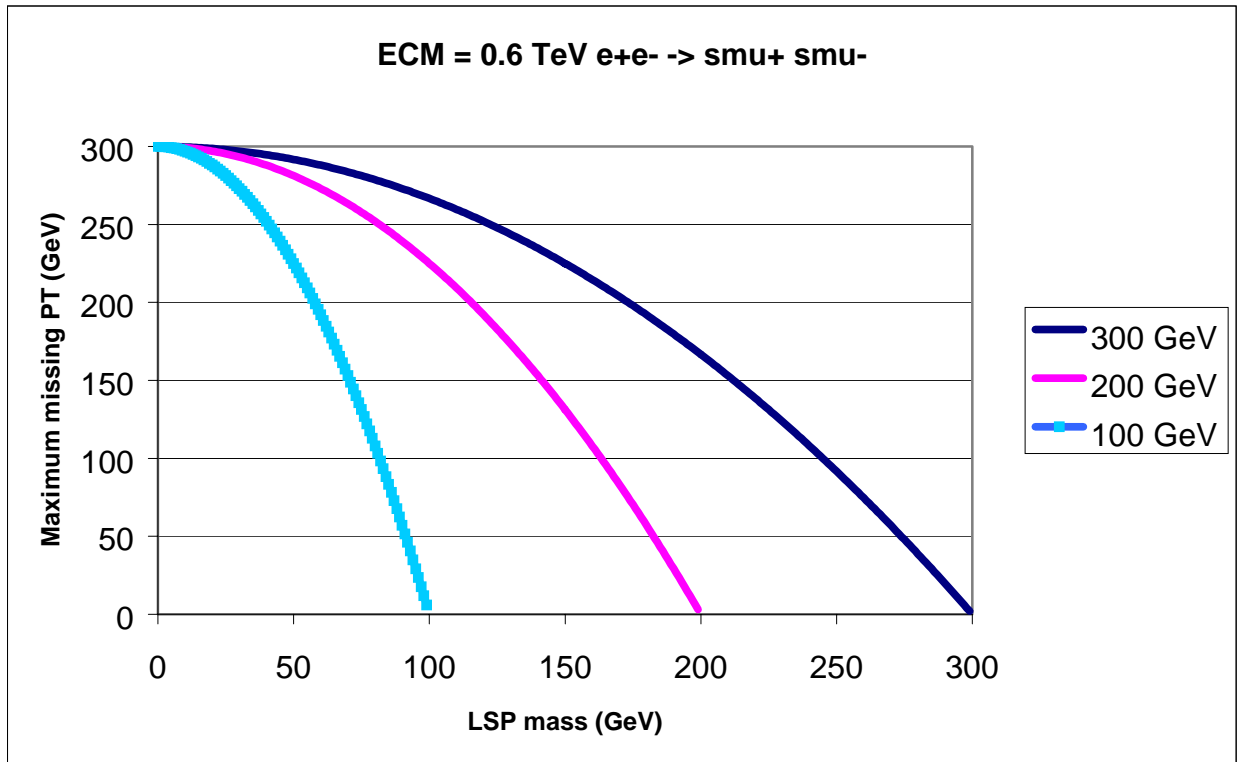


Figure 76 Maximum missing P_T as a function of the LSP mass for smuon masses: 100, 200, and 300 GeV/c^2 . The beam energy is 300 GeV ($\sqrt{s} = 600 \text{ GeV}$).

² LHC-LC Study Group, "Physics Interplay of the LHC and the ILC", hep-ph/0410364, 2004.

The main background comes from the two photon process $e^+e^- \rightarrow e^+e^- X$, where X is ee , $\mu\mu$, or $\tau\tau$ for the slepton search. This background process has no missing P_T ; however, if we miss both electrons then the missing $P_T \leq 2\theta_{\min} E_{beam}$. This is the kinematic limit. Generally one photon is on-shell, so usually the missing $P_T \leq \theta_{\min} E_{beam}$. Others³ have studied a detector which covers down to 3 mrad with a challenging scenario which assumed a lightest slepton mass of 217 GeV and the LSP mass of 212 GeV. They found a slepton-LSP mass difference resolution of 0.54 GeV, which gave an excellent 7% uncertainty on the cosmological dark matter density. Thus we can tell whether the LSP can explain all the dark matter, or if axions, for example, are also necessary. For a finite crossing angle, there is a hole in the veto, but by making a cut on the missing transverse momentum which points to the hole they found a 25% loss of efficiency for the signal, with negligible increase in background. One can't go much below ≈ 3 mrad, as the rate of false vetoes due to Bhabha events where only one electron is detected becomes prohibitive. We plan detailed simulations of how well the hermeticity requirement is satisfied in the presence of Bhabhas and beam-strahlung pairs, since the veto efficiency requirement on a high energy electron is 99.9%.

III.E.2 Monitoring the Instantaneous Luminosity with BeamCal and GamCal

The colliding electron and positron bunches at the ILC experience intense electromagnetic fields as they pass each other. These fields generate large Lorentz forces, which cause radiation of gammas called beam-strahlung. A small fraction of the beam-strahlung gammas convert into pairs. Others⁴ have studied how measurements of the pairs can be used as a bunch diagnostic tool. The beam-strahlung gammas go down the beam-line into a water beam-dump ≈ 100 m away. The Cerenkov light could be collected and directed to a GamCal detector, for example. We have found that the optimum quantity to optimize the instantaneous luminosity is the energy in the BeamCal divided by the energy in the GamCal. Briefly, this is because when the bunches overlap, the electric fields cancel, while the magnetic fields add. However, when the bunches miss each other by an amount small compared to the bunch width, both the electric and magnetic fields contribute, which gives the maximum gamma beam-strahlung, but effectively no pairs, because the gammas do not convert. Thus the energy in the pairs and the energy in the gammas give complementary information, with the ratio being effectively proportional to the instantaneous luminosity. The BeamCal and GamCal results should be available within $1\mu\text{s}$ for feed-back to the accelerator control system.

The BeamCal is a highly segmented electromagnetic calorimeter just before the final focus quadrupole magnets which covers the region 3mrad to 20mrad. The BeamCal

³ P. Bambade et al., "Experimental Implications for a Linear Collider of the SUSY Dark Matter Scenario", hep-ph/10406010, 2004.

⁴ Achim Stahl, "Diagnostics of Colliding Bunches from Pair Production and Beam-strahlung at the IP", LC-DET-2005-003.

intercepts $\approx 2 \times 10^4$ beam-strahlung electrons and positrons of average energy ≈ 1 GeV per beam crossing when the bunches have maximum overlap. This is obviously enough for instantaneous luminosity monitoring, as our goal is at the ten percent level per beam crossing.

Table 8 BeamCal and LumCal parameters.

Calorimeter	Polar angle	Average Energy/BX
BeamCal	3-20 mrad	$\approx 2 \times 10^4$ GeV
LumCal	20-140 mrad	≈ 10 GeV

One issue is the low energy electron and positron albedo from the BeamCal which is directed back to the vertex detector by the solenoid field lines. A previous study found that 10cm of Be in front of the BeamCal reduced this albedo by more than an order of magnitude, since the albedo electrons and positrons are typically very low energy and stop in the Be absorber. We plan to study this, including the effect of the anti-solenoid magnetic field in the final focus region.

III.E.3 LumCal Physics Requirements

We discuss first the Bhabha scattering specification, and then the hermeticity requirements. The lowest order Bhabha cross-section for t channel one photon exchange is given by:

$$\frac{d\sigma}{d\Omega} = \frac{\alpha^2}{8E^2} \left(\frac{1 + \cos^2 \theta / 2}{\sin^4 \theta / 2} \right)$$

We use this simple formula to estimate the polar angle coverage needed, although, obviously, the complete electro-weak s and t channel cross-section will later be needed in order to do the physics. The number of Bhabha events per bunch crossing for a detector with minimum and maximum polar angle coverage θ_{\min} and θ_{\max} (in mrad) is:

$$N = 0.5 pb \frac{L}{R} \int_{\theta_{\min}}^{\theta_{\max}} \frac{d \cos \theta}{\sin^4 \frac{\theta}{2}} \approx 8 \left(\frac{1}{\theta_{\min}^2} - \frac{1}{\theta_{\max}^2} \right)$$

for $\sqrt{s} = 0.5$ TeV, $L = 3 \times 10^{34}$ cm⁻²s⁻¹, and bunch crossing rate $R = 1.4 \times 10^4$ s⁻¹. Our goal is to measure the luminosity normalization with an accuracy of 10^{-4} for the Giga Z option ($\sqrt{s} = 0.09$ TeV), and several 10^{-4} for $\sqrt{s} = 0.5$ TeV. To do this one needs $\approx 10^8$ events collected over $\approx 10^7$ s, or about ten events per second. One can then calculate the absolute luminosity with $\approx 10\%$ statistical error every several minutes during the run, which will be very useful. With a bunch crossing rate of 1.4×10^4 s⁻¹, we need $>10^{-3}$ events per bunch

crossing. Measurement of the luminosity weighted E_{cm} is discussed later (see $e^+e^- \rightarrow \mu^+\mu^- (\gamma)$ section).

To achieve this statistical accuracy, we start the fiducial region for the precision luminosity measurement well away from the edge at $\theta_{\text{min}} = 20\text{mrad}$, with a fiducial region beginning at $\approx 30\text{mrad}$, which gives $\approx 10^{-2}$ events per bunch crossing in the fiducial region. We need to know the polar angle with respect to the IP to 10^{-4} , ie. the radial distance from the beam center and the distance to the IP. The distance to the IP is $L_{IP} \approx 3\text{m}$, so we need to know the average $dL_{IP} < 0.3\text{mm}$. This is not a problem with standard survey techniques with the vertex information. Also, since we have two detectors in coincidence with distance between them of $2L_{IP}$, the average L_{IP} is insensitive to small shifts in the z coordinate of the IP, to first order. The radial distance to the center of the beam is more challenging. This is our plan: the circumference through the center of the sensors at the beginning of the fiducial region will be accurately measured, as well as the end. The circumference at 30mrad $2\pi R_{\text{fid}}$ is $\approx 56\text{cm}$, so it needs to be measured to better than 0.05mm . We will know from the data whether the LumCal is centered on the beam center: offline we will make the beginning of the fiducial region so that the data is azimuthally symmetric. We need to understand the higher order effects (ISR, etc.) to high precision, so we want reasonable energy resolution in order to compare the $(E_+ + E_-)$ and missing transverse momentum distributions with that expected from ISR, etc. To achieve our goal, the Bhabha background and Bhabha efficiency must be understood at the 10^{-4} level for the Giga Z ($L = 5 \times 10^{33} \text{ cm}^{-2} \text{ s}^{-1}$ at $\sqrt{s} = 0.09 \text{ TeV}$) option and several times 10^{-4} level for the $\sqrt{s} = 0.5 \text{ TeV}$ option.

In order to maintain the excellent SiD detector hermeticity, the LumCal is split into a “near LumCal” contiguous with the EndCap ECAL, and a “far LumCal” contiguous with the BeamCal. The issue becomes how well we maintain hermeticity at the boundary. We plan to simulate this in the future. The precision luminosity measurement will be done separately in the “near LumCal” and “far LumCal” with fiducial cuts well away from the boundaries.

III.E.4 Occupancy Issues in the Forward Direction

The issue here is how “deep” we need to make the readout buffer to hold one train of events for the LumCal (the BeamCal has to be read out every bunch crossing for feedback). One train is $\approx 3 \times 10^3$ bunch crossings. The largest physics process cross-section in the forward direction is Bhabha pairs, which go as the inverse of the polar angle to the third power in the very forward direction: $d\sigma/d\theta \propto d\theta/\theta^3$. Figure 77 shows the mean number occupancy per pixel per train from Bhabha pairs vs. polar angle. For this calculation we assumed that a Bhabha electron ($\approx 250 \text{ GeV}$) puts energy above threshold within a radius of 2cm , and estimated the radiative Bhabha events also. We plan for a threshold for the LumCal of $\approx 0.25 \text{ mip}$ in order to maintain the ability to tag muons, although we still need to study the efficiency for muons in the high rate forward environment. From Figure 77, around 30 mrad , which is the beginning of the LumCal fiducial region, each pixel has energy above threshold from one Bhabha event per train, on average. In order to keep the loss to less than one event in 10^4 , we then need the “train buffer” to be at least seven deep to contain just the Bhabha events. Background events are

discussed below. This can be compared to the central ECAL region, where one is planning the readout buffer to be only four deep. The break at 44mrad is going from the far LumCal ($L_{IP} \approx 3.3m$) to the near LumCal ($L_{IP} \approx 2m$).

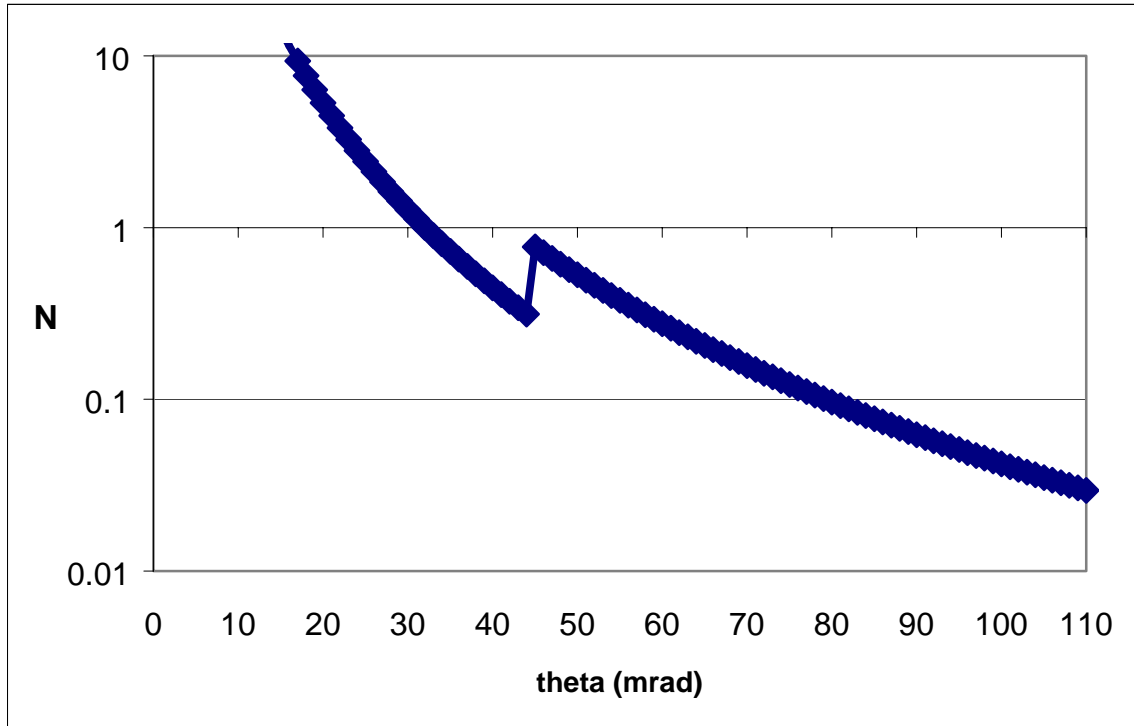


Figure 77 The mean number occupancy per pixel per train from Bhabha pairs versus polar angle.

The largest non-physics background in the forward direction is, of course, beam-strahlung pairs. They are produced in the forward direction, but are in a very large horizontal magnetic field up to 0.6 KT due to the colliding bunches, which bends them in the vertical direction. In the impulse approximation, the maximum P_T is about $0.1\text{ GeV}/c$. Luckily, they are focused by the $5T$ solenoid field:

$$P_T = 0.3BR$$

The maximum radius of the betatron oscillation is then about 7 cm .

$$x = R - R \cos \omega_c t$$

$$y = R \sin \omega_c t$$

$$\omega_c t = \frac{1.76 \times 10^{11} \text{ rad}}{\gamma} \frac{5T \times L_{IP} (m)}{3 \times 10^8 \text{ m/s}} = \frac{(1.5 \text{ rad}) \times L_{IP} (m)}{E(\text{GeV})}$$

Figure 78 shows the maximum betatron oscillation amplitude vs. electron energy at $L_{IP} = 2m$ from a simple analytical calculation. This is in reasonable agreement with a

simulation ⁵, which shows a sharp edge at 5cm for a 3T field at $L_{IP} = 2.1m$, and 4cm for a 4T field. Beyond this the simulation shows a long tail at the 10^{-3} level, which, presumably, is due to scattering in vacuum chamber walls, etc. We plan a complete simulation in the future.

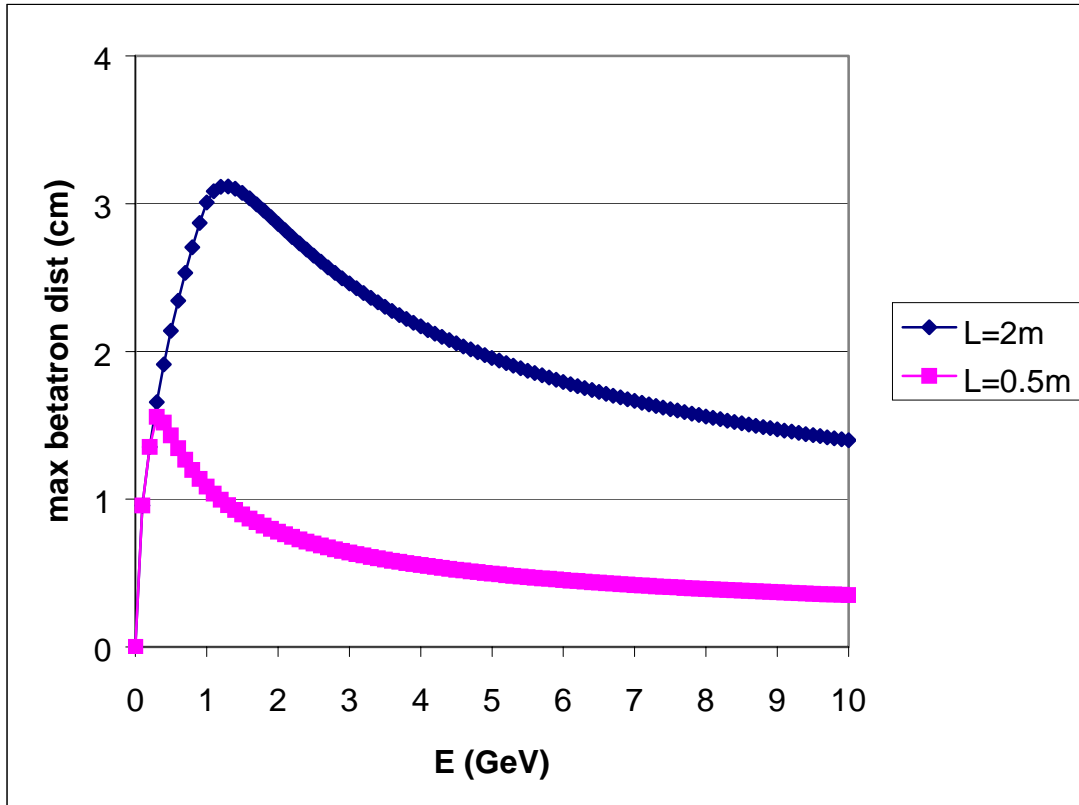


Figure 78 Maximum betatron amplitude (cm) of e^+/e^- vs. e^+/e^- energy at $L_{IP} = 2m$ and $0.5m$ from a simple analytical calculation.

III.E.5 Radiation Damage Issues in the Forward Direction

The dose in the BeamCal from the beam-strahlung pairs is 10^7 Gy/year. This is at the inner edge. At the outer edge it is three orders of magnitude lower, ie. 10^4 Gy/year. The main source of neutrons is from photons in the energy range 5-30 MeV, which excite the giant nuclear dipole resonance. The rate of neutron production from a 7 GeV electron incident on an infinite block of copper has been calculated to be 1.2 neutrons, 0.8 neutrons (iron), and 0.4 neutrons (aluminum)⁶. The pair intensity in one $0.5cm \times 0.5cm$ BeamCal detector segment is ≈ 0.5 TeV per beam crossing. The number of neutrons produced in one $0.5cm \times 0.5cm$ BeamCal detector segment per year is then approximately:

⁵ C. Hensel, "Beam Induced Background at a Tesla Detector", LC-DET-2000-00155

⁶ P. Job and J. Alderman, "Neutron Fluence Estimates Inside the APS Storage Ring", LS-294, 2002.

$$\frac{500 \text{ GeV}}{7 \text{ GeV}} \frac{1.2n}{0.5 \text{ cm} \times 0.5 \text{ cm}} (1.4 \times 10^4 \text{ s}^{-1}) 10^7 \text{ s} = 5 \times 10^{13} \text{ n/cm}^2$$

We have estimated the electromagnetic shower part of the radiation damage from data obtained with a cobalt 60 source, which is the reason we must separately estimate the radiation damage from the neutrons⁷. We have estimated the neutron radiation damage from data taken at a Van der Graaf accelerator. We plan to do a full simulation in the future. The radiation damage from protons, pions, kaons, etc. is negligible compared to that from the pairs.

We have identified two radiationhard candidates: FZ (Float Zone) n-type Si wafers, and MCZ (Magnetic Chocoski Zone) Si wafers which look promising for the BeamCal, and plan further studies. They may have to be cooled to below zero C to control the annealing process.

III.E.6 Space, Support and Integration Issues

The Beam and Luminosity calorimeters are located in front of the Q0 magnet. The back face of the calorimeter is at about 3.3m from the IP (see Figure 79). The front face of the calorimeter will be determined by the optimization of the number of radiation lengths needed and the effective density that we can reach. We assume that we will need of order 25 radiation length and the length of the calorimeter will be of order 25 cm. In addition to the BeamCal and the Far LumCal, the support tube has to support the Near LumCal. The Near LumCal has both an EM and a Hadronic section. All these calorimeters will have to be supported off the forward support tube. The services (readout cables, power etc) need to be channeled along the inner diameter of the support tube and have to be cleared for the opening scenario. All these questions will need to be answered by detailed integration engineering studies of the forward section.

The integration of the calorimeters and their services is a complex engineering task that needs to be understood in detail. The aim to maximize the acceptance of the calorimeters requires that they should be integrated with the incoming and outgoing beam pipes and IP vacuum chamber. This is complicated by the needed transition between the cold and warm pipe that is taking place at the Q0 magnet. In Figure 80 we show a possible transverse view of the BeamCal/LumCal.

The BeamCal/LumCal should be centered on the outgoing beam pipe to take into account the center of mass motion. The optimal longitudinal and transverse segmentation of the calorimeters needs to be studied taking in to account hermeticity and electron identification requirement as well as costs and space constrains on the calorimeters and services. The transverse segmentation is expected to be of order 0.5 cm with longitudinal sampling every radiation length.

⁷ J.A. Lauber et al., “Energy Dependence of Damage to Si PIN Diodes Exposed to β Radiation”.

Figure 81 shows a possible read-out architecture for the BeamCal. This data with other data (GamCal, BPM, etc.) will be used to monitor the instantaneous luminosity (see Sect. 3). The first few longitudinal layers will provide a good map of the low energy beam-strahlung pairs and will be used as feedback to the machine to correct tuning within the first few bunch crossings. The total energy, first moment, and LR/TB/FB asymmetries will be used to monitor the bunch characteristics. The feedback information should be sent in $<1\mu\text{s}$ from the bunch crossing. Detailed studies are needed to understand how to implement this in real-time.

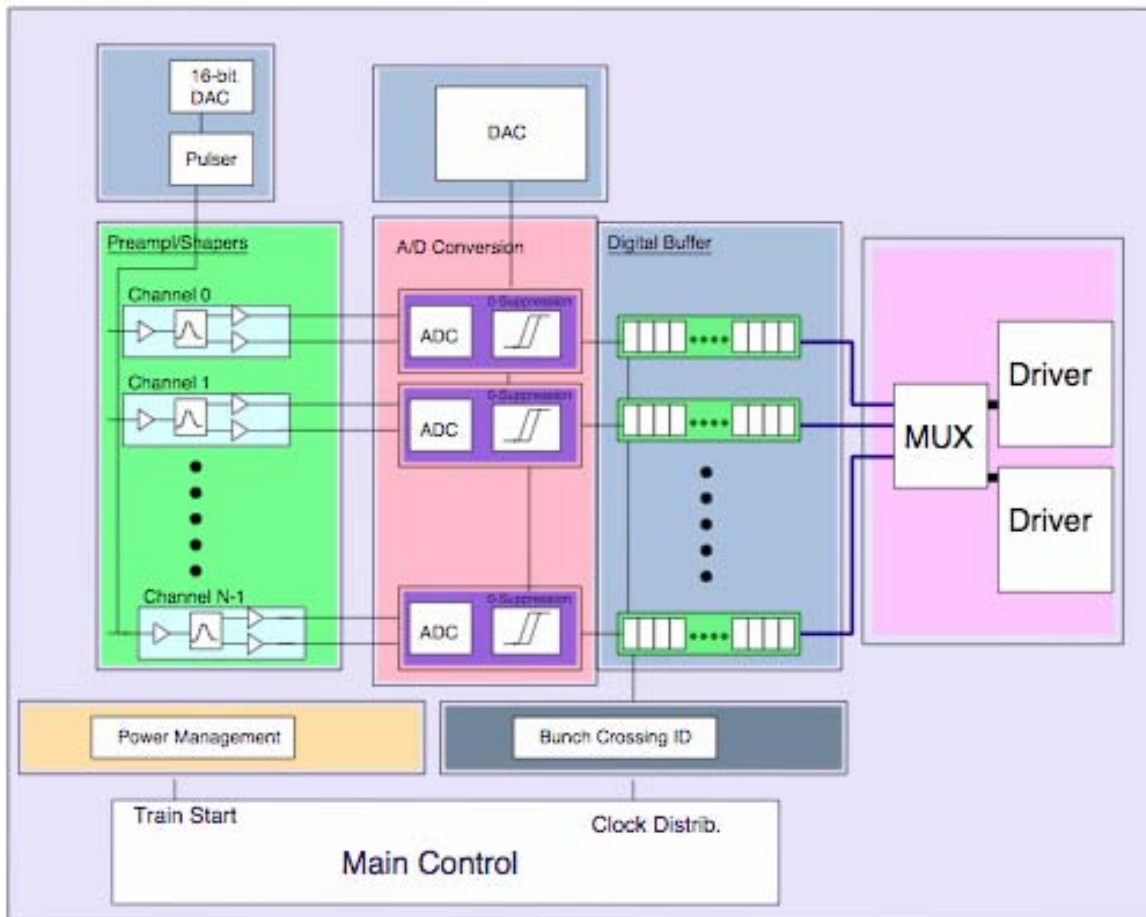


Figure 81 Possible readout architecture for the BeamCal.

The LumCal readout is being studied. As discussed above, it is clear that we can not just copy the barrel ECAL readout architecture, as the rate of Bhabha and background events is too high. We may just copy the BeamCal readout, or we may design a separate readout, which may be compatible with the EndCap ECAL also.

The needs for a calibration system have to be investigated separately for the two detectors. It will be required for the LumCal, given the high accuracy required in the determination of the luminosity normalization. To implement a calibration system one could envision to use a fraction of the machine data cycle to inject precise signals and fully process the detector response. For the BeamCal it is certainly less critical and should be addressed what calibration scheme is required. The radiation hardness issues of the readout need to be addressed. 14-16 bit dynamic range should be adequate for the

LumCal, which may require a dynamically switchable feedback capacitor as a gain selection as in the Barrel ECAL. A more detailed understanding of the occupancy of the detector is necessary for this scheme to work, essentially because it implies a lower limit on the peaking time of the shaped signals. It is certainly possible in the Barrel ECAL where the occupancy is relatively low compared to the occupancy in the forward region. Further studies are necessary to optimize the shaping time of the main amplifier. 10-12 bit dynamic range should be adequate for the BeamCal. Detailed simulations are needed to finalize this question. DAQ bandwidth issues will also need to be considered and studied being a potential limiting factor as far as integration is concerned and may potentially conflict with space availability for support and cabling.

III.E.8 R&D Plan

The R&D issues for the forward calorimeter are divided into the following topics. Some of the R&D is in common with the rest of the SiD EM calorimeters. The items we list here are unique to the forward region.

Simulation studies: Optimization of the design taking in to account space, cost and technology. This includes segmentation, both longitudinal and transverse and the dynamic range needed. We expect that the simulation studies will need a few iterations to help in optimizing the system integration aspects as well as cost. Preliminary decisions Dec. '06, Baseline Detector Layout: Mid '07. The baseline should define in details the specifications and the parameters for the Beam Cal and the Luminosity Cal. Studies to be done by Physicists – assume baseline support.

Integration studies: The forward region is very crowded and the space needs to be shared with the magnets of the final focus, beam pipes, forward calorimeters and their services. Detailed engineering studies to integrate and coordinate these requirements needs to be done at an early stage. Conceptual design for space allocation, services, access and installation by fall of '06 and a baseline design by mid '07. Design effort: ¼ Designer time. Baseline should be ready in one year to allow for space allocation between the different detector and first layout of services routing.

Mechanical Design: The forward calorimeters have special requirements. For example, we expect that the beam pipes will need to be integrated with the Beam Cal to achieve maximal coverage. Detailed mechanical design that takes into account the constraint imposed by the space limitation needs to take place. This should include the support of the calorimeters off the forward tube. Conceptual design end of '06. Baseline design fall of '07. Mechanical Engineer/Designer: ½ FTE. Technician: Prototype work on assembly concepts.

Readout: Define readout architecture, develop readout solutions and test some of the ideas in the Lab and/ or test beams. The readout work should include calculations of the Beam Cal feedback needed for the machine as well as for physics events. Conceptual design and detail specifications by end of '06, Baseline readout architecture 18 month from now. Electronic Eng: 1/3 of an electronic Eng.

Detail Detector design: Once the readout and the mechanical layout are established a detail integration of the readout and the mechanical set up is needed. This will include the layout of the Si sensors, routing of the signals to the readout and cabling of the detector.

Material Studies: The radiation level in the forward direction implies that one will need to probably specify specialized Si material. One needs to select the materials and expose them to radiation levels equivalent to what will be seen at the ILC forward region over period of 5 years. BNL Instrumentation Division has a facility that will allow us to do this. Selection of material and radiation tests – end of '06 early '07. Selection of Sensor material mid '08. ¼ designer for preparation of Si wafers for tests, plus material costs.

Hadronic Calorimeter: Depending on the technology choice for the Hadronic calorimeter for SiD, the Forward section of the Hadronic calorimeter might need to have a different technology. The R&D part will include choice of technology for the forward hadronic calorimeter and a detail design. Designer 1/3 time, Technician ½ time, ME 1/3 time. For the above we would like to test some of the ideas and build a mechanical prototype and, given the financial resources, to test it in a beam. This effort should be coordinated with other prototypes in SiD.

Cost: The main question here is to try and get some prototypes going. We need to see if we can join a single prototype that should be built for the SiD and tested in the test beam and will help in answering some of the questions.

III.F Magnet Systems

III.F.1 Detector Main Solenoid

The performance of the SiD detector has been optimized around a large 5 Tesla superconducting solenoid which provides a clear bore 5.0 m in diameter by 5.6 m long. A steel flux-return that limits the fringe field of the solenoid and also provides muon identification and tracking is an integral part of the system. Such a magnet system unquestionably transcends present engineering experience. It has been suggested by at least one author [1] that mechanical considerations lead to an upper limit of about 60 T²m for the figure-of-merit B²R for superconducting solenoids. For the SiD solenoid this quantity is 62.5 T²m, suggesting that the feasibility of such a magnet is best determined by appeal to experience and careful engineering extrapolation from that experience where required. The fact that this is a challenging solenoid is illustrated in Figure 82, which displays Energy/cold mass vs. Stored Energy for existing solenoids, as well as planned solenoids.

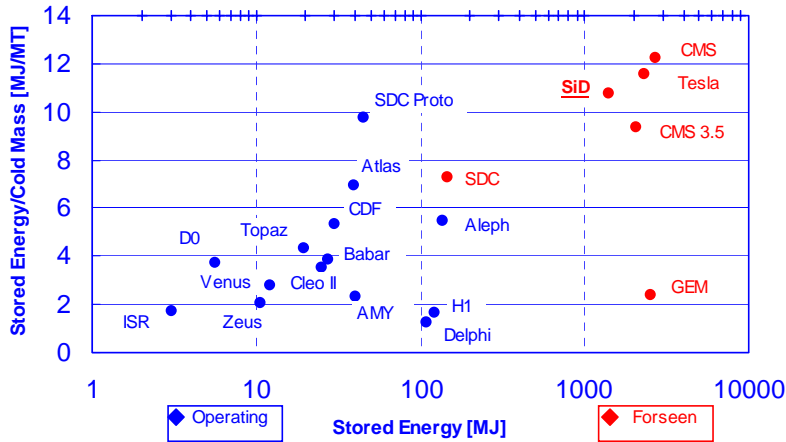


Figure 82 Over view of existing and planned solenoids

III.F.1.a An Appeal to the State-of-the-Art

The CMS solenoid [2], presently undergoing first cooldown⁸ at the CERN Large Hadron Collider, will provide a 4 Tesla field in a bore 5.9 m in diameter and 13 m long. We will show in what follows that this magnet provides a substantial proof-of-concept for the SiD solenoid. We say substantial because the CMS solenoid is yet to be operated. Although providing 20% lower field than the SiD solenoid, the CMS solenoid is physically larger and stores 2.6 Giga-Joules (GJ) magnetic energy vs. 1.4 GJ stored by the SiD solenoid. As with the CMS detector, no special field uniformity beyond that of a uniformly wound solenoid is required by SiD, and the radiation transparency of the magnet is not a constraint. As has become common with large detector solenoids, the CMS coil is wound inside a thin support cylinder which is cooled by forced-flow two-phase helium circulating in tubing welded to the support cylinder. We propose to take this general approach in developing a conceptual design for the SiD solenoid.

At this point a specific winding design must be proposed that provides sufficient linear current density to generate a 5 Tesla central field with a manageable number of winding layers. The winding design must incorporate a specific conductor design that makes a choice of operating current that balances magnet inductance, cryogenic efficiency, and conductor fabrication and winding practicalities. We find the CMS conductor design provides a strong candidate for the SiD solenoid.

III.F.1.b The CMS Conductor

Because the winding radius for the SiD coil (2.645 m) is not so dissimilar from that of CMS (3.160 m), and the optimum operating current of the magnet is likely not to be substantially different (~20 kilo Amperes) from CMS, it is reasonable to begin with the CMS conductor design without change. Likewise the key features of the CMS winding design are found to provide a credible proof-of-concept for SiD.

⁸ The CMS magnet will be commissioned early in 2006

The CMS conductor consists of a 32-strand NbTi cable, stabilized by a coextrusion of high-purity aluminum, which is welded to two bars of strong aluminum alloy. The conductor is shown in Figure 83.

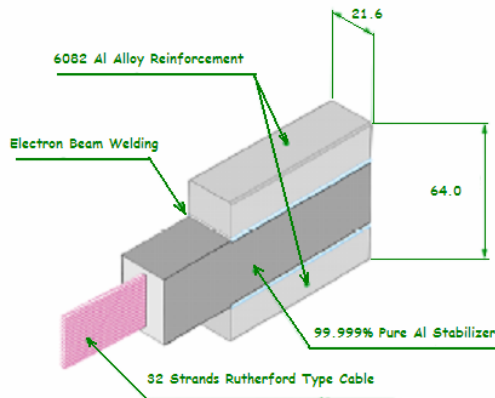


Figure 83 The CMS conductor design

To make such a composite conductor CMS has shown that continuous extrusion of pure aluminum onto the superconducting cable, and continuous electron-beam welding for the attachment of the reinforcing bars, are available in industry, and that piece lengths of finished conductor 2700 m long are possible.

III.F.1.c A Winding Design for SiD

CMS achieves its design field with four winding layers; SiD will require six layers using the same conductor. The smaller aspect ratio (magnet length divided by diameter) of SiD vs. CMS -- approximately one for SiD but more than two for CMS -- means that more linear current density than simple proportionality to the higher field is required. CMS operates at 19.5 kilo-Amperes (kA) and its windings provide a linear current density of approximately 3500 A/mm; SiD requires 4800 A/mm, a factor of almost 1.4 more than CMS for a field 1.25 times as intense. To ensure no conductor joints within a winding layer, CMS subdivided the coil into five modules each 2.5 m long. The modules are independently wound inside their support cylinder segments, impregnated and cured, then transported to the assembly site where they are bolted together at the interface plane between the modules at bosses provided in the outer support cylinder segments.

The SiD winding design chooses two modules, each 2.5 m long, joined as does CMS. Each winding layer consists of 116 turns, and as with CMS, the interturn insulation is 0.64 mm thick and the interlayer insulation 1.04 mm thick. The SiD winding design is shown in Figure 84.

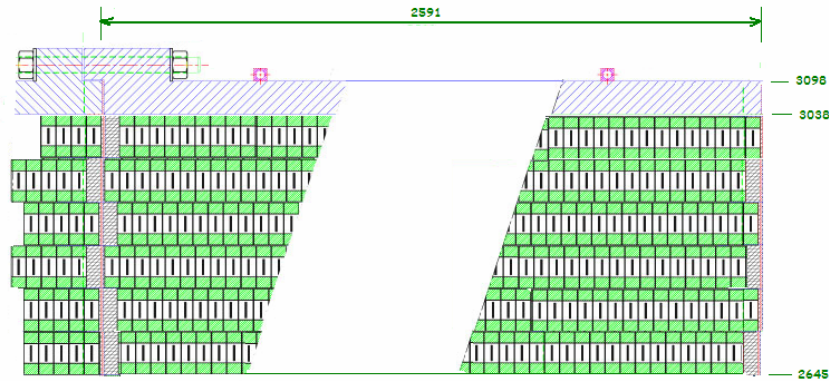


Figure 84 The SiD coil winding design

III.F.1.d Stability and Safety

The operational stability of the magnet is paramount – it must charge readily, discharge safely, and never quench unexpectedly. For CMS, detailed modeling analysis [3] indicated the Minimum Quench Energy (MQE -- that pulse of energy absorbed by the coil that is just able to initiate quenching) is of the order 0.5 – 1.0 J. Such an energy pulse might come from e.g. epoxy cracking, etc. The analysis showed that the MQE is essentially unchanged if a single turn of conductor, or the entire four winding layers, was allowed to participate in the energy absorption. This indicates that the increase in the number of winding layers for SiD, even though it moves the innermost layer 50% farther from the cooling piping than does CMS, is not expected to reduce its stability from that of CMS, if the critical current margins of the superconductor are not less than those of CMS.

For CMS the peak field on the conductor is 4.6 T and the conductor achieves a critical current of ~59 kA at 5 T. The “fraction of short-sample” is approximately $19.5/59 = 0.33$ (ignoring small corrections for the magnet peak field vs. the conductor test field, and the magnet operating temperature vs. the conductor test temperature -- the two corrections tend to offset each other). For SiD the conductor operates at 18000 Amperes and the peak field on the conductor is 5.8 T. The first factor increases the margin by $\sim 19.5/18 = 1.08$; the second decreases it by ~ 0.79 . Evidently only small changes in the CMS conductor design (e.g. increasing the number of strands in the cable) might be necessary to provide the same or even greater operating margin than the CMS conductor.

Upon electrical or cryogenic upset, a fast discharge of the magnet may be triggered by the safety system. In this case the magnet will quench. A quantity that characterizes the safety of a large magnet is the ratio of stored energy to cold mass (see Figure 82); the less cold mass able to absorb the stored energy deposited during a quench, the more likely thermal damage to the magnet is to occur in such an upset. For CMS this ratio is 12.3 MJ/MT; for SiD it is 10.8 MJ/MT. The peak coil temperature after a quench for CMS in which the protection system has failed has been calculated to be 146 K; for SiD this number would be less.

III.F.1.e Mechanical Analysis

A figure-of-merit (FOM) for the radial magnetic loads on the coil, based on the hoop stress σ in a thin-walled pressure vessel, is $FOM = 2\mu_0\sigma = B^2R/t$, where $B^2/2\mu_0$ is the magnetic pressure in the magnet bore, R the mean radius of the coil, and t the thickness of the coil. For CMS this FOM is 160 and for SiD it is 158. This indicates that a detailed calculation of the hoop stresses should be very similar for both solenoids. For CMS the end iron yokes are partly “reentrant” into the magnet bore. This suggests that the radial fields at the ends of the coil, which determine the axial loads on the coil, most likely will be higher than simple proportionality for SiD than those for CMS. An axial stiffness FOM for the coil is the fraction Rt/L , where L is the half length of the magnet. For SiD this FOM is about 3 times that of CMS, suggesting that SiD is better able than CMS to resist the axial loadings on the coil, thereby helping to reduce the shear on the epoxy bond between the coil and the outer support cylinder.

A detailed finite-element model of the SiD coil was created with ANSYS [4], incorporating the details of each turn, to evaluate the stresses and strains in the coil generated by cool down and energization. The model shows the expected cool down strains (uniform displacement inward radially and axially) and the expected energization strains (which bow the cylindrical coil into a barrel shape, fatter at $Z = 0$ than at the ends, and overall axial displacement of the ends of the windings towards $Z = 0$). The net peak outward radial strain (cold, energized) is about 6 mm at $Z = 0$ and 3 mm at $Z = 2.5$ m; the net axial strain at $Z = 2.5$ m is about 3 mm towards $Z = 0$.

Of interest is the state of stress in the high purity aluminum near the conductor cables. As seen in Figure 85, these stresses (Von Mises) peak at about 22.4 MPa (3.2 ksi) nearest the superconducting cables. This stress places the soft aluminum in the plastic regime, but this is very comparable to that calculated for CMS (22 MPa).

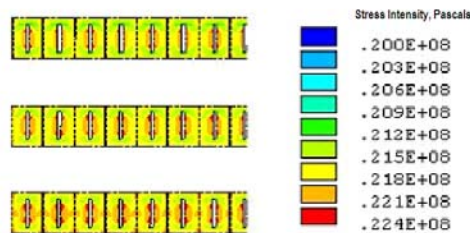


Figure 85 Detail of Von Mises stresses in the high purity aluminum, SiD cold and energized (outer 3 layers omitted from figure).

III.F.1.f Iron Yoke

The conceptual design includes an iron yoke, consisting of an octagonal central barrel and endcaps of steel plates 10 cm thick, with 5 cm gaps for muon chambers. A total of 23 layers of steel was chosen for both the barrel and the endcaps to adequately shield the

region external to the detector from stray magnetic field. The barrel extends from $R = 3.428$ m to $R = 6.828$ m and is 5.6 m long in Z . The end steel plates are flush with the central barrel plates, i.e. they do not “reenter” the bore of the solenoid. They extend from $Z = 2.847$ m to 6.247 m. A system of end gusset plates, staggered on the two ends to allow the insertion of muon detectors into the gaps, supports the barrel shells from one another and the solenoid and calorimeters inside. The geometry of the coil and steel plates used in the ANSYS model is seen in Figure 86.

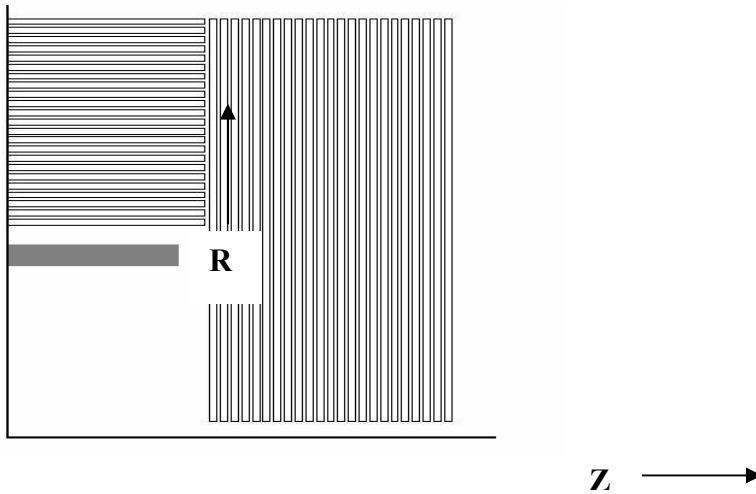


Figure 86 Vertical cross section of the SiD steel model used in ANSYS. R is up in the figure, and Z is horizontal to the right. The central barrel steel plates form an octagon about the cylindrical coil (shaded), and the octagonal end plates contain a circular hole at $R = 0$ to permit the beam to enter the detector.

The gusset plates that space the annular octagonal barrel layers from one another, and also support the magnet cryostat within the barrel, result in a structure sufficiently stiff to be “free-standing”. No other structural members beyond good support at the base of the barrel is required to achieve sufficiently low deflections and stresses required by the muon chambers that will be installed in the gaps between the plates of the barrel.

III.F.1.g *Field Shape*

Two-dimensional and three-dimensional magnetic field calculations of the magnet were performed with ANSYS, and the resulting field shape in the central region of the detector is seen in Figure 87. The inner radius of the windings are at $R = 2.645$ and the windings extend to $|Z| = 2.591$ m. Shown in the figure is a quadrant of the detector, with Z along the horizontal and R along the vertical axis, with $Z=R=0$ at the origin.

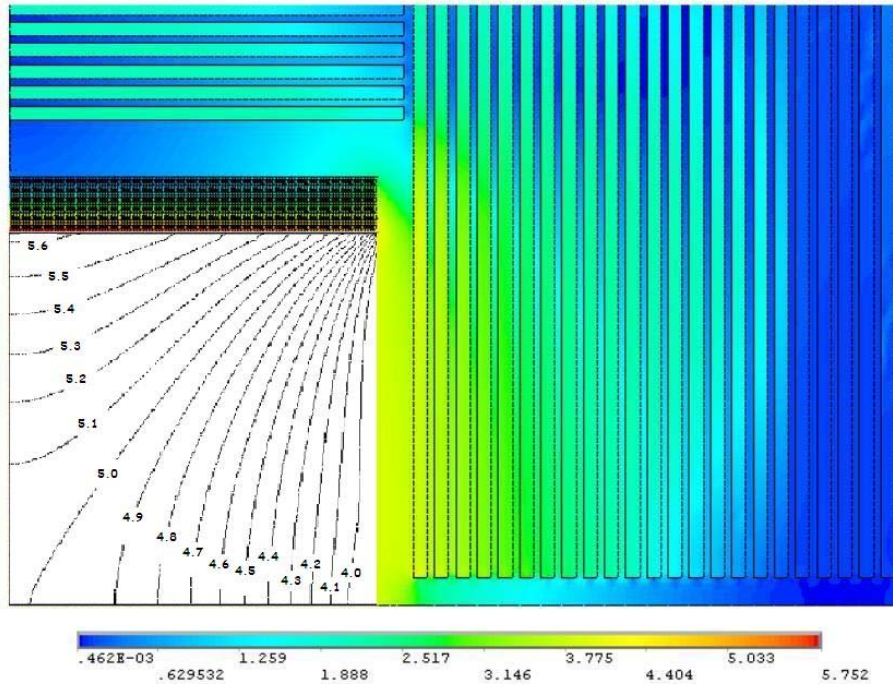


Figure 87 SiD central field contours in $|B|$, fields in the iron shown by intensity scale. Outer layers of barrel steel omitted from the figure.. The cryostat (not shown in the figure) has a clear bore radius of 2.5 m and extends to $|Z| = 2.8$ m.

III.F.1.h General Mechanical Comparison

From the ANSYS studies the following comparisons can be made to similar analyses made for the CMS solenoid. The stresses in the coil shown in Table 9 are evaluated after cooldown and energization.

Table 9 Comparing SiD and CMS

Quantity	SiD	CMS
Von Mises Stress in High Purity Aluminum	22.4 MPa	22 MPa
Von Mises Stress in Structural Aluminum	165 MPa	145 MPa
Von Mises Stress in Rutherford Cable	132 MPa	128 MPa
Maximum Radial Displacement	5.9 mm	~5 mm
Maximum Axial Displacement	2.9 mm	~3.5 mm
Maximum Shear Stress in Insulation	22.6 MPa	21 MPa

Radial Decentering Force	38 kN/mm	31 kN/m
Axial Decentering Force	230 kN/mm	85 kN/m
Stored Energy	1.4 GJ	2.6 GJ

III.F.1.i *Cryostat and Cryogenics*

The requirements for the cryostat and cold mass support system don't differ strongly from CMS so likely similar design approaches could be taken – long metallic axial members and tangential radial members at each end in the vacuum space of the cryostat for cold mass support, and cooling by forced-flow two-phase helium – thermosiphon or pump assisted. Both the CMS and SiD solenoid cryostats support the calorimeters and tracking detectors within, so the engineering of the SiD cryostat will not present novel challenges to the engineers who will develop the final design of the SiD cryostat.

III.F.2 Adding the Detector Integrated Dipole

Beam particles entering SiD at a finite horizontal crossing angle will deviate in the vertical plane. This deviation can be corrected by a special Detector Integrated Dipole (DID) field [5] at the intersection region. The DID corrector can also be used to compensate for rotation of the beam polarization or beam size growth due to synchrotron radiation. In the following paragraphs we show that this special field can be provided by saddle coils mounted directly on the outer support cylinder of the SiD solenoid.

III.F.2.a *Location of the DID Coils*

Locating the DID coils on the solenoid outer support cylinder offers an ideal environment for them. There is minimal solenoidal field in that region, a slight increase in the size of the solenoid cryostat readily provides for the dipole coils, and the large winding radius of the dipole coils ensures a high quality dipole field on the beam axis with modest attention to the dipole winding geometry. Extending the ANSYS model developed for the solenoid, we find approximately 550 kA-turns are required for the desired ~ 600 G dipole field from each of the coils. Figure 88 shows the DID coil geometry superimposed on the solenoid coil:

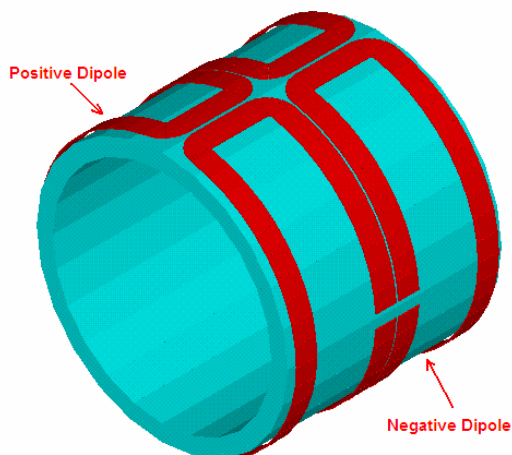


Figure 88 Detector Integrated Dipole saddles

III.F.2.b *The DID Magnetic Field*

A DID coil could be wound with a single layer saddle-shaped pancake composed of ~ 110 turns of conductor operating at ~ 5000 amperes. The conductor could be a small superconducting cable stabilized with high purity aluminum of overall cross section 15 x 15 mm. The field provided by the DID coils is seen in Figure 89:

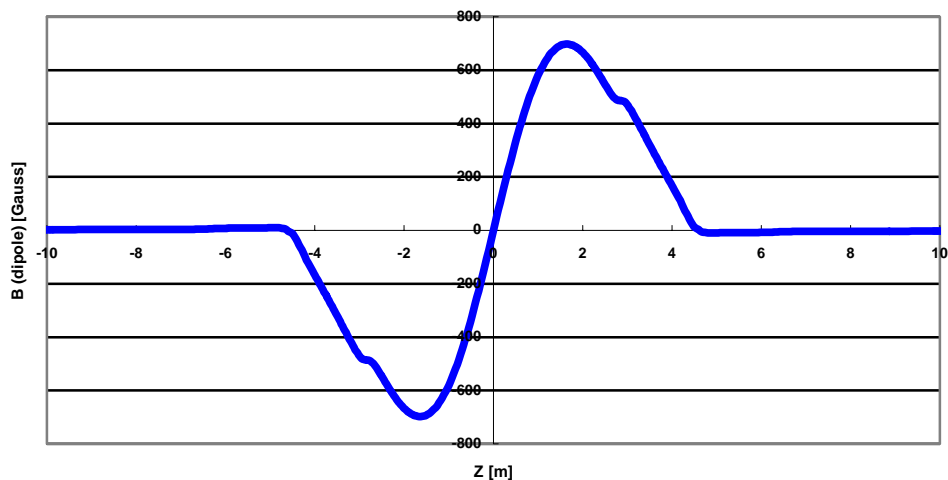


Figure 89 The DID field on the colliding beam axis. The small deviations at $|Z| \sim 2.8$ m align with the upstream edges of the muon steel in the endcaps of SiD.

III.F.2.c *Solenoid – Dipole Interactions*

The DID coils couple modestly to the solenoid and some attention must be given to their mutual behavior during upsets. Likewise, attention must be paid to the forces of interaction between the two magnet systems. Almost purely radial forces exist on the inner ends of the DID saddles as seen in Figure 90, and almost purely axial forces exist on the outer ends of the saddles. The forces on the coils, though large in sum (4137 kN radial, 7800 kN axial), are rather uniformly spread along the ends of the saddles so that engineering their support should be straightforward. The radial forces on the inner end of one saddle are directed opposite the forces on the inner end of the adjoining saddle. It should be relatively straightforward to engineer the required support into the details of the solenoid outer support cylinder.

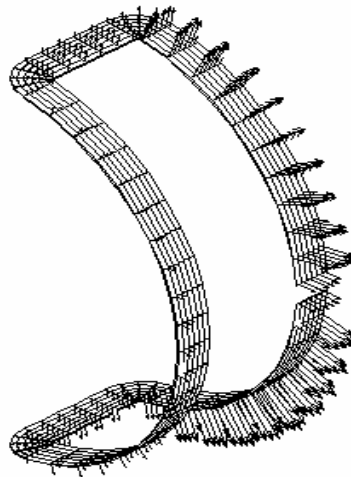


Figure 90 Radial forces on a DID saddle.

III.F.3 Conclusions

The conceptual design study has indicated that the realization of the SiD solenoid is not greatly less credible than that of CMS. Detailed study is required to quantify the stability and safety of the winding design, and to select the optimum final conductor design and choice of operating current. Likewise the requirements of the muon system will evolve and influence the details of the iron design. Since none of these efforts for the solenoid apparently need stray very far from the general approaches taken for CMS, the CMS fabrication and cost experiences can guide the planning for SiD.

Preconceptual design work for a Detector Integrated Dipole also indicates that engineering such a system is not likely to be unduly difficult, nor costly to fabricate. Effort must be expended to understand the quench safety of the dipole coils, but given the highly intimate thermal relationship between the dipole saddles and the solenoid outer support cylinder, it is not anticipated that the coils will be difficult to protect in the event of an unexpected upset of the solenoid. Likewise, given the understood safe quench discharge of the solenoid, an unexpected discharge of the dipole coils is not likely to compromise the safety of the solenoid.

III.F References

- [1] F. Kircher, “Magnetic Field Geometries”, 42nd INFN ELOISATRON Workshop, Erice, IT, Sept 28, 2003.
- [2] A. Herve, et.al., “Status of the Construction of the CMS (Compact Muon Spectrometer) Magnet”, Proc. Eighteenth Intern. Conf. Magnet Technology, V 14, No 2, pages 548—551, IEEE Sup, June 2004.
- [3] F-P. Juster, et. al, “Stability of Al-stabilized Conductors for LHC Detector Magnets”, IEEE Trans App Superconductivity (June 1977), Sup Vol 7 N2, 633-637.
- [4] Swanson Analysis Systems, Houston, PA, USA
- [5] B. Parker, A. Seryi, “Compensation of the Effects of Detector Solenoid on the Vertical Beam Orbit in NLC”, LCC-0143, SLAC-TN-04-044, BNL-MDN-637-40, June 3, 2004.

III.G Muon System

III.G.1 Muon System Overview

The SiD muon system is designed to identify muons from the interaction point with high efficiency and to reject almost all hadrons (primarily pions and kaons). The system should generate SiD triggers for energetic muons and for cosmic rays (as calibration). The muon detectors will be installed in the gaps between steel layers of the solenoid flux return. The required position and rate capabilities of the detectors are modest and can be met by several different detector technologies. Under consideration are extruded scintillator strips read out by multi-anode or Si PMTs, and resistive plate chambers (either glass or Bakelite). Cost, reliability and physics capabilities will determine the preferred choice.

SiD muon selection will combine information from the central tracker, calorimeter, and muon detectors in a unified algorithm. Muon candidates will be required to penetrate a number of interaction lengths consistent with the muon momentum. In addition, the energy loss and multiple scattering along the fitted track length can be used to further discriminate against hadrons. The muon system may also be useful in identifying neutral hadrons that interact beyond the beginning of the calorimeter.

III.G.2 General Design Goals

Muon systems characteristically cover large areas and are difficult to access or replace. Reliability and low cost are the major requirements. Over 2 meters of steel thickness will be required for the solenoid flux return providing more than ten hadron interaction lengths to filter hadrons emerging from the hadron calorimeter and solenoid. Since the

central tracker will measure the muon candidate momentum with great precision, the muon system only needs sufficient position resolution to unambiguously match calorimeter tracks with muon tracks. Present studies indicate that a resolution of $\sim 1\text{-}2$ cm is more than adequate. This can be achieved by extruded scintillators of 4 cm width or by RPCs with pickup strips less than 3 cm wide.

Optimization of the muon system design has not been completed. Although the total steel thickness is set by the solenoid requirements, the optimum number of detector layers is being studied. The baseline design has 22 five cm gaps between the steel plates. Not every gap need be instrumented. Several detector planes are needed at the innermost radii to establish the candidate track position and direction. It is expected that the number of hadrons misidentified as muons will decrease with the amount of steel penetrated but vary only weakly with the steel segmentation. Therefore the outermost layers should also be instrumented. The overall design should be highly redundant so that the loss of a few detector planes should not significantly decrease the muon identification efficiency.

III.G.3 Physics requirement

To date physics benchmark/detector studies have been carried out for single muons and pions, S muon pair production (see Section IV-4 of this report) and b -pair production at 500 GeV.

The single particle studies were done to develop algorithms to use in determining muon ID efficiency and hadron punch-through probability vs. momentum⁹. The results of these studies show that muon identification efficiency is greater than 96% above a momentum of 4 GeV/c. Muons perpendicular to the e^+e^- beamline reach the SiD muon system when their momentum exceeds ~ 3 GeV/c.

The discussion of punch-through is given later, since the analysis of purity for muons in b -pair events has required the development of Kalman filtering.

III.G.4 Detector Choices

III.G.4.a Scintillator/Fiber Muon Detectors

In 2000 it was noted that the ILC muon system requirements could be met with a MINOS type scintillator detector design¹⁰ that would give both muon identification and be used to measure the tails of late developing or highly energetic hadron showers. This seems rather appropriate since the depth of the ILC calorimeters is limited to keep them inside the superconducting solenoid. As an example, neutral hadrons that represent ~ 11 of the

⁹ Milstene, C., G. Fisk, A. Para “Tests of the Charged Particle Stepper with Muons”; <http://xx.lanl.gov/ftp/physics/papers/0604/0604197.pdf>

¹⁰ Para, A. “Solid Scintillator-based Muon Detector for Linear Collider Experiments” Physics and Experiments with Future Linear e^+e^- Colliders, ed. A. Para and H. E. Fisk (2001)pg. 865-869, American Institute of Physics, Melville, New York (Vol. 578)

final-state energy in Higgs and W-W production, primarily neutrons and K_L 's, prove to be difficult to identify and measure¹¹. The physics case for tail catching of showers is being considered by members of the ILC calorimetry effort. A tail catching calorimeter is under construction. Its response to charged hadrons will be measured in the Fermilab MTest beam with an anticipated schedule of the summer and/or fall of 2006.

The MINOS experiment has already proved that a strip-scintillator detector works well for identifying muons and for measuring hadronic energy in neutrino interactions. The ILC R&D muon scintillator detector effort is directed at understanding how to deploy such detectors in the ILC environment and to understand possible improvements that could lead to reduced complexity and /or cost, possibly with alternative photon detection, simpler transfer of light pulses from WLS to clear fibers or the deployment of wire chambers as needed in reducing ambiguities from hadronic background in the muon identification process.

III.G.4.b Resistive Plate Chambers

RPCs have often been used as muon detectors (BaBar and BELLE) and will be used in both LHC experiments. RPCs are inexpensive to build and can be easily constructed in a variety of shapes and sizes. Glass RPCs are likely to be proposed as the SiD hadron calorimeter. RPCs use fluorocarbon gases which may be regulated in the future as greenhouse warming gases and require nontrivial gas delivery systems. The major concern with RPCs are their aging characteristics (BaBar was forced to replace its original RPCs and BELLE had startup problems). However, significant progress has been made in recent years in understanding aging mechanisms. Many of the aging processes are proportional to current passing through the gas gap. LHC detectors will run in avalanche mode which has much lower charge per track. The 2nd generation BaBar RPCs and the Belle RPCs have performed reliably at low signal rates (<0.2 Hz/cm²). Given the low background rates expected at the ILC (10⁻³ Hz/cm²) either technology should be reliable.

III.G.5 Backgrounds

Backgrounds in the muon system are expected to come primarily from beam losses near the detector. The muon system is shielded from backgrounds generated at the collision point or along the internal beam lines by the calorimeters, which are greater than 4 absorption lengths thick. Therefore only penetrating backgrounds, such as high-energy muons or neutrons, affect the barrel muon detectors. Calculations by N. Mokhov et al¹² of the expected background from muons produced by collimators near the detector hall predict a rate of 0.8 muons/cm² per pulse train (~1 ms) without muon spoilers, which is reduced to 2.4×10^{-4} /cm² per pulse train with the addition of muon spoilers. In the endcaps

¹¹ Frey, R. "Experimental Issues for the Workshop", International Conference on Linear Colliders – LCWS 2004, p 29 Eds. H. Videau & J-C. Brient, Editions de l'Ecole Polytechnique, Julliet 2005, 91128 Palaiseau Cedex

¹² N. V. Mokhov, A. I. Drozhdin, M. A. Kostin "Beam Collimation and Machine Detector Interface at the International Linear Collider" PAC 2005 Paper Fermilab-Conf-05-154-AD May 2005

the average occupancy per pulse would be ~ 0.3 per readout strip, indicating the need to use timing information to further reduce the background. The endcap detectors can in addition be hit by electromagnetic shower debris from local beam losses and may require additional shielding.

III.G.6 Design

The muon system will start outside of the highly segmented electromagnetic and hadronic calorimeters (4.6λ) and the 5T solenoid coil and cryostat (1.27λ) at a radius of 3.5 m. The solenoid flux return is ~ 230 cm thick in the barrel (14λ). In the baseline design shown in Figure 91 the flux return is divided into 23 layers of 10 cm steel in octagonal barrel geometry. The central barrel will be 5.7 m long. Endcaps of 23 10 cm thick steel octagons will cap both ends of the barrel. The muon detectors will be inserted in the 4-5 cm gaps between the plates. The thickness of the gaps will be determined not only by the detector thickness but by the flatness of the large plates making up the flux return. The first barrel layer is approximately 2.9m by 5.7 m and the last layer is ~ 5.6 m by 5.7m. The total detector area needed depends on the final number of layers built ($\sim 8600 \text{ m}^2$ for 18 layers).

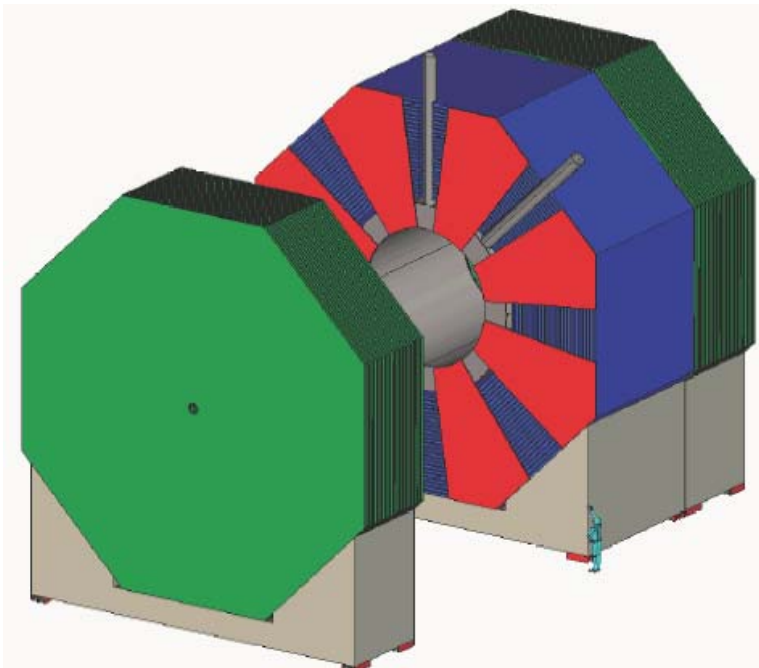


Figure 91 Muon system

III.G.6.a Extruded scintillators

The ALC Muon Studies group (UC Davis, Fermilab, Indiana U, NIU, U Notre Dame, Wayne State) is testing a four $\frac{1}{4}$ sized (1.25m X 2.5m) prototype planes, assembled at the University of Notre Dame, to understand issues and costs associated with the application of strip-scintillator technology to an LC muon system. The tests are an exploration of

construction issues: fiber splicing and fiber routing and calibration with LEDs and radioactive sources. The operational characteristics of the MAPMT readout (pulse timing, amplitude, gain and cross-talk) will be determined. The response of the entire scintillator, wavelength shifter and MAPMT chain to charged tracks will measure the WLS decay times, signal dispersion and attenuation, and longitudinal position (determined from pulse arrival time) with prototype signal processing and data acquisition electronics.

Testing apparatus is stationed at Lab 6 in the Fermilab Village and the MTest beam at Fermilab. MAPMT testing apparatus has been developed at Wayne State and prototype signal processing and DAQ system have been developed at UC Davis. Indiana U and NIU are involved in scintillator strip testing and the testing of prototype planes. Preliminary test results on the prototype modules show that the integrated charge from cosmic charged particles passing through the strips result in $\sim 3-4$ pC which is approximately what is expected for a MAPMT gain of $3E06$ and 6 - 8 photo-electrons. The pulses that are observed exhibit a decay time that is consistent with a recently measured Y-11 in-fiber measurement of ~ 12 ns. It should be emphasized that the measurements to date are preliminary. Conclusions to date encourage us to press on with tests and development of a scintillator-based muon system.

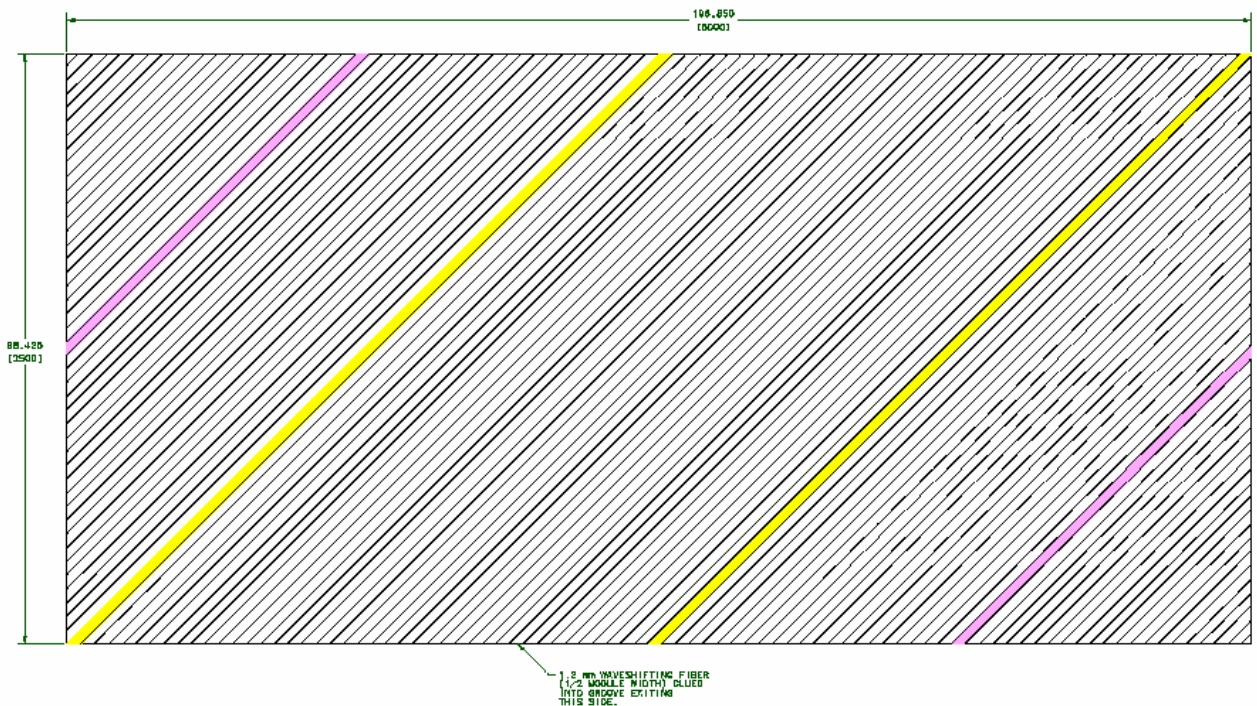


Figure 92 Layout of a barrel muon scintillator plane. The length of the module is 5.7m and the variable height of the module shown is 2.9m. The long strips are 4.1 m and the width of the scintillator strips is 4.1cm.

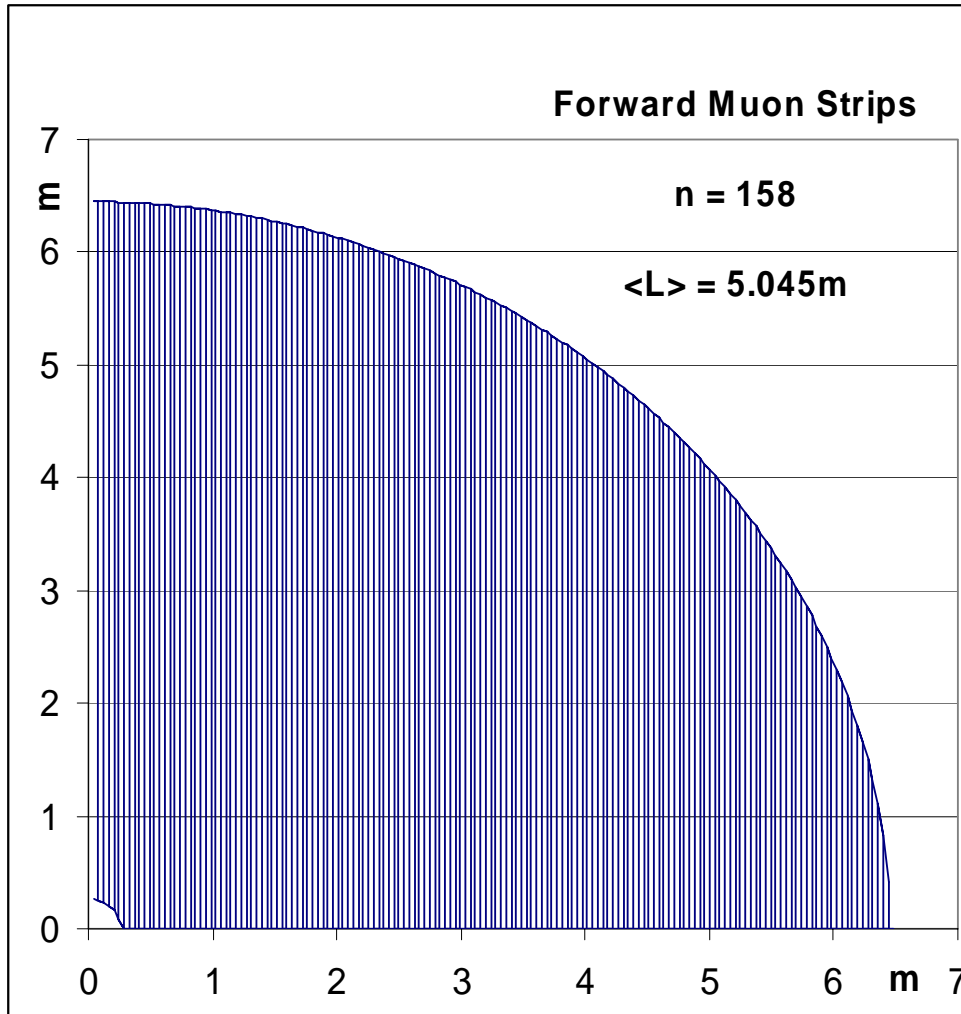


Figure 93 Layout of quadrant strips for the forward muon system.

Figure 93 shows the layout of quadrant strips for the forward muon system. Alternate planes of detectors are rotated by 90° relative to each other. Each quadrant contains ~ 158 strips 4.1 cm wide and of variable length. The mean strip length is 5.05 m. Readout clear fibers from the perimeter of the module carry the light pulses to MAPMTs outside the stray magnetic field or SiPM electronic signals at the outer perimeter are transported to readout electronics outside the detector.

III.G.6.b RPC Option

RPC R&D will continue to focus on further aging studies in these and existing RPC systems.

III.I SiD Electronics

The ILC time structure is expected to be trains of 3000 or 6000 very short pulses over 1 ms, with the trains repeating at 5 Hz. In general, hit rates are quite small except for the inner layer of the vertex detector and for very forward regions of SiD that are hit by e^+e^- pairs. To optimize the SiD electronics, the problem is divided into 3 major categories: vertex detector electronics; very forward regions; and everything else. The vertex detector readout problem is significant, and is driving the development of new technologies which are discussed in the Tracking/Vertexing Section above. The very forward regions are beginning development. At this time, most effort has gone into the development of a read out chip for the “everything else” regions called KPiX. The chip was motivated by the following major requirements of the EMCal:

- Readout of many pixels with minimal interconnection cost.
- Efficient Readout of min I signals.
- Wide dynamic range
- Sensitive to single bunch crossing
- Identify bunch crossing in train
- Allow for 4 measurements of different bunches per train.
- Servo out DC coupled detector leakage
- Minimal power dissipation

These requirements are addressed by:

KPiX will be a 1024 channel chip with a 200 x 500 micron pitch array for bump bonding the chip directly to a Si detector. KPiX power and IO connections are also made by bump bonding to traces on the detector.

The KPiX charge amplifier utilizes a first ~ 1 pF feedback capacitor around the charge amplifier, and a second switched capacitor of ~ 10 pF that is utilized when the signal exceeds the range of the first. The output of the amplifier is shaped and then stored on a sample and hold capacitor if the signal exceeds a DAC settable threshold. The signal is digitized by a Wilkinson ADC to 13 bits during the inter-train period.

The KPiX counts a bunch clock and utilizes a discriminator on the charge amplifier to clock a time logging register.

The circuitry for signal and time storage is duplicated 4 times per pixel.

The KPiX is designed for DC coupled devices with finite leakage, and uses a servo amplifier to balance the leakage current. It may be used with an AC coupled device without change.

Power dissipation is major concern in the EMCal (and in the tracker). By choking the current to the front ends when there are no beams, the calculated average power dissipation is ~ 20 mW. Of course, this means that the detector is insensitive when the electronics are powered down.

KPiX internally stores data during the ILC train. It should be relatively immune to ILC EMP compared to a system that is moving data out during the train.

For the EMCal, the 1024 inputs of KPiX matches the detector pixellization, so there is one chip per detector. It was soon realized that this device seems well matched to the Si strip detectors of the SiD tracker, with two improvements possible. The dynamic range is much smaller, thus obviating the relatively large second feedback capacitor. With the removal of this capacitor, it should be possible to go to a smaller cell pitch and realize 2048 cells per chip, which is a perfect match to the strip detectors being studied.

The detectors for the HCal and the muon system are not as settled as the EMCal and tracker. However, RPC's seem a serious possibility, and the KPiX seems both suitable and economic. There have been some concerns that it is difficult to route signals from RPC signal collection boards with 1 cm^2 pads to the KPiX input connections. A demonstration board that would have the KPiX mounted on an intermediate header is being designed to study the issue. Another HCal option is a GEM detector, that would necessarily collect e^- . The next version of the KPiX chip will have a register controlled inverter for opposite polarity signals

There will be a need for beam tests of these systems. While SLAC can adequately match the time structure of the ILC for these purposes, FNAL and CERN probably can not. Consequently an optional trigger is being designed for the next version. Note that SiD does not foresee a trigger; all data will be transmitted out of the detector, and a computed filter might be used to discard background events.

The KPiX is being designed by a collaboration of SLAC, BNL and Oregon. The first submission is being tested, and preparations are well along for a second submission in March 2006. Rather specialized cables are required for the EMCal KPiX to outside connections, since the goal is a 1mm gap between the tungsten plates. UCD is designing these cables.

The higher level of DAQ is at the conceptual design stage. The KPiX communicates by a clock pair and read, reset, and command lines at a maximum speed of 20 MHz. A data concentrator chip, probably an FPGA, collects data from and manages ~ 100 KPiX. The concentrators transmit to some next level concentrator/processor over optical fibers. (If this system were being implemented a few years ago, this level might be VME). If each concentrator processor handles 32 fibers, then the full EMCal would be ~ 32 processors. The tracker, HCal, and muon systems appear to have similar or smaller loads.

The very forward systems, such as the Lumcal, Beamcal, and small radius tracking systems, are different. They are occupied ~every pulse, and so must measure amplitudes for each pulse in a train. Furthermore, the radiation environment is fierce, with estimates ~100 MRad per year. It is not clear what the actual detectors might be, although diamond and low resistivity silicon have been mentioned. Different architectures are being studied at BNL and SLAC. (See Bill Morse's writeup for their thoughts);

III.J DAQ

Data are collected from the front end readout chips by data concentrator chips servicing ~100 front end chips during the first ~100ms of the inter-train period. The number of channels on these chips is expected to be 2048 for the tracker and 1024 for the other "barrel" systems excluding the vertex detector. The forward system readout is being architected now, but 64 channels per chip seems likely. Zero suppression will happen either in the front end chip or the concentrator. Interestingly, with the expected data rates, this does not seem an important issue now.

Data from the concentrators are shipped by optical fibers to processors that will organize the data by time bucket and event build within a subsystem. Each processor is expected to receive 32 fibers, and a very modest number of processors should service a system. These processors might be VME, but it is likely that there will be more evolved standards by the time a decision is needed.

Data from the processors are collected by yet another set of processors where SiD level event building and event filtering occur. A filter is distinct from a trigger in that no control information is sent back to front end systems, but the filter can decide that an event be discarded. Accepted events can be queued for archival storage. Disk storage on reliable arrays seems quite possible, but more attractive technologies may emerge. Data rates are expected to be much, much lower than LHC detectors or even astronomical telescopes.

The next stage accepts events for sample analysis. This stage is primarily for subsystem quality assurance, but it seems likely that a preliminary physics scale reconstruction can be done. Server structures then can distribute both events and standard analysis results to users over the web. An idea of the mean data load flowing in the concentrators and downstream is provided by a Monte Carlo study that included bhabhas, radiative bhabhas, μ pairs, $\gamma\gamma \rightarrow$ hadrons, and e^+e^- pairs. This study counted the multiple hits in a pixel when they occurred. To be conservative, it is assumed that each hit produces 2 bytes of amplitude, 2 bytes of timing, and 4 bytes of location information. The results are indicated below:

Table 10 Data rates for subsystems.

subDetector	mean # hits per train	Mbytes per train	Data Rate Mbytes/sec

Tracker Barrel	36211	0.3	3
Tracker Endcap	238522	1.9	19
EM Barrel	38090	0.3	3
EM Endcap	253035	2.0	20
HAD Barrel	6531	0.1	1
HAD Endcap	336037	2.7	27
Total		7.3	

The column for data rate assumes the entire subdetector data is pushed through one pipe, and that the data in one train must go in 100 mS. No credit is taken for multiple pipes or buffering. The system will have to handle fluctuations. Also, the vertex detector and the LumCal and BeamCal have not been studied.

IV. Physics Performance and Benchmarking

IV.A Simulation of SiD.

In order to design a detector which is capable of exploiting the full physics discovery potential of the ILC, a fairly sophisticated and mature simulation and reconstruction environment is needed. The Simulation & Reconstruction Working Group has concentrated its efforts on assembling a flexible framework to allow different detector designs to be simulated and multiple reconstruction algorithms to be implemented and used for physics and detector analyses. The code, binary executables, and documentation in the form of Application Programming Interface (API) and tutorials are all available online at <http://lcsim.org>.

Event Generation

A number of different event samples has been generated for detector design studies, ranging from single particles to inclusive Standard Model processes.

Single particle studies are essential for developing reconstruction algorithms and understanding the basic detector response and resolution. Accordingly, the following set of single particles is available:

1. Single particles: $e, \gamma, \mu, \pi, n, K_L^0$
2. Simple resonances: $\pi^0, K_S^0, \psi \rightarrow \mu^+ \mu^-, \rho$
3. Complicated decays: τ, c, b, Z, W

A large sample of events was also generated at a center of mass energy of 91 GeV. This

“Z Pole” sample is primarily intended as a test-bed for evaluating different reconstruction algorithms. By concentrating on the reconstructed event energy as a figure of merit, complications arising from such things as jet-finding algorithms are minimized.

The following canonical set of benchmark signal processes was generated for the default ILC configuration at 500 GeV:

1. $e^+e^- \rightarrow q\bar{q}, q = u, d, s, c, b, t$
2. $e^+e^- \rightarrow f\bar{f}, f = \mu, \tau$
3. $e^+e^- \rightarrow Z\gamma, ZZ, WW$
4. $e^+e^- \rightarrow Zh, m_h = 120 \text{ GeV}$

Finally, an almost complete set of Standard Model processes at 500 GeV was generated using the Whizard Monte Carlo program¹³. All 0, 2, 4 and 6 fermion final states, as well as top quark-dominated 8 fermion processes were generated. Samples were generated with electron and positron polarizations of 100%. Arbitrary polarization samples can be generated by properly combining events from the four data samples. PYTHIA¹⁴ was used for final state QED and QCD parton showering, fragmentation and decay to provide final-state observable particles. Included in this sample are backgrounds arising from interactions between virtual and beamstrahlung photons. This sample is intended to serve as an unbiased background sample for physics analyses. Because of the large size of the dataset, these events have not been processed through the full detector simulation, but have been used in fast MC studies.

Full Detector Simulation

The simulation of the response of the detector to the generated events is based on the Geant4 toolkit, which provides the classes to describe the geometry of the detector, the transport and the interactions of particles with materials and fields. A thin layer of Linear Collider-specific code provides access to the Monte Carlo events, the detector geometry and the output of the detector hits. The geometries are fully described at runtime, so physicists can vary detector parameters without having to rebuild the simulation executable binaries. The output uses the standard LCIO format, so that detectors modeled using other simulation packages could be analyzed, and data generated using this system could be analyzed in other reconstruction and analysis frameworks.

¹³ <http://www-ttp.physik.uni-karlsruhe.de/whizard/>

¹⁴ <http://www.thep.lu.se/~torbjorn/Pythia.html>

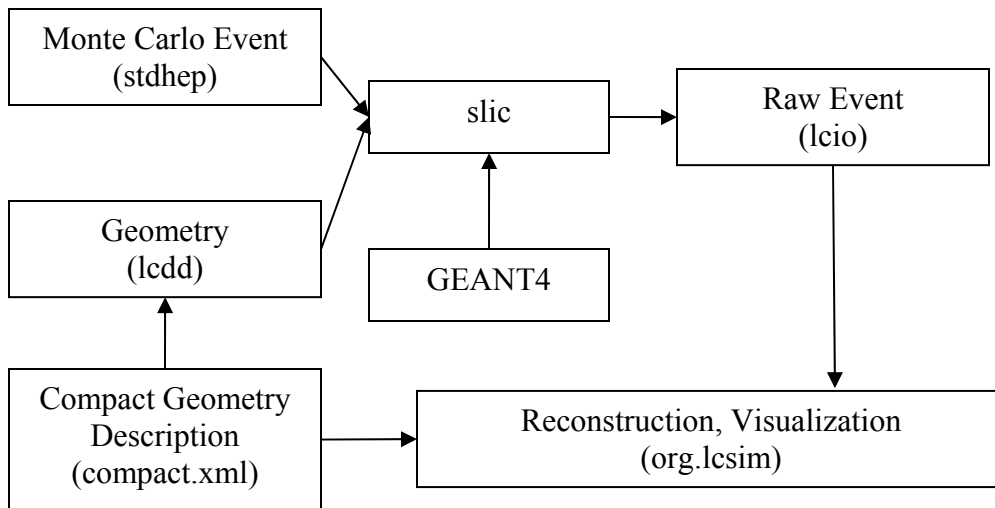


Figure 94

Fast Detector Simulations

Although the main purpose of the SiD simulation and analysis effort is to define the detector performance using full simulations, some analyses still need to be able to quickly simulate the response of the detector in a parameterized fashion. Two packages are available for such fast MC studies. The first is a fully parameterized package which simply smears the resolution of input particles. See the benchmarking section for more details. The other package is *lelaps* (<http://lelaps.freehep.org>). This program propagates particles through the detector using helical propagation through a simple solenoidal magnetic field. It is capable of handling decays in flight, multiple coulomb scattering and energy loss in tracking detectors. It parameterizes the shower development of particle interactions in the calorimeters using functional forms which have been shown to be very good approximations to electromagnetic showers, and statistically reasonable facsimiles of hadronic showers. It produces hits in detector sensitive elements which can be used in subsequent reconstruction and analysis. It is, therefore, an intermediate between the fast Monte Carlo, which provides *ReconstructedParticle* objects which are directly usable in physics analysis, and the full *Geant4* simulation which simulates the detector interactions much more realistically.

Detector Variants

The XML format allows variations in detector geometries to be easily set up and studied, e.g.

- Stainless Steel vs. Tungsten hadronic calorimeter absorber material
- RPC vs. scintillator readout
- Calorimeter layering (radii, number of layers, composition, ...)

Readout segmentation (pad size, projective vs. fixed cell size)
 Tracking detector topologies (“wedding cake” vs. Barrel + Cap)
 Magnetic field strength

In addition to the baseline Silicon Detector (sid00), a number of variants has been developed in order to study the dependence of the performance on detector options.

sid00

For reference, we include here a fairly complete textual description of the baseline detector. Full details can be found at <http://lcsim.org/detectors/#sid00>.

Beampipe:

The beampipe is composed of three sections: a cylindrical central tube and forward and backward conical sections. The central tube has an inner radius of 1.2cm and a z extent of +/- 6.251cm and is made of 0.040cm thick beryllium. The conical sections are 1mm thick beryllium and flare from 1.2cm inner radius at 6.25cm to 6.97cm at the edge of the tracking region. The beam pipe has a titanium inner liner .0025cm thick for the central barrel section and 0.0075cm thick for the conical sections.

Vertex Detector:

The vertex detector is composed of a central barrel system with five layers and forward systems composed of four disks. The barrels are all 12.5cm long and are composed of 001cm silicon, of which the outer 0.002 is sensitive. The inner radii of the layers are: 1.4, 2.5, 3.6, 4.8, 6.0cm.

There are four forward disks on either end, composed of a total of 0.022cm of silicon, of which the inner 0.002 is sensitive. All of the disks extend to a maximum radius of 7.5cm. The z positions and inner radii for the four disks are:

z (cm)	inner radius (cm)
7.6	1.6
9.5	1.6
12.5	2.0
18.0	2.0

The barrel vertex detector is supported by a beryllium cage and the whole vertex detector is surrounded by a foam cryostat. The barrel support is a cylinder of 0.1cm beryllium with inner radius 7.0cm and z extent +/- 6.5cm. The barrel support endplate composed of a mixture of ladder blocks, annuli, plate and cable/fiber is represented by 0.58cm thick G10, with inner radius 1.5cm, outer radius 7.3cm and inner z of 6.5cm. The mechanical supports for the endcap disks are modeled as a pair of beryllium rings behind each disk at the inner and outer rims, with a thickness of 0.1cm and radial span of 0.7cm each. The VXD utility mixture of cooling channels, cables and fibers etc. is represented by a layer of 0.99cm thick G10 around the conical section of the beampipe at each end. The barrel cryostat is a cylinder of 1.5cm polystyrene foam with inner radius 11.2cm and z extent +/- 24.0cm. The endplate cryostats are disks of 3.0cm polystyrene foam with inner radius

2.3cm, outer radius 11.2cm and inner z of 21.0cm. The cryostat coatings and Faraday cage are represented by 0.02cm aluminum placed at the inner surfaces of the cryostat.

Tracker:

The tracker is composed of five cylindrical barrels with five disk-shaped endplanes. The z extent of the barrels increases with radius and the endplane for each extends beyond its cylinder in radius to provide overlap. The sensitive medium is silicon, assembled into carbon-fiber/Rohacell/PEEK modules and read out via a bump-bonded chip and Kapton/copper cables. These modules are supported by carbon-fiber/Rohacell/carbon-fiber barrels or disks. Each barrel cylinder is supported from the next barrel out by an annular carbon fiber-ring. Outside each of these support rings in z, G10/copper printed circuit boards are mounted for power and readout distribution to all silicon modules in a layer.

Barrels:

The radii and z extent of the barrel silicon are:

layer	z (cm)	inner radius (cm)
1	26.7	20.0
2	61.7	46.3
3	96.7	72.5
4	131.7	98.8
5	161.7	121.3

For the barrels, the support tubes are composed of 0.025cm carbon fiber, 1.3cm of Rohacell31 and 0.25cm carbon fiber. The sensor modules for the barrel are single-sided and have 0.03cm of silicon mounted on carbon fiber/Rohacell31 frames that clip into PEEK (Polyetheretherketone) mounts. The average thickness of the carbon fiber, Rohacell31 and PEEK in the modules of each barrel layer are 0.016cm, 0.14cm and 0.02cm respectively. The average thicknesses of the readout materials are 0.00048cm of silicon, 0.0064cm of Kapton and 0.00065cm of copper, however, the thickness of the cable material varies by layer.

Endcap:

The z positions and radial extents of the endcap silicon are:

layer	z (cm)	inner radius (cm)	outer radius (cm)
1 inner	30.0	4.0	25.0
1 outer	30.4	4.0	25.0
2 inner	65.0	7.9	51.3
2 outer	65.4	7.9	51.3
3 inner	100.0	11.8	77.5
3 outer	100.4	11.8	77.5

4 inner	135.0	15.6	103.8
4 outer	135.4	15.6	103.8
5 inner	165.0	18.9	126.3
5 outer	165.4	18.9	126.3

where each layer is composed of double-sided sensor modules to measure coordinates in two views. The forward disk supports are composed of .039cm carbon fiber, 2.5cm Rohacell31 and 0.039cm of carbon fiber. The sensor modules mounted outside of the disks are double-sided and have 0.03cm of silicon mounted on either side of carbon fiber/Rohacell31 frames that clip into PEEK (Polyetheretherketone) mounts. The average thickness of the carbon fiber, Rohacell31 and PEEK in the modules of each disk double-layer is assumed to be the same as that for the barrel modules. The average thicknesses of the readout material are also assumed to be the same, but are repeated on both sides of the modules for double-sided readout. The z-positions and radial extents of the annular support rings that complete the structure of the tracker are:

layer	z (cm)	inner radius (cm)	outer radius (cm)
1	26.7	18.0	44.3
2	61.7	44.3	70.5
3	96.7	70.5	96.8
4	131.7	96.9	119.3
5	161.7	119.3	127.0

These rings are composed of 0.15cm thick carbon fiber. The readout and power distribution boards are mounted on the outside surfaces of these support rings. The regions occupied by these boards and the average thickness of the material they represent are given by:

layer	z (cm)	inner radius (cm)	outer radius (cm)	G10 thickness (cm)	copper thickness (cm)
1	27.0	25.5	44.3	0.057	0.0038
2	62.0	51.8	70.5	0.102	0.0068
3	97.0	78.0	96.8	0.108	0.0072
4	132.0	104.3	119.3	0.186	0.0124
5	162.0	104.3	119.3	0.246	0.0164

Note that in layer five, due to the constraints of the calorimeter, the readout boards are not mounted on this annular ring, but rather at smaller radius.

Calorimeters:

Electromagnetic Calorimeter:

This element sets the basic size and aspect ratio for the rest of the detector. The inner radius for the barrel is 127cm. The aspect ratio is set to $\cos(\theta)=0.8$, meaning the

inner z of the endcap EM calorimeter is at z of 168cm. The EM calorimeter is a sampling calorimeter composed of 30 layers of

material	thickness (cm)
Tungsten	0.250
G10	0.068
Silicon	0.032
Air	0.025

The endcap plug sits inside the barrel cylinder, so the barrel z extent is +/- 179.5cm. The endcap starts at an inner radius of 26cm and extends out to 125cm.

Hadron calorimeter:

The hadron calorimeter is a sampling calorimeter composed of 34 layers of

material	thickness (cm)
Steel	2.0
G10	0.3
PyrexGlass	0.11
RPCGas	0.12
PyrexGlass	0.11
Air	0.16

It begins immediately outside of the EM calorimeters, with the endcap plug sitting inside the barrel. The barrel inner radius is 138.5 with a z extent of +/- 277cm. The endcap extends from an inner radius of 26.0 cm to an outer radius of 138.25, inner z of 179.5

Solenoid:

The solenoid is modeled as a cylinder with an inner radius of 250cm. This is larger than the outer radius of the hadron calorimeter since we will not be building a cylindrical detector, but a polygonal one (current thinking is octagonal). The barrel composition is as follows:

material	thickness (cm)	z (cm)
Steel	6.0	271.0
Air	8.5	271.0
Aluminum	39.3	262.5
Steel	6.0	262.5
Air	20.0	271.0
Steel	3.0	271.0

This is capped with disk endplates of 6cm steel from r=250cm to 332.8cm

Muon System:

The muon system is implemented as a sampling calorimeter composed of 48 layers of:

material	thickness (cm)
Iron	5.0
G10	0.3
PyrexGlass	0.11
RPCGas	0.12
PyrexGlass	0.11
Air	0.86m

The barrel inner radius is 333.0cm with z extent of +/- 277cm. The endcap sits outside the barrel at an inner z of 277.5cm and radius from 26.0cm to 645.0cm. The field is solenoidal, constant 5 Tesla along z up to half the coil thickness and -0.6 outside.

Masks and Far Forward Detectors

Designs for crossing angles of both 2 and 20mr were developed. The detector designed for the 2mr beam crossing solution has a far forward plug which extends out to a radius of 25cm. It starts with an electromagnetic calorimeter with the same composition as the endcap calorimeter, extending from 8.69cm out to 25cm. The calorimeter is backed up by a conically tapered tungsten mask, inner radius 8.69 at z of 179.5, tapering to 16cm at z of 330cm. The outer radius is constant at 25cm. There is a far forward low-Z shield (10cm thick beryllium) at z of 285cm, with a 1.5 cm central aperture. This is followed by a 50 layer silicon-tungsten calorimeter at z of 295cm, with a single aperture for both the incoming and outgoing beams, radius 2cm.

The 20mr design has a somewhat smaller far-forward geometry. The inner radius of the endcap calorimeters is 20cm and the outer radius of the far forward assembly has an outer radius of 19cm. The far forward, low-Z shield and calorimeters have two apertures for the incoming and outgoing beamlines, with an opening angle of 20 milliradians. The calorimeter has apertures with radii of 1.0cm and 1.5cm for the incoming and outgoing beams, respectively. The low-Z shield also has a 1.0cm radius aperture for the incoming beam, but a somewhat smaller (1.2cm) outgoing beam aperture radius to provide shielding from the calorimeter and dump albedo.

Event Samples

The single particle, Z Pole and signal events have been processed through the baseline detector and will be processed through the variants. The output is easily available using anonymous ftp. Directions and documentation is available at:

<http://lcsim.org/datasets/ftp.html>.

IV.B Benchmark Reactions

Physics performance studies are needed to quantify the present performance of SiD, revisit the performance requirements on the various ILC detector subsystems, and ultimately optimize the SiD design by studying how the performance changes as one varies the basic detector parameters. In a broader context, these studies further the physics case of the ILC.

Benchmark Processes for Studying SiD

A list of physics benchmark reactions¹⁵ was presented to the ILC community at Snowmass 2005. This list of about 30 reactions provides comprehensive coverage of ILC physics topics and detector challenges, but is probably too long to be addressed by detector concept groups at this time. Thus, a reduced list of 7 reactions was also proposed which is more appropriate for studies on the time scale of the December 2006 Detector Concept Report.

The SiD Benchmarking group participated in the development of these lists and plans to use them in evaluating the physics performance of the SiD detector. For studies during the calendar year 2006, the SiD intends to investigate the seven reactions in the reduced benchmarks list:

1. $e^+e^- \rightarrow f\bar{f}$, $f = e, c, b, \tau$ at $\sqrt{s}=1.0$ TeV;
2. $e^+e^- \rightarrow Zh$, $\rightarrow \ell^+\ell^-X$, $m_h = 120$ GeV at $\sqrt{s}=0.35$ TeV;
3. $e^+e^- \rightarrow Zh$, $h \rightarrow c\bar{c}$, $\tau^+\tau^-$, WW^* , $m_h = 120$ GeV at $\sqrt{s}=0.35$ TeV;
4. $e^+e^- \rightarrow Zhh$, $m_h = 120$ GeV at $\sqrt{s}=0.5$ TeV;
5. $e^+e^- \rightarrow \tilde{e}_R\tilde{e}_R$ at $\sqrt{s}=0.5$ TeV;
6. $e^+e^- \rightarrow \tilde{\tau}_1\tilde{\tau}_1$ at $\sqrt{s}=0.5$ TeV;
7. $e^+e^- \rightarrow \chi_1^+\chi_1^- / \chi_2^0\chi_2^0$ at $\sqrt{s}=0.5$ TeV;

The evaluation of SiD's performance is presently performed at the level of Fast Monte Carlo studies. The studies reported below generally make use of simulated data, which has included not only the physics process of interest, but also a full suite of Standard Model processes that can appear as physics backgrounds. We report results here on the following benchmark processes: $e^+e^- \rightarrow Zh \rightarrow l^+l^-X$; $e^+e^- \rightarrow Zh \rightarrow qqbb$; $e^+e^- \rightarrow Zh \rightarrow ZWW^*$; $e^+e^- \rightarrow Zhh$; and $e^+e^- \rightarrow \tilde{e}_R\tilde{e}_R$. We have also included SiD performance studies on $e^+e^- \rightarrow \mu^+\mu^-(\gamma)$, which will help in determining the center-of-mass energy. Several of these studies serve the dual purpose of quantifying the physics

¹⁵ M. Battaglia, T. Barklow, M. Peskin, Y. Okada, S. Yamashita, and P. Zerwas, <http://arxiv.org/pdf/hep-ex/0603010>

performance of the SiD baseline detector, and exploring the physics payoffs as fundamental detector resolutions are changed.

Fast Monte Carlo Physics Object Simulation

In benchmarking studies, physics objects (electrons, muons, charged hadrons, photons, neutral hadrons) that have been produced by the event reconstruction software are used to calculate measurement errors for a variety of physics processes.

Although physics performance can only be correctly evaluated using full GEANT4 MC simulation of the detector and optimized event reconstruction software, in some circumstances such a complete simulation may not be available or may be impractical to implement. Physics benchmarking studies utilizing a Fast Monte Carlo can then provide initial estimates until the full simulation is available.

In the context of physics benchmarking, a Fast Monte Carlo should be considered a *Fast Physics Object Monte Carlo*. Such a program emulates the bottom line performance of the event reconstruction software in producing the electron, muon, charged hadron, photon and neutral hadron physics objects. A Fast Monte Carlo with LCIO output which emulates the reconstruction of physics objects by an ILC detector has been developed for this purpose and is included in the org.lcsim JAVA package¹⁶. This Monte Carlo uses parameterized covariance matrices to smear the momenta and impact parameters of charged tracks. The energies and angles of individual photons and neutral hadrons are smeared using single particle electromagnetic and hadronic calorimeter resolutions. Additional parameters include minimum energies and angles for charged particles, photons and neutral hadrons, and global identification efficiencies for electrons, muons, protons and charged kaons. Global resolutions and efficiencies will be replaced by angle-dependent polynomials as more is learned from full detector simulation of the SiD.

ΔE_{jet} Parameterization

It is convenient to be able to specify a desired jet energy resolution as input to the Fast Monte Carlo. In order to achieve such a jet energy resolution the Fast MC scales individual particle energy resolutions.

In the limit of no charged-neutral confusion and negligible tracker momentum error, the jet energy resolution is given by $\sigma^2(E_{\text{jet}}) = A_\gamma^2 w_\gamma E_{\text{jet}} + A_h^2 w_h E_{\text{jet}}$ where

$A_{\gamma,h} = \sigma(E_{\gamma,h}) / \sqrt{E_{\gamma,h}}$ are the single particle electromagnetic and hadronic energy resolutions, and $w_\gamma = 28\%$, $w_h = 10\%$ are the average jet energy fractions for photons and neutral hadrons. Note that the constant term in the single particle energy resolution term has been dropped.

Within the Fast MC the single particle electromagnetic and hadronic energy resolutions are determined through the parameterization

¹⁶ <http://www.lcsim.org>

$\sigma^2(E_{jet}) = (1 + \lambda(1-r))A_\gamma^2 w_\gamma E_{jet} + (1 + \lambda r)A_h^2 w_h E_{jet} = c^2 E_{jet}$ where $c = 0.3, 0.4, 0.5, 0.6$ is the desired jet energy resolution and r is the hadronic resolution degradation fraction. For example, one sets $r = 1$ to only degrade the single particle hadronic resolution and $r = 0$ to only degrade the electromagnetic energy resolution. Full MC studies currently indicate that one should use $r = 1$. Given a desired jet energy resolution c the parameter λ is given by

$$\lambda = \frac{c^2 - A_\gamma^2 w_\gamma - A_h^2 w_h}{(1-r)A_\gamma^2 w_\gamma + rA_h^2 w_h}$$

The single particle resolution for photons is then degraded by $1 + \lambda(1-r)$ and the single particle resolution for neutral hadrons is degraded by $1 + \lambda r$. The following plot shows the jet energy resolution for 250 GeV u quark jets, where E_{rec} and E_{true} are the reconstructed and true jet energies, respectively. The true jet energy E_{true} has been adjusted for neutrinos and particles outside the detector acceptance.

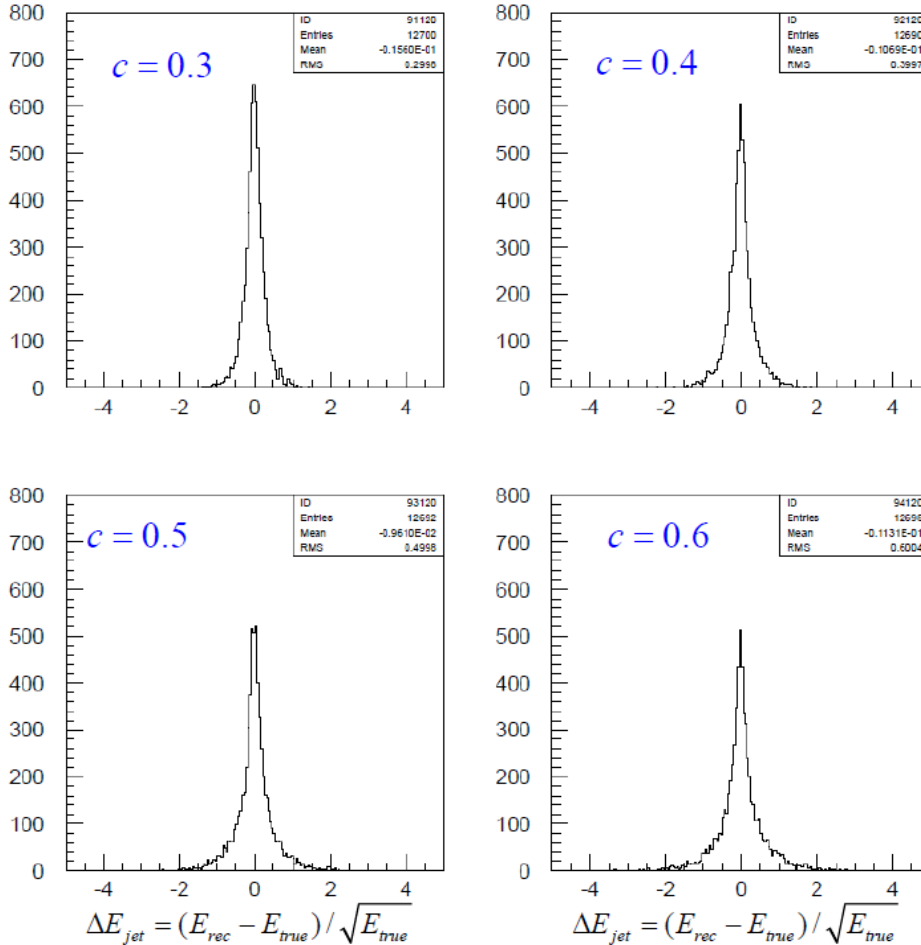


Figure 95 Distributions of ΔE_{jet} for 250 GeV light quarks jets for different values of the Fast Monte Carlo jet energy resolution parameter c .

In this way, one can approximate the effects of imperfections in the full reconstruction and parameterize the physics performance of the detector in terms of a single effective jet energy resolution.

IV.C Performance of SiD

IV.C.1 Tracker Physics Performance

Higgs Mass Using Lepton Pair Recoil in $e^+e^- \rightarrow e^+e^-H, \mu^+\mu^-H$

Studies of the Higgs Boson are expected to be center stage at the ILC. The production of the Higgs through “Higgs-strahlung” in association with a Z, will allow a precision Higgs mass determination, precision studies of the Higgs branching fractions, measurement of the production cross section and accompanying tests of SM couplings, and searches for invisible Higgs decays. When the associated Z decays leptonically, it is possible to reconstruct the mass of the object recoiling against the Z with high precision. The resolution in the recoil mass, which translates into how sharply the Higgs signal rises above the Z Z background, depends on the initial beam energy spread, which at ILC is about 0.1%, and the precision with which the lepton momenta are measured. Assuming the Higgs mass is 120 GeV, $\sqrt{s} = 350$ GeV, and the integrated luminosity is 500 fb^{-1} , we find that the Higgs mass can be determined with a precision of 100 MeV in SiD for Z decays to muon pairs.

It is interesting to see how the precision of the mass measurement depends on the momentum resolution of the SiD tracker. Figure 96 shows the recoil mass distribution opposite the Z for four different values of tracker momentum resolution, characterized by the parameters a and b. Here the momentum resolution is written $\delta p_t/p_t^2 = a \oplus b/p_t \sin\theta$. Accuracy in the mass measurement improves significantly as the tracker momentum resolution improves, even as it improves beyond the $a = 5 \times 10^{-5}$ level often cited as the goal for tracker resolution at the ILC. The SiD detector has superb momentum resolution, with a $\sim 2 \times 10^{-5}$; the dilepton recoil mass measurement will benefit accordingly.

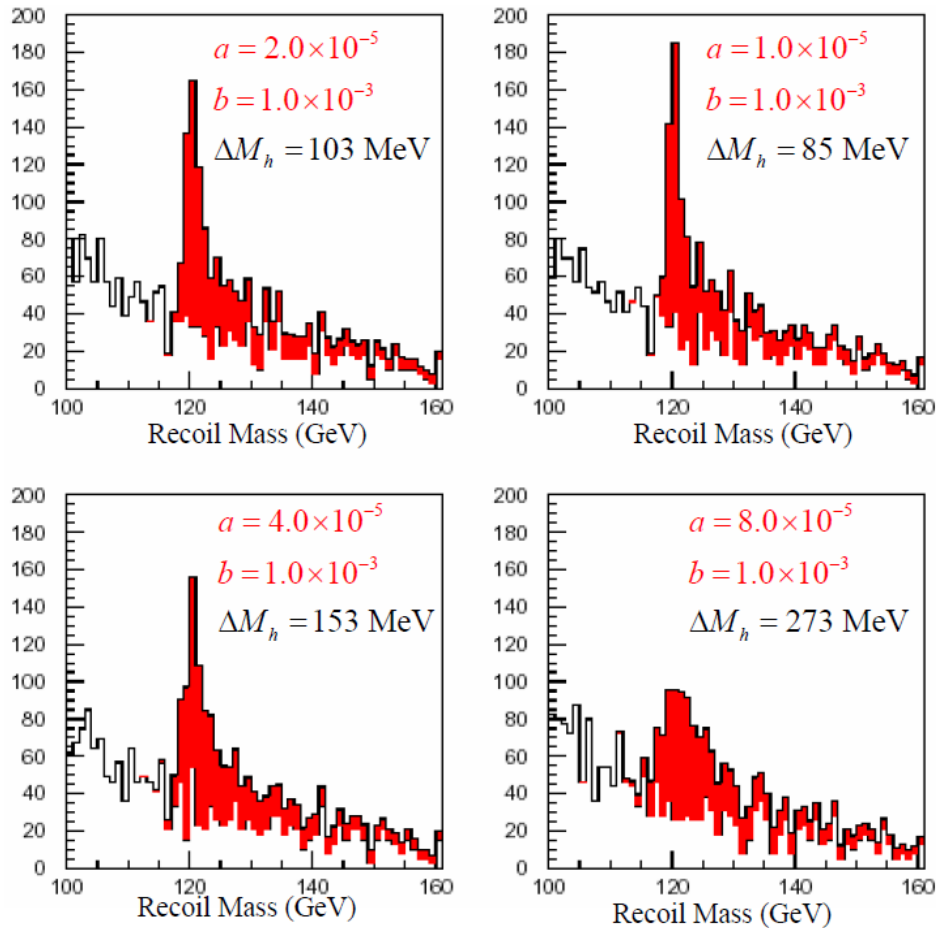


Figure 96 Higgs recoil mass spectra for several values of parameters characterizing the tracker momentum resolution.

The 4-jet channel provides a better measurement of the mass of the Standard Model Higgs, but the recoil mass technique will provide the best measurement of the Higgs mass if the Higgs has a substantial invisible branching ratio. Measurements of the ZH cross-section and Higgs branching ratios show little dependence on tracker performance since events outside the peak are used to maximize statistics.

Smuon and Selectron Mass Measurements

The ILC offers the possibility of determining the masses of the sleptons to high precision if their masses are within the machine's kinematic reach. Studies of the production of smuon and selectron pairs, and their subsequent decays to charged leptons and neutralinos, demonstrate SiD performance for this mass measurement and provide another example where the measurement sensitivity can depend on the tracker's momentum resolution.

Two studies have been performed. In the first we consider measuring the mass of a smuon in the coannihilation region, with mass 224 GeV, where the neutralino mass is 212 GeV. The study assumed running at $\sqrt{s} = 500$ GeV, and an integrated luminosity of 500 fb^{-1} . The measured momentum spectrum of the muon produced in the smuon's decay is

shown in Figure 97 for a variety of choices of the parameters a and b , which characterize the momentum resolution, $\delta p_t/p_t^2 = a \oplus b/p_t \sin\theta$. The visual impression that the measured spectra are essentially identical is confirmed quantitatively. The accuracy of the smuon mass, in fits where the neutralino mass is assumed to be held fixed at some predetermined value, is independent of variations of a in the range 1.0×10^{-5} to 8.0×10^{-5} , and independent of those in b in the range 0.5×10^{-3} to 4.0×10^{-3} . This is somewhat unsurprising, since the muon momentum spectrum is relatively soft and the tracker's momentum resolution in this region is especially good. The beam energy spread and radiative tail are reflected in the low and high ends of the muon energy spectrum, respectively, and dominate the observed spectral shape. Hence even the multiple scattering component of the tracker resolution, characterized by b , has essentially no impact on this measurement. For these closely degenerate smuon and neutralino masses, SiD can determine the smuon mass with an accuracy of 34 MeV.

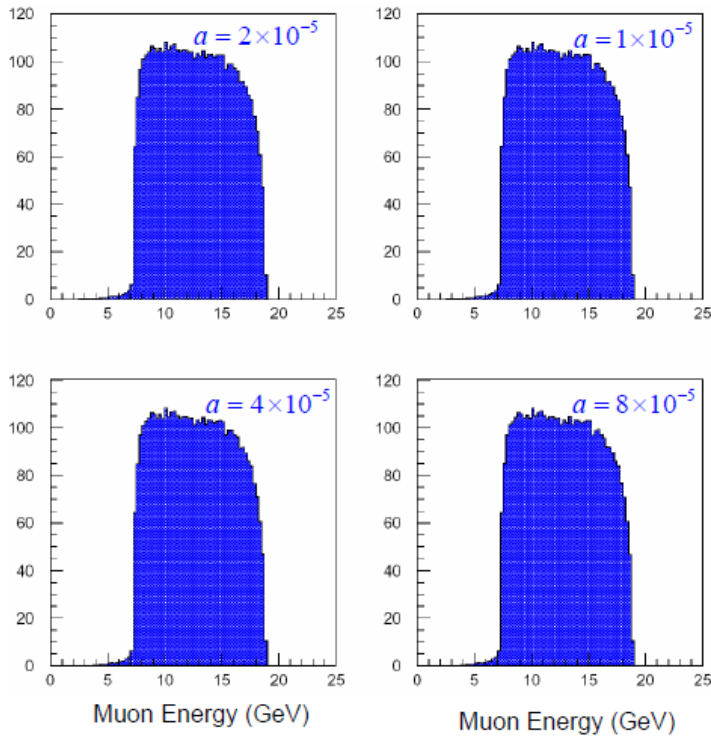


Figure 97 Muon energy spectrum for muons from the decay of 224 GeV smuons into a 212 GeV neutralino and a muon at $\sqrt{s} = 500$ GeV.

In a second study of selectron pair-production at $\sqrt{s} = 1000$ GeV, the combination of a much larger mass difference between the slepton and the neutralino (now 143 GeV and 95 GeV respectively) and operation at a higher energy, lead predictably to a very much higher lepton energy endpoint, 225 GeV in contrast to the 25 GeV above. See Figure 98. In this case, the tracker momentum resolution does influence how sharply the spectrum falls at the upper endpoint, and thus how accurately the mass of the slepton is determined. Assuming an integrated luminosity of 115 fb^{-1} , they determine the accuracy of the smuon mass will be about 80 MeV. As Figure 99 shows, this result depends on the beam spread,

and could be improved upon significantly if the tracker resolution was essentially “perfect”.

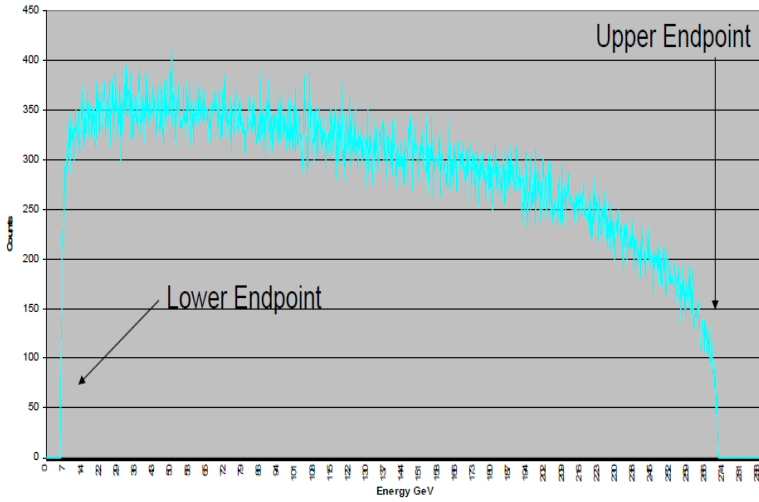


Figure 98 Energy spectrum for electrons from the decay of 143 GeV selectrons into a 95 GeV neutralino and an electron at $\sqrt{s} = 1000$ GeV.

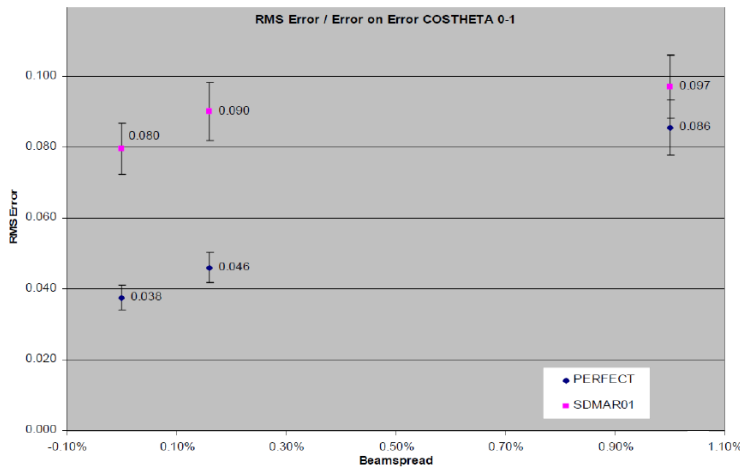


Figure 99 Accuracy of the determination of the selectron mass as a function of the beam energy spread. ILC has an energy spread about 0.1%. Accuracies are shown for the SiD tracker and for a perfect tracker.

E_{cm} Measurement Using $e^+e^- \rightarrow \mu^+\mu^-(\gamma)$

Accurately determining the center of mass energy at the ILC is prerequisite for many physics studies, and major efforts are being devoted to measuring the beam energy before and after the interaction. Because the E_{cm} measured upstream and downstream of the interaction point can differ from the luminosity-weighted E_{cm} by as much as 250 ppm, it is important to be able to compare such measurements with a direct detector measurement of the center-of-mass energy based on physics events. The latter measurement directly measures the luminosity-weighted center-of-mass energy. As we show below, the high performance of the SiD tracker is particularly advantageous in this measurement, which can be done by studying muon pair production, and radiative returns to the Z, where the Z subsequently decays to muon pairs.

E_{cm} measurements at LEP using $e^+e^- \rightarrow \mu^+\mu^-\gamma$ relied solely on lepton angle measurements because little additional information could be gleaned from a direct muon momentum measurement. The resolution was inadequate. However, with the tracker being considered for SiD, the momentum measurement can significantly improve the E_{cm} measurement over what can be achieved with angles alone. Figure 100 shows the accuracy with which E_{cm} can be determined with a data sample of 100 fb^{-1} by utilizing radiative returns ($Z\gamma$) or full energy muon pairs ($\mu\mu$) as a function of the parameters which describe the momentum resolution. For comparison, the accuracy obtained by using an angles-only measurement is also shown. For full energy mu pair production there is a strong dependence on curvature error, and for both methods there is a strong dependence on multiple-scattering because so many of the events are in the forward region. In any case, utilizing these reactions will improve the determination of E_{cm} to about 20 MeV. The superb resolution of the SiD tracker will impact these measurements.

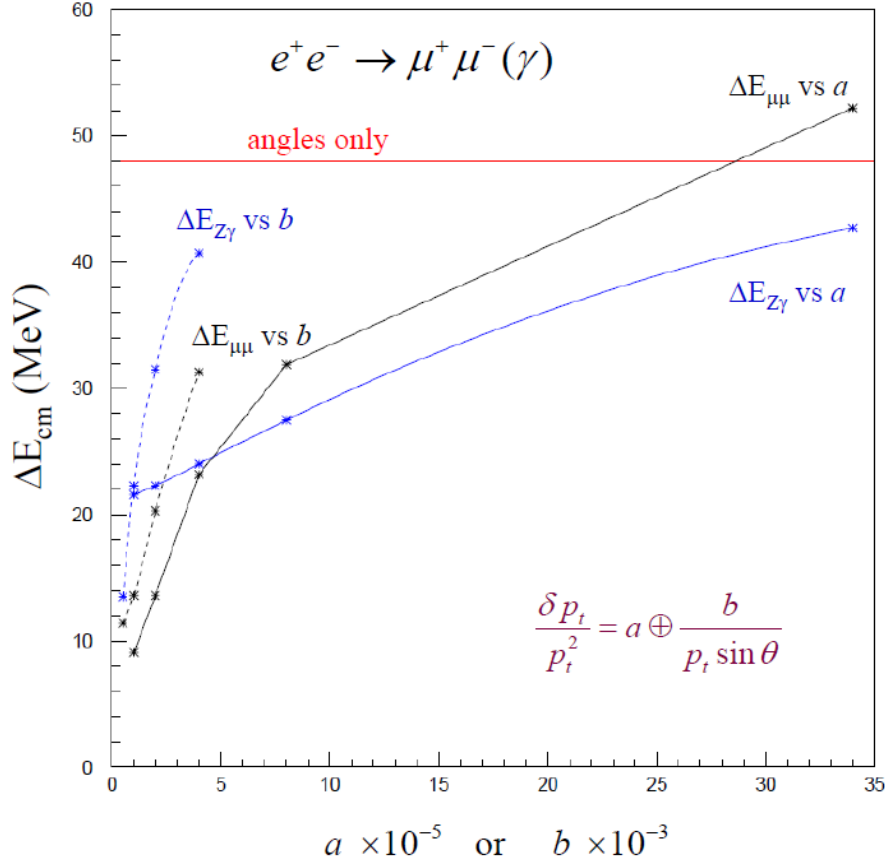


Figure 100 Error in E_{cm} as a function of the parameters describing the tracker momentum resolution coming from several possible measurements.

IV.C.2 Calorimeter and Energy Flow Physics Performance

Higgs Mass in the 4-jet Channel $e^+e^- \rightarrow ZH \rightarrow qqbb$

The measurement of the Higgs mass through the recoil mass technique is limited statistically by the relatively small branching ratio for Z boson decays to charged lepton pairs. The much larger statistics associated with hadronic Z boson decay can be utilized by measuring the Higgs mass in the 4-jet channel $e^+e^- \rightarrow ZH \rightarrow qqbb$ so long as the Higgs branching ratio to b quark pairs is large enough. We have studied the Higgs mass measurement in this channel assuming a Standard Model Higgs with a mass of 120 GeV, where the branching ratio to b quark pairs is 68%.

Following canonical cuts for hadronic final states with large visible energy, the charged and neutral tracks in an event are forced into 4 jets. If one jet-pair has a mass consistent with a Z boson and the other is consistent with two b -quark jets then the b -quark jet-pair is considered a Higgs candidate. The distribution of the reconstructed mass of the Higgs candidates is shown in Figure 101 for signal only, assuming several different values for the jet energy resolution. Note the asymmetry in the distributions. The shape of the curves to the right of each peak is determined by the detector's jet energy resolution while the structure to the left is dominated by undetected neutrinos in B meson decays.

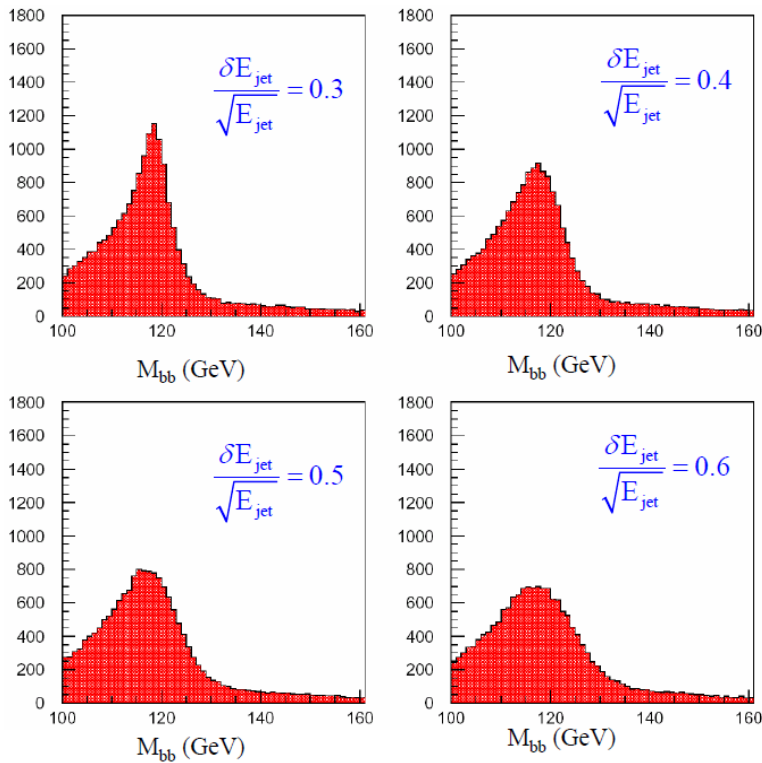


Figure 101 Reconstructed mass of Higgs candidate jet-pairs using particle flow information only (no beam energy-momentum constraint is used).

The asymmetry in the Higgs reconstructed mass distributions can be removed and the overall resolution can be improved by imposing beam energy-momentum constraints in a least-squares fit of the components of the four-vectors of the four jets in the event. The result is shown in Figure 102 where now both signal and background are displayed, along with the total statistical error on the Higgs mass.

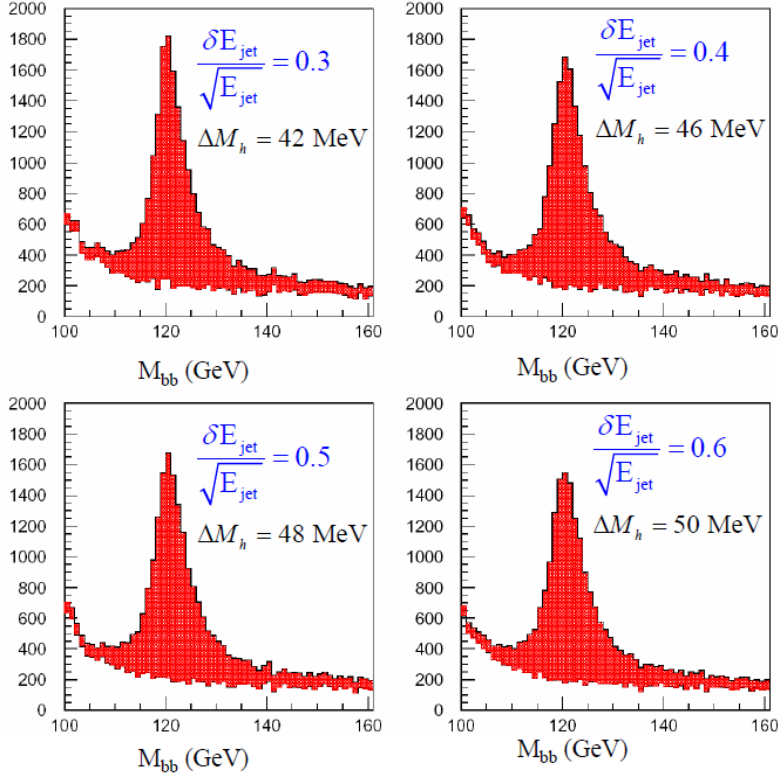


Figure 102 Reconstructed mass of Higgs candidate jet-pairs with beam energy-momentum constrained fits of jet 4-vectors included. Both the Higgs signal (red) and Standard Model background (white) are shown.

Beam energy-momentum constrained fits considerably improve the Higgs mass resolution in the 4-jet channel, but there is still something to be gained from better particle flow jet energy resolution. There is a factor 1.2 improvement in going from $\delta E_{\text{jet}} / \sqrt{E_{\text{jet}}} = 60\%$ to 30% , corresponding to an equivalent 40% luminosity gain.

Measurement of $BR(H \rightarrow WW^*)$

One of the principal motivations for building a detector with excellent jet energy resolution is the need to distinguish hadronically decaying W bosons from Z bosons in events where beam energy-momentum constraints either cannot be imposed or have limited utility (the improvement in resolution from energy-momentum constraints is greatly reduced in events with 6 or 8 fermions in the final state). A test of this kind of W/Z separation is provided by the measurement of the Higgs WW^* branching ratio in the reaction $e^+e^- \rightarrow ZH \rightarrow ZWW^* \rightarrow qqql\nu$. The results from a study¹⁷ of the dependence of the Higgs WW^* branching ratio error on jet energy resolution are summarized in Figure 103. There is a factor of 1.2 improvement in the branching

¹⁷ J.-C. Brient, <http://www-flc.desy.de/lcnotes/notes/PREL-LC-PHSM-2004-001.ps.gz>

fraction error in going from $\delta E_{\text{jet}} / \sqrt{E_{\text{jet}}} = 60\%$ to 30% , corresponding again to an equivalent 40% luminosity gain.

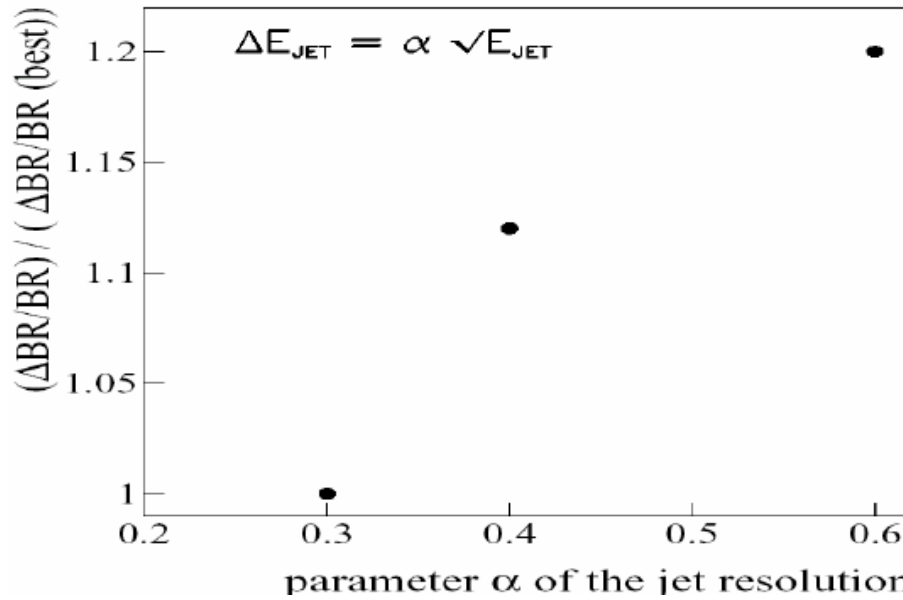


Figure 103 Measurement of $BR(H \rightarrow WW^*)$ from $e^+e^- \rightarrow ZH \rightarrow ZWW^* \rightarrow qqqlv$

Higgs Self-Coupling Measurement

The Higgs self-coupling measurement at $\sqrt{s} = 500$ GeV using $e^+e^- \rightarrow ZHH \rightarrow qqbbbb$ is a challenging measurement that requires excellent W, Z and H boson identification in a chaotic high track multiplicity environment with 6 jets. The total cross-section for $e^+e^- \rightarrow ZHH$ before factoring in Z and H branching ratios is only 0.18 fb. Major backgrounds include $e^+e^- \rightarrow t\bar{t} \rightarrow bbWW \rightarrow bbccss$ and $e^+e^- \rightarrow ZZZ, ZZH \rightarrow qqbbbb$.

The Higgs self-coupling measurement performed for the TESLA TDR¹⁸ has shown the strongest dependence on jet energy resolution of any physics study to date. The results are summarized in Figure 104.

¹⁸ C. Castanier et al., <http://arxiv.org/pdf/hep-ex/0101028>

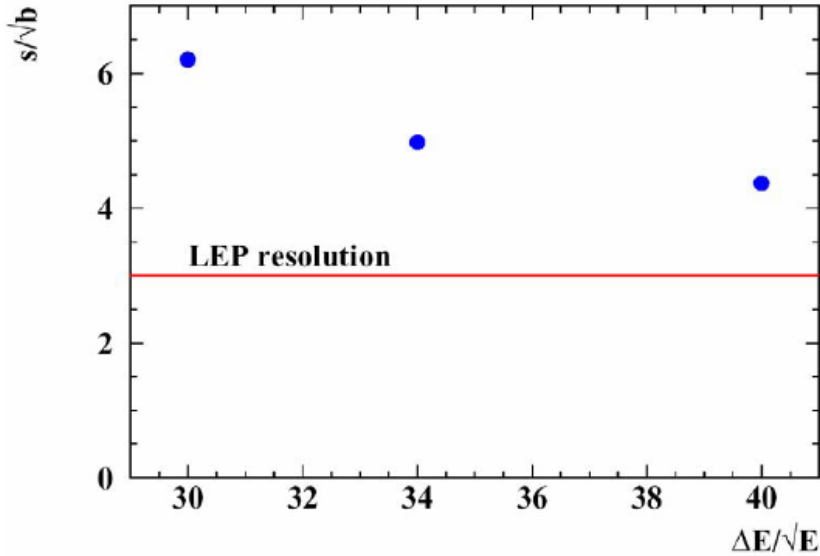


Figure 104 The jet energy resolution is important in reconstructing final state W, Z, and H bosons in the signal process $e^+e^- \rightarrow ZHH$ and in the backgrounds $e^+e^- \rightarrow ZZ, ZH, ZZH, WW, tt$.

The SiD is currently studying this process using the `org.lcsim` Fast Detector Monte Carlo. Preliminary results from a study of $e^+e^- \rightarrow ZHH \rightarrow qqbbbb$ show a weaker dependence on jet energy resolution than indicated by the TESLA TDR result. Neutrinos in the decay of bottom hadrons limit the Higgs mass resolution, while neutrinos in the decay of charm and bottom hadrons degrade the Z boson mass resolution relative to what is obtained assuming Z decays to u,d,s quarks only. For this particular analysis, excellent b-quark tagging may be more important than exquisite jet energy resolution. Final results from this study will be published soon.

V. SiD R&D Needs

V.A. R&D Issues

The period 2005 through 2009 is seen as the primary period for creating and testing new ideas for subsystem technologies, prior to specific proposals from eventual ILC detector collaborations. This period is not overlong for sorting through many technology choices, for instance, for tracking/vertex sensors, nor for constructing and beam testing major calorimeter stacks, and understanding the results.

The following sections describe all the current R&D activities for SiD in each sub-detector area. In each area we first give a list of the areas of activity and the institutions involved. Then we expand on the hardware R&D needs in these areas.

Vertex Detector

- a) Sensor options: SLAC, U. Oregon, and Yale
- b) Monolithic Active pixels: Fermilab
- c) Very thin hybrid pixels: Fermilab
- d) 3D devices: Fermilab
- e) Mechanical design: Fermilab, Annecy
- c) Pixel Vertex Detector Simulation and Design Optimization: SLAC, Fermilab, LCFI with collaboration/coordination with: U. Oklahoma, KEK, and RAL.

Materials R&D for Sensor support

To realize a vertex detector design that will achieve the ILC physics goals it is essential that the sensor layers be very thin and the support medium be of low mass material compatible with the cooling requirements for the whole detector. Possible candidates for the low mass material which require further study are Silicon Carbide Foam, Reticulated Vitreous Carbon foam and high modulus carbon fiber.

Power reduction

It is also critical to keep the heat dissipation low to reduce the mass required to extract this heat. Options under study are pulsed power and power starved circuits.

Sensor Technologies R&D

The sensor technologies that will require significant development to be considered as viable choices for the vertex detector include Monolithic Active Pixel Sensors (MAPS), Silicon on Insulator (SOI), 3D devices, and thinned Hybrid Pixel Detectors (HPD). MAPS sensors are being developed using both standard CMOS and specialized processes. The critical R&D issues for these devices are small signal levels, readout speeds, and radiation hardness. SOI devices offer the prospect of thin radiation hard sensors. 3D devices consist of multiple semi-conducting layers bonded into a monolithic structure. The challenges with these devices are the bonding and thinning down of the various layers. The HPD devices have a separate detector bonded to a readout chip. Dealing with devices thinned to thicknesses as low as 25 microns has never before been done in our field. There is significant R&D required to develop this technology. The electrical

characteristics of the devices need to be verified for the various thicknesses. Techniques for handling these devices and for construction of rigid readout structures will have to be developed. Furthermore, the radiation resistance will have to be mapped. Since the technology for ILC vertex detectors are very innovative based on new fabrication technologies, all R&D to establish the viability of this new technology as particle detector will have to be developed.

Beam Pipe design

Closely coupled to the vertex detector design is the design of the beam pipe which has a cylindrical center section, and conical end sections to reduce the pair background. Since the beampipe for a linear collider detector is very unconventional, some R&D is needed for the transition regions from the cylindrical sections to the conical sections. In addition, the linear collider environment requires the beamline to have a thin liner to reduce the negative effect of photons. Studies of applications of thin liners is required. The beampipe is thought to be made of Beryllium. There may be alternative materials to Beryllium, which are as reliable but significantly cheaper, that will need to be explored.

Tracking system

- a) Silicon strip sensor design and layout: SLAC and Fermilab
- b) Double-sided silicon sensors: BARC, Kyungpook National University
- c) Long shaping time thin Si-strips: UC Santa Cruz with collaborators from Fermilab, LPNHE Paris.
- d) Detector mounting frame/materials; the detector technology; detector ROC and cabling: SLAC, Fermilab
- e) Thin Si sensors: Purdue University.
- f) Simulation and alignment: University of Michigan.
- g) Reconstruction Studies: University of Colorado.
- h) Simulation Studies for Si tracker: Brown University.
- i) Calorimeter-based tracking for Particle Flow and Reconstruction of Long-Lived Particles: Kansas State University, collaborating with Fermilab, SLAC, University of Iowa, Northern Illinois University.

Tracker

Optimization of the SiD detector design calls for the use of a low mass tracking system which is foreseen to be implemented in the form of silicon strips. The ILC beam time structure allows the possibility of using a long shaping time, which has advantages in terms of noise reduction. The beam timing also potentially removes the need for an active cooling system, with consequently reduced mass for the tracker. Chip design is ongoing for the long shaping time readout, and a beam test of an initial system is expected in 2007-8.

For forward/low angle tracks it is essential to reduce the amount of material seen when traversing the tracker. Development of thin sensors is ongoing with critical issues being the yield of such devices, their signal/noise ratio, and aspects of mechanical support. The low mass and somewhat flexible tracking structures contemplated for SiD call for a new approach to sub-detector alignment in order to minimize systematic effects that

could impact momentum resolution. Under development is a Frequency Scanned Interferometry system first developed for the ATLAS Experiment at CERN. This system should provide knowledge of short term changes in alignment. Future developments will include the design of a multiple interferometer system, and a possible move from optical to infrared lasers to take advantage of mass-production in industry.

Tracker Alignment

A better quantitative understanding of the alignment will have to be obtained. In the very near future the conditions under which the dual-laser FSI¹⁹ system achieves adequate and better-than-adequate precision will be explored and better quantified. More extreme environmental disturbances will be introduced, including multi-component vibrations. Soon afterward we plan to start addressing a major milestone in this research: miniaturization of the FSI optical components, as preparation for building a partial prototype of the alignment system.

At the same time, we wish to begin confronting the technical issues in constructing multiple interferometers fed by common lasers through an optical fiber fan-out. Once the multiple fiber interferometers have been obtained, one can verify with a benchtop movable-stage test that 3-D reconstruction of positions of tracker element mockups can be achieved.

For now, the work has been done with optical lasers and corresponding optical components. For development of techniques on a benchtop, that choice has proven wise in dramatically shortening the turn-around time on configuration changes, in allowing us to exploit existing laser/optics infrastructure in our laboratory, and in fostering a safer work environment. In the long term, however, in building a full alignment system for a Linear Collider Detector, we expect significant cost reductions to be possible by using mass-produced infrared lasers and beam components, because of the prevalence of infrared devices, including scannable lasers, in the telecommunications industry. Also a decision has to be taken on whether to continue working at optical frequencies or to switch to infrared. The decision will depend not only on the relative speeds of commercial technology improvements at those frequencies, but also on the status of the Linear Collider development itself and the availability of funds to move to infrared technology. The faster the ILC effort moves, the sooner we will have to confront this important technology decision.

It should also be noted that the methods we develop for central and forward tracker alignment may also prove useful for a vertex detector, where again, there is a strong desire for thin detector material that may be subject to short-term position fluctuations.

¹⁹ "Frequency Scanned Interferometry (FSI)": The Basis of a Survey System for the ATLAS ID using fast automated remote interferometry", A.F. Fox-Murphy (et al.), Nuc. Inst. and Meth. (A383), 229 (1996); "Frequency Scanned Interferometer for ILC Tracker Alignment", H. Yang, S. Nyberg and K. Riles, Presentation at International Linear Collider Physics and Detector Workshop at Snowmass, Colorado, August 14-27, 2005, <http://tenaya.physics.lsa.umich.edu/~simshyang/talks/Snowmass-FSI-2005.pdf>, to appear in the workshop proceedings.

Similarly, our methods may prove useful for alignment monitoring of accelerator components far upstream of the detector (e.g., in the main linacs). Given the natural wide distribution of accelerator components versus a relatively compact tracker system, however, it's not clear that a tracker solution will be cost effective for the accelerator. In any case, we will stay cognizant of vertex detector and accelerator needs and explore these possibilities, as the tracking alignment system design evolves.

A longstanding question in the Linear Collider Detector community is the importance of material burden in the central tracking system. One naturally wishes to avoid introducing unnecessary material in the tracker because it creates multiple scattering, affecting momentum resolution for low-momentum tracks, and because it leads to photon conversions and electron bremsstrahlung, causing confusion in event reconstruction. On the other hand, as discussed above, going to the extreme of an ultra-lightweight silicon tracker, to avoid material burden, invites mechanical support and alignment issues. This tradeoff needs to be quantified. Simulation work on slepton spectral endpoints indicates that one can, in fact, tolerate relatively large material in the tracker, but the not-yet-addressed case of nearly degenerate sparticle masses could lead to final states of very low momenta, where the effects of multiple scattering are more pronounced. Simulation studies will be carried out addressing these issues.

Integration of Vertex Detector and Tracker and Beam Pipe

Continuing design work is required to understand the mounting of the vertex detector and forward silicon tracking elements on the beam pipe, and the coupling of the beam pipe and vertex detector assembly to the tracker – including mechanical and heat load transfers between these elements.

Electromagnetic Calorimetry

Silicon/Tungsten.

- a) Silicon sensors: University of Oregon, SLAC
- b) Kpix chip: SLAC, BNL, University of Oregon, University of California at Davis.
- c) Mechanical design: LAPP(Annecy)

The first silicon sensors are under test at U.Oregon and show good results. The short to medium term goal is to assemble a full-depth e.m. stack of sufficient transverse dimensions to contain electromagnetic showers. Testing of sensors planes and measurement of the tungsten plates will proceed in 2006-7. Development is also required to achieve the bump bonding the Kpix chip to the sensor. Subject to the availability of components, it is anticipated that the full-depth module will be tested in beam towards the end of 2007. Mechanical design of SiD EM calorimeter modules is underway with a shell and beam approach, locating the beams which penetrate through the calorimeter layers, at the corners of the hexagonal silicon sensors. This design will be further developed within the context of the overall SiD detector.

Hadronic Calorimetry

a) GEM-based: University of Texas at Arlington, University of Washington, Changwon National University, Tsinghua University.

In 2006 the 30cm x 30cm chambers will be exposed first to a low energy electron beam in Korea for characterization studies, and then to hadron beams at the Fermilab MTBF. In parallel, 1m x 30cm foils are being developed with 3M Corporation. We expect the first of these large foils to be available in Fall 2006. They will be used in full-size GEM planes that will also be exposed at MTBF as the first step towards building a full 1m³ stack for tests of fully contained hadronic showers versus an equivalent GEANT4 simulation, and for assessing the overall performance of a GEM-based digital hadron calorimeter system for SiD.

In a parallel development new “Thick GEM” planes will be built and tested at UTA. If these prove to be reliable and, particularly if they are cheaper to produce than the 50 μ m foils, then a program will be rapidly instigated to produce large chamber using this alternative approach.

b) RPC-based: ANL, Beijing, Boston University, University of Chicago, Fermilab, University of Iowa, Princeton.

Further development will be pursued thinner chambers, possibly by using only one glass plate and the front-end board to complete the gas volume. The key issues are the robustness and longevity of such an arrangement. Other R&D centers on the readout electronics and data concentration. It is desirable to increase the number of channels multiplexed through one front-end ASIC, and to develop more multiplexing at the data concentrator level.

c) Scintillator-based: NIU The viability of a ScSiPM-based HCal is being studied through the CALICE collaboration DHCal/TCMT test module with results expected at the end of 2006. Work is underway on mechanical and electronic engineering, large-scale production and assembly, and calibration. Innovative designs with SiPM’s mounted directly onto the scintillator would allow for smaller cell sizes, but are contingent on industrial development of suitable SiPM’s.

d) Particle Flow Studies (simulation only): University of Iowa, ANL, NIU, SLAC, UTA

Muon system and tail catcher

RPC Option Many large RPC systems have been built within the last 10 years and understanding their performance will provide strong guidance to a SiD design. Other smaller scale studies are attempting to understand the role of gas pollutants in RPC aging. All of the working RPC systems utilize Freon as a major gas constituent. Several researchers have found significant levels of HF acid in the exhaust gas indicating the breakdown of the Freon or SF₆ during the gas avalanche or streamer. BELLE found that in the presence of water vapor that the HF would etch the glass surface, generating sizable noise currents and lowering efficiency. The effect on Bakelite RPCs is less understood, but there is clear evidence that pollutants generated by high rate in the gas can affect both the noise rate and dark current.

Groups from the University of Wisconsin and Roma are measuring the fluorine levels of the exhaust gas in both streamer and avalanche RPCs at BaBar and correlating these levels with the chamber current, noise rate, and efficiency. They will also study the rate

of fluorine absorption on the RPC Bakelite surfaces. Longer term goals are to develop RPC gas mixes which either eliminate or substantially reduce the Freon component. A group at Princeton University is also studying the effect of HF on Bakelite surfaces and will extend these studies to the new RPCs developed for the BESIII experiment which have plastic coating the inner Bakelite surfaces.

Extruded Scintillator Option The Muon system and tail catcher specifications are not yet fully developed. To reach a final system design simulations can provide numbers to use as the basis for parameter choices. Examples include studies of muon identification efficiency and purity for semi-muonic decays for inclusive b-pairs. Present preliminary conclusions using Kalman filter tracking, show, that for a total of 8.4 interaction lengths (λ) in the barrel (after 16 planes of muon detectors) for a geometry where the Fe plates were 2" thick, the muon identification is >92% while the purity reaches 88%. These studies need to be extended to $\sim 18\lambda$. Extending the present studies from 8.4λ to 18λ requires the development of Kalman-filter muon-tracking in the forward muon systems.

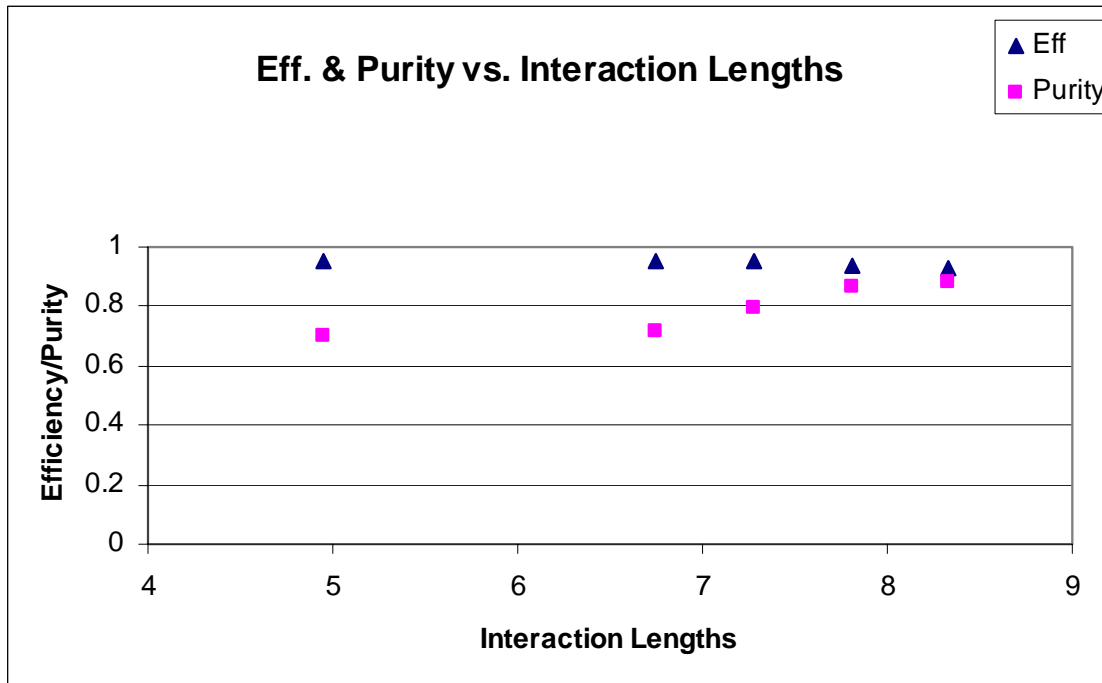


Figure 105 Muon Identification and Purity vs. Interaction lengths for inclusive b-pair production at 500GeV. Preliminary studies have been carried out for barrel muons only where the minimum muon momentum is required to be greater than 3 GeV/c.

It is also important to understand the impact of hadron shower leakage into the muon system for two reasons: (1) to understand how frequently a hadron from a b-jet is confused with a nearby muon from the same jet at the entrance of tracks into the muon system and (2) to characterize the use of the muon system in the measurement of jet energy in the region downstream of the solenoid after 6.9λ . A set of 4 equally-spaced wire chamber planes, over a distance of 30 cm, at the entrance to the muon system is calculated to give position and angular resolution for entering tracks that is significantly better than is obtained by projecting the tracks through the 1.3λ SC solenoid plus cryostat

system. This more precise starting point for muons as they enter the muon system would provide better rejection of charged hadrons that are near muon candidates. The additional rejection could be determined from further studies of simulated b-pair production in which one of the b's contains a muon in its decay chain. This study would require a modified SiD muon layout and regeneration and analysis of simulated inclusive b-pair production. Russian groups at IHEP and JINR have indicated interest in working on this problem.

As mentioned in the muon system design section earlier, the design is based on the use of multi-anode photomultiplier tubes for scintillator light detection. Measurement of $\frac{1}{4}$ sized scintillator strip planes using cosmic ray muons indicate the MAPMT signals are very fast rising/falling pulses (20% to 80% in ~ 1 ns) with a mean accumulated charge of ~ 3.5 pC for charged particles that pass through the middle of a 2m long strip. Four $\frac{1}{4}$ sized strip-scintillator detector planes are setup in the Fermilab MTest beamline for further tests to measure the strip-scintillator properties. Because the WLS fiber (Kuraray Y-11) measured decay time of 12ns is longer than the dE/dx produced light pulses it may be important to develop/test faster WLS fiber with equivalent light output if that is possible.

We need to understand if it is possible to collect light from two 1.2mm fibers in one 2mm square pixel. In principle it looks almost possible, but the response across the 2mm square pixel is larger than 50% for only slightly more than half the pixel.

We also expect to procure so-called Silicon based photon detectors (SiPMs) for tests with our planes. The most straight-forward way to compare the SiPMs and MAPMT detectors would be to build an additional set of essentially identical planes to be evaluated at the MTest beam. It is already known that both the Russian SiPMs and the Hamamatsu Multi-Pixel Photon Counters (MPPC) work in the limited Geiger and Geiger mode where the signal is the sum over many 10μ cells. The ALC scintillator-based muon R&D group is following closely the research of the Colorado State University physicists who are working with a Boston firm, APeak, to develop limited Geiger mode APDs. All of these detectors suffer from saturation and they have high noise rates $\sim 500 - 900$ KHz at 20 C, but these problems may be tolerable since they work well in magnetic fields and do not require optical fiber beyond the WLS associated with the extruded scintillator.

Finally we know that an ILC muon detector will require both monitoring and calibration. Our planes at the MTest beam have built-in illumination strips (Beer sign technology) that we pulse with blue LEDs. The illumination strips are optically coupled to the WLS fibers as they exit the scintillator strip, thereby being sensitive to a calibration pulse. Each LED is also viewed by a PIN diode so we can keep track of the absolute LED output. We are just beginning to look at the scintillator clear fiber output when the LEDs are pulsed. Our goal is to record the standard fiber input to digitizing electronics that is used to take test beam data. This can be compared with MTest beam MIPs and measured MAPMT gains using photons in bench tests. Our first priority has been to understand

MIPs with the MAPMT system and then to develop the in situ calibration with external light sources. The measurement of MAPMT gain is described in Karchin's report²⁰

Forward Region (BNL and Univ. of Oregon):

a) Simulation

A baseline detector layout is expected by mid-2007 and will include the specifications and parameters for the Beam Cal and Luminosity Cal.

b) Integration

The crowded forward region needs careful design to accommodate the final focus magnets, beam pipes, and the forward calorimeters and their services. A baseline design is anticipated by mid-2007.

c) Mechanical Design

Design studies are needed to understand space constraints, and the support of the calorimeters off the forward tube. A baseline design is expected in Fall 2007.

d) Electronics

R&D is needed on the readout architecture, including feedback from the Beam Cal to the accelerator.

e) Materials

Testing of specialized silicon material to withstand the high radiation levels of the forward region will be needed. These will be carried out at the BNL Instrumentation facility.

f) Forward Had Calorimeter

It may be necessary to implement the forward parts of the HCal in a different technology from the main calorimeter system. Material studies and radiation testing will be required, including beam testing.

General electronics:

KPix, High-density front-end chip: SLAC, BNL, University of Oregon.

A 64-channel prototype chip has been made and is being tested. A second chip submission will be made in March 2006. The final KPix chip will have 1024 channels. The chip has initially been developed for the EM calorimeter, but is also applicable to the Si-strips of the tracker and to the gas calorimetry options for the HCal, subject to the development of suitable readout boards, and an opposite polarity version for the GEM-DHCal.

Magnet: CMS-style superconductor: Fermilab.

The immediate development goal for the SiD Solenoid is closely tied to monitoring the turn-on and initial operation of the CMS solenoid. The first design ideas indicate that a

²⁰ P. Karchin, "A Scintillator Based Muon Detector for the Linear Collider," in proceedings of the meeting of the Division of Particles and Fields of the American Physical Society, University of California, Riverside, August, 2004, International Journal of Modern Physics A, World Scientific Publishing Company.

CMS-style conductor should be viable for SiD. For an SiD specific design, detailed studies will be needed for the winding design to verify stability and safety, to optimize the conductor design, and to define the operating characteristics. Studies are also required for the design of a detector Integrated Dipole system. Items to be investigated include DID coil location, support and forces, interaction of the DID field with that of the main solenoid and DID quench safety versus critical events in the main solenoid.

V.B Schedule for answering Issues

While the R&D schedules for the various SiD subsystems will naturally vary according to level of new development needed, the effort available, and provision of the necessary funding, we can anticipate the following general timeline:

- 2005-2006 Many approaches to each subsystem, sorting through and understanding options.
- 2007-2008 Medium scale tests of selected technology(s), data analysis, technology comparisons and selection(s).
- 2008-2009 Design and prototyping phase for selected technology for each subsystem, iteration towards final design for SiD full detector proposal.

V.C Beam Tests needed

- a) Vertex sensors
Demonstration of viability of all possible technologies, in particular, charge collection, charge sharing, pixel uniformity, position resolution, readout speeds, electromagnetic interference effects and so on.
- b) Tracking sensors/ladders
Demonstration of long shaping time readout of Si ladders 2007-8.
Tests of new sensor technologies for the vertex detector ~2008-2010.
- c) Calorimeter – Ecal
Tests of single planes with KPix readout in SLAC test beam 2006-7
- d) Calorimeter – Hcal
Tests of single RPC and GEM planes in 2006, followed by full 1m³ stack(s) in 2007-8
- e) Muon system/tail catcher
- f) Very forward systems
Tests of prototype sections for Beam Cal and Luminosity Cal.
- g) Readout Electronics
DCal chip testing with single RPC and GEM planes in 2006-7.
KPix chip tests in association with EM Cal, Si-strip, and HCal prototypes.

V.D Estimating R&D costs

We have considered two approaches to estimating SiD R&D costs. The first approach uses information on past support and what is known about requests for the near future. This information was supplied to the WWS R&D Panel in 2005.

(Show the FY05 etc levels of funding and the mismatch between FY06 etc. requests and what we anticipate to be available – US only??)

In the second approach we attempted to take a more comprehensive, long-term view of R&D costs. We started from the total estimated detector cost of ~\$600M, and, from experience, estimated that overall we would spend 15% of this on R&D (initial studies and all the way through design and prototyping, to the start of final detector construction. Each subsystem was assigned a percentage and a contingency, based on prior experience, and perceived risk. The results are given below and should be taken only as a first coarse estimate:

Table 11 Estimated R&D costs by subsystem.

SiD Subsystem	System Cost (M\$)	R&D % (%)	R&D Cost (M\$)	R&D Contingency (%)	R&D Cost w/Contingency (M\$)
VXD	6.0	50	3.0	20	3.6
Tracker	19.9	15	3.0	20	3.6
EMCal	74.7	20	14.9	20	17.9
HCal	74.2	15	11.1	20	13.4
Muon system	52.1	10	5.2	20	6.3
Electronics	37.5	50	18.8	20	22.5
Magnet	167.1	10	16.7	20	20.1
MDI	20.0	10	2.0	20	2.4
Forward Region	3.0	50	1.5	20	1.8
TOTALS/AVG	457.5	25.6	77.7	20	93.4

VI Costs

A preliminary cost model for SiD has been developed consisting of two components – a static set of costs for detector components that depend only weakly on the major SiD parameters, and a parametric cost model for those costs that strongly depend on the parameters. Examples of the first set are engineering for electronics or the luminosity monitors themselves. Examples of the second are the solenoid and iron, the silicon detectors for the EMCal, and the tungsten for the calorimeters.

The parametric model allows the calculation of cost derivatives. The driving term appears to be the cost of the superconducting solenoid, but this is very preliminary. The cost model is based on the PDG power law parameterization based on the stored energy, but is

fit to the present information on the cost of the CMS solenoid. It is shown in Figure 106 along with a linear fit.

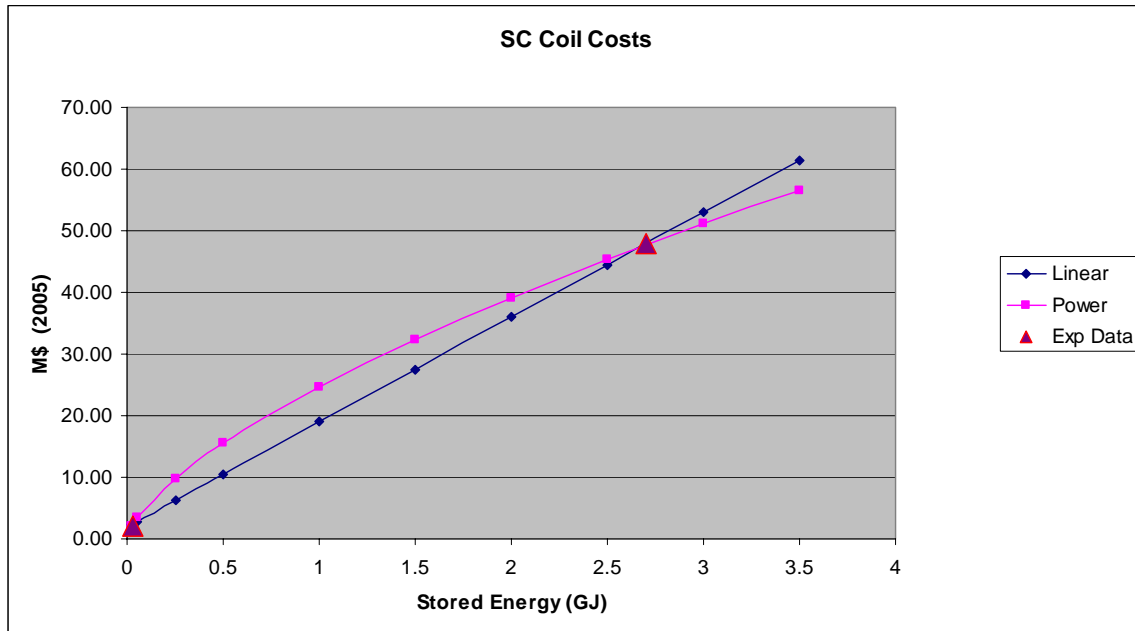


Figure 106 Crude estimate of cost of CMS style solenoid parameterized by stored energy. The curve is $AE^{0.662}$, where E is the stored energy.

There are about ten unit costs that are critical to the validity of the model. These include the solenoid, EMCal detectors, Si strip detectors, and the HCal radiators and detectors. Little progress has been made on developing a consensus on these unit costs among the concepts. It also is clear that the detector radius is expensive, and that calorimeter gaps (between radiators) should be minimized for both physics performance and cost. Figure 107 is an example of a plot showing the cost dependence of varying the tracker radius while holding BR^2 fixed. It is quite possible that the variation is out of the range of validity for the solenoid cost.

Examples of the unit costs presently used are:

\$3/cm² for Si detectors (35% contingency) (in very large quantities procured more than 5 years from now). Note that this is for the detector only without electronics or mounting;

\$3.50/Kg (35% contingency) for machined finished iron for the flux return.

\$63/Kg (50% contingency) for 2.5 mm tungsten plate.

In electronics and DAQ, an estimate is made for online computing, actual data acquisition, and slow controls, but not for data analysis and Monte Carlo computing. Front end electronics costs are believed to be dominated by cables and connections, with the “sophistication” of the Si chips rather weakly affecting costs.

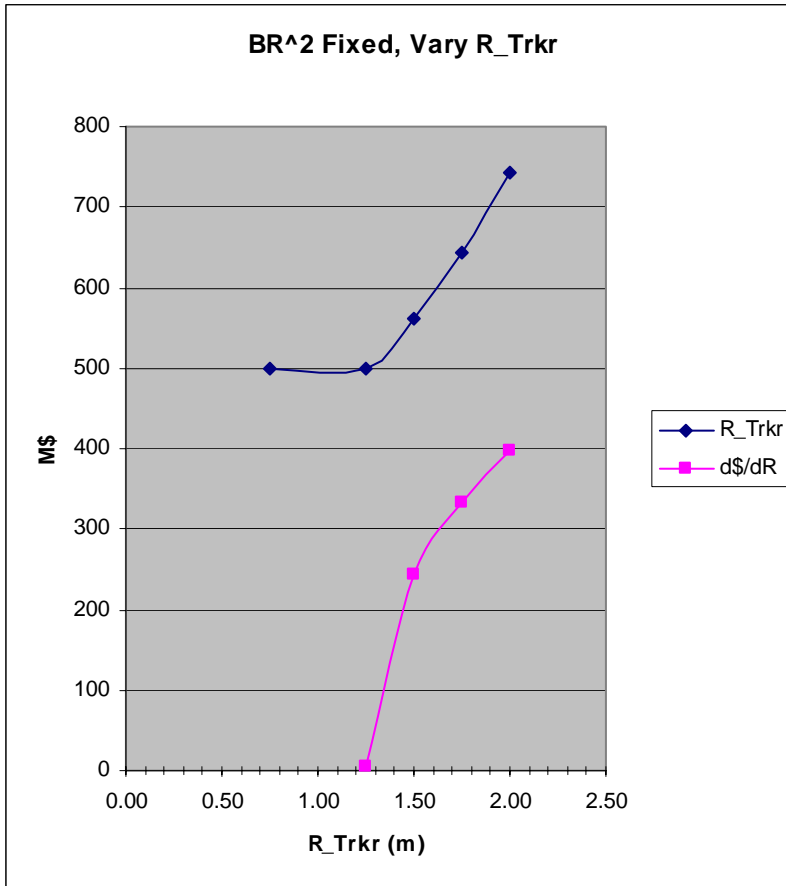


Figure 107 SiD total cost vs R_Trkr, holding BR² fixed. See caveats in the text.

The model is done in US DOE costing style, with explicit contingency, costed labor, indirects, and escalation. The base cost is defined as M&S + labor, without contingency, and is \$255M. The contingency, at \$98M, is 39% of the base. Labor, including the labor contingency, is 27% of the base. Escalation is based on a yearly inflation rate of 3%, a construction start in 2011, and 6 years to complete. This is likely optimistic. Indirects, which cover various host organization administrative costs such as purchasing or offices, are calculated at 6% on M&S, and 20% on labor. These numbers are based on SLAC's indirects for large projects, but these vary widely and may also be optimistic. Figure 108 indicates the costs for each system, including labor and contingencies for each item.

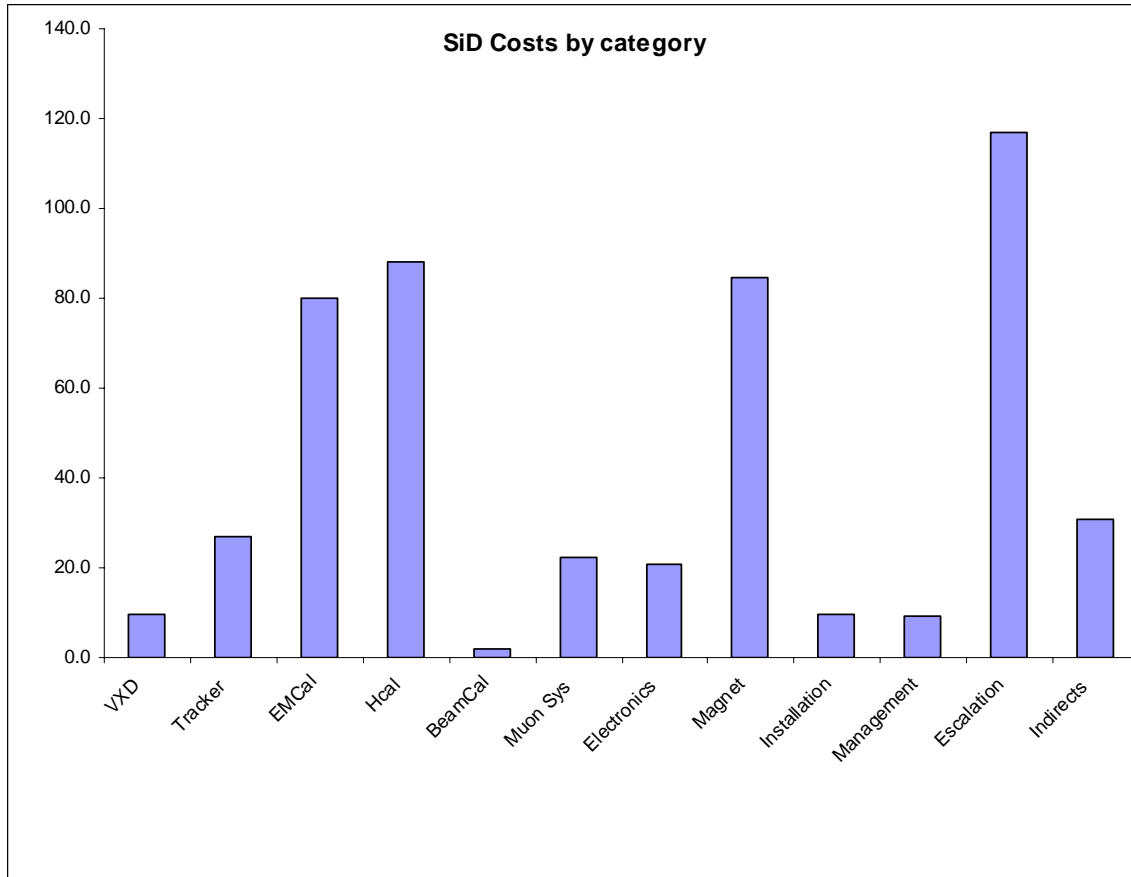


Figure 108 SiD costs by subsystem. Note that labor and contingency are included in each technical system.

Figure 109 breaks down costs by category.

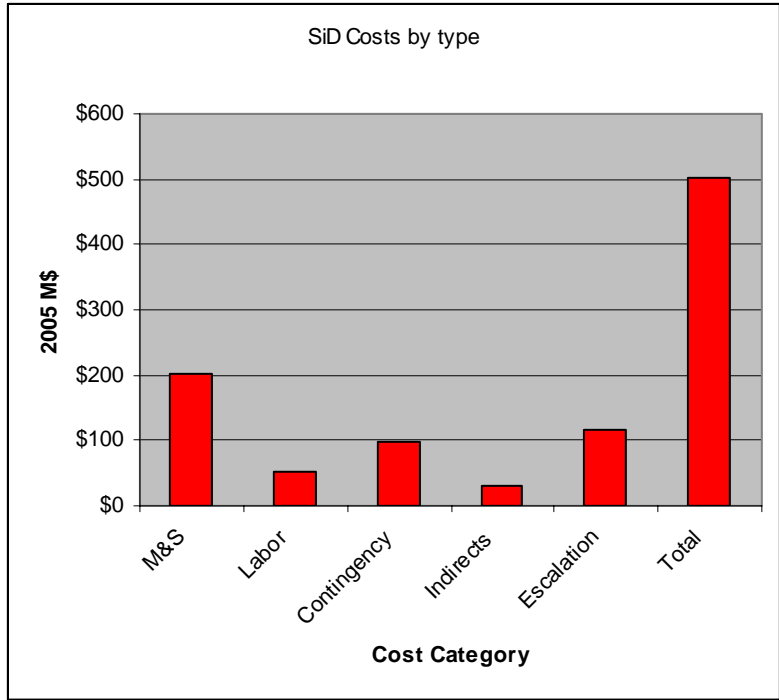


Figure 109 SiD Costs by category.

There is some pressure to change to “ITER style” costing, but there has been little progress in really understanding how the ITER system works. For this SiD estimate, the base M&S costs are \$203M, or 40% of the “total”. For amusement, it has been suggested that the ITER poloidal magnet has an ITER value of \$0.5B, but that it has a US price of \$1.3B – or 38%. This may be suggestive!

VII. Conclusions and future plans

The principal goal of the SiD Design Study has been, and remains, to design a detector optimized for studies of 0.5-1.0 TeV $e+e-$ collisions, which is rationally constrained by costs, and which utilizes Si/W electromagnetic calorimetry and all silicon tracking. Concomitant goals have been to identify and encourage the R&D needed to realize the SiD detector, select technologies appropriate for each of the detector subsystems and to document SiD's mechanical designs, subsystem performance, and integrated physics performance. This Detector Outline document serves to record the considerable progress made to date toward these goals.

What has been accomplished, and what has been documented here, is a first realistic detailing of the conceptual starting point given by Brau and Breidenbach. Toward this end we have developed conceptual mechanical designs that realistically account for the material budget of sensors, supports, and readout, and that are buildable and serviceable. These designs have been captured in a full Geant4 description of SiD in sufficient detail that SiD's physics performance can be reliably simulated.

Full Monte Carlo tracking pattern recognition code, calorimeter particle flow algorithms, detailed device simulations, and realistic background simulations have been developed, and are being further refined, in order to bring a new level of realism to the simulation of ILC detectors. The driving term in this simulation effort is particle flow algorithm development, which is still actively evolving but nearing the stage where it can be put to use. We have felt all this essential if we are to make informed design decisions and accurately characterize SiD's physics performance. We have nearly realized the goal of developing a full and realistic Monte Carlo simulation of the detector's response to physics, backgrounds, and noise, so that we can evaluate subsystem performance and analyse benchmark reactions in the ILC environment.

Detector technologies for each of the SiD subsystems are being developed by those in the Design Study as well as others worldwide. We are in the process of assessing which technology is best for which system, and actively planning for the R&D needed to establish proofs of principle for the various subsystem technologies.

Re-evaluating the sub-system performance requirements, and the as-designed performance obtained, and benchmarking the integrated detector performance on key physics measurements are the final ingredients to the optimization process. Ultimately, we plan to study SiD's physics performance as we vary key geometrical parameters, and as we vary subsystem design parameters. Lots of work remains, and lots of workers are needed for this real work on optimization. We have only just begun to characterize SiD's physics performance.

With the conclusion of the Detector Outline, the SiD Design Study will resume the process of evaluating and optimizing the SiD design. The original assumptions behind the design are still untested, most of the "SiD Critical Questions" are still unanswered,

and the simulation tools needed for these tests and answers are now coming on line. Using particle flow algorithms to characterize the jet energy resolution, and full tracking pattern recognition code to monitor reconstruction efficiency and resolution, we will study SiD's integrated physics performance and cost as we vary the global detector parameters, B field strength, ecal inner radius, and ecal length. These studies should lead to an optimized design and informed choices of subdetector technologies as well as document for the worldwide physics community the performance and cost of the SiD detector.

As the ILC moves forward toward realization as a funded project, detector designs will require further detail and proofs of principle and detector performance studies will need more breadth and documentation. We anticipate the eventual call for Detector Concept Conceptual Design Reports, and expect this present document, the SiD Detector Outline, will serve as a basis for that next step.